Transactions of the ASME®

Journal of Fluids Engineering

Published Quarterly by The American Society of Mechanical Engineers

VOLUME 109 • NUMBER 3 • SEPTEMBER 1987

Announcements and Special Notices

(Contents continued on page 323)

FLUIDS ENGINEERING DIVISION
Technical Editor
FRANK M. WHITE (1989)
Executive Secretary
L. T. BROWN (1989)
Calendar Editor
M. F. ACKERSON

Associate Editors
Fluid Machinery
WIDEN TABAKOFF (1988)
RICHARD F. SALANT (1987)
Fluid Measurements
ALEXANDER DYBBS (1987)
Fluid Mechanics
J. A. MILLER (1987)
HUGH W. COLEMAN (1987)
STANLEY F. BIRCH (1988)
WILLIAM W. DURGIN (1988)
Fluid Transients
FREDERICK J. MOODY (1989)
Numerical Methods
PATRICK J. ROACHE (1988)
Multiphase Flow
M. C. ROCO (1988)
GEORGES L. CHAHINE (1986)
Review Articles
K. N. GHIA (1988)

BOARD ON COMMUNICATIONS
Chairman and Vice President
K. N. REID, Jr.

Members-at-Large
J. T. COKONIS
M. FRANKE
M. KUTZ
F. LANDIS
J. R. LLOYD
T. C. MIN
R. E. NICKELL
R. E. REDER
R. ROCKE
F. W. SCHMIDT
W. O. WINER

President, **R. ROSENBERG**
Executive Director
D. L. BELDEN
Treasurer,
ROBERT A. BENNETT

PUBLISHING STAFF
Mng. Dir. Publ., **J. J. FREY**
Dep. Mng. Dir. Publ.,
JOS. SANSONE
Managing Editor,
CORNELIA MONAHAN
Editorial Production Assistant,
MARISOL ANDINO

Transactions of the ASME, The Journal of Fluids Engineering (ISSN 0098-2202) is published quarterly (Mar., June, Sept., Dec.) for $105 per year by The American Society of Mechanical Engineers, 345 East 47th Street, New York, NY 10017. Second class postage paid at New York, NY and additional mailing offices. POSTMASTER: Send address changes to The Journal of Fluids Engineering, c/o THE AMERICAN SOCIETY OF MECHANICAL ENGINEERS, 22 Law Drive, Box 2300, Fairfield, NJ 07007-2300.

CHANGES OF ADDRESS must be received at Society headquarters seven weeks before they are to be effective. Please send old label and new address.

PRICES: To members, $24.00, annually; to nonmembers, $105. Add $6.00 for postage to countries outside the United States and Canada.

STATEMENT from *By-Laws.* The Society shall not be responsible for statements or opinions advanced in papers or . . . printed in its publications (B7.1, Par. 3).

COPYRIGHT © 1987 by The American Society of Mechanical Engineers. Reprints from this publication may be made on condition that full credit be given the TRANSACTIONS OF THE ASME, JOURNAL OF FLUIDS ENGINEERING and the author, and date of publication be stated.

INDEXED by Engineering Information

Downloaded 03 Jun 2010 to 171.66.16.159. Redistribution subject to ASME license or copyright; see http://www.asme.org/terms/Terms_Use.cfm

Contents (Continued)

Downloaded 03 Jun 2010 to 171.66.16.159. Redistribution subject to ASME license or copyright; see http://www.asme.org/terms/Terms_Use.cfm

ERRATUM

A. M. Godon and J. H. Milgram, "Mixing of Fluids in Tanks by Gas Bubble Plumes," JOURNAL OF FLUIDS ENGINEERING, Vol. 109, June 1987, pp. 186–193.

The following section was omitted from the published version of the paper.

Conclusions

The rapid mixing which can be achieved with bubble plumes can be characterized by equation (18) for square based tanks and a considerable range of liquid heights, gas flows and plume distribution pipe configurations. This characterization of mixing versus the dimensionless time, t'', was accurate in our experiments except when the fluid depth and gas flow were both small. The most likely cause of this is the artifact of premixing by the method of dye introduction. Thus equation (18) may even be accurate for the small depth and gas flow conditions. Since equation (18) predicts the mixing for three different overall flow patterns the equation may be applicable to a broader range of conditions than we tested. For example, it might be applied to rectangular base tanks by substituting the base area for L^2.

The characteristic mixing time T_m is mainly dependent on the time it takes to circulate a tank volume of fluid through the plume. An important result is that $T \sim L_{bp}^{-1/3}$. This characterizes the reduction in mixing time resulting from lengthening the gas release path with a fixed total flow rate. Another important result is that the mixing time is independent of the liquid depth, h, at least for pressure ratios close to 1.

The steeper slope in U versus t'' for $t'' > 2.65$ can be interpreted as follows: Typically, at $t'' = 2.65$, the total flow that has passed through the plume is roughly one tank volume. Once all the fluid has passed through the plume, large scale concentration fluctuations are eliminated and the turbulence outside the plume can contribute to effective mixing.

Reducing the gas-liquid surface tension by a factor of 2 reduces bubble diameter by about 30 percent. Haberman and Morton [4] show that this reduction (from roughly 1 cm to 0.7 cm) does not cause a significant change in slip speed. Thus, our finding (described in detail by Godon [3]) that reducing the gas-liquid surface tension by a factor of two did not alter the mixing versus time shows that the direct influence of bubble size is weak, at most.

In going from laboratory scale to very large scale, the principal scale effect not accounted for by equation (18) is the variation in $[(1-r)/k^2]^{1/3}$. Although $g^{1/15}Q^{-2/15}L_{bp}^{1/3}$ exhibits the proper behavior when Q and L_{bp} are varied for a given scale, L, this factor is constant under Froude scaling. Because of the small reduction in r and the small increase in k expected with an increase in scale, mixing times at a scale ten times greater than that of our experiments are expected to be somewhat less (~ 10 percent) than predicted by equation (18).

Copyright © 1987 by ASME

Downloaded 02 Jun 2010 to 171.66.16.66. Redistribution subject to ASME license or copyright; see http://www.asme.org/terms/Terms_Use.cfm

Studies of the Configuration and Performance of Annular Type Jet Pumps

Yukimaru Shimizu
Associate Professor,
Department of Mechanical Engineering,
Mie University,
Kamihama-cho, Tsu, Mie, Japan 514

Shogo Nakamura
Engineer,
Fuji Electric Co. Ltd,
Tanabeshinden,
Kawasaki-ku, Kawasaki,
Kanagawa, Japan 210

Sadao Kuzuhara
Professor,
Department of Mechanical Engineering,
Mie University,
Mie, Japan

Shigemitsu Kurata
Teacher,
Hamamatsu Blind School,
Aoi-cho, Hamamatsu,
Shizuoka, Japan 433

In this paper, we investigated experimentally the relation between configuration and performance of the annular type jet pump and compared it with that of the central jet type. Twenty-five different kinds of pumps were used in the experiments. These pumps reached a maximum efficiency of thirty-six percent. This corresponds with that of the conventional central jet type pump. We also studied the effect of the swirl component in the driving jet, and compared it with the result without swirl component.

1 Introduction

Even though its efficiency is low, the jet pump is being used in many fields for different purposes because of its simple construction and easy operation. In general, a jet pump has a driving line in the center and a suction line on the outside (called the central jet type from now on). Many theoretical or experimental studies on this type of pump have been reported [1]-[6].

In contrast to this, there is another type of jet pump which has the suction line in center and the annular driving jet on the outside (namely, the annular jet type), but information is limited because only a few studies have thus far been conducted [7].

In this paper, we investigated experimentally the relation between configuration and performance of the annular type jet pump and compared it with that of the central jet type. Twenty-five different kinds of pumps were used in the experiments. These pumps reached a maximum efficiency of thirty-six percent. This corresponds with that of the conventional central jet type pump.

We also investigated the effect of the swirl component in the driving jet, and the results obtained were presented. A weak jet swirl was somewhat effective on the performance of the pump in certain cases, but an intensive swirl reduced the pumps' efficiency.

2 Test Apparatus Used

Figure 1 shows the test apparatus used. Driving water pumped by a centrifugal pump ① flows into the rectifying chamber ③ via the flow measuring orifice ② . It then discharges from the annular clearance outside of the central suction nozzle after straightening out through eight guide vanes ④. The suction line consists of the suction pipe, electro magnetic flow meter ⑥, and suction nozzle⑤. Driving water and raised water mix together in the mixing chamber and flow out from the delivery line after recovering pressure in a diffuser. Wall pressures P_s, P_j, and P_d in the suction pipe,

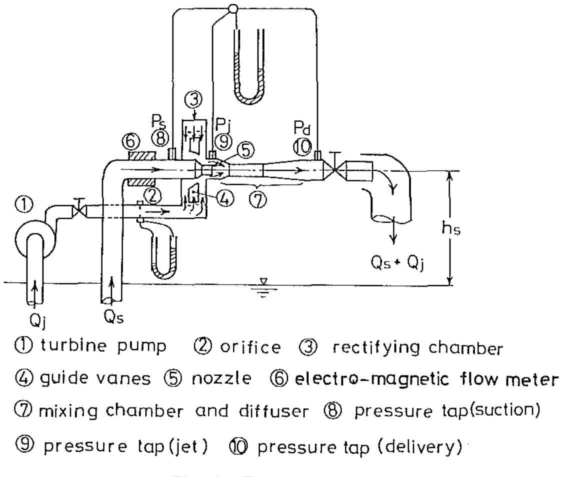

Fig. 1 Test apparatus

Contributed by the Fluids Engineering Division for publication in the JOURNAL OF FLUIDS ENGINEERING. Manuscript received by the Fluids Engineering Division September 4, 1984.

Copyright © 1987 by ASME

Downloaded 02 Jun 2010 to 171.66.16.66. Redistribution subject to ASME license or copyright; see http://www.asme.org/terms/Terms_Use.cfm

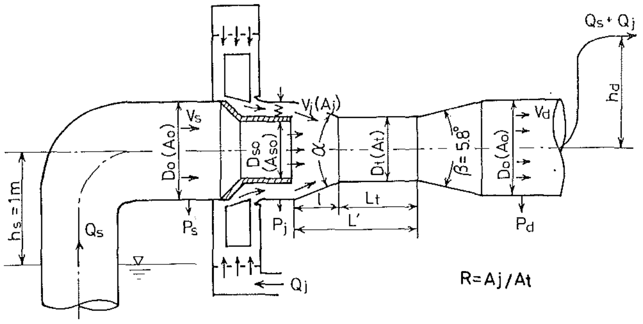

Fig. 2 Configuration and dimensions

annular nozzle, and delivery pipe are taken from pressure tappings ⑧, ⑨, and ⑩ and are measured by mercury manometers.

In this experiment, the performance of many pumps with different configurations was investigated for different jet quantities Q_j, while the suction height was kept constant $h_s = 1\text{m}$.

Figure 2 illustrates the configuration of the pump, and Fig. 3(*a*) is the nozzle in detail. As this experiment was carried out at constant diameter $D_0 = 55\text{mm}$, A_j decreases as A_{s0} increases. Area ratio A_{s0}/A_0 was changed from 0.5 to 0.61 and then to 0.73. Clearance $\tilde{W}$ is, respectively, 6, 4, and 2 (mm) in these cases. Five kinds of mixing chamber entrances from the straight type ($\alpha = 0$ deg) to the reduction type ($\alpha = 18$, 30, 45, 60 deg) were used as shown in Fig. 3(*b*). Area ratio A_t/A_0 is 1, 0.48, and 0.2 for $D_t = 55$ mm, 38 mm, and 24.3 mm. The length of the mixing chamber is $L_t = (0 \text{ to } 8)\ D_t$.

A diffuser with the divergence angle $\beta = 5.8$ deg is connected to the mixing chamber in order to recover the pressure. The diameter of its outlet is $D_0 = 55$ mm. Table 1 shows the dimensions of the twenty-five pumps used.

3 Expression of the Results

Flow ratio M is defined by the jet and suction flow rates as follows

$$M = Q_s/Q_j \tag{1}$$

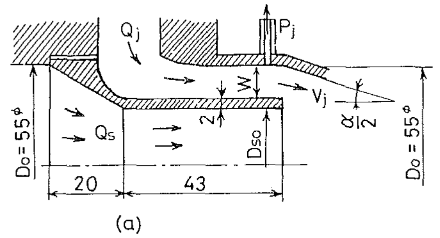

(a)

Fig. 3(*a*) Detail of nozzle

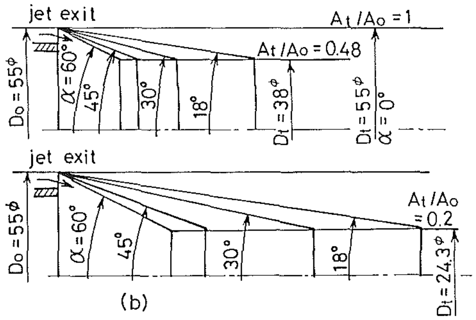

(b)

Fig. 3(*b*) Configuration of mixing chamber entrance (Uncertainty in D_0, D_t = 55 mm ±0.2 mm, in $A_t/A_0 = 1.0 \pm 0.015$, in $\alpha = 60$ deg ± 1 deg)

and we define the head ratio N as

$$\left.\begin{aligned} N &= \frac{(K_k - K_p)V_d{}^2/2g + P_d/\rho g - V_s^2/2g - P_s/\rho g}{K_j V_j{}^2/2g + P_j/\rho g - (K_k - K_p)V_d{}^2/2g - P_d/\rho g} \\ K_j &= 1 + \left(\int_{D_0/2-w}^{D_0/2} V_\phi r dr \Big/ \int_{D_0/2-w}^{D_0/2} V_z r dr\right)^2 \end{aligned}\right\} \tag{2}$$

where v_d and v_s are the mean velocity, obtained by the flow measurement, in the delivery and suction pipes, respectively. P_d and P_s are pressures on the wall where ρ represents water density.

The denominator of equation (2) expresses the head drop of the jet, and the numerator is the head which the suction flow is given.

Nomenclature

(reference Fig. 2)

A_0, D_0 = area, inner diameter of suction line and delivery line
A_{s0}, D_{s0} = area, exit diameter of central suction nozzle
A_t, D_t = area, inner diameter of mixing chamber
A_j = sectional area of annular jet
An = annular area of thickness of nozzle
I_j' = normalized jet swirl intensity, equation (6)
K_j = correction factor of velocity head at jet nozzle, equation (2)
K_k = correction factor of kinetic energy, equation (3)
K_p = correction factor of pressure head at delivery pipe, equation (4)
L_t = length of mixing chamber
a, l = reduction angle, length of mixing chamber entrance
M = flow ratio
N = head ratio
$P(P_j, P_s, P_d)$ = wall pressure (jet nozzle, suction pipe, delivery pipe)
$Q(Q_j, Q_s)$ = flow rate (jet, suction)
R = A_j/A_t, area ratio of jet and throat
r, r_w = length of radius position, radius of delivery pipe
$V(V_j, V_s, V_d)$ = mean axial velocity (jet nozzle, suction pipe, delivery pipe)
V_m = V_d, mean velocity at the exit section
v_z, v_ϕ = local axial and peripheral velocities
A_{s0}/A_0 = area ratio at suction nozzle
A_t/A_0 = area ratio at mixing chamber

Subscripts

j = jet
s = suction
d = delivery
$0p$ = values at the maximum efficiency

Downloaded 02 Jun 2010 to 171.66.16.66. Redistribution subject to ASME license or copyright; see http://www.asme.org/terms/Terms_Use.cfm

Table 1 Dimensions of twenty-five kinds of pumps used (Uncertainty in $D_t = 55$ mm ±0.2 mm, in $A_t/A_0 = 1.00 \pm 0.015$, in $\alpha = 60$ deg ±1 deg, in $\ell = 53.7$ mm ±0.2 mm, in $L_t = 102.3$ mm ±0.2 mm, in $L_t/D_0 = 1.86 \pm 0.02$, in $L'/D_0 = 2.84 \pm 0.02$, in $L'/D_t = 4.11 \pm 0.02$, in $A_{s0}/A_0 = 0.73 \pm 0.01$, in $R = 0.29 \pm 0.005$)

No	D_t mm	A_t/A_0	$\alpha°$	ℓ mm	L_t mm	L_t/D_0	L'/D_0	L'/D_t	$A_{s0}/A_0(A_j/A_t = R)$
1	55	1	0	0	385	7	7	7	0.73(=0.14) 0.61(=0.27) 0.5 (=0.39)
2	38	0.48	18	53.7	0	0	0.98	1.41	0.73(=0.29) 0.61(=0.57) 0.5(=0.82)
3			30	31.7			0.58	0.83	
4			45	20.5			0.37	0.54	
5			60	14.7			0.27	0.39	
6			18	53.7	102.3	1.86	2.84	4.11	
7			30	31.7			2.44	3.53	
8			45	20.5			2.23	3.23	
9			60	14.7			2.13	3.08	
10			18	53.7	179.4	3.26	4.24	6.13	
11			30	31.7			3.84	5.56	
12			45	20.5			3.63	5.26	
13			60	14.7			3.53	5.11	
14			18	53.7	293.4	5.33	6.31	9.13	
15			30	31.7			5.91	8.56	
16			45	20.5			5.70	8.26	
17			60	14.7			5.60	8.11	
18	24.3	0.2	18	96.9	123.3	2.24	4.00	9.06	0.73(=0.72) 0.61(=1.38) 0.5(=1.99)
19			30	57.3			3.28	7.43	
20			45	37.0			2.91	6.60	
21			60	26.6			2.72	6.17	
22			18	96.9	199.2	3.62	5.38	12.19	
23			30	57.3			4.66	10.56	
24			45	37.0			4.29	9.72	
25			60	26.6			4.10	9.29	

K_k and K_p are modification coefficients for kinetic energy and the pressure on the delivery side obtained from velocity distribution, as shown in the following equations:

$$K_k = \frac{(\rho/2)\int_0^{r_w} 2\pi(V_z^2 + V_\phi^2)V_z r\,dr}{(\rho/2)V_d^2(Q_j + Q_s)} \tag{3}$$

$$K_p = \frac{\int_0^{r_w} 2\pi V_z r\left\{\rho\int_r^{r_w}(V_\phi^2/r)dr\right\}dr}{(\rho/2)V_d^2(Q_j + Q_s)} \tag{4}$$

V_z: axial velocity $\quad V_\phi$: peripheral velocity

Figure 4 shows an example of the velocity distribution corresponding to the calculated values of K_k and K_p. In this case, the pump has a large jet area in comparison to the suction area, for example, $A_{s0}/A_0 = 0.5$, 0.61, so that the flow rate of the jet becomes higher than that of the the suction flow allowing the effect of the jet to extend to the diffuser exit. As a result, very little drop in velocity is seen near the wall. On the contrary, if the jet area is as small as $A_{s0}/A_0 = 0.73$, the effect of the jet does not extend to the diffuser exit, producing the same velocity distribution shape as observed at the exit of an ordinary diffuser.

The efficiency of a jet pump is defined as the ratio of the entire effective energy given to the suction flow to the energy which the jet consumes in the pump, namely, defined by the equation

$$\eta = MN \tag{5}$$

4 Discussion of Obtained Results

4.1 Pressure Distribution in the Flow Direction. First, we investigated the mixing length of the annular high speed driving jet and the suction flow along the center line. Figure 5 shows the pressure coefficient C_p versus axial position X/D_0 from the jet exit. The mixing chamber in this case is parallel ($A_t/A_0 = 1$), and the flow ratios covered by the experiments are from 0.01 to 0.34. From this figure, it is seen that, in these cases, the wall pressure increases until $X/D_0 = 7$ and then begins to decrease downstream from there. Mixing reaches approximate equilibrium at this point. We chose this point as the wall pressure measuring point in the downstream section.

Figure 6 is the pressure distribution for a mixing chamber with a conical entrance. Area ratios A_{s0}/A_0 or $A_j/A_t(=R)$ are 0.5 ($R = 0.82$), 0.61 ($R = 0.57$), and 0.73 ($R = 0.29$). In every case, the pressure in the mixing chamber drops (x/D_0) = 0 to 3.8) and then recovers in the diffuser ($X/D_0 = 3.8$ to 6.9) until it becomes almost constant. We chose point $X/D_0 = 7.8$ for the downstream pressure tapping position. Compared to the parallel type, the suction flow through the mixing chamber with a conical entrance occurs more readily because of pressure reduction.

Downloaded 02 Jun 2010 to 171.66.16.66. Redistribution subject to ASME license or copyright; see http://www.asme.org/terms/Terms_Use.cfm

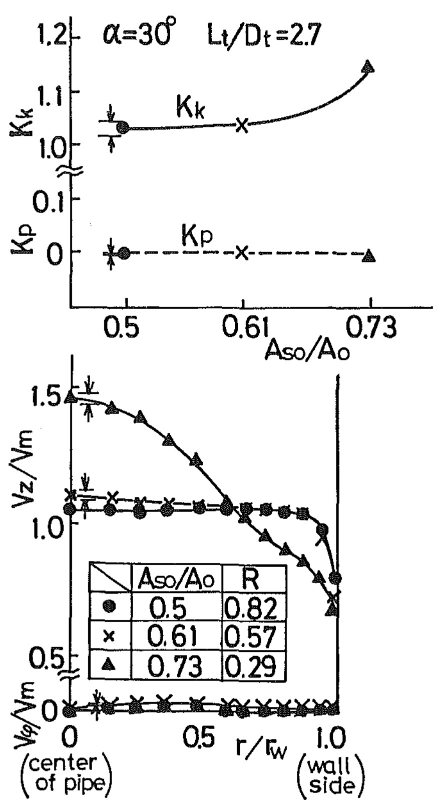

Fig 4 Velocity distribution, velocity head coefficient K_k and pressure coefficient K_p. (Uncertainty in $K_k = 1.0 \pm 0.015$, in $K_p = 0.01 \pm 0.0002$, in $V_z/V_m = 1.0 \pm 0.015$, in $V_\varphi/V_m = 0.03 \pm 0.0005$, in $r/r_w = 0.5 \pm 0.008$, A_{s0}/A_0: see Table 1.)

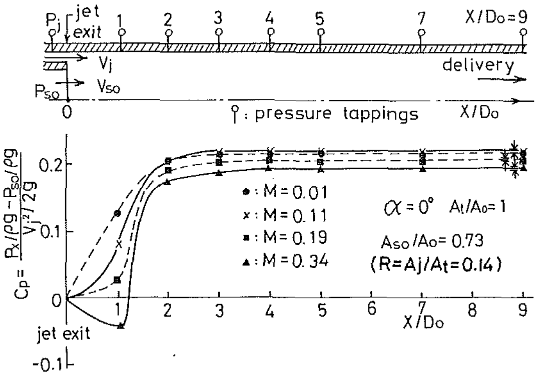

Fig. 5 Pressure distribution of straight type pump. (Uncertainty in $C_p = 0.2 \pm 0.003$, in $X/D_0 = 5.0 \pm 0.08$, in $M = 0.34 \pm 0.005$.)

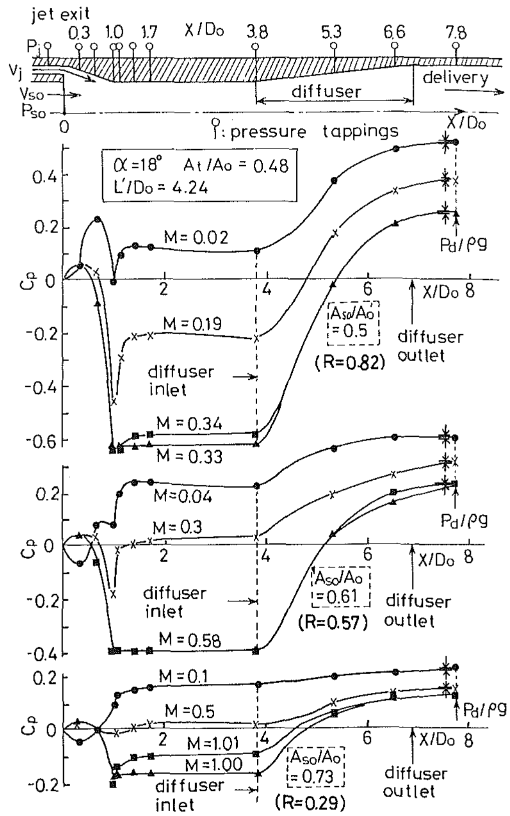

Fig. 6 Pressure distribution of convergent-divergent type pumps. (Uncertainty in $C_p = 0.2 \pm 0.003$, in $X/D_0 = 5.0 \pm 0.08$, in $M = 1.0 \pm 0.015$.)

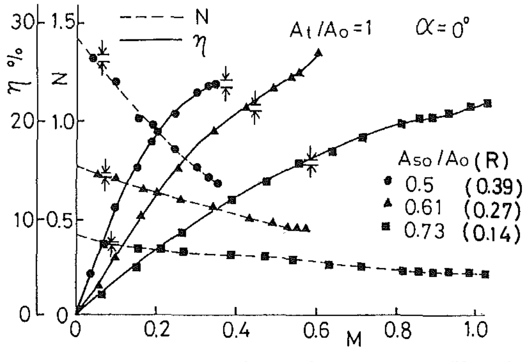

Fig. 7 Characteristic curves of straight type pump (Uncertainty in $\eta = 30$ percent ± 0.5 percent, in $N = 1.0 \pm 0.015$, in $M = 1.0 \pm 0.015$, A_{s0}/A_0: see Table 1)

4.2 Characteristic Curves. Next, we investigated the performance of several typical pumps. The relation between head ratio, efficiency, and flow ratio for the parallel chamber type pump is shown for $A_{s0}/A_0 = 0.5$, 0.61, and 0.73 ($R = 0.39$, 0.27 and 0.14) in Fig. 7. The M-N curve for $A_{s0}/A_0 = 0.5$ ($R = 0.39$) has a steep slope, and maximum efficiency $\eta_{\max} = 23.8$ percent was obtained at flow ratio $M_{0p} = 0.35$. On the other hand, the curve has a mild slope and $\eta_{\max} = 21.6$ percent at $M_{0p} = 1.03$ for $A_{s0}/A_0 = 0.73$ ($R = 0.14$). This value of 1.03 is about three times that of the former. Thus, the suction flow decreases but the delivery head increases at a small area ratio, and it is reversed at a large ratio. This is based on the rate of the energy given to the suction flow from the driving jet passing through the annular nozzle of which the area varies with the area ratio A_{s0}/A_0 or R.

Figure 8 shows the characteristic curves of the pump with a conical mixing chamber entrance. The conical angle is $\alpha = 18$, 30, 45, and 60 deg, the area ratio is $A_{s0}/A_0 = 0.61$ ($R = 0.57$, $\bar{W} = 4$mm), $A_t/A_0 = 0.48$ ($D_t = 38$mmϕ), and the length of the mixing chamber is $L_t/D_0 = 0$, 1.86, and 3.26, respectively. The upper figures show the M-N relations, and the lower ones are for M-η relations.

The central figure, for $L_t/D_0 = 1.86$, shows relatively high efficiency compared with those for 0 and 3.26. Before investigating the relation between the length of the mixing chamber and efficiency (Fig. 12), the general features of the M-N and M-η relations, laying stress on the results for $L_t/D_0 = 1.86$, will be examined thoroughly.

$\alpha = 18$ deg: N reaches 1.63 at $M = 0$ and then goes down at an almost constant slope with increasing flow ratio. Cavitation comes into existence at $M = 0.56$ and fine bubbles begin to appear at the entrance edge of the parallel part of the mixing chamber. Efficiency is $\eta = 36.0$ percent in this condition. Maximum efficieny as high as $\eta_{\max} = 36.6$ percent at $M_{0p} = 0.57$, but at this point, noise and bubbles occur intermittently. The suction flow is reduced from this point due to the cavitation,

Downloaded 02 Jun 2010 to 171.66.16.66. Redistribution subject to ASME license or copyright; see http://www.asme.org/terms/Terms_Use.cfm

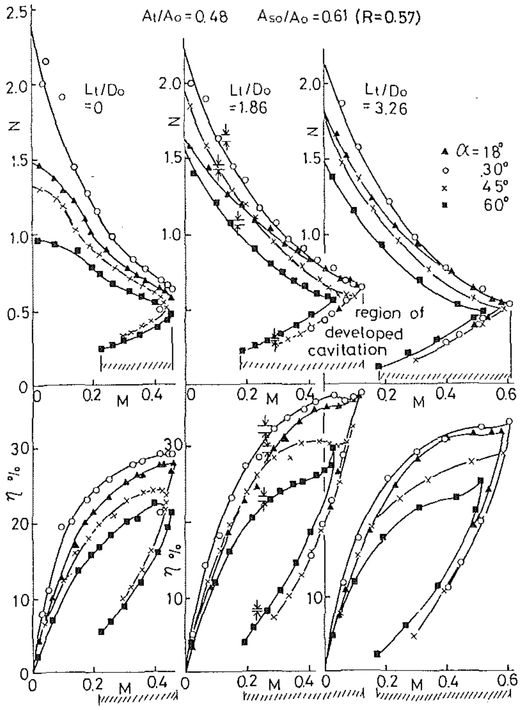

Fig. 8 Characteristic curves of 4 convergent-divergent type pumps. ($A_t/A_0 = 0.48$, $R = 0.57$) (Uncertainty in $\eta = 30$ percent ±0.5 percent, in $N = 1.0 \pm 0.015$, in $M = 0.4 \pm 0.006$, α: see Table 1.)

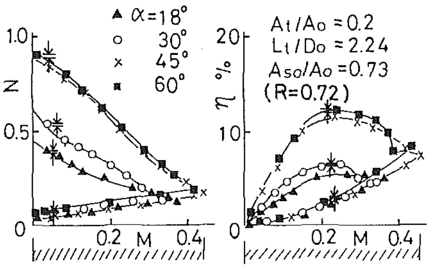

Fig. 9 Characteristic curves of convergent-divergent type pump. ($A_t/A_0 = 0.2$, $R = 0.72$) (Uncertainty in $N = 1.0 \pm 0.015$, in $\eta = 10$ percent ±0.15 percent, in $M = 0.4 \pm 0.006$, α: see Table 1.)

in spite of the increased driving jet, and the M-N curve traces a return course back. The efficiecny also diminishes as shown by the M-η curve. The oblique lines in the figure show the region of developed cavitation.

$\alpha = 30$ deg: The general tendencies are similar to those for $\alpha = 18$ deg except that both N and η are somewhat larger. In this case as well, cavitation occurs at $M = 0.56$, $\eta_{\max} = 36.6$ percent is reached at $M_{0p} = 0.58$, and the efficiency drops rapidly beyond this point.

$\alpha = 45$, 60 deg: A similarity to the preceding two angles is also seen in this case, but the efficiency decreases as the angle increases. The relation between conical angle and efficiency will be explained in detail in Fig. 11.

Figure 9 shows the relations between M-N and M-η for a pump with a narrow and parallel mixing chamber with area ratios of $A_t/A_0 = 0.2$ and $A_{s0}/A_0 = 0.73$ ($R = 0.72$). Cavitation quickly occurs in this case, and the maximum efficiency is 12.3 percent ($\alpha = 60$ deg). This is about one-third of that at $A_t/A_0 = 0.48$.

In this connection, the central driving jet type pumps' efficiency is high even if it has a narrow mixing chamber; cavitation not quickly occurring. This is one of the distinguishing contrasts between the two types of jet pumps.

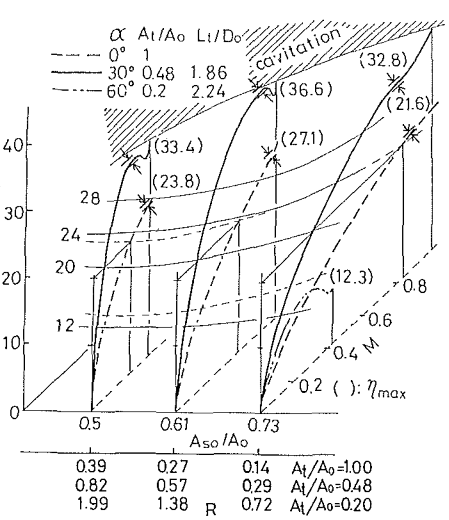

Fig. 10(a) Efficiency-Flow ratio curves versus A_{s0}/A_0 or R. (Uncertainty in $\eta = 30$ percent ±0.5 percent, in $M = 1.0 \pm 0.015$, A_{s0}/A_0, R, α, A_t/A_0, L_t/D_0: see Table 1.)

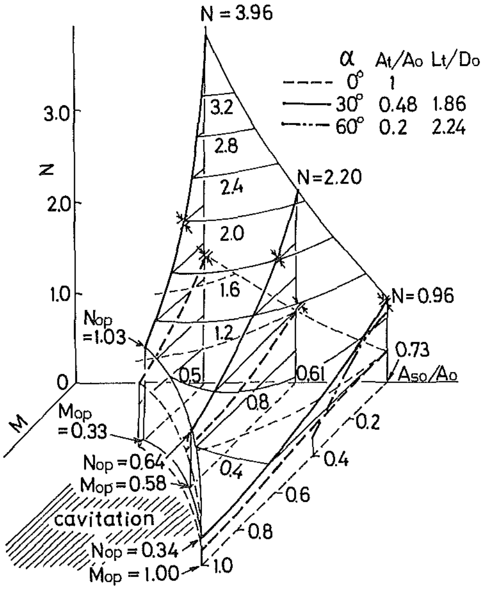

Aso /Ao		0.5	0.61	0.73
R	At /Ao = 1.00	0.39	0.27	0.14
	= 0.48	0.82	0.57	0.29
	= 0.20	1.99	1.38	0.72

Fig. 10(b) Head ratio-flow ratio curves versus A_{s0}/A_0 or R. (Uncertainty in $N = 1.0 \pm 0.015$, in $M = 1.0 \pm 0.015$, A_{s0}/A_0, R, α, A_t/A_0 Lt/D_0: see Table 1.)

4.3 Relation Between the Area Ratio of the Suction Nozzle and the Performance. Figures 10(a) and 10(b) show the effect of the area ratio of the suction nozzle on the performance of several typical pumps chosen from Figs. 7 to 9 for discussion. Figure 10(a) is the relation between the flow ratio M and η and A_{s0}/A_0 or R. Each of these, full line, broken line, and chain line, show the results for $\alpha = 30$, 0, and 60 deg, respectively, as written in the figure. When $\alpha = 30$ deg at $A_{s0}/A_0 = 0.5$ (the smallest suction area), the M-η curve has a steep slope and $\eta_{\max}$ attains a value of 33.4 percent, and at a middle area ratio of 0.61, η attains a maximum value of 36.6 percent. This is the highest value in these experiments. At the largest area ratio of 0.73, the M-η curve shows a relatively mild slope where $\eta_{\max} = 32.8$ percent. When $\alpha = 0$ deg, the maximum efficiency shows the highest value at $A_{s0}/A_0 = 0.61$ and the lowest one at 0.73; but for all area ratios, the maximum efficiencies are smaller than those when $\alpha = 30$ deg by about 10 percent.

Downloaded 02 Jun 2010 to 171.66.16.66. Redistribution subject to ASME license or copyright; see http://www.asme.org/terms/Terms_Use.cfm

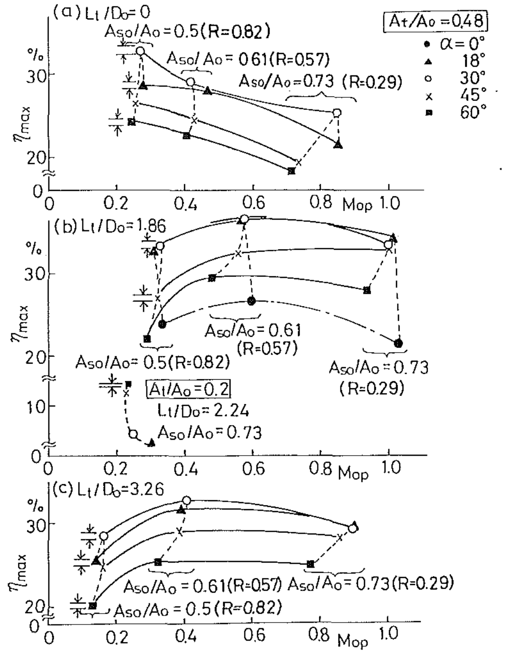

Fig. 11 $\eta_{max} - M_{0p}$ curves versus reduction angle α. (Uncertainty in $\eta_{max} = 30$ percent ±0.5 percent, in $M_{0p} = 1.0 \pm 0.015$, A_{s0}/A_0, R, α: see Table 1.)

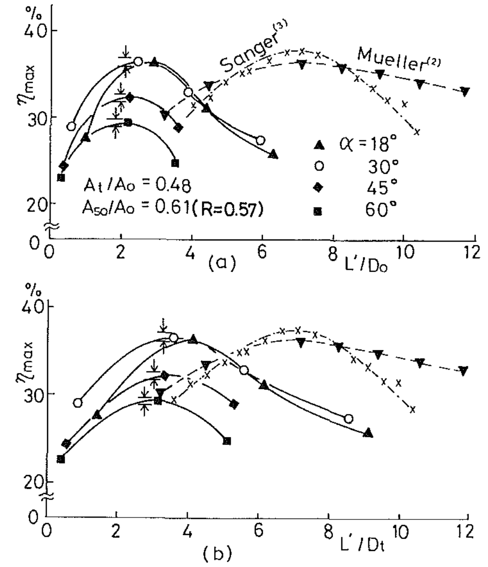

Fig. 12 Optimum length of the mixing chamber, Comparison between annular and central types. (Uncertainty in $\eta_{max} = 30$ percent ±0.5 percent, L'/D_t, L'/D_0, α: see Table 1.)

The relation between the flow ratio, head ratio, and the area ratio is illustrated in Fig. 10(*b*). When $\alpha = 30$ deg (full line), the *M-N* curve has a steep slope at the area ratio of 0.5 and, generally, a large head ratio but a small flow ratio. But this changes into a form of small head ratio at a large flow ratio for the large area ratio.

The flow ratio M_{0p} at maximum efficiency is 0.33, 0.58, and 1.00 at each area ratio, but the head ratio N_{0p} shows the opposite tendency. From this, it can be understood that for an appropriately shaped mixing chamber, the large-suction area pump is a large-flow ratio, low-head ratio type, and the small-suction area pump is a small-flow ratio, large-head ratio type.

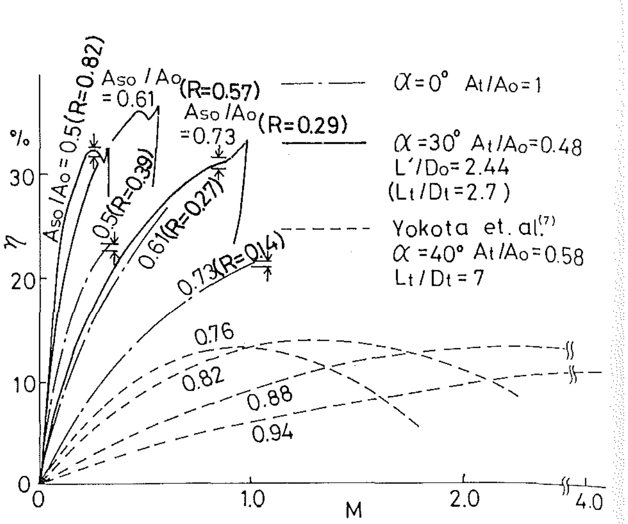

Fig. 13 Comparison between present results and those of other authors (annular type). (Uncertainty in $\eta = 30$ percent ±0.5 percent, in $M = 1.0 \pm 0.015$, A_{s0}/A_0, R: see Table 1.)

4.4 Relation Between the Entrance Angle of the Mixing Chamber and the Performance. It has been shown that the performance of the pump depends on the reduction angle α, as in Figs. 8 and 9. We shall thoroughly examine this fact in Fig. 11 (*a*), (*b*), and (*c*) which show the maximum efficiency and the flow ratio M_{0p} for each pump at $A_{s0}/A_0 = 0.5$ to 0.73. The figures correspond to $L_t/D_o = 0$, 1.86, and 3.26, respectively, from top to bottom. The full lines are for $A_t/A_0 = 0.48$ ($\alpha = 18$ to 60 deg), and the chain line (Fig. (*b*)) is for $A_t/A_0 = 1$ ($\alpha = 0$ deg). The results for the narrow and long mixing chamber type pump ($A_t/A_0 = 0.2$) is, for reference, shown by a thick broken line.

In these three figures, we can see that the highest rate of efficiency is obtained at $\alpha = 18$ and 30 deg, whereas it decreases at larger or smaller entrance angles. In fact, the lowest rate of efficiency is at $\alpha = 0$ deg.

From these results, we see that pump efficiency drops for both the abruptly reduced type and the straight type. We assume this decrease to be derived from the internal velocity distributions, as was mentioned in another report [8].

4.5 Relation Between the Performance of the Pump and the Length of the Mixing Chamber. Next, we investigated the optimum length of the mixing chamber. Figure 12 shows the relations between the maximum efficiency η_{max} and the length of the mixing chamber L'/D_0 for each pump. But the area ratios of the mixing chamber and suction nozzle, A_t/A_0 and A_{s0}/A_0 keep constant, where $A_t/A_0 = 0.48$ and $A_{s0}/A_0 = 0.61$. The maximum efficiencies are taken at $L'/D_0 = 2.1$ to 2.8 for all α. Similar results were obtained at $A_{s0}/A_0 = 0.5$, 0.73 (these are not illustrated). The results obtained by Mueller [2] and Sanger [3] for conventional jet pumps with a central driving nozzle are shown for comparison in the figure. η_{max} attains the highest value at $L'/D_0 \fallingdotseq 7$ in both cases.

Figure 12(*b*) compares the results of this experiment and those of Mueller and Sanger by using the ratio of total length to inner diameter of the mixing chambers' straight section, L'/D_t. Maximum efficiencies in our experiment were obtained at $L'/D_t = 3.5$ to 4.0. This is about one-half of those of Mueller and Sanger. From this, it can be said that the total length of the mixing chamber of the annular jet type pump can be considerably shortened in comparison with the usual type. In addition, $L_t \fallingdotseq 2D_0$ is the most suitable for the type with a converging entrance section in front of the mixing chamber.

4.6 Comparison With the Results Obtained by Others. In Figure 13, the results obtained in this experiment (full lines, chain lines) are compared with those by Yokota et

Downloaded 02 Jun 2010 to 171.66.16.66. Redistribution subject to ASME license or copyright; see http://www.asme.org/terms/Terms_Use.cfm

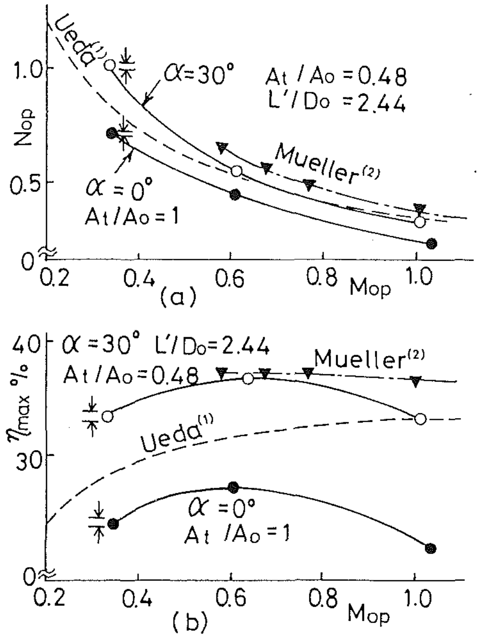

Fig. 14 Comparison between present results and those of other authors (central type). (Uncertainty in $N_{0p} = 1.0 \pm 0.015$, in $M_{0p} = 1.0 \pm 0.015$, in $\eta_{max} = 30$ percent ±0.5 percent.)

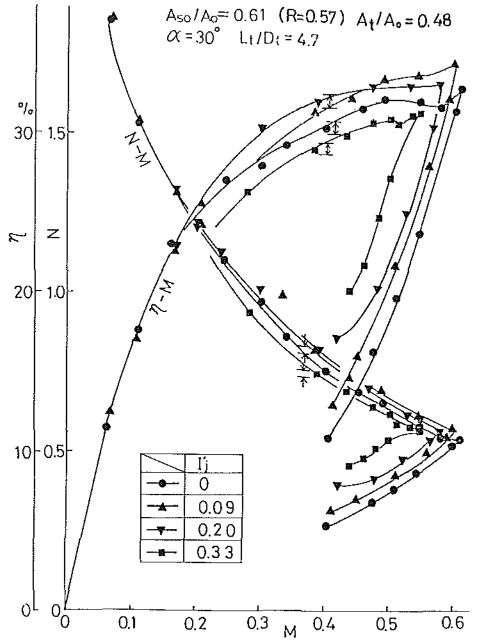

Fig. 15 Characteristic curves in the case of the driving jet with a swirl component. (Uncertainty in $\eta = 30$ percent ±0.5 percent, in $N = 1.0 \pm 0.015$, in $M = 0.4 \pm 0.006$, in $I_j' = 0.33 \pm 0.005$.)

al. [7] for the annular jet type pump (broken lines). The curves by Yokota et al. cover a wide range of flow ratios, M, but show low $\eta_{max} = 14$ percent efficiency at best. The pumps used by Yokota et al. are large-flow rate, low-head type where $A_{s0}/A_0 = 0.76$ to 0.94, $\alpha = 40$ deg, $L_t/D_t = 7$. These geometrical values may be excessive with regard to maximizing efficiency.

Figure 14 is the comparison of the results where $\alpha = 0$ deg, $A_t/A_0 = 1$ and $\alpha = 30$ deg, ad $A_t/A_0 = 0.48$ with the conventional central jet type pumps used by Ueda [1] and Mueller [2]. The flow ratio M_{0p} and the head ratio N_{0p} at maximum efficiency are shown in Fig. 14(a). In this respect, the results for both the annular jet type and the central jet type show good agreement. Figure 14(b) expresses the relation between M_{0p} and η_{max}. The results for $\alpha = 30$ deg in the present study and that by Mueller show a maximum efficiency of about 37 percent.

5 Experiments Using a Driving Jet With a Swirl Component

Energy exchange between the driving jet and the suction flow, namely, the mixing of the two, is important. In the case of a free jet, promotion of the mixing is reported by Chiger and others [9], but in their presentation, the effect of the swirl component on the annular jet type pump is not clear. The present authors carried out some experiments, and will now briefly present the results obtained.

The swirling driving jet was produced by means of eight guide vanes ④in the rectifying chamber ③in Fig. 1. The intensity of the swirl of the jet is expressed by nondimensional angular momentum flux I_j' in the following equation:

$$I_j' = \left(\rho \int_0^{r_w} 2\pi v_z v_\phi r^2 dr\right) \Big/ \{\rho V_m r_w (Q_j + Q_s)\} \qquad (6)$$

Figure 15 shows the influence on the characteristic curves of the swirl intensity of the jet. Variations of the head ratio N and efficiency η against the flow ratio M are similar to those shown in Fig. 8. Remarkable differences are not seen through the addition of the swirling component. In order to thoroughly investigate the swirling effect on the performance of the pump, the curves η_{max} versus α (reduction angle of mixing chamber) for the highest efficiency pump in many experiments were compared to that of no swirl in Fig. 16.

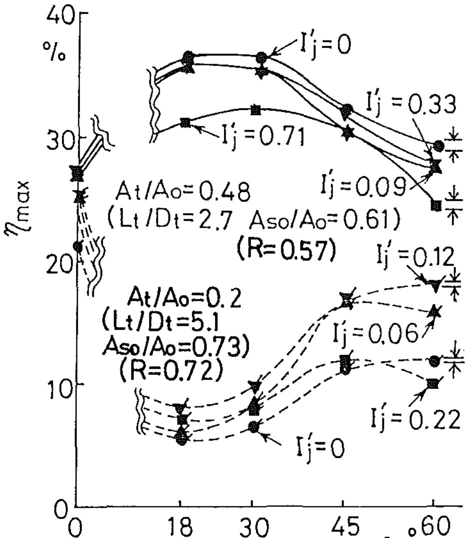

Fig. 16 $\eta_{max} - \alpha$ curves versus intensity of the swirl I_j' in case of the driving jet with the swirling component. (Uncertainty in $\eta_{max} = 30$ percent ±0.5 percent, in $I_j' = 0.33 \pm 0.005$, α: see Table 1.)

For the pumps with a reducing path area, a weak swirl component in the driving jet does not affect its efficiency, and only a small change occurs at medium swirl. In comparison, an intensive swirl reduces the efficiency and provokes flow instability. The above phenomenon may be explained from the view point of an increase of the flow rate due to the reduction of the boundary layer thickness in the converging or straight part of the pump and the degree of energy loss with a weak or intensive swirl.

Further details of these experiments are reported in the literature [8].

Downloaded 02 Jun 2010 to 171.66.16.66. Redistribution subject to ASME license or copyright; see http://www.asme.org/terms/Terms_Use.cfm

6 Conclusions

(1) The annular jet type pump can demonstrate efficiency as high as 36 percent. This is equal to that of the conventional central jet type pump.

(2) A configuration with a reduction angle of 18 to 30 deg and a suitable sectional area, $A_t/A_0 \doteqdot 0.48$, in the mixing chamber is desirable for the annular jet pump. A pump of this type can be about half the length of the conventional central jet pump.

(3) A pump with a large-flow ratio and low-head ratio or, inversely, small-flow ratio but high-head ratio can, respectively, be designed by selecting the appropriate nozzle area ratio.

(4) Though a weak jet swirl component shows, in certain cases, some effects on the performance of the pump, no remarkable effect can be seen in general. On the other hand, a strong swirl component causes a decrease in pump efficiency.

References

1 Ueda, T., "Study on the Water Jet Water Pump," *Trans. JSME*, Vol. 20, 1954, p. 25

2 Mueller, N. H. G., "Water Jet Pump," *J. Am. Soc. Civil Eng.*, Vol. 90-HY3, 1964-1965, p. 83.

3 Sanger,N. L., "An Experimental Investigation of Several Low-Area-Ratio Water Jet Pumps," ASME *Journal of Basic Engineering*, Vol. 92, Nov. 1970. p. 11.

4 Razinsky, E., and Brighton, J. A., "Confined Jet Mixing for Nonseparating Conditions," ASME *Journal of Basic Engineering*, Vol. 93, No. 3, 1971, p. 333.

5 Cunningham, R. G., et al., "Jet Pump Cavitation," ASME *Journal of Basic Engineering*, 1970, p. 483.

6 Weber, M., et al., "New Experimental Results Regarding Extreme Operating Conditions in Air Lifting and Vertical Hydraulic Transport of Solids According to the Jet Lift Principle and Its Applicability to Deep-Sea Mining." *BHRA Hydrotransport*, Vol. 5, 1978, F7-1.

7 Yokota, A., et al., "On the Annular Ring Type Jet Pump, Japan Miner. Eingrs. Soc., No. 90-1038, 1974, p. 539.

8 Shimizu, Y., et al., "Studies on the Annular Jet Pumps with Swirling Components in Driving Jet Flow," *Trans JSME*, Vol. 49-448, 1983, p. 2746.

9 Chigier, N. A., and Chervinsky, A., "Experimental Investigation of Swirling Vortex Motion in Jets," ASME *Journal of Applied Mechanics*,1967, p. 443.

APPENDIX

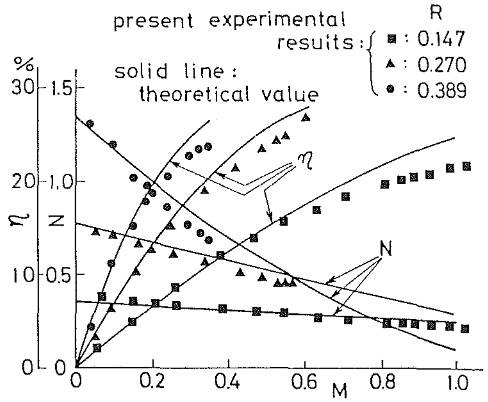

Fig. A1 In case of straight type pump. Comparison Gosline's theoretical values (1) and present experimental results (see Fig. 7).

The theoretical values and the authors' experimental results were compared in Fig. A1[1]. Gosline's one dimensional theoretical model, equation (16) was used.

$$N_{jl} = \eta/M = \frac{2R + \dfrac{2M^2R^2}{1-R} - (1+K_{th}+K_{di})R^2(1+M)^2 - (1+K_{en})\dfrac{M^2}{C^2}}{1+K_{nz} - 2R - \dfrac{2M^2R^2}{1-R} + (1+K_{th}+K_{di})R^2(1+M)^2 + \beta(1+K_{en})\dfrac{M^2}{C^2}} \qquad (16)$$

Friction coefficients K_{th}, K_{nz}, K_{en}, and K_{di} in equation (16) were estimated as the following.

K_{th} = 0.102: friction loss coefficient for mixing throat,
K_{nz} = 0.036: friction loss coefficient for nozzle,
K_{en} = 0.14: friction loss coefficient for throat entry,
K_{di} = 0.102: friction loss coefficient for diffuser.

In Fig. A1, theoretical values, equation (16), are written by the solid lines and the authors' experimental results are written by the symbols ●, ▲ and ■ (see Fig. 7).

Both values agree well. The annular type jet pump used to compare in Fig. A1 is the type of straight pipe which have no convergent and no divergent portions. It is ensured by the comparison in Fig. A1 that Gosline's theory is correct.

---

[1] R. G. Cunningham, BHRA, Proceedings of 2nd Symposium on *Jet Pumps and Ejectors and Gas Lift Techniques*, March 24th-26th (1975), F1-1.

Downloaded 02 Jun 2010 to 171.66.16.66. Redistribution subject to ASME license or copyright; see http://www.asme.org/terms/Terms_Use.cfm

Improved Approach to the Streamline Curvature Method in Turbomachinery

S. Abdallah

R. E. Henderson

Applied Research Laboratory,
The Pennsylvania State University,
State College, PA 16804

Quasi three dimensional blade-to-blade solutions for stators and rotors of turbomachines are obtained using the Streamline Curvature Method (SLCM). The first-order velocity gradient equation of the SLCM, traditionally solved for the velocity field, is reformulated as a second-order elliptic differential equation and employed in tracing the streamtubes throughout the flow field. The equation of continuity is then used to calculate the velocity. The present method has the following advantages. First, it preserves the ellipticity of the flow field in the solution of the second-order velocity gradient equation. Second, it eliminates the need for curve fitting and strong smoothing under-relaxation in the classical SLCM. Third, the prediction of the stagnation streamlines is a straightforward matter which does not complicate the present procedure. Finally, body-fitted curvilinear coordinates (streamlines and orthogonals or quasi-orthogonals) are naturally generated in the method. Numerical solutions are obtained for inviscid incompressible flow in rotating and non-rotating passages and the results are compared with experimental data.

Introduction

Attempts to calculate the three-dimensional flows in rotating and stationary blade passages assume that the three-dimensional flow can be represented by two two-dimensional flows. This approach, originally propsed by Wu [1], leads to blade-to-blade (S1 surface) solutions and S2 surface solution representing the spanwise variation of the blade-to-blade flow. A further simplification is then introduced which eliminates the twist of the S1 surface by assuming rotational symmetry. The S2 surfaces are then streamsurfaces describing the spanwise variation of the mean blade-to-blade flow.

The methods which have been employed to solve the governing flow equations on the S1 and S2 surfaces include the Matrix method [1], [2], and [3] for example, and the streamline curvature method (SLCM), [4] and [5]. The difference between these methods is the form of the equations of motion and the approach used to obtain a numerical solution. The Matrix method solves for the stream function in the region of interest while the SLCM determines the velocity field from the radial equation of motion on the S2 surface and the tangential momentum equation on the S1 surface. A comparison of the two methods in obtaining solutions in the S2 surface is given in reference [6].

Novak and Hearsey [5] describe a SLCM which provides a solution of the flow on the S1 surface by solving for the velocity field. This approach is similar to that employed by Wilkinson [4] and formulates the momentum and energy equations in terms of the velocity gradients occurring in the flow. A comparison of the predicted surface velocities with those measured in a NACA 65(18)10 compressor cascade show that the SLCM is a very effective approach.

This paper addresses the same flow problem, i.e., the flow on the S1 surface, but introduces a different formulation of the governing momentum equation. Instead of the traditional form of a first-order velocity gradient equation used in SLCM solutions, a second-order elliptic differential equation is used to trace the streamlines throughout the flow field. The velocity field is then determined from the equation of continuity.

The advantage of the present approach is that it preserves the elliptical characteristics of the flow making the solution tractable. It also eliminates the need for curve fitting and strong under relaxation necessary in the usual SLCM approach; while naturally generating the body-fitted curvilinear coordinates from the streamlines and orthogonals.

Governing Equations

The continuity and momentum equations are written in a coordinate system that rotated with the blades at angular velocity ω.

$$\nabla \cdot (\rho \bar{W}) = 0 \tag{1}$$

$$\bar{W} x (\nabla x \bar{V}) = \nabla I - T \nabla S \tag{2}$$

$$\bar{V} = \bar{W} + \bar{\omega} x \bar{r} \tag{2a}$$

Where $\bar{V}$ and $\bar{W}$ are the absolute and relative velocity vectors, respectively, I is the rothalpy, S is the entropy, ρ is the density, and T is the temperature.

The Velocity Gradient Equation. Consider the orthogonal curvilinear coordinates (m, θ, n) on the stream surface S_1 as

---

Contributed by the Fluids Engineering Division of the AMERICAN SOCIETY OF MECHANICAL ENGINEERS and presented at the Winter Annual Meeting, Miami Beach, Fla., November 17-21, 1985. Manuscript received by the Fluids Engineering Division August 15, 1985.

Copyright © 1987 by ASME

Downloaded 02 Jun 2010 to 171.66.16.66. Redistribution subject to ASME license or copyright; see http://www.asme.org/terms/Terms_Use.cfm

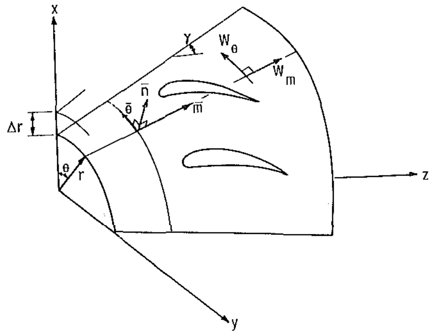

Fig. 1 S_1 stream surface and coordinates

shown in Fig. 1. The S_1 surface is assumed to be a body of revolution (variations in r are neglected in the θ-direction). The coordinates m and θ lie on the surface while n is the normal to the surface. The velocity vector $\bar{W}$ has two non-zero components, the meridional velocity W_m and the tangential velocity W_θ. The normal velocity component $W_n = 0$.

The θ-component of the momentum equation (2) is

$$-W_m\left[\frac{\partial}{\partial m}(rV_\theta)-\frac{\partial}{\partial m}(V_m)\right]=\frac{\partial I}{\partial \theta}-T\frac{\partial S}{\partial \theta}. \qquad (3)$$

Using equation (2a) and the relation

$$W_m^2=W^2-W_\theta^2$$

and substituting in equation (3), one obtains:

$$W\frac{\partial W}{\partial \theta}-\left[W_m\frac{\partial}{\partial m}(rW_\theta)+\frac{W_\theta}{r}\frac{\partial}{\partial \theta}(rW_\theta)\right]$$
$$-\omega W_m\frac{d}{dm}(r^2)=\frac{\partial I}{\partial \theta}-T\frac{\partial S}{\partial \theta} \qquad (4)$$

The second term in equation (4) is rewritten as:

$$W_m\frac{\partial}{\partial m}(rW_\theta)+\frac{W_\theta}{r}\frac{\partial}{\partial \theta}(rW_\theta)$$
$$=W\frac{d}{dl}(rW_\theta)=W_m\frac{d}{dm}(rW_\theta) \qquad (4a)$$

where d/dl is the derivative along a streamline. Using the above identity, the governing equation (4) takes the form

$$W\frac{\partial W}{\partial \theta}-W_m\frac{d}{dm}(rW_\theta)$$
$$-\omega W_m\frac{d}{dm}(r^2)=\frac{\partial I}{\partial \theta}-T\frac{\partial S}{\partial \theta}. \qquad (5)$$

Since $W_\theta = W_m r\, d\theta/dm$, then equation (5) becomes

$$r^2W_m\frac{d^2\theta}{dm^2}+\frac{d}{dm}(r^2W_m)\frac{d\theta}{dm}=\sigma \qquad (6a)$$

or

$$\frac{d}{dm}\left[r^2W_m\frac{d\theta}{dm}\right]=\sigma \qquad (6)$$

where

$$\sigma=\frac{W}{W_m}\frac{\partial W}{\partial \theta}-\omega\frac{d}{dm}(r^2)-\left(\frac{\partial I}{\partial \theta}-T\frac{\partial S}{\partial \theta}\right)/W_m.$$

Equation (6) is an elliptic second-order differential equation for the streamline tangential locations $\theta(m)$. Equation (6) is known as the velocity gradient equation.

The Continuity Equation. Equation (1) is written in the orthogonal coordinates, m, θ, and n as

$$\frac{\partial}{\partial m}(\rho brW_m)+\frac{\partial}{\partial \theta}(\rho bW_\theta)=0 \qquad (7)$$

Equation (7) can be identically satisifed using the relations

$$W_m=\frac{1}{pbr}\frac{\partial \psi}{\partial \theta} \qquad (8a)$$

and

$$W_\theta=\frac{\tan(\beta)}{pbr}\frac{\partial \psi}{\partial \theta} \qquad (8b)$$

where β is the streamline angle relative to the meridional direction and b is the streamtube thickness (normal distance between two stream surfaces).

The stream function ψ in equations (8a) and (8b) is determined from the mass flow in each streamtube at the inlet station.

Boundary Conditions. Two boundary conditions are required for the solution of the elliptic second-order equation (6). Referring to Fig. 2,

Nomenclature

a, b, c, d = coefficients defined in equation (11)
b = streamtube thickness (normal distance between two stream surfaces)
I = relative stagnation rothalpy
m = distance along meridional stream surface
m, θ, n = orthogonal curvilinear coordinates, Fig. 1
M = number of grid points in m-direction
ML = number of grid points upstream of the leading edge in m-direction
MT = number of grid points upstream of the trailing edge in m-direction
N = number of streamlines
P_0 = total pressure
P = static pressure
r = radius of meridional stream surface
S = entropy
S_1, S_2 = Wu's stream surfaces
SLCM = streamline curvature method
SSL = stagnation streamlines
T = temperature
$\bar{V}, \bar{W}$ = absolute and relative velocity vectors respectively
ρ = density
ω = rotation speed
$\Delta\theta$ = blade tangential thickness
θ_s = suction surface relative tangential coordinate
β = $\tan^{-1}(r\, d\theta/dm)$, Fig. 2
γ = $\tan^{-1}(dr/dz)$, Fig. 1
ζ = transformed meridional coordinate = $\int dm/r$
Δr = radial thickness increment between two meridional stream surfaces

Subscripts

m, θ, n = refer to components in m, θ and n directions respectively
e = refer to exit conditions
i = refer to inlet conditions
sl = refer to suction surface near the leading edge
st = refer to suction surface near the trailing edge

Downloaded 02 Jun 2010 to 171.66.16.66. Redistribution subject to ASME license or copyright; see http://www.asme.org/terms/Terms_Use.cfm

(1) Far-Upstream ($m=0$)

$$\theta_j=\theta_{j-1}+\Delta\theta_{j-1}; \quad j=2,3,\ldots,N \tag{9a}$$

where $\Delta\theta_{j-1}$ is the streamtube width specified in the input data.

(2) Far-Downstream ($m=m_e$)

$$r\frac{d\theta}{dm}=\tan(\beta_e) \tag{9b}$$

where β_e is the flow exit angle, see Fig. 2.

Determination of the Stagnation Streamlines. The upstream and downstream stagnation streamlines are determined from the solution of equation (6) with the following boundary conditions (see Fig. 2.).

Upstream stagnation streamlines:

$$r\frac{d\theta}{dm}=\tan(\beta_i) \qquad \text{at } m=0 \tag{10a}$$

$$\theta=\theta_{sl} \qquad \text{at } m=m_{sl} \tag{10b}$$

where β_i is the flow inlet angle.

Downstream stagnation streamlines:

$$\theta=\theta_{st} \qquad \text{at } m=m_{st} \tag{10c}$$

$$r\frac{d\theta}{dm}=\tan(\beta_e) \qquad \text{at } m=m_e. \tag{10d}$$

Since the lower stagnation streamlines are extensions of the blade suction surface, the choice of θs_l and θ_{st} on the surface is arbitrary. In the present analysis θ_{sl} and θ_{st} are chosen at the first and last grid points on the suction surface, respectively. The same argument holds for the pressure surface. Further tests for the choice of θ_{sl} and θ_{st} are shown in reference [8].

In case the flow exit angle β_e is not known, an iterative procedure is adopted to satisfy the Kutta condition. We start by estimating the exit angle β_e and solve for the flow field. An increment $\Delta\beta$ is then added to the exit angle and the flow field is recalculated. This process is repeated until the velocity (or pressure) at the cutoff points of the blade are equal.

Numerical Solutions

Numerical solutions for the governing equations (6) and (8) with the boundary conditions equations (9) and (10) are obtained using the finite-difference method. Finite difference equations are derived using central difference approximations for the first and second order derivatives in equations (6) and (8).

Finite-Difference Equations for Equation (6)

$$a_i\theta_{i-1}+b_i\theta_i+c_i\theta_{i+1}=d_i \tag{11a}$$

where

$$a_i=\frac{2(r^2W_m)_1}{(m_{i+1}-m_{i-1})(m_i-m_{i-1})} \tag{11b}$$

$$b_i=\frac{-2}{(m_{i+1}-m_{i-1})}\left[\frac{(r^2W_m)_2}{m_{i+1}-m_i}+\frac{(r^2W_m)_1}{m_i-m_{i-1}}\right] \tag{11c}$$

$$c_i=\frac{2(r^2W_m)_2}{(m_{i+1}-m_{i-1})(m_{i+1}-m_i)} \tag{11d}$$

$$d_i=\sigma \tag{11e}$$

$2\le i\le M-1$.

M is the number of grid points in the meridional direction.

The subscripts 1 and 2 in the above equations refer to the grid locations $(i-1/2)$ and $(i+1/2)$, respectively. Equation (11) is solved numerically using the L-U decomposition.

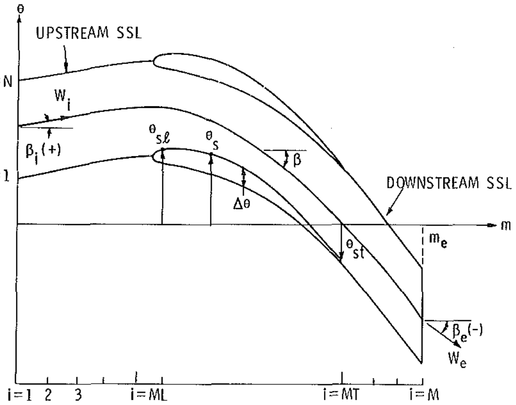

Fig. 2 Blade-to-blade geometry and dimensions

Finite-Difference Equations for Equation (8).

$$W_m(j)=\frac{\Delta_j^2\psi_{j+1}-\Delta_{j+1}^2\psi_{j-1}-(\Delta_j^2-\Delta_{j+1})\psi_j}{\Delta_j\Delta_{j+1}(\Delta_j+\Delta_{j+1})pb_jr_j} \tag{12a}$$

$$W_\theta(j)=W_m(j)\tan(\beta_j) \tag{12b}$$

where

$$\Delta_j=\theta_j-\theta_{j-1} \tag{12c}$$

$$\Delta_{j+1}=\theta_{j+1}-\theta_j \tag{12d}$$

$$2\le j\le N-1. \tag{12e}$$

At the locations $j=1$ and $j=N$, second-order, one-sided formulas are used to approximate equations (8*a*) and (8*b*).

Iterative Procedure. The iterative procedure adopted for solving the governing equations (6) to (10) is as follows:

(1) Initial guess is made of the position of the streamlines and the velocity field. The location of the streamlines at the inlet station defines the mass flow in each streamtube and consequently the distribution of the stream function ψ (ψ is constant on each streamline).

(2) The upstream stagnation streamlines are determined from the solution of equation (6) and the boundary conditions, equations (10*a*) and (10*b*). The streamlines at the inlet station are then located relative to the stagnation streamlines using the mass flow in each streamtube.

(3) The downstream stagnation streamlines are determined from the solution of equation (6) and the boundary conditions, equations (10*c*) and (10*d*). The streamlines at the exit station are then located relative to the stagnation streamlines using the mass flow in each streamtube. Another option which may be used is to specify the slope of the streamlines, equation (9*b*), at the exit station.

(4) Equation (6) is solved for the location of the streamlines with Dirichlet boundary conditions at the inlet station and Dirichlet or Neumann boundary conditions at the exit station.

(5) The velocity field is computed from equations (8*a*) and (8*b*).

(6) Steps (2) to (6) are repeated until convergence is achieved.

Results and Discussion

Numerical results have been obtained for three test cases: Wilkinson's stator and rotor turbine blades [4] and a NACA-65 compressor cascade. The first two test problems include the effects of three-dimensionality at the change of annulus area and radius of the meridional stream surface. Also they include the effects of relative vorticity on rotating blades.

Downloaded 02 Jun 2010 to 171.66.16.66. Redistribution subject to ASME license or copyright; see http://www.asme.org/terms/Terms_Use.cfm

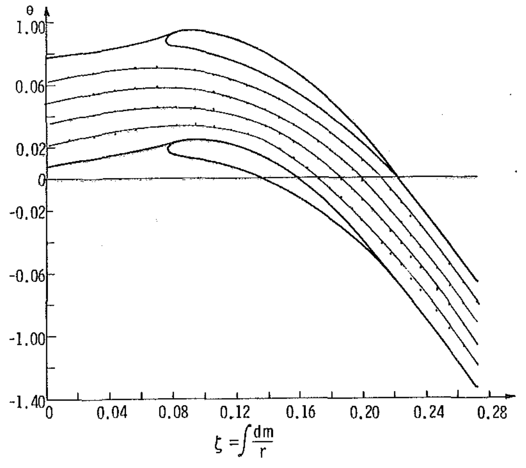

Fig. 3 45 deg flare case relative streamlines for rotating blades

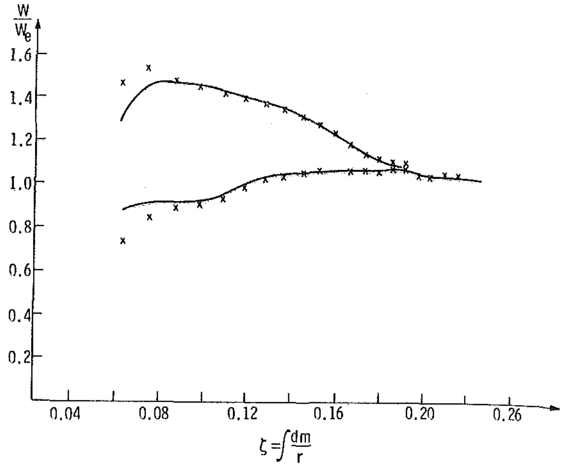

Fig. 5 45 deg flare case fixed blade

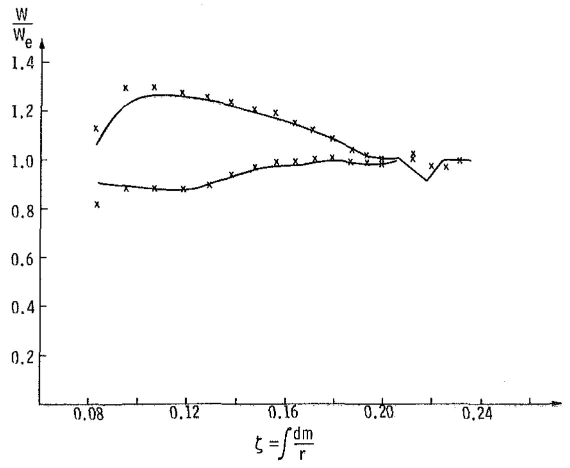

Fig. 4 45 deg flare case rotating blade

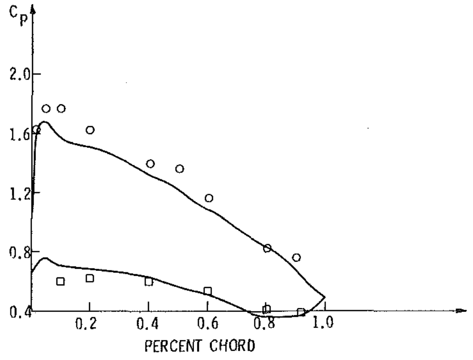

Fig. 6 Blade-surface pressure distributions for NACA 65-(18) 10

The computed results for these two cases are compared with the results of Wilkinson streamline curvature method [4]. The results of the cascade test problem are compared with the experimental data of reference [7].

Figure 3 shows the computed relative streamlines for a 45 deg flare which is defined in reference [4]. The streamlines are plotted in the Wilkinson's transformed plate (ζ, θ) where ξ is defined as $\int dm/r$. The predicted streamlines are identical with those given in reference [4] with the exception of slight differences near the leading edge of the blades. Figure 4 shows the velocity distributions on the pressure and suction surfaces. There is close agreement with the results of Wilkinson, especially with the flow outlet angle. The differences between the two results at the leading edge are mostly due to the treatment of the leading and trailing edges of the blades.

The computed results for a stator with the same blade section and the same relative flow conditions is shown in Fig. 5. The effects of the relative vorticity can be shown by comparing the loading in Figs. 4 and 5.

Figure 6 shows the results of the cascade test problem. The pressure coefficient $C_p = P_0 - P/\frac{1}{2}\rho W_1^2$ is plotted against the percentage chord and compared with experimental data of reference [7]. The differences between the computed results and the experimental data in Fig. 6 are due to two reasons. First, the smoothing of the blade thickness distribution which slightly deformed the blade geometry and curvature. The smoothing process was necessary in order to obtain accurate coordinates and slopes of the blade surface.

Table 1

Run	Type	M	N	CPU time in seconds VAX 11/782
1	Stator	30	6	33
2	Rotor	30	6	33
3	Cascade	42	3	15
4	Cascade	42	7	51
5	Cascade	42	10	75

Computer time and grid requirements for each test case are given in Table 1.

Conclusions

The present method is different from the classical SLCM in two aspects. First, the roles of the momentum and continuity equations in the SLCM are reversed in the present method. The velocity field is computed from the continuity equation instead of the momentum equation. The use of the momentum equation to trace the streamlines models the ellipticity of the flow field directly through the boundary conditions. It also eliminates the need for curve-fitting and under-relaxation of the streamlines that commonly are used in the SLCM. The second difference between the two methods is the use of the differential form of the continuity equation in the present approach which makes it possible to employ a stream function.

The present approach is as flexible as the classical SLCM in its application to compressible flow analysis.

Downloaded 02 Jun 2010 to 171.66.16.66. Redistribution subject to ASME license or copyright; see http://www.asme.org/terms/Terms_Use.cfm

Acknowledgments

This work was sponsored by the Naval Sea Systems Command, Contract No. N00024-79-C-6043.

References

1 Wu, Chung-Hua, "A General Through-Flow Theory of Fluid Flow with Subsonic or Supersonic Velocity in Turbomachines of Arbitrary Hub and Casing Shapes," NACA TN 2302, 1951.

2 March, H., "A Digital Computer Prorgram for the Through-Flow Fluid Mechanics in an Arbitrary Turbomachine Using a Matrix Method," Aeronautical Research Council R&M No. 3509, 1968.

3 Katsanis, T., and McNally, W. D., "Fortran Program for Calculating Velocities and Streamlines on Hub-Shroud Mid-Channel Flow Surface of an Axial or Mixed-Flow Turbomachine," NASA TN D-7343, 1973.

4 Wilkinson, D. H., "Calculation of Blade-to-Blade Flow in a Turbomachine by Streamline Curvature," Aeronautical Research Council R&M No. 3704, 1972.

5 Novak, R. A., and Hearsey, R. M., "A Nearly Three-Dimensional Intrablade Computing System for Turbomachinery," ASME JOURNAL OF FLUIDS ENGINEERING, Vol. 99, 1977, pp. 154–166.

6 Marsh, H., "The Through-Flow Analysis of Axial Flow Compressor," AGARD Lecture Series on Advanced Compressor, AGARD-LS-39-70, 1970.

7 Emery, J. C., et al., "Systematic Two-Dimensional Cascade Test of NACA 65-Series Compressor Blades at Low Speeds," NACA Report 1368, 1958.

8 Abdallah, S., Smith, C. F., and McBride, M. W., "Unified Equation of Motion (UEM) Approach as Applied to S1 Turbomachinery Problems," Accepted for publication at the 32nd International Gas Turbine Conference, USA, 1987.

Downloaded 02 Jun 2010 to 171.66.16.66. Redistribution subject to ASME license or copyright; see http://www.asme.org/terms/Terms_Use.cfm

A. Stirnemann

J. Eberl
Laboratory for Vibrations and Acoustics.

U. Bolleter
Pump Division.

Sulzer Bros. Ltd.,
Winterthur, Switzerland

S. Pace
Electric Power Research Institute,
Palo Alto, Calif.

Experimental Determination of the Dynamic Transfer Matrix for a Pump

Dynamic instability in pumping systems can be the cause of a wide variety of difficulties. Analytical investigations of the dynamic behavior of such systems depend on the proper mathematical model of the dynamic performance of the pump. This paper is concerned with the experimental means and analysis procedures for obtaining the transfer matrix representing the pump as a four-pole element. Direct measurement of the pulsating flow is omitted in favor of an indirect determination utilizing multiple pressure measurements in reference pipe sections attached to the pump. The method of parameter extraction from redundant experimental data, as well as the modeling by an equivalent electrical network is shown. Results are presented for noncavitating and slightly cavitating flows. The quality of the results is an indication that the method utilized represents a successful way to determine the dynamic transfer matrix for a pump.

Introduction

The phenomenon of dynamic instability in pumping systems can create a wide variety of difficulties ranging from simple acoustic annoyance to strong pressure pulsations and pipe vibrations which may render the system inoperable. Analytical investigations of the dynamic behavior of such systems require that each component of the circuit be represented by an appropriate mathematical model. While most of the essential system elements are well understood and amenable to a relatively simple mathematical description, pumps usually represent a much more complex sub-system. This becomes even more pronounced when cavitation is present. It is common practice to base this model on the acoustic properties, pressure and volume velocity (fluctuating mass flow rate), and to relate the inlet quantities to the corresponding outlet ones by means of linear equations. The limitation to linear behavior is acceptable for most response analyses of hydraulic systems.

Greitzer [1] presents a broad review on instabilities encounterd in pumping systems. Physical mechanisms for dynamic instability are discussed using a simple idealized model.

Early attempts to establish a mathematical model for the dynamic response of a pump were limited to noncavitating flows, and have concentrated attention on a single complex impedancelike parameter. Fanelli [2] estimated analytically the internal impedance of a centrifugal pump. Considerable research has been initiated as a result of pump system instabilities in liquid propelled rockets. Anderson et al. [3] performed dynamic measurements on such a centrifugal pump, still confined to noncavitating flows. Later, work carried out at the California Institute of Technology included the cavitating flow regimes. Brennen and Acosta [4] utilized results from free streamline cascade theory to evaluate the transfer matrix for a high specific speed cavitating inducer. Ng and Brennen [5] and Brennen et al. [6] described experiments performed to determine the dynamic transfer parameters of noncavitating and cavitating inducers. In these investigations much attention had been put on the direct measurement of the fluctuating mass flow rate. Initially laser doppler velocimeter techniques (LDV) were used and later supplemented by an electro-magnetic flow meter. On the analytical side Brennen [7] presented a bubble flow model to explore possible mechanisms governing the dynamic characteristics of cavitating pumps. Fanelli [8] reported upon experiments with a centrifugal pump, also employing LDV techniques but confined to noncavitating flow.

This paper is concerned with the experimental determination of the dynamic transfer matrix for a centrifugal pump. The measurements include both noncavitating and slightly cavitating operation. Direct measurement of the pulsating flow was omitted in favor of an indirect determination from multiple pressure measurements. The need for a better interpretation of the measured transfer matrix elements led to an electrical network model which can be related to the physical pump parameters. Using such a model it is possible to fit the measured data with sufficient accuracy. It is shown that the model impedances can be represented by a few simple elements (masses, compliances and resistances). These investigations are part of a research project "Feed Pump Hydraulic Performance and Design Improvement," carried out under a contract from Electrical Power Research Institute (EPRI). A small test loop has been used to develop the method. It will later be applied to full scale stages of boiler feed pumps, with the purpose of evaluating the sensitivity to instability of different hydraulic designs.

Contributed by the Fluids Engineering Division of THE AMERICAN SOCIETY OF MECHANICAL ENGINEERS and presented at the Winter Annual Meeting, Miami Beach, Fla., November 17–22, 1985. Manuscript received by the Fluids Engineering Division, December 30, 1985, Paper No. 85-WA/FE-7.

Copyright © 1987 by ASME

Downloaded 02 Jun 2010 to 171.66.16.66. Redistribution subject to ASME license or copyright; see http://www.asme.org/terms/Terms_Use.cfm

Approach and Parameter Estimation Procedures

For a linear dynamic four-pole model of a hydraulic system the vectors describing pulsating pressure p and mass flow (volume velocity q) between any two points, denoted i and $i+1$, are related by a transfer matrix $[T]$.

$$\begin{bmatrix} p_i \\ q_i \end{bmatrix} = \begin{bmatrix} T_{11} & T_{12} \\ T_{21} & T_{22} \end{bmatrix} \cdot \begin{bmatrix} p_{i+1} \\ q_{i+1} \end{bmatrix} \qquad (1)$$

Connecting an unknown system in series with two theoretically known reference systems, one on each side, the above stated principle leads to three individual four-pole equations for such an assembly. The problem is then to eliminate the volume velocity terms and express the unknown system only in terms of matrix parameters of the known system and pressure responses. This approach is explained in detail in the references [9 to 12]. It may be appropriate to mention that equation (1) differs insignificantly from the form used by the authors [4 to 7], and was chosen for convenience when chaining transfer matrices of systems having components in series.

Assuming plane-wave propagation, with the mean flow velocity negligible compared to the speed of sound, and neglecting losses between the measuring points at the attached pipe sections, the transfer matrix for the reference systems becomes

$$\begin{bmatrix} T \end{bmatrix} = \begin{bmatrix} \cos(k\cdot\ell) & (j\rho c/A)\cdot\sin(k\cdot\ell) \\ (jA/\rho c)\cdot\sin(k\cdot\ell) & \cos(k\cdot\ell) \end{bmatrix} \qquad (2)$$

Where k and l are the wavenumber and the distance between measurement locations, respectively, of the corresponding reference pipe having cross-sectional area A. The quantitiy ρc denotes the characteristic acoustic impedance.

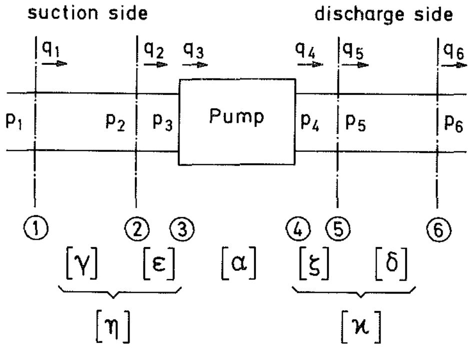

Fig. 1 Schematic representation of the basic system, and its nomenclature

For the investigations reported herein an assembly consisting of known and unknown systems as depicted in Fig. 1 is taken as a basis. The system limits of the pump are chosen at the suction and discharge flanges (stations 3 and 4 in Fig. 1). In order to keep the pressure transducers away from possible disturbances arising in the immediate vicinty of the pump, the measurement stations 2 and 5 have been placed at some distance from the flanges. Reference sections as well as extension pipes are assumed to comply with the model described by equation (2). $[\eta]$ and $[\kappa]$ denote the transfer matrices for the known system derived from multiplying the matrices for the corresponding sections as indicated in Fig. 1.

In terms of this model the four-pole equation for the pump becomes

$$\begin{bmatrix} p_3 \\ q_3 \end{bmatrix} = \begin{bmatrix} \alpha \end{bmatrix} \begin{bmatrix} p_4 \\ q_4 \end{bmatrix} \qquad (3)$$

Nomenclature

A = cross-sectional area of reference pipes
c = speed of sound
C = compliance in electrical network model
f = perturbation frequency
g = acceleration of gravity
G = conductance in electrical network model
H = pressure transfer function
H_p = head rise
j = imaginary unit
k = acoustic wavenumber
l = distance between measurement locations in reference systems
L = inertance in electrical network model
N = number of independent sets of measured data
p = oscillatory pressure
q = oscillatory volume velocity (mass flow)
Q = flow rate
R = resistance in electrical network model
$[T]$ = general designation for dynamic transfer matrix
U = impeller eye peripheral velocity
Y = parallel admittance in electrical network model
y = acoustic admittance at specified point
Z = series impedance in electrical network model
$[\alpha]$ = pump transfer matrix, and its elements
$[\gamma]$, $[\delta]$, $[\epsilon]$, $[\xi]$, $[\eta]$, $[\kappa]$ = transfer matrices for reference pipe sections (Fig. 1)
ρ = liquid density
σ = cavitation number = inlet pressure minus vapor pressure divided by $\rho U^2/2$
ω = pump speed
ω_s = $\omega\cdot\sqrt{Q}/(g\cdot H_p)^{3/4}$ = dimensionless specific speed

Subscripts 1 to 6 refer to measurement and analysis locations, respectively (Figs. 1 and 2). This applies also to double subscripts in connection with transfer functions and transfer admittances, otherwise it denotes matrix elements.

Downloaded 02 Jun 2010 to 171.66.16.66. Redistribution subject to ASME license or copyright; see http://www.asme.org/terms/Terms_Use.cfm

or explicitly written

$$p_3 = \alpha_{11} p_4 + \alpha_{12} q_4 \tag{4}$$

$$q_3 = \alpha_{21} p_4 + \alpha_{22} q_4 \tag{5}$$

An examination of these equations clearly indicates that two independent sets of data are necessary for the extraction of the four unknown matrix elements. To enhance the reliability of the parameters and to provide an error estimate, redundant sets of data can be employed yielding a system of N independent linear equations.

For experimental reasons pressure transfer functions are acquired. This transfer function approach is described by Chung and Blaser [13 and 14]. An application of this method to pump systems is reported upon by Bolleter [15]. The extraction of the transfer parameters makes use of the following transfer functions and admittances

$$H_{12} = p_1/p_2 \qquad y_{34} = q_3/p_4$$

$$H_{25} = p_2/p_5 \qquad y_4 = q_4/p_4$$

$$H_{56} = p_5/p_6$$

$$H_{34} = p_3/p_4$$

Proceeding from equations (4) and (5) the system of equations to determine the α coefficients then becomes:

$$\begin{bmatrix} (H_{34})_1 \\ \bullet \\ \bullet \\ \bullet \\ (H_{34})_N \end{bmatrix} = \begin{bmatrix} 1 & (y_4)_1 \\ \bullet & \bullet \\ \bullet & \bullet \\ \bullet & \bullet \\ 1 & (y_4)_N \end{bmatrix} \bullet \begin{bmatrix} \alpha_{11} \\ \alpha_{12} \end{bmatrix} \tag{6}$$

$$\begin{bmatrix} (y_{34})_1 \\ \bullet \\ \bullet \\ \bullet \\ (y_{34})_N \end{bmatrix} = \begin{bmatrix} 1 & (y_4)_1 \\ \bullet & \bullet \\ \bullet & \bullet \\ \bullet & \bullet \\ 1 & (y_4)_N \end{bmatrix} \bullet \begin{bmatrix} \alpha_{21} \\ \alpha_{22} \end{bmatrix} \tag{7}$$

The quantities H_{34}, y_{34}, and y_4 can now be expressed in terms of known matrices representing the pipe sections, and of the measured functions H_{12}, H_{25}, H_{56}.

$$H_{34} = \frac{H_{12}(\eta_{11}\gamma_{12} - \eta_{12}\gamma_{11}) + \eta_{12}}{H_{65}(\kappa_{11}\delta_{12} - \kappa_{12}\delta_{11}) + \kappa_{12}} \bullet \frac{H_{25}\delta_{12}}{\gamma_{12}} \tag{8}$$

$$y_{34} = \frac{H_{12}(\gamma_{11}\eta_{11} - \eta_{21}\gamma_{12}) - \eta_{11}}{H_{65}(\kappa_{11}\delta_{12} - \kappa_{12}\delta_{11}) + \kappa_{12}} \bullet \frac{H_{25}\delta_{12}}{\gamma_{12}} \tag{9}$$

$$y_4 = \frac{H_{65}(\kappa_{21}\delta_{12} - \kappa_{11}\delta_{11}) + \kappa_{11}}{H_{65}(\kappa_{11}\delta_{12} - \kappa_{12}\delta_{11}) + \kappa_{12}} \tag{10}$$

To solve the system of linear equations (6) and (7) for each frequency value a method described by Jennrich [16] was extended to complex quantities. This multiple regression algorithm allows to calculate the coefficients by "sweeping" a matrix of cross products of deviations (in our case the functions H_{34}, y_4 and y_{34}, y_4 respectively). Sweeping is a method of inverting the matrix of cross products so that at each step (as each variable is entered into the regression equation), the coefficients α, the partial correlations, the multiple correlation and the residual sum of squares are computed as part of the matrix inversion. After performing two sweeping steps for each equation system (6) and (7) one obtains the coefficients α. The standard deviations of these regression coefficients are calculated by using the square roots of the diagonal elements of the covariance matrix of the regression coefficients. Plots of α and corresponding error estimates allow one to readily judge the experimental uncertainty.

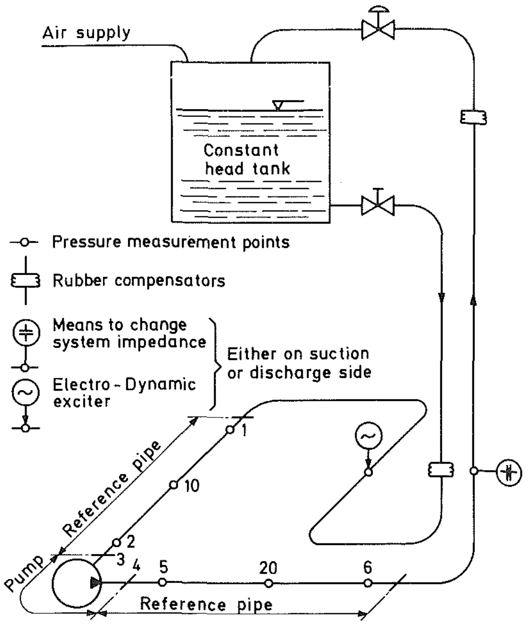

Fig. 2 Schematic of the experimental facility

Test Facility and Method of Measurement

The experimental investigations covered in this paper have been conducted on a small laboratory test loop incorporating a single stage centrifugal pump with a single volute. Its main features are shown diagrammatically in Fig. 2. The pump has an impeller diameter of 169 mm and can be characterized hydraulically by its specific speed of .95 (nondimensional form). To vary the suction conditions the constant-head tank contains means to maintain a preload higher or lower than the atmospheric pressure. The piping within the measurement stations is of particularly rugged design, in order to avoid erroneous effects from cross-sectional vibration modes (diameter to wall thickness ratio about 7). Regarding the assumption of plane-wave propagation is to mention that the diameter to wavelength ratio is .009 or smaller. For the variation of the system impedance a total of 5 hydraulic capacitors (membrane accumulators) are attached to the piping and arranged in such a way as to yield significant changes of the dynamic system characteristics over the frequency range of interest. Also attached to the piping is an electro-dynamic exciter which is mounted on the discharge side of the pump when the impedance changer assembly is placed on the suction side, and vice versa.

Of the pressure measurement locations shown in Fig. 2 the stations 10 and 20 were employed only for the experimental determination of the speed of sound. Each station was equipped with a pair of quartz pressure transducers arranged in a face to face position, with the charge signals being added directly before entering the charge amplifier. Preliminary tests have proved the usefulness of this arrangement to average out the effect of transversal water column vibrations on the pressure measurements. The calibration of the complete pressure measurement channels had been done in a separate calibration device using channel 1 as reference signal. By carefully selecting the transducers and adjusting the amplifiers it was possible to keep amplitude and phase deviations well below 1 percent and 0.5 degree, respectively, within the frequency range of interest.

From the beginning of these investigations the data processing was performed in two major sub-tasks. First, the data acquisition and data reduction, up to a convenient extent, was performed by means of a mini computer-based multi-channel data acquisition and analyzer system. Second, the extraction

Downloaded 02 Jun 2010 to 171.66.16.66. Redistribution subject to ASME license or copyright; see http://www.asme.org/terms/Terms_Use.cfm

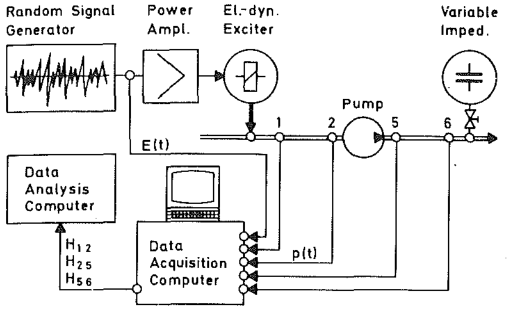

Fig. 3 Block diagram showing test set-up and data handling

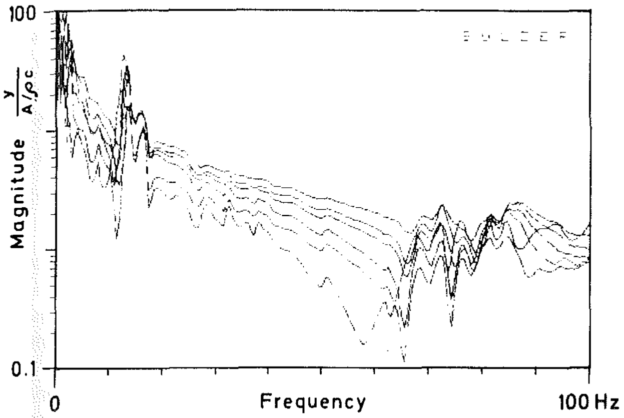

Fig. 4 Measured admittance variation (normalized) at the pump discharge, obtained from employing the hydraulic capacitors. (Uncertainty in $y = \pm 3$ dB for frequencies $f > 5$ Hz or $y = \pm 1.2$ dB for $f > 10$ Hz)

of the transfer matrix parameters from redundant sets of data and the curve fitting for the establishment of equivalent electrical network models was conducted on a main-frame computer. The data interface was chosen at the pressure transfer function level. Thus the intention of the first sub-task was to generate a transfer file (for each set of measurements) containing primarily the following information: (*a*) Pressure transfer function H_{12}, between stations 1 and 2. (*b*) Pressure transfer function H_{25}, across the pump. (*c*) Pressure transfer function H_{56}, between stations 5 and 6. (*d*) Speed of sound estimations for both sides of the pump.

The term "set of measurements" here refers to one particular configuration of the impedance changers. Six sets of data have generally been taken for all steady state conditions investigated, resulting from changing the system impedance in steps as explained above.

A number of preliminary tests were carried out to evaluate excitation techniques, averaging methods, and data correlation. Free-run random excitation and averaging in the frequency domain was chosen, cross correlating the pressure spectra with the exciter input voltage. The excitation was band-limited to a usable response up to 100 Hz. Data sampling was set to give a frequency resolution of 0.5 Hz. Figure 3 depicts the major elements of the measurement procedure. As an example for the effectiveness of the impedance changers Fig. 4 shows the measured admittance variation at the pump discharge. For the indirect determination of the fluctuating mass flow an accurate knowledge of the speed of sound is essential. An experimental method used by Margolis and Brown [17] was adapted. It is based on the wave propagation within three equidistant stations in a uniform pipe. The estimation of the speed of sound then results from a curve fit of a cosine function in a least squares manner. This method has been applied to the measurement sections of the suction side and the discharge side separately but simultaneously. The accuracy attainable lies well within one percent.

Measurements have been taken under various operation parameters, such as pump speed, flow rate, and degree of cavitation. The test results presented in the proceeding part of this paper are confined to the comparison of standstill and three different suction conditions at the best efficiency operating point (BEP). Without pressurizing the constant head tank, the cavitation number at BEP is $\sigma = 0.7$, and lies near the inception point of cavitation. For this pump speed and flow rate the suction condition corresponding to three percent head drop is given by $\sigma = 0.23$. By pressurizing the tank $\sigma = 1$ can be reached at which cavitation is completely suppressed. Tests under moderate cavitation conditions are in progress. Although the signal to noise ratio decreases significantly, preliminary results are promising.

Test Results

If the transfer matrix coefficients of the pump are really independent of the piping system connected to it, then one must get the same coefficients for excitation on the suction as well as for excitation on the discharge side. The impedance changers are in each case on the opposite side of the pump. The tests carried out show a very good agreement between the corresponding curves. These results have been proved not only for standstill but also for different operating points.

For example Fig. 5(*a*) shows the coefficent α_{22} for the pump at best efficiency point (BEP) with excitation on the suction side and extracted from six different impedance changer positions at the discharge side. The dotted curve represents the error estimate of the coefficient resulting from the least squares procedure. If the error estimate is much lower than the coefficient, one can suppose that the accuracy of the result is good. In some frequency regions where also the phase of the coefficient is very uncertain the error estimate reaches about the same value as the coefficient, corresponding to an uncertainty of approximately 100 percent (standard deviation). This effect is due to an insufficient variation of the system impedance and is specific for the excitation and impedance changer configuration. At these frequency regions the variation of the measured transfer functions is mainly produced by the fluid fluctuations.

Figure 5(*b*) shows the coefficient α_{22} with error estimate for the same pump operating point but with excitation on the discharge side and impedance changers on the suction side. Apart from the upper frequency range the coefficient to error ratio is better than in the case before. At the single frequency of about 27 Hz the error peak corresponds with the very conspicuous phase jump.

The use of a least squares algorithm makes it possible to combine the different measurements in a simple way. The six data sets from the suction side excitation can be entered into the computer program together with the data from the discharge side excitation without any modification. The result is shown in Fig. 5(*c*). The coefficient to error ratio is quite good now over the full frequency range from about 5 Hz to 90 Hz. This error ratio of about 3 to 10 percent is typical for all 4 matrix elements as well as for the coefficients for other pump operating points.

Thus all the transfer matrix coefficients presented in this paper are extracted in this way from six measurements with excitation on the suction side and six measurements with the excitation on the discharge side.

In Fig. 6 the transfer matrix coefficients for standstill and for BEP (2900 RPM, 45 *l*/s) are compared. If the acoustic compliance in the pump is negligible against the inertance one can approximate the pump as a four-pole with only one series impedance. In this case it is known from the four-pole theory, that the coefficients α_{11} and α_{22} are equal to one and α_{12} is identical with the series impedance. The curves in Fig. 6 show

Downloaded 02 Jun 2010 to 171.66.16.66. Redistribution subject to ASME license or copyright; see http://www.asme.org/terms/Terms_Use.cfm

that we have this situation for the present pump. On the one hand, the coefficients α_{11} and α_{22} are nearly equal to one over the whole frequency range. On the other hand, the series impedance given by α_{12} is clearly smaller for all frequencies than the parallel impedance which is the inverse of α_{21}. So the pump transfer matrix is dominated by the acoustic inertance and its resistive component. This impedance is represented by α_{12}. For higher frequencies it is proportional to the frequency and the phase is about +90°. For lower frequencies the resistive component begins to dominate and turns the phase to 0°. Here one can see the first remarkable difference between standstill and operation. While the inertance at the higher frequencies is the same, the phase of the BEP impedance turns earlier to 0° than the phase of the impedance at standstill. This means that the real part of the inertance increases clearly when the pump is running. The amount of this effect is discussed later.

The coefficient α_{21} is the most critical element to determine, because it represents the parallel admittance of the four-pole (when it is supposed that there is only one). In the case of the pump this admittance is given by the total acoustic compliance inside the pump. It consists therefore of the compliance of the housing, the water and possible gas- or vapor bubbles. When there is no cavitation the compliance of the housing and the water is very small and that is the reason for the difficulties to determine the element α_{21}. However we succeeded in measuring this quantity as it is shown in Fig. 6(*c*). From about 20 Hz to 100 Hz the coefficient α_{21} has the typical properties of the admittance of a compliance. The phase is 90° and the amplitude increases with frequency. As it is the most critical element it is very sensitive to changes of the operation conditions. From standstill to the BEP one notes a difference of more than a factor of three. This is due to the additional compliance of cavitation bubbles which occur when the pump is running. Further discussion of this element will follow later.

From these results discussed above one can summarize that the measured transfer matrix coefficients could be explained physically and that the differences between standstill and operation can be understood and interpreted.

Electrical Network Model

The need for a quantitative description of the measured curves as well as the reduction of the measured data to some few significant parameters leads to an electrical network model. This model is related to the physical pump elements and describes the acoustic pump properties.

The simpliest configuration that satisfies these requirements is represented by a π-section as shown in Fig. 7(*a*). The π-section consists of two parallel admittances Y_1 and Y_3 and of a series impedance Z_2. Such a passive network can only be used if the determinant of $[\alpha]$ is equal to one. The

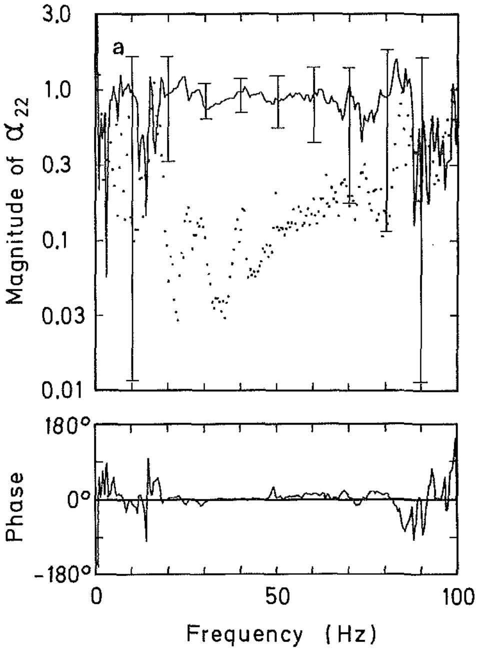

(*a*)

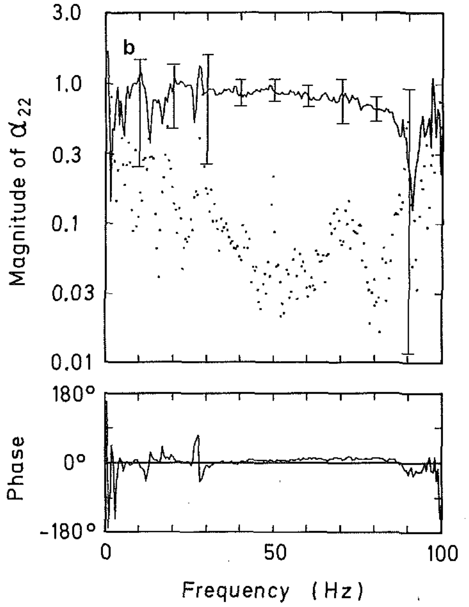

(*b*)

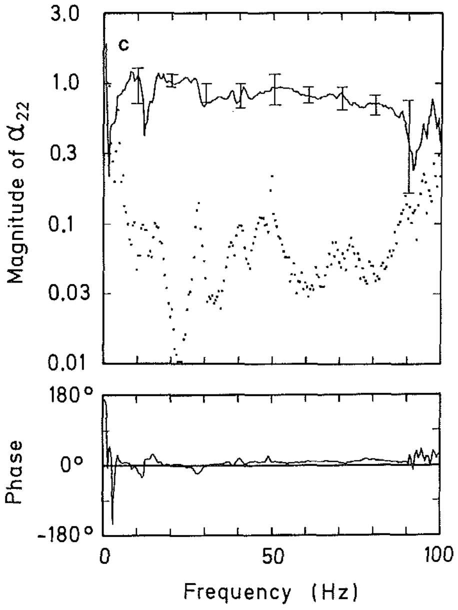

(*c*)

(*a*) obtained from excitation on the suction side.
(*b*) obtained from excitation on the discharge side.
(*c*) obtained from a combination of both measurements.
Dotted lines represent the estimates of the standard deviation of the element. Bars indicate the corresponding 95 percent confidence limits, represented by the means from the frequency intervals of 10 Hz, degree of freedom $f = 4$ for (a) and (*b*) and $f = 10$ for (*c*). A relative uncertainty of the magnitude of 10 percent corresponds to an absolute phase uncertainty of 5.7 deg.

Fig. 5 Transfer matrix element α_{22} for slightly cavitating flow at BEP (point D in Fig. 9),

Downloaded 02 Jun 2010 to 171.66.16.66. Redistribution subject to ASME license or copyright; see http://www.asme.org/terms/Terms_Use.cfm

measurements of the α coefficients have shown that this condition is satisfied well enough for a first approximation. For the case of strong cavitation the model might have to be supplemented by an active element, a source.

The general network matrix formulations one can easily deduce the expressions for the model admittances Y_1 and Y_3 and the model impedance Z_2:

$$Y_1 = (\alpha_{22} - 1)/\alpha_{12} \tag{11}$$

$$Y_3 = (\alpha_{11} - 1)/\alpha_{12} \tag{12}$$

$$Z_2 = \alpha_{12} \tag{13}$$

The corresponding α matrix has the following form:

$$[\alpha] = \begin{bmatrix} 1 + Z_2 Y_3 & Z_2 \\ Y_1 + Y_3 + Y_1 Z_2 Y_3 & 1 + Y_1 Z_2 \end{bmatrix} \tag{14}$$

One can see from this matrix that α_{12} represents the series impedance Z_2 which is a combination of the inertia and its resistive component. The total compliance inside the pump is contained in the admittances Y_1 and Y_3. The admittance Y_1 on the suction side influences mainly the coefficient α_{22} and in the same way is the influence of Y_3 on α_{11}. As the product $Z_2 \bullet Y_3$ is $\ll 1$ in the whole frequency range, α_{21} describes approximately the admittance of the total pump compliance.

The knowledge of the pump geometry on the one hand and the calculated curves Y_1, Y_3, and Z_2 from the measurements on the other hand led to an electrical network as shown in Fig. 7(*b*). The series impedance Z_2 is therefore represented by a resistor R_2 and an inertance L_2. The two compliances C_1 and C_3 in the suction and on the discharge side are completed with inertances L_1 and L_3 to fit the data at the lowest frequencies.

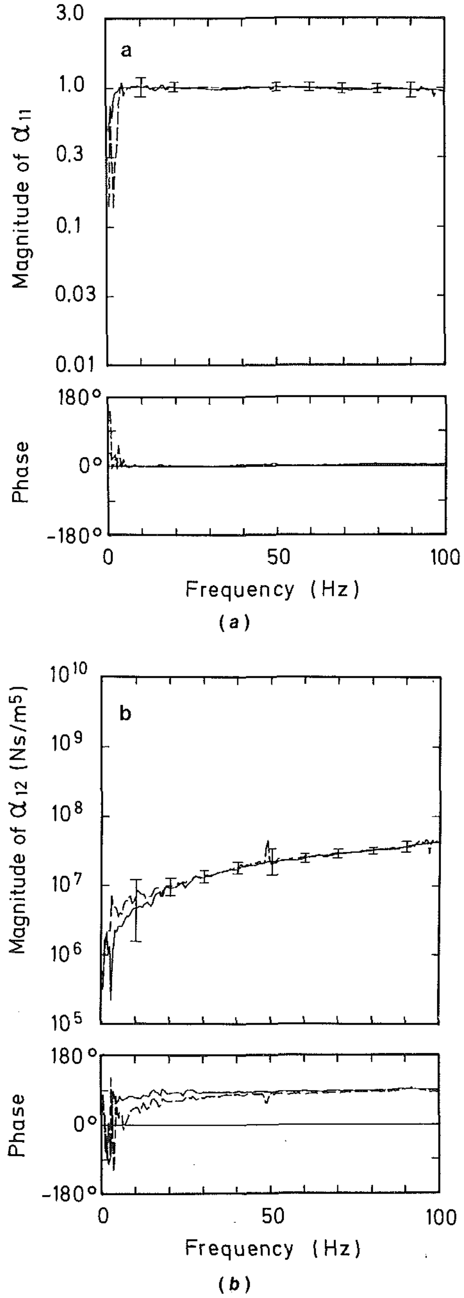

(*a*)

(*b*)

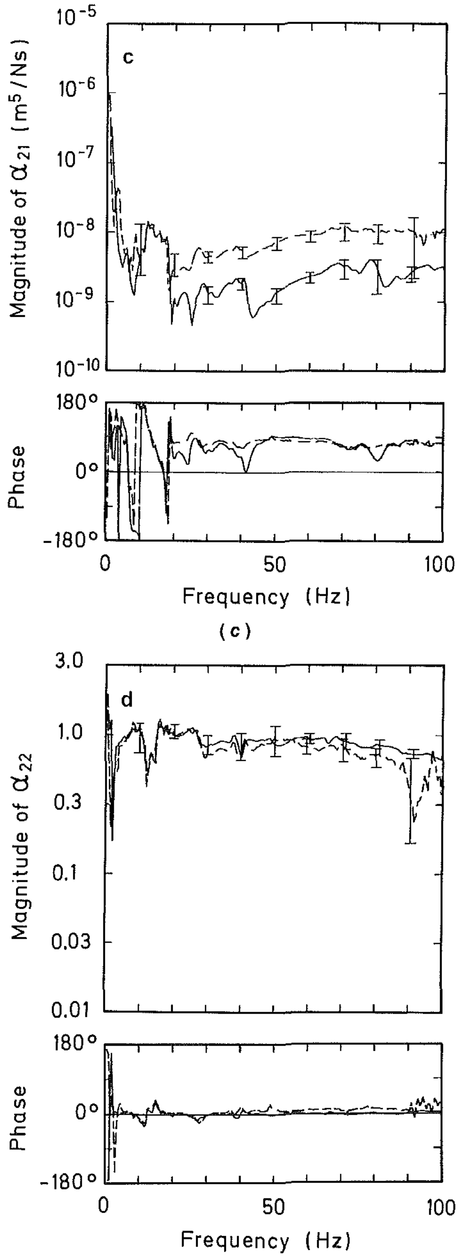

(*c*)

(*d*)

Fig. 6 Comparison of transfer matrix elements for standstill and for cavitating flow at BEP (point D in Fig. 9).
Solid line = standstill
Dashed line = best efficiency point (BEP)
Bars indicate the 95 percent confidence limits of the results at BEP. The variation of the results at standstill is generally much smaller, except for the element α_{21}, where the bars are drawn for both cases. A relative uncertainty of the magnitude of 10 percent corresponds to an absolute phase uncertainty of 5.7 deg.

Downloaded 02 Jun 2010 to 171.66.16.66. Redistribution subject to ASME license or copyright; see http://www.asme.org/terms/Terms_Use.cfm

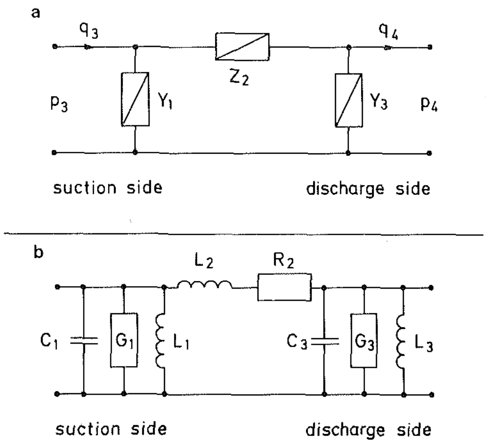

Fig. 7 Electrical network model for the dynamic behavior of the pump. (*a*) simplified passive Pi-type network; (*b*) detailed model showing the parameters as extracted from measurements

For damping purposes the two conductances G_1 and G_3 are added.

To demonstrate the curve fits (Fig. 8) the data from the measurements at BEP with $\sigma = 1.0$ (case B in Fig. 9) are taken as an example. Figure 8 shows real and imaginary part of the series impedance Z_2 in the frequency range from 5 to 80 Hz. The real part of Z_2 (Fig. 8(*a*)) was approximated by a simple resistor R_2. The imaginary part of Z_2 (Fig. 8(*b*)) has an excellent linearity with frequency. The straight line represents the fitted imaginary part $2 \cdot \pi \cdot f \cdot L_2$.

At higher frequencies the admittances Y_1 and Y_3 are dominated by the compliances C_1 and C_3. For this reason the main attention was concentrated to the determination of these two elements, which were extracted from the imaginary parts of the corresponding admittances. Now the values of these important elements and their change with different operating conditions of the pump can be discussed. Figure 9 shows the values for the pump at standstill and at best efficiency point (BEP) with three different cavitation numbers $\sigma = 0.7 \ldots 1.0$.

One important parameter of the pump is the series impedance Z_2 consisting of the resistive component R_2 and the inertance (acoustic mass) L_2. From Fig. 9 one can see that the dynamic resistor R_2 (mean from 5 Hz to 80 Hz) changes significantly from standstill to operation by a factor of more than 2. There is only a slight upward tendency with decreasing σ. The value of R_2 that one gets from the static Q-H-curve is only about a factor two lower than measured dynamically. Thus the two values are surprisingly close.

The inertance L_2 is independent from the operating point and has the same value even for standstill. Also shown is the value that was estimated roughly from the pump geometry, and which is of the same order of magnitude.

From the two parallel admittances Y_1 and Y_3 only the compliance elements C_1 and C_3 are of interest. From Fig. 9 one can see that the compliance C_3 on the discharge side is very small and does not vary much with σ. However the value from standstill is clearly smaller than those from pump operation. In contrast the compliance C_1 on the suction side is 5 to 15 times larger. There is a very significant relation between this quantity and the cavitation number σ. From standstill to operation with $\sigma = 0.7$ the value of C_1 increases from 5.1×10^{-12} to 19×10^{-12} m^5/N. If one considers that the pump is operating in the region of cavitation inception, it is remarkable how sensitive this measurement method is. This is also demonstrated when the equivalent gas volumes of the observed difference of C_1 which is 14×10^{-12} m^5/N are calculated. The equivalent air volume with that compliance is 2.0 ccm, the corresponding volume of vapor is 0.045 ccm.

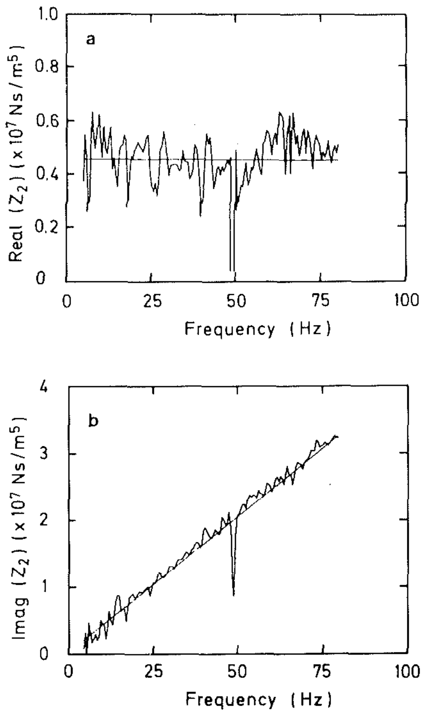

Fig. 8 Curve fits to determine series impedance Z_2 for the electrical network model. Operation at BEP without cavitation, according to point B in Fig. 9.

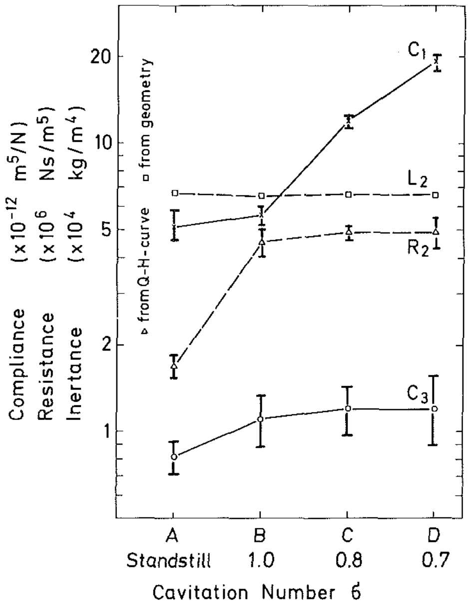

Fig. 9 Electrical network parameters for standstill and for different cavitation numbers at best efficiency point. Shown are also the elements of the series impedance, obtained from the steady state performance curve. Bars indicate that 95 percent confidence limits of the values represented.

Thus cavitation bubbles with a total volume of some few cubic millimeters are detectable with the measuring method used.

Conclusions

The main feature of this work was the method used to determine the transfer matrix elements of a pump by the omission of the direct measurement of the volume velocity by using pressure measurements only. As an advantage no correction curves have to be used and the system is easy to calibrate, but

Downloaded 02 Jun 2010 to 171.66.16.66. Redistribution subject to ASME license or copyright; see http://www.asme.org/terms/Terms_Use.cfm

there is the need to determine the speed of sound on both sides of the pump.

It has been shown that the extracted transfer matrix coefficients do not vary with the excitation direction and therefore they permit a system independent description of the dynamic pump performance. However the outer system may influence the accuracy of the matrix coefficients when a sufficient variation of the boundary conditions does not exist. For this reason it is of advantage to use a least squares technique which combines the data from different excitation directions into one single estimation procedure. The resulting error estimates have demonstrated that the measurements yield reliable coefficients from about 5 to 100 Hz.

The electrical network model developed reduces the data to eight elements for one pump operating point. So the effort to describe a pump as a single element of a complex pipe system is strongly reduced by using this model. In addition the values of the model elements are very sensitive indicators of the physical processes inside the pump.

The successful application of the measurement principle presented in this paper as well as the high quality of the results make it possible to use this method as an important tool for further investigations on larger pump systems. Should further tests, especially with stronger cavitation, indicate a dynamically active behavior of the pump, then the network model will have to be adapted. Furthermore, from the measured dynamic models criteria will be developed for describing in a simple manner the capacity of the pump to enhance or reduce dynamic stability of a hydraulic system.

Acknowledgment

The work described in this paper was conducted as a part of the contract RP 1884-10 from the Electric Power Research Institute (EPRI), Palo Alto, Calif., under the project management of Stanley E. Pace. The permission to publish the results of this investigation is gratefully acknowledged.

References

1 Greitzer, E. M., "The Stability of Pumping," ASME JOURNAL OF FLUIDS ENGINEERING, Vol. 103, June 1981, pp. 193-242.

2 Fanelli, M., "Further Considerations on the Dynamic Behaviour of Hydraulic Turbo-Machinery," *Water Power*, Vol. 24, June 1972, pp. 208-222.

3 Anderson, D. A., Blade, R. J., and Stevans, W., "Response of a Radial-Bladed Centrifugal Pump to Sinusoidal Disturbances for Non-Cavitating Flow," NASA Technical Note, TN D-6556, Dec. 1971.

4 Brennen, C., and Acosta, A. J., "The Dynamic Transfer Function for a Cavitating Inducer," ASME JOURNAL OF FLUIDS ENGINEERING, Vol. 98, June 1976, pp. 182-191.

5 Ng, S. L., and Brennen, C., "Experiments on the Dynamic Behavior of Cavitating Pumps," ASME JOURNAL OF FLUIDS ENGINEERING, Vol. 100, June 1978, pp. 166-176.

6 Brennen, C. E., Meissner, C., Lo, E. Y., and Hoffmann, G. S., "Side Effects in the Dynamic Transfer Functions for Cavitating Inducers," ASME JOURNAL OF FLUIDS ENGINEERING, Vol. 104, Dec. 1982, pp. 428-433.

7 Brennen, C., "Bubble Flow Model for the Dynamic Characteristic of Cavitating Pumps," *Journal of Fluid Mechanics*, Vol. 89, Part 2, 1978, pp. 223-240.

8 Fanelli, M., Angelico, G., and Escobar, P., "The Behaviour of a Centrifugal Pump in a Steady Pulsating Hydraulic System. Experimental Results," Paper presented at the 7th Conference on Fluid Machinery, held in Budapest, Hungaria, Sept. 13-16, 1983.

9 To, C. W. S., and Doige, A. G., "A Transient Testing Technique for the Determination of Matrix Parameters of Acoustic Systems, I: Theory and Principles," *Journal of Sound and Vibration*, Vol. 62, 1979, pp. 207-222.

10 To, C. W. S., and Doige, A. G., "A Transient Testing Technique for the Determination of Matrix Parameters of Acoustic Systems, II: Experimental Procedures and Results," *Journal of Sound and Vibration*, Vol. 62, 1979, pp. 223-233.

11 To, C. W. S., and Doige, A. G., "The Application of a Transient Testing Method to the Determination of Acoustic Properties of Unknown Systems," *Journal of Sound and Vibration*, Vol. 71, 1980, pp. 545-554.

12 Lung, T. Y., and Doige, A. G., "A Time-Averaging Transient Testing Method for Acoustic Properties of Piping Systems and Mufflers with Flow," *Journal of the Acoustical Society of America*, Vol. 73, March 1983, pp. 867-876.

13 Chung, J. Y., and Blaser, D. A., "Transfer Function Method of Measuring In-Duct Acoustic Properties, I. Theory," *Journal of the Acoustical Society of America*, Vol. 68, Sept. 1980, pp. 907-913.

14 Chung, J. Y., and Blaser, D. A., "Transfer Function Method of Measuring In-Duct Acoustic Properties. II. Experiment," *Journal of the Acoustical Society of America*, Vol. 68, Sept. 1980, pp. 914-921.

15 Bolleter, U., "Using Transfer Function Measurements to Determine Energy Propagation in Fluid Lines, with Applications to Centrifugal Pump Systems," *Proceedings of the Conference on Recent Developments in Acoustic Intensity Measurement*, held in Senlis, France, Sept. 30-Oct. 2, 1981.

16 Jennrich, R. I., *Statistical Methods for Digital Computers*, Edited by K. Enslin, A. Ralston, and H. S. Wilf, Wiley, New York, 1977.

17 Margolis, D. L., and Brown, F. T., "Measurement of the Propagation of Longwavelength Disturbances Through Turbulent Flow in Tubes," ASME JOURNAL OF FLUIDS ENGINEERING, Vol. 98, Mar. 1976, pp. 70-78.

Downloaded 02 Jun 2010 to 171.66.16.66. Redistribution subject to ASME license or copyright; see http://www.asme.org/terms/Terms_Use.cfm

K. N. Ghia
Professor.

U. Ghia*
Research Associate Professor.

C. T. Shin*
Graduate Research Assistant.

Department of Aerospace Engineering
and Applied Mechanics,
University of Cincinnati,
Cincinnati, Ohio 45221

Study of Fully Developed Incompressible Flow in Curved Ducts, Using a Multi-Grid Technique

Fully developed flows inside curved ducts of rectangular as well as polar cross sections have been analyzed using the Navier-Stokes equations in terms of the axial velocity and vorticity and the cross-flow stream function. Numerical solutions of the three second-order coupled elliptic partial differential equations governing this flow have been obtained using efficient numerical schemes. For curved-duct flows, the similarity parameter of significance is the Dean number K, rather than the Reynolds number Re. Results have been obtained for curved ducts with square cross sections for K up to 900 which, in the present study, corresponds to Re = 9,000 for this internal flow configuration. The fine-grid calculations show that, for square cross-section ducts, Dean's instability occurs at K ≈ 125 and, further, that this phenomenon does not disappear even for K = 900. In ducts of polar cross sections, which are geometrically more representative of turbomachinery cascade passages, the phenomenon of Dean's instability is not seen to occur for K up to 600.

Introduction

Modern air-breathing propulsion systems are not only comprised of the major gas turbine engine components such as turbine, compressor, nozzle, etc., but also utilize several complex duct configurations primarily to efficiently transfer the flow from one element of the system to another. The inlet diffuser, the transition duct and the lobe mixer are some of the configurations wherein an accurate and reliable analysis of the prevailing internal flow is essential for obtaining improved performance of the overall propulsion system. These duct analyses can also provide further insight into the analysis of flow in passages of turbomachinery components such as the centrifugal compressor or the gas turbine. Therefore, the ability to predict the details of the flow process in highly curved ducts of some simple cross sections (Fig. 1) can also lead to improved design of these components.

An important feature distinguishing curved-duct flows from straight-duct flows is the secondary flow induced in the cross planes of the curved duct due to the centrifugal forces generated by the duct curvature which can be characterized by the Dean number K. Typically, this secondary flow consists of a pair of counter-rotating vortices in the cross plane and persists even asymptotically far downstream. The result is a distortion of the axial flow profile, additional mixing of the fluid and, hence, enhanced rates of heat, mass and momentum transfer, and increased pressure drop. For curved ducts of square cross section, numerical calculations [Joseph, Smith and Adler (1975), Chen, Lin and Ou (1976) and Ghia and Sokhey (1977)] as well as experimental observations [Cheng, Nakayama and Akiyama (1977)] reveal that, for K larger than a certain critical value, an additional pair of counter-rotating vortices makes its appearance at the concave wall, so that the secondary flow now consists of four vortices. Since the additional vortices appear rather abruptly, i.e., with a small change in the Dean number beyond the critical value, the phenomenon is termed as Dean's instability [see Cheng, Lin and Ou (1976)] and is accompanied by a further abrupt increase in the pressure losses in the flow. In contrast, coiled tubes of circular cross section revealed only a single pair of secondary-flow vortices at all Dean's numbers up to 1000 [Austin and Seader (1973)]. Recently, however, four-vortex cross-flow patterns have been obtained by Dennis and Ng (1982) and Nandakumar and Masliyah (1982) for the circular cross-section curved pipe also. According to the bifurcation phenomenon of Benjamin (1978), both two-vortex and four-vortex cross-flow patterns constitute valid solutions; which of the two patterns is attained depends on the initial condition used to start the numerical solution of the nonlinear governing equations. Also, for ducts of polar cross sections, which are more typical of turbomachinery applications, U. Ghia, K. Ghia, and Goyal (1979) did not observe the Dean instability for K up to 630 for the aspect ratios and the Reynolds numbers they considered.

---

*Present Titles and Affiliations: U. Ghia, Professor, Department of Mechanical and Industrial Engineering, University of Cincinnati. C. T. Shin, Engineer, General Electric Company, Evendale, Ohio.

Contributed by the Fluids Engineering Division of THE AMERICAN SOCIETY OF MECHANICAL ENGINEERS and presented at the Winter Annual Meeting, Washington, D.C., November 15-20, 1981. Manuscript received by the Fluids Engineering Division July 23, 1982.

Copyright © 1987 by ASME

Downloaded 02 Jun 2010 to 171.66.16.66. Redistribution subject to ASME license or copyright; see http://www.asme.org/terms/Terms_Use.cfm

The present study was undertaken with the following objectives:

- (i) to perform fine-grid flow calculations and conclusively determine whether Dean's instability is encountered for some combination of the parameters for curved ducts of polar cross section;
- (ii) to provide accurate and efficient results for this model problem using the velocity-vorticity formulation, so that these solutions can be used to verify results obtained using different formulations and other solution algorithms;
- (iii) finally, with this model problem, to develop the methodology for the multigrid-strongly-implicit (MG-SI) procedure as well as the alternating-direction implicit (ADI) method for the coupled nonlinear governing equations at high Reynolds number.

To satisfy these objectives, emphasis was placed both on developing the numerical analysis to effectively combine the multigrid method with an efficient semi-implicit scheme, as well as on obtaining accurate results in order to study Dean's instability for square and polar ducts at high Dean's number, that is, at higher Reynolds numbers.

Mathematical Formulation

Governing Differential Equations. For the model problem of fully developed flow through ducts of simple cross sections, use is made of the toroidal coordinates (r, θ, ϕ) shown in Fig. 1. The starting equations are the steady Navier-Stokes equations in terms of the primitive variables. However, if these are recast in terms of the streamwise vorticity ζ and the cross-flow stream function ψ, the resulting velocity-vorticity stream-function formulation is somewhat simpler than the primitive-variable formulation. It will also facilitate satisfying one of the present objectives, namely, that of obtaining a set of results using a formulation different from previous formulations for this problem [U. Ghia, K. Ghia and Goyal (1979)]. Hence, the nondimensional secondary velocities and the streamwise component of vorticity are defined as

$$u=\frac{1}{(R+rc^m)^n r^m}\frac{\partial\psi}{\partial\theta}, \quad v=-\frac{1}{(R+rc^m)^n}\frac{\partial\psi}{\partial r} \tag{1}$$

and

$$\zeta=\frac{\partial v}{\partial r}+m\frac{v}{r}-\frac{1}{r^m}\frac{\partial u}{\partial\theta}. \tag{2}$$

Use of equations (1) and (2) in the Navier-Stokes equations enables derivation of the following equations for the streamwise component of vorticity, the cross-flow stream function, and the streamwise velocity w.

Streamwise Vorticity Equation

$$\begin{aligned}&\frac{1}{r^m(R+rc^m)^n}\frac{\partial\psi}{\partial\theta}\frac{\partial\zeta}{\partial r}-\frac{1}{r^m(R+rc^m)^n}\frac{\partial\psi}{\partial r}\frac{\partial\zeta}{\partial\theta}\\&\quad-\left(ms\frac{\partial\psi}{\partial r}+\frac{c^m}{r^m}\frac{\partial\psi}{\partial\theta}\right)\frac{n\zeta}{(R+rc^m)^2}\\&\quad+\left(ms\frac{\partial w}{\partial r}+\frac{c^m}{r^m}\frac{\partial w}{\partial\theta}\right)\frac{2nw}{(R+rc^m)}\\&=\frac{1}{\text{Re}}\left[\frac{\partial^2\zeta}{\partial r^2}+\left(\frac{m}{r}+\frac{nc^m}{(R+rc^m)}\right)\frac{\partial\zeta}{\partial r}+\frac{1}{r^{2m}}\frac{\partial^2\zeta}{\partial\theta^2}\right.\\&\quad\left.-\frac{mns}{r(R+rc^m)}\frac{\partial\zeta}{\partial\theta}-\frac{n\zeta}{(R+rc^m)^2}\right]\end{aligned} \tag{3}$$

Cross-Flow Stream-Function Equation

$$\begin{aligned}&\frac{1}{(R+rc^m)^n}\frac{\partial^2\psi}{\partial r^2}+\frac{1}{r^{2m}(R+rc^m)^n}\frac{\partial^2\psi}{\partial\theta^2}\\&\quad+\left(\frac{m}{r(R+rc^m)^n}-\frac{nc^m}{(R+rc^m)^{n+1}}\right)\frac{\partial\psi}{\partial r}\\&\quad+\frac{mns}{r(R+rc^m)^{n+1}}\frac{\partial\psi}{\partial\theta}=-\zeta\end{aligned} \tag{4}$$

Streamwise Momentum Equation

$$\begin{aligned}&\frac{1}{r^m(R+rc^m)^n}\frac{\partial\psi}{\partial\theta}\frac{\partial w}{\partial r}-\frac{1}{r^m(R+rc^m)^n}\frac{\partial\psi}{\partial r}\frac{\partial w}{\partial\theta}\\&\quad+\left(\frac{c^m}{r^m}\frac{\partial\psi}{\partial\theta}+ms\frac{\partial\psi}{\partial r}\right)\frac{nw}{(R+rc^m)^2}\\&=-\frac{1}{(R+rc^m)^n}\frac{\partial p}{\partial\phi}+\frac{1}{\text{Re}}\left[\frac{\partial^2 w}{\partial r^2}\right.\\&\quad+\left(\frac{m}{r}+\frac{nc^m}{(R+rc^m)}\right)\frac{\partial w}{\partial r}+\frac{1}{r^{2m}}\frac{\partial^2 w}{\partial\theta^2}\\&\quad\left.-\frac{mns}{r(R+rc^m)}\frac{\partial w}{\partial\theta}-\frac{n}{(R+rc^m)^2}w\right]\end{aligned} \tag{5}$$

The abbreviations and symbols used in these equations are given as $c=\cos\theta$, $s=\sin\theta$ and $\text{Re}=w_{\text{avg}}D/\nu$. These equations for fully developed flow through curved ducts are obtained from those given by Ghia and Sokhey (1977) by dropping the streamwise variation in the dependent variables. Under these conditions, $\partial p/\partial\phi$ becomes independent of ϕ, although p itself continues to vary with ϕ. The use of indices m and n facilitates choice of the duct geometry. For $m=0$, the cross section is rectangular and $(r, \theta)\rightarrow(x, y)$ and, for $m=1$, it is either circular or polar. Similarly, the parameter n facilitates the inclusion of longitudinal curvature ($n=1$), whereas $n=0$ leads to a straight duct. In equations (1)-(5), all lengths have been made dimensionless using the hydraulic diameter D of the duct cross-section as the reference length and all velocities have been referred to the average mass-flow velocity w_{avg} through the duct.

Equations (3)-(5) constitute three equations for the three unknowns, ζ, ψ, and w. They contain the two parameters Re and $\partial p/\partial\phi$. However, only one of these parameters may be prescribed independently since a specific value of the pressure gradient $\partial p/\partial\phi$ is required for maintaining a flow with a prescribed value of Re through the duct. Cheng et al. (1976) scaled Re out of the problem by using the quantity ν/D to nondimensionalize the velocities and then prescribe the parameter $\partial p/\partial\phi$; the Reynolds number Re was computed from the converged solution, using the global continuity equation, as

$$\frac{1}{A}\int_A\frac{w^*}{\nu/D}\,dA=\frac{1}{A}\int_A\left(\frac{w^*}{w_{\text{avg}}}\right)\text{Re}\,dA=\text{Re} \tag{6}$$

where w^* is the dimensional streamwise velocity. This procedure of nondimensionalization can permit simultaneous solution of equations (3)-(5). However, it has the disadvantage that Re must be determined from the computed solution and, hence, the Reynolds number does not generally turn out to be a round number.

In the present study, it is preferred to scale $\partial p/\partial\phi$ out of the streamwise momentum equation (5) by introducing a new streamwise-velocity variable $\tilde{w}$ defined as

$$\tilde{w}=\frac{w^*}{w_{\text{avg}}}\cdot\frac{1}{(\partial p/\partial\phi)}=w\frac{1}{(\partial p/\partial\phi)}. \tag{7}$$

Formulated in terms of $\tilde{w}$, the streamwise momentum equation (5) no longer contains $\partial p/\partial\phi$ in it explicitly, and can be solved to provide the $\tilde{w}$ distribution for a prescribed value of

Downloaded 02 Jun 2010 to 171.66.16.66. Redistribution subject to ASME license or copyright; see http://www.asme.org/terms/Terms_Use.cfm

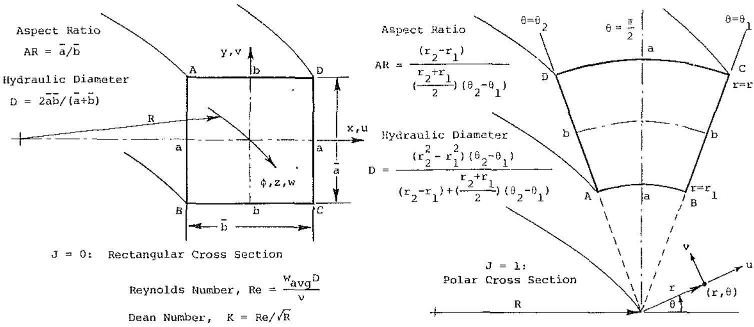

Fig. 1 Curved-duct geometry and coordinate system

Re. The associated value of $\partial p/\partial\phi$ is computed from the global mass balance as

$$\frac{1}{A}\int_A \tilde{w}\,dA = \frac{1}{A}\int_A w\,\frac{1}{(\partial p/\partial\phi)}\,dA = \frac{1}{(\partial p/\partial\phi)} . \qquad (8)$$

However, the use of $\tilde{w}$ in the ζ and ψ equations (4) and (5) introduces $\partial p/\partial\phi$ in these latter equations. Hence, the original variable w is retained in the cross-flow equations; it is determined from $\tilde{w}$, using equations (7)-(8), as part of the evolving solution. The disadvantage of this approach is that it does not admit simultaneous solution of the complete set of coupled governing equations. The main advantage is that it can provide flow solutions for prescribed values of Re. The present work employs both approaches, namely,

(*a*) prescribing $\partial p/\partial\phi$ and obtaining Re using equation (6); and

(*b*) prescribing Re and computing $\partial p/\partial\phi$ using equation (8).

The latter approach (*b*) is considered preferable because it allows Re to be specified, while the loss in computational efficiency due to decoupling the $\tilde{w}$ equation from the ζ, ψ equations can be compensated for by the use of a multi-grid [MG] solution technique as described in the Appendix.

Boundary Conditions. For nonporous walls, the condition of zero slip yields the conditions $u = v = w = 0$ on the entire boundary. The use of equation (1) for the cross-flow stream function, together with the stream-function equation (4), leads to the appropriate boundary conditions for ψ and ζ as follows, (see Fig. 1).

At the walls AB and CD:

$$w=0,\ \psi=0,\ \zeta=-\frac{1}{(R+rc^m)^n}\frac{\partial^2\psi}{\partial r^2} . \qquad (9a)$$

At the walls BC and AD:

$$w=0,\ \psi=0,\ \zeta=-\frac{1}{(R+rc^m)^n}\frac{1}{r^{2m}}\frac{\partial^2\psi}{\partial\theta^2} . \qquad (9b)$$

In equations (9*a*, *b*), r and c will assume appropriate values corresponding to the indicated boundaries.

Numerical Analysis

Remarks on the Semi-Implicit Methods Used. As stated earlier in the Introduction, one of the objectives of the present study is to develop the methodology for semi-implicit procedures, namely, ADI and SI, that can lead to accurate and efficient solutions at high Reynolds number for the model problem of fully developed flow through curved ducts. This objective was motivated by the fact that the convergence rates of even some of the highly efficient semi-implicit techniques slows down significantly in the presence of strong cross-flow recirculation as well as for fine-grid calculations essential for accurate solutions at high Re. The ADI method is primarily applicable to parabolic equations. Therefore, fictitious time-derivative terms are appropriately included in the present governing equations in order to adapt them to solution by the ADI procedure. The steady-state solution is then obtained as the time-asymptotic solution of the time-dependent equations. Similar remarks apply for the SI procedure also; however, the values of the time steps employed may be infinitely large for cases with small K.

In view of these observations, the following solution procedure using the ADI method was formulated in the initial phase of the present study. Step 1 of this procedure consisted of solving the streamwise momentum equation for $\tilde{w}$, followed by step 2 which consisted of simultaneous solution of the (ζ, ψ) equations. This simultaneous solution of the (ζ, ψ) equations permits implicit treatment of the wall vorticity boundary condition as shown by K. Ghia and Davis (1974) and Mikhail and K. Ghia (1978) and aids in the stability of the overall algorithm. Steps 1 and 2 were repeated consecutively until convergence was achieved. To improve the convergence rate of the overall solution, each governing equation was relaxed with its appropriate time step. However, these time steps were observed to be dependent on the Dean number K (= Re/√R) which is the main similarity parameter for curved-duct flows. To minimize this dependence of the ADI method on the time steps used, it was decided to couple all three governing equations. Also, it was felt that the primary and secondary flows in highly curved ducts are strongly inter-dependent and should best be determined simultaneously. The result was, as predicted, that solutions could be obtained for the duct of polar cross-section, with a (21×21) grid, for K up to 300 without changing any of the time steps. It should be noted that, with radius of curvature $R = 100$, K = 300 corresponds to Re = 3,000. An examination of the solution for K = 300, revealed that the gradients near the duct boundaries were relatively high and that a uniform grid was only marginally satisfactory for this configuration. Hence, mesh points were clustered near the boundaries via a tangent transformation of the cross-plane coordinates [K. Ghia, Hankey and Hodge (1977)]. These functions have been shown by Vinokur (1980) to be amongst the most suitable stretching functions from the point of view of minimum truncation error as well as invertibility. With a (21×21) grid and stretching ratio of 6:1 near the duct boundaries, the resolution appeared satisfactory near the boundary and solutions were obtained for K up to 600 for the duct of polar cross section. However, for K above 300, the solution convergence rate was, again, dependent on the value of K.

In order to improve the overall solution algorithm and make it more robust, it was decided to use the strongly-implicit (SI) scheme of Rubin and Khosla (1981). This algorithm is relatively insensitive to the time steps as compared to the ADI scheme and enables the determination of flow for large values of K. Again, the method was implemented in such a way that step 1 consisted of solving the streamwise momentum equation for $\tilde{w}$, followed by step 2 consisting of the simultaneous solution

Downloaded 02 Jun 2010 to 171.66.16.66. Redistribution subject to ASME license or copyright; see http://www.asme.org/terms/Terms_Use.cfm

of the ζ and ψ equations. Although it is possible to couple all three equations, and such fully coupled solutions were actually obtained, it was felt that coupling the w equation with the (ζ, ψ) equations did not show any significant improvement in the overall convergence of the SI procedure. Hence, it was decided to solve the w equation separately because this also permits the analysis of flow configurations with prescribed Re, rather than the final solution yielding the value of Re.

Since the SI scheme is almost insensitive to the time steps used in each of the governing equations at moderate Re, this scheme can also efficiently provide numerical solutions with a finer grid. This characteristic of the SI scheme makes the method particularly suitable for use with the multi-grid technique [Brandt (1980)] for further enhancing the convergence rate of fine-grid solutions. Hence, a combined multi-grid-strongly implicit (MG-SI) procedure was implemented in this study to obtain accurate solutions efficiently, using a fine grid, for a wide range of values of K. The coupled ADI and SI schemes as well as the MG-SI scheme used by the authors is as described by K. Ghia et al. (1981). Therefore, included here are only some remarks pertinent to the usage of the MG technique when all three coupled equations are not solved simultaneously (see Appendix).

Treatment of Boundary Conditions. The efficiency of a computational algorithm can be significantly influenced by the manner in which the boundary conditions are implemented. Accordingly, if an implicit algorithm is to perform at its best efficiency, it is necessary to treat the boundary conditions also implicitly. Similarly, consistency must be maintained in the order of accuracy of the discretized representation of the conditions at the boundaries and the governing equations in the interior. In this respect, particular care is required in implementing the vorticity boundary conditions, since the Dirichlet conditions for the velocity and the stream function are generally easy to treat implicitly.

The proper implementation of the vorticity boundary condition requires, first of all, a second-order accurate discretized representation of ψ'' at the boundaries. For example, at the boundary $i=1$,

$$\psi_1'' = \frac{1}{h^2}\left[-\frac{7}{2}\psi_1 + 4\psi_2 - \frac{1}{2}\psi_3 - 3h\,\psi_1'\right] + 0(h^2)\ . \quad (10)$$

Here, the prime denotes differentiation with respect to the normal at the boundary, h is the uniform spatial step size, subscript 1 denotes boundary value, while subscripts 2 and 3 denote subsequent points off the boundary. Similarly, an analogous expression is obtained for ψ'' at the boundary $i=i_{\max}$ as

$$\psi''_{i_{\max}} = \frac{1}{h^2}\left[-\frac{7}{2}\psi_{i_{\max}} + 4\,\psi_{i_{\max}-1} - \frac{1}{2}\psi_{i_{\max}-2} + 3h\,\psi'_{i_{\max}}\right] + 0(h^2). \quad (11)$$

For the coupled ADI scheme, expressions of the form given by equation (11) are employed in equations (9a, b) which are then arranged in the form of the recursion relation defining this scheme, using $i=i_{\max}$ to yield the elements of the recursive coefficient matrices at $i_{\max}$. The required value of ζ_1 at the boundary $i=1$ is obtained by use of equations (9a, b) and equation (10) wherein ψ_2 and ψ_3 are replaced in terms of ψ_1 and ζ_1 via repeated application of the recursion relation of the scheme, with $i=2$ and $i=3$. A similar procedure is followed at the boundaries $j=1$ and $j=j_{\max}$. It is important to note that this treatment of the second-order accurate vorticity boundary condition is fully implicit only along the boundaries $i=1$ and $j=1$ because the evaluation of the recursive coefficients along $i=i_{\max}$ and $j=j_{\max}$ must consider the terms $\psi_{i_{\max}-2,\,j}$ and $\psi_{i,\,j_{\max}-2}$ in an explicit manner.

In the coupled SI procedure, two adjoining boundaries are considered simultaneously. In this procedure, expressions of the form given by equation (10) are employed in equations (9a, b), which are arranged to resemble the form of the recursion relation defining the SI scheme, along the boundaries $i=1$ and $j=1$, to yield the elements of the recursion coefficients along these boundaries. The values of ζ at the remaining boundaries $i=i_{\max}$ and $j=j_{\max}$ are obtained from equations (9a, b) and equation (11) with ψ along $i=i_{\max}-1$ and $j=j_{\max}-1$ replaced by use of the recursion relation, with $i=i_{\max}-1$ and $j=j_{\max}-1$. Again, this treatment of the vorticity boundary condition is second-order accurate and "nearly" implicit.

For comparison with the corresponding first-order accurate expression, equation (10) may be re-arranged in the following form:

$$\psi_1'' = \left[2\,\frac{(\psi_2-\psi_1)}{h^2} - \frac{2}{h}\,\psi_1'\right] + \left[\frac{-3\psi_1+4\psi_2-\psi_3}{2h^2} - \frac{1}{h}\,\psi_1'\right]. \quad (12)$$

The first bracketed term in equation (12) is a first-order accurate expression for ψ_1'', so that the second bracketed term may be viewed as a second-order correction that makes the overall expression in equation (12) second-order accurate. In the nearly implicit treatment described in this section for the vorticity boundary conditions, it is possible to lag either the entire second bracketed term in equation (12) or merely the term ψ_3 as this is the only term that is inconvenient to treat implicitly. The latter procedure was adopted in the present calculations. However, both approaches become equivalent as convergence is approached.

Initial Conditions. For values of the Dean number up to 100, the solution behavior was not significantly affected by the initialization employed. A uniform distribution for w, together with null values for ζ and ψ were found satisfactory for yielding the desired converged solutions. However, for values of $K \geq 100$, the results of a calculation with a lower value of K were used to initiate the solution. This procedure of continuation in K avoids nonlinear numerical instability and ensures convergence. It may also be necessitated by the bifurcation phenomenon [Benjamin (1978)].

Convergence Criteria. For the coupled ADI method, the rates of change in w, ζ, and ψ were evaluated and were required to be less than a preassigned value of $\epsilon = 10^{-4}$, i.e.,

$$\frac{\left|f_{i,j}^{n+1} - f_{i,j}^{n+1/2}\right|}{\left|f_{i,j}^{n+1}\right|_{\max} \Delta t_f} < \epsilon \quad (13)$$

where f denotes w, ζ or ψ, and Δt_f denotes the time step used in the corresponding equation.

A similar convergence criterion, without the Δt_f term, is appropriate for the SI procedure also. This is not the case, however, when the scheme is used in conjunction with the multi-grid technique since, as the name indicates, this technique employs a hierarchy of grids, each with its own associated truncation error.

Application of MG Technique to System of Equations. The multi-grid (MG) technique has gained widespread recognition owing to its potential for enhancing the convergence rate of numerical solutions of boundary-value problems. The gain in computational time becomes particularly significant as the mesh is refined. However, most applications

Downloaded 02 Jun 2010 to 171.66.16.66. Redistribution subject to ASME license or copyright; see http://www.asme.org/terms/Terms_Use.cfm

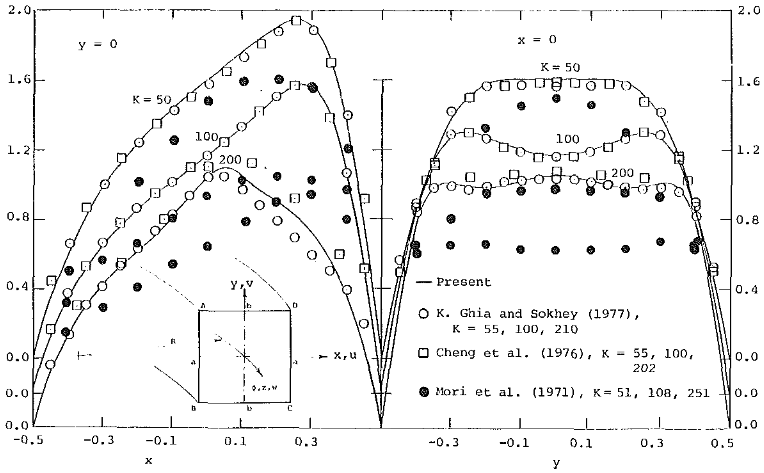

Fig. 2 Comparison of streamwise velocity profiles; AR = 1, R = 100

considered in the literature have been for model problems governed by Laplace or Poisson equations. Application of the MG technique to a system of coupled partial differential equations is not necessarily straightforward. This is particularly true if the equations are linearized, decoupled and solved sequentially. An alternative is to quasilinearize the equations and solve them simultaneously as was done by U. Ghia, K. Ghia and Shin (1982) for the coupled equations governing the vorticity and the stream function for flow in a driven square cavity. In the present work, simultaneous solution of all three governing equations is not recommended if results are desired to be obtained for a specified value of Re. The MG procedure, as applied in this circumstance, is outlined in the Appendix at the end of this paper.

Discussion of Results

Results from ADI Scheme. For the model problem of fully developed flow in curved ducts, the velocity, vorticity and stream function equations were solved by the coupled-ADI method. Since all three equations were solved simultaneously, the normalization used in the analysis was such that $\partial p/\partial \phi$ was required to be prescribed, while Re was computed from the converged solultion. Solutions were obtained first for ducts of square cross-section and the analysis was extensively verified by comparing the computed results with those of Cheng et al. (1976) as well as K. Ghia and Sokhey (1977); the latter results were obtained using a marching technique and primitive variables. Although overall satisfactory agreement was obtained, Dean's instability was observed to occur at $K = 125$, rather than at 202 as reported by Cheng et al. (1976) or at 143 as determined by K. Ghia and Sokhey (1977). The present value of 125 is in excellent agreement with the value 124.5 reported in the experimental work of Cheng et al. (1977). For $K \leqq 300$, a (21×21) uniform mesh seemed satisfactory. A (21×21) nonuniform grid was used for the flow calculations with $K \geqq 300$. For the flow configuration with $K \approx 600$, grid stretching of 6:1 near the wall was determined to be necessary, based on the numerical experiments conducted. For square cross-section ducts, the secondary pair of vortices persisted even in the case with $K = 600$. This is contrary to the findings of Cheng et al. (1976) who reported that this additional pair of vortices disappears for $K \geqq 520$.

At this stage, it is important to make the following observations. Cheng et al. (1976) also used $R = 100$, as in the present calculations, for their cases with $K = 151$ and 202 and did not show a four-vortex cross flow for $K = 151$. (However, their ψ contours for $K = 151$ appear as though small additional vortices could be present). The different critical values obtained for K by Cheng et al. (1976) and in the present calculations are most likely due to the different grids employed. K. Ghia and Sokhey (1977) obtained $K = 143$ as the critical value, but that calculation used $R = 36$ and a uniform (21×21) grid. K. Ghia and Sokhey (1977) have shown quantitatively that the flow does depend on the parameter R, but this dependence is minimal for curved-duct flows. While this may be generally the case, it is possible that R gains on influence as K approaches the critical value. If the two-vortex solutions of Cheng et al. (1976) for $K = 520$ with $R = 4$ are accurate, this may also partly explain why a different (four-vortex) solution persists in the present cases with $K \geqq 500$, $R = 100$. Alternatively, the differences in these solutions may be indicative of solution bifurcation [Benjamin (1978)]. Nevertheless, the excellent agreement of the present value of 125, obtained using $R = 100$, with the experimentally determined value of 124.5 [Cheng et al. (1977)] using $R = 5$ suggests that R is only a weak parameter of the problem and that the present results are very accurate.

On the AMDAHL 470/V6 computer, a typical run time varied from 25 to 40 seconds, the higher values corresponding to higher K. Typical quantitative results using the ADI method have been given by K. Ghia et al. (1980).

Although the coupled ADI procedure yields satisfactory results, it exhibits a disadvantage that the time steps used in the problem are sensitive to the grid size, the grid stretching ratio, as well as Dean's number. As stated earlier, one of the objectives of this study is to develop a robust method which can yield accurate and efficient solutions in the presence of strong secondary flows. This objective is accomplished to much greater degree by the MG-SI procedure. Hence, quantitative results are presented here for this latter approach.

Comparative Study Using MG-SI Scheme. The SI scheme was used in conjunction with the multi-grid technique to first obtain solutions for some square-duct configurations for which published data is available from experiments as well as previous numerical computations. The use of $\tilde{w}$ permits calculations to be performed for prescribed values of Re while the streamwise pressure gradient $\partial p/\partial \phi$ is computed as part of the evolving solution. In Fig. 2, profiles of the streamwise velocity w resulting from the present study are compared with the experimental data of Mori et al. (1971) and also with the predictions of Cheng et al. (1976) and K. Ghia and Sokhey (1977). The present results deviate from the experimental data of Mori et al. (1971) by a maximum of about 30 percent for the profiles at both the centerlines $(a-a)$ and $(b-b)$. A careful examination of the experimental conditions indicates that Mori et al. (1971) had measured the total velocity in a

Downloaded 02 Jun 2010 to 171.66.16.66. Redistribution subject to ASME license or copyright; see http://www.asme.org/terms/Terms_Use.cfm

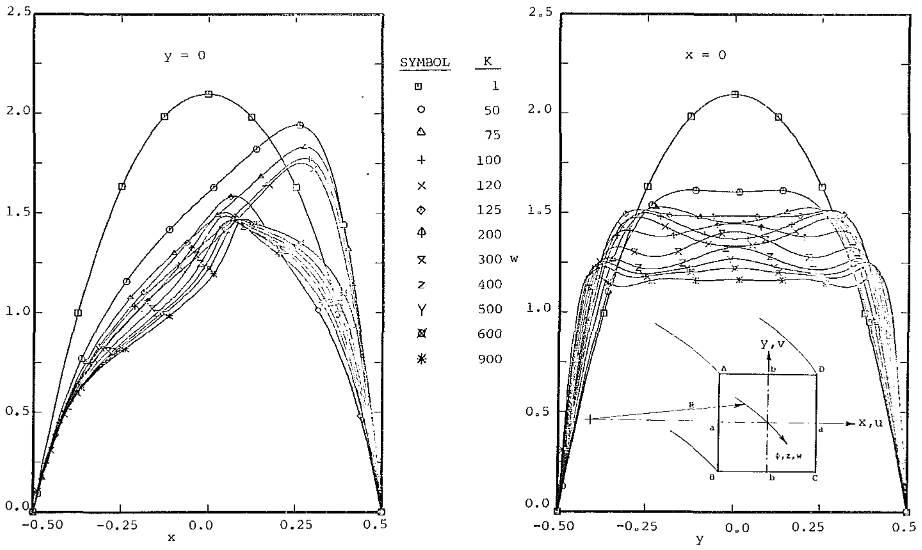

Fig. 3 Effect of Dean number on streamwise velocity for square curved ducts; AR = 1, R = 100

heated duct with the help of thermistor anemometers and had suggested that the secondary velocities be ignored and that the total velocity be considered approximately the same as the streamwise velocity. Also, the total velocity distributions were measured under the condition of zero heat flux at the walls; how well this condition was actually maintained throughout the experiments is not clear in their paper. In fact, from an examination of their Figs. 6, 10, and 11 and the accompanying text, it is not clear whether the wall temperature along the perimeter of the duct cross section is constant or a constant temperature gradient is maintained at the duct walls. The thermistor resistance is strongly dependent on the temperature and, unless the experimental temperature distributions are exactly uniform and the same as in the present predictions, complete agreement between the two sets of results is not possible.

Two additional sets of experimental data have become available in the literature; these are due to Humphrey, Taylor and Whitelaw (1977) and Taylor, Whitelaw and Yianneskis (1981). However, neither of these are suitable for comparison with the downstream asymptotic, i.e., fully developed, curved-duct flow solutions; they were designed for verification of developing-flow solutions. The curved portion of the duct configuration consists of a 90°-bend and is followed by a straight section. It is doubtful that fully developed conditions can be achieved within the bend, because of the 90 deg limit on ϕ, as well as due to upstream effects of the ensuing straight duct.

For the MG-SI scheme, the AMDAHL 470/V6 computer CPU time for a typical solution, with a uniform (81×81) grid, was less than one minute for $K < 125$, while it was about 3 minutes for $125 < K < 400$ and 6 minutes for $K > 400$. The last figure is to be approximately compared with the 40 CPU seconds required, for this range of values of K, by the coupled ADI scheme using a nonuniform (21×21) grid, i.e., 16 times fewer grid points.

In Fig. 2, the numerical predictions of Cheng et al. (1976) are shown by the square symbol. The w-velocity profiles for $K = 55$ and 100 agree satisfactorily with the present results whereas, for $K = 202$, the agreement is only fair. Nevertheless, the differences observed at $K = 202$ are as should be expected, if one takes into account the fact that, in the present case, Dean's instability first occurs at $K \approx 125$, whereas the predictions of Cheng et al. (1976) show its occurrence first at $K = 202$. In fact, these results actually lead to the deduction that w is not very sensitive to small changes in K. Also shown in this figure are the results of K. Ghia and Sokhey (1977) obtained from the solution of the parabolized Navier-Stokes equations for the developing flow formulated in terms of primitive variables. For all three values of K shown, the agreement with their results is good. These indicate that the present analysis is properly formulated and the numerical methods have been correctly implemented.

Fine-Grid Results for Square Curved Ducts. The results obtained using the MG-SI procedure are now presented for the square curved duct. In the multi-grid technique, five different uniform grids, namely, (6×6), (11×11), (21×21), (41×41) and (81×81) were used. In the transient stages, the numerical solutions are required to be convergent only on the coarser grids whereas, at convergence, the finest-grid solution converges to within the truncation error of that grid.

Effect of Dean Number on Streamwise Velocity. The profiles of the w velocity along the centerlines $(a-a)$ and $(b-b)$ are shown in Fig. 3 for a wide range of values for K $(1 \leq K \leq 900)$ which, with $R = 100$, correspond to Re between 10 and 9000. It is quite possible that, in reality, as Re increases, the flow may undergo transition to turbulence, so that the flow is no longer laminar for Re ≥ 3200. Nevertheless, the high-Re cases have been analyzed as laminar-flow cases with the purpose of assessing the numerical analyses developed in the present study. The value $K = 1$ corresponds to a nearly straight duct with negligible longitudinal curvature, whereas $K = 900$ corresponds to a duct configuration with strong curvature. As K varies from 1 to 120, the centrifugal forces generated due to the presence of longitudinal curvature, cause the peak of the w-velocity profile along the centerline $(a-a)$ to shift toward the outer wall and lead to the asymmetry in these profiles as seen in this figure. Then, due to Dean's instability at $K = 125$, there is a reversal in this trend and the streamwise-velocity peak shifts back toward the center. Further increase in K has a similar effect as when K varied from 1 to 125, that is, the peak in the w-velocity profile again shifts gently towards the outer wall with further increase in K. The w-profiles along the centerline $(b-b)$ are symmetric about the duct center. For $K = 1$, the maximum value occurs almost at the duct center but increasing K up to 120 shows two distinct peaks in these profiles. At $K = 125$, an additional peak is observed in the w-velocity profile indicated as the curve with the diamond symbol. As will be shown in Fig. 4, an additional pair of secondary vortices makes its appearance at $K = 125$ and continues to persist even at $K = 900$.

Downloaded 02 Jun 2010 to 171.66.16.66. Redistribution subject to ASME license or copyright; see http://www.asme.org/terms/Terms_Use.cfm

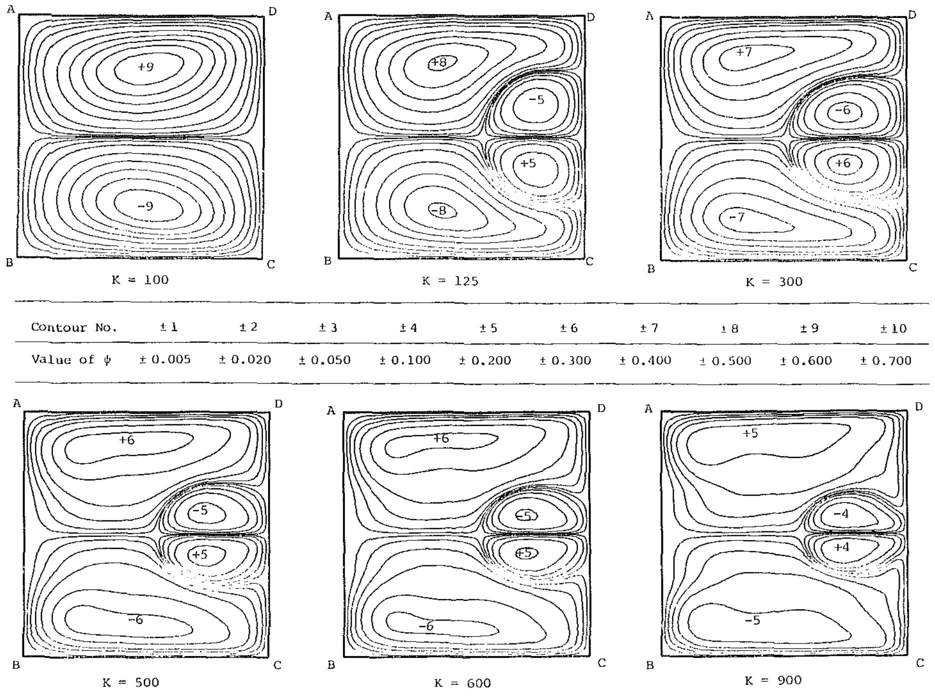

Contour No.	±1	±2	±3	±4	±5	±6	±7	±8	±9	±10
Value of ψ	±0.005	±0.020	±0.050	±0.100	±0.200	±0.300	±0.400	±0.500	±0.600	±0.700

Fig. 4 Effect of Dean number on secondary flow for square ducts—cross-flow streamline contours

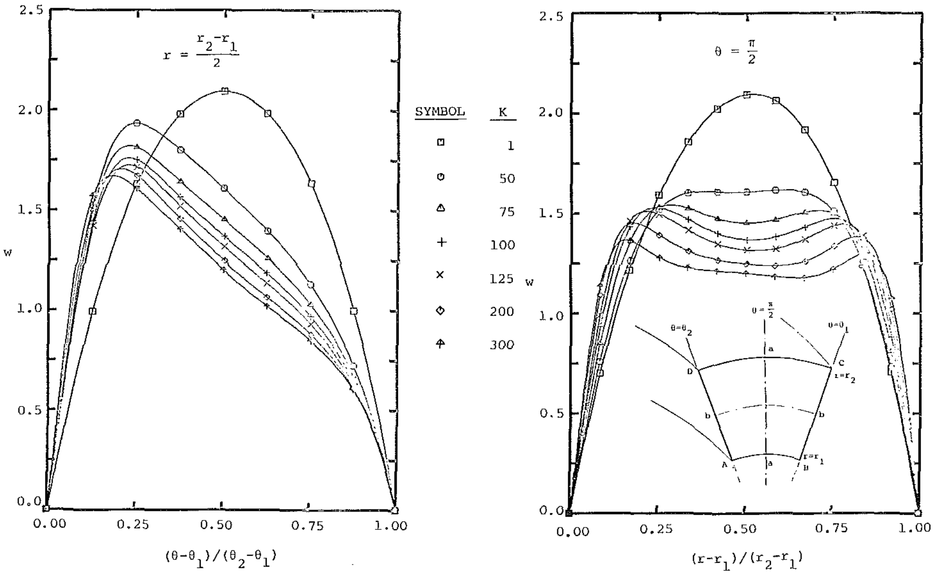

Fig. 5 Effect of Dean number on streamwise velocity for polar curved ducts; AR = 1, R ≈ 100

Effect of Dean Number on Cross Flow. The effect of Dean number on the secondary flow is depicted in Fig. 4 in terms of the cross-flow streamline contours presented for six different values of K from 100 to 900. As seen in this figure, the additional pair of counter-rotating vortices near the outer wall first makes its appearance at $K \approx 125$. As K is increased further up to 900, this pair of additional vortices still persists near the outer wall. To compare the ψ values shown here with those of Cheng et al. (1976), the present ψ should be multiplied by Re/R.

The contour plots for $K = 100$ suggest that, in addition to the boundary-layer regions near the duct walls, a fine grid is also desired near the centerline $(a-a)$ in order to adequately resolve the shear layer that develops there. Further, as the additional pair of vortices appears for $K = 125$, the flow structure becomes quite complex and shear layers also develop in regions away from the centerline. As K increases, all these shear layers become thinner, thus generating severe gradients across them. It is clear then that simple stretching of the boundary-layer regions at the duct walls is not adequate and some form of adaptive grid is required for appropriate resolution everywhere. In the present study, although one-dimensional stretching functions were used in conjunction with the ADI scheme, the calculations with the MG-SI scheme have been carried out using uniform grids, with the finest grid consisting of (81×81) points.

Fine-Grid Results for Polar Curved Ducts. The results for the fully developed flow in curved ducts of polar cross section are presented next. These duct configurations possess longitudinal as well as transverse curvature. The multi-grid method used for these computations employs four levels of

Downloaded 02 Jun 2010 to 171.66.16.66. Redistribution subject to ASME license or copyright; see http://www.asme.org/terms/Terms_Use.cfm

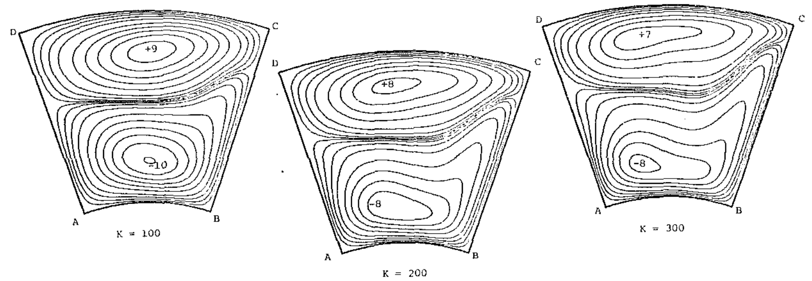

Fig. 6 Effect of Dean number on secondary flow for polar ducts—cross-flow streamline contours

Contour No.	± 1	± 2	± 3	± 4	± 5	± 6	± 7	± 8	± 9	± 10
Value of ψ	± 0.005	± 0.020	± 0.050	± 0.100	± 0,200	± 0.300	± 0.400	± 0.500	± 0.600	± 0.700

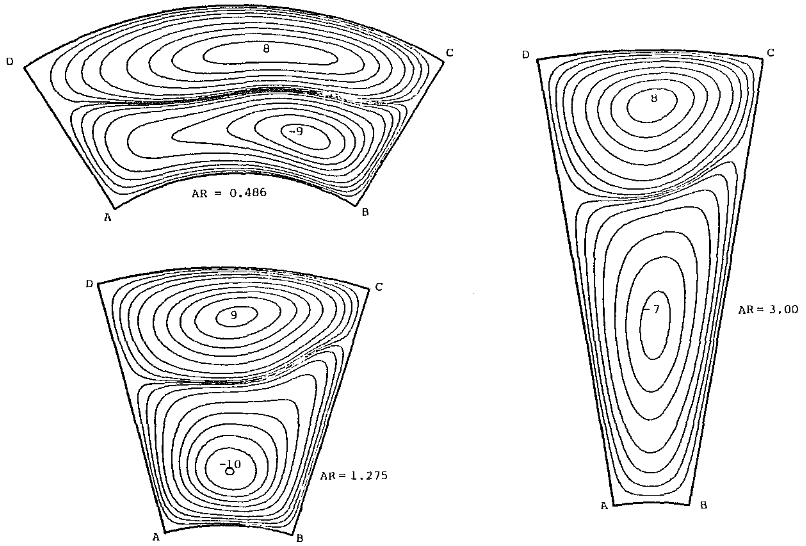

Fig. 7 Effect of aspect ratio on secondary flow for polar ducts; K = 100, R = 100

grids; for AR = 1, the finest grid consisted of (121×81) points in order to maintain $\Delta r = \Delta\theta$. For aspect ratio AR = 2/3, the results obtained were compared with those of U. Ghia, K. Ghia and Goyal (1979). The latter results were obtained as a solution of the parabolized Navier-Stokes equations in terms of primitive variables for the entrance flow in curved ducts of polar cross-section. Good agreement was observed between the two sets of results. The results obtained for AR = 1 are, to the authors' best knowledge, new and are presented here in detail. Only configurations with $K \leq 300$ are presented, since, for $K > 300$, numerical experiments indicated that further improvement in the grid resolution is required in order to adequately resolve the various boundary layers and shear layers that occur in these configurations.

Effect of Dean Number on Streamwise Velocity. The w-velocity profiles along the centerlines $(a-a)$ and $(b-b)$ of the polar cross section of curved ducts with K ranging from 1 to 300 are shown in Fig. 5. In the polar coordinates used for this geometry, θ is measured counterclockwise and $\theta = \theta_1$ corresponds to the outer wall with the maximum radius of longitudinal curvature (Fig. 1). As K is increased from 1 to 300, the increasing centrifugal forces cause the peaks of the w-velocity profiles, along centerline $(a-a)$, to shift monotonically towards the outer wall $\theta = \theta_1$, thereby increasing the degree of asymmetry in these profiles. For this curved duct of polar cross section, the presence of nonzero longitudinal as well as transverse curvature leads to the non-existence of any symmetry in the cross plane. This fact is reflected in the w-profiles along the centerline $(b-b)$; they appear almost symmetric up to K = 50, but with further increase in K, the asymmetry becomes quite evident.

Effect of Dean Number on Secondary Flow. The cross-flow streamline contours for K = 100, 200 and 300 are plotted in Fig. 6. The flow in curved ducts with polar cross-section exhibits no symmetry and the primary vortex pair shows that the upper vortex is slightly weaker than the lower vortex. This figure also shows that the strength of both the upper as well as the lower vortices decreases monotonically as K increases from 100 to 300. Again, the structure of the flow suggests that simple one-dimensional coordinate stretching is not sufficient for resolving the prevailing boundary layers and shear layers. The migration of the fluid towards the outer wall and, in particular, towards the upper right corner C, due to the centrifugal forces, can be seen clearly from this figure.

Effect of Aspect Ratio on Secondary Flows. For the case of K = 100, the aspect ratio was varied between AR = 0.1926 and 6.7871 and its effect on the flow field was studied. Figure 7 shows the cross-flow streamline contours for AR = 0.486, 1.275 and 3.0. The strength of the upper and lower vortices decreases as the aspect ratio departs from unity. These results are also obtained using the mesh aspect ratio to be 1; hence, for AR = 0.486 and 3.00, the finest grids used are (81×121)

Downloaded 02 Jun 2010 to 171.66.16.66. Redistribution subject to ASME license or copyright; see http://www.asme.org/terms/Terms_Use.cfm

and (241×41), respectively. For the MG-SI solutions with AR = 1 and Dean number up to 300, as well as for the ADI solutions with K as large as 600 for AR = 1, the cross flow did not reveal the occurrence of any additional pair of vortices that were indicative of Dean's instability for curved square ducts. In their study with AR = 2/3, U. Ghia, K. Ghia and Goyal (1979) also had not observed this phenomenon of Dean's instability for the curved duct of polar cross section for K as high as 630. It was felt that, for certain combinations of the geometrical parameters R, r_1, r_2, θ_1, θ_2, the flow for polar configurations would differ significantly from the curved-tube flow and perhaps qualitatively develop some of the square-duct flow features. However, such a combination has not yet been arrived at.

Examination of Secondary-Flow Vortices. The effect of Dean number on the strengths of the various primary and secondary vortices for square and polar curved ducts is depicted in Fig. 8. The quantity plotted for the stream function is $|\psi|$ Re/R which is denoted here as ψ_C for convenience in writing. In terms of ψ_C, for the square duct, the strength of the primary vortex increases as K increases from 1 to 125 where it experiences an abrupt decrease, corresponding to the occurrence of Dean's instability, and the secondary vortex-pair first appears. For K > 125, ψ_C again increases with K up to K = 900. The strength of the secondary vortex also increases with increase in K but the rate of increase is slower compared to that of the primary vortex. It is significant to observe that the curves of ψ_C for the primary as well as the secondary vortices exhibit a certain low-order discontinuity (i.e., a discontinuity in a higher-order derivative) near K ≈ 500. This value is coincidentally very close to the value of K for which the results of Cheng et al. (1976) had shown that the secondary vortex pair disappears. Perhaps, a narrow range of K near this value needs further examination.

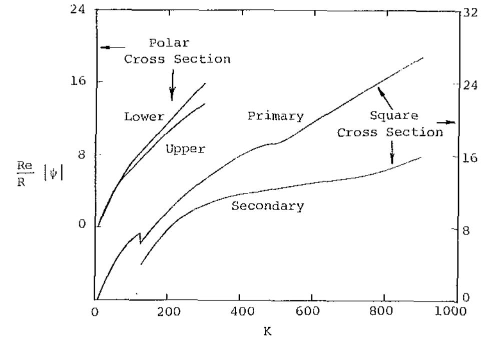

Fig. 8 Strength of cross-flow vortices for curved square and polar ducts; AR = 1, R = 100

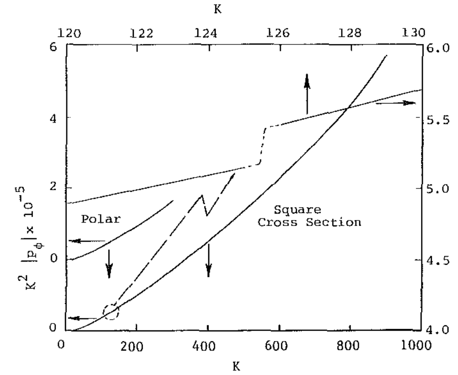

Fig. 9 Variation of streamwise pressure gradient with Dean number for curved ducts; AR = 1, R = 100

Also shown in Fig. 8 is the variation of the strengths of the upper and lower vortices occurring in the polar duct configurations for K up to 300. The lower vortex has a slightly higher strength compared to the upper primary vortex, except for very small values of K where the reversed trend is observed.

The effect of Dean's number K, with R = 100, on the magnitude of $\partial\bar{p}/\partial\phi$ is depicted in Fig. 9, where $\bar{p}$ is defined as $K^2 p$. For the square duct, $|\partial\bar{p}/\partial\phi|$ monotonically increases as Re increases from 10 to 9000. In the vicinity of K = 125, the variation of $|\partial\bar{p}/\partial\phi|$ has also been plotted with an enlarged scale. This helps to show an abrupt increase in $|\partial\bar{p}/\partial\phi|$ when Dean's instability occurs, as the generation of the additional pair of vortices leads to a larger pressure drop. Also shown in this figure is the variation of $|\partial\bar{p}/\partial\phi|$ for the duct of polar cross section with AR = 1; accounting for the shift in the origin for this curve, its values are almost identical to the corresponding square-duct values.

The movement of the vortex centers with increase in Dean number for both square and polar ducts is presented in Fig. 10. For the square duct, the center of the primary vortex is almost at the geometric center of the half duct for K = 1; it shifts towards the outer wall for K up to 50 when it reverses trend and shifts towards the inner wall for further increase in K. The secondary vortex, which first comes into detectable existence for K ≈ 125, also shifts towards the inner wall, but much more gradually. For the polar duct, both upper and lower primary vortices have a trend similar to that of the primary vortex for the square duct.

Conclusion

The fully developed flow in curved ducts of rectangular and polar cross sections have been analyzed using the Navier-Stokes equations. The velocity-vorticity formulation leads to a set of three coupled nonlinear partial differential equations

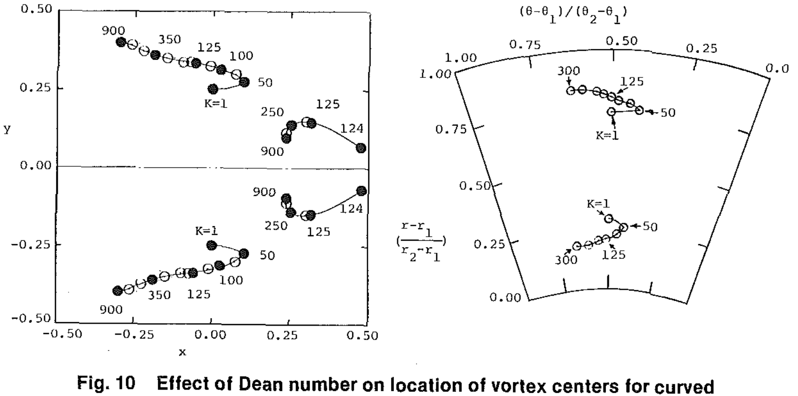

Fig. 10 Effect of Dean number on location of vortex centers for curved ducts; AR = 1, R = 100

Downloaded 02 Jun 2010 to 171.66.16.66. Redistribution subject to ASME license or copyright; see http://www.asme.org/terms/Terms_Use.cfm

which have been solved using semi-implicit techniques. Use of $\partial p/\partial \phi$ to scale the w-velocity in the streamwise momentum equation permits the determination of this flow at specified values of the Dean number and, hence, Reynolds number. On the other hand, scaling by the Reynolds number enables simultaneous solution of all three governing equations. The coupled ADI scheme was used to determine the flow for K up to 600 for both the square as well as the polar ducts, but the solution for K > 300 required initialization by the solution for the preceding lower-K configuration. The coupling of the equations makes it possible to obtain the solution satisfactorily for K up to 600. Solutions for K > 300 with a (21×21) grid required the use of one-dimensional stretching functions. The results are accurate and efficiently obtained.

The SI scheme was also used in conjunction with the multigrid technique. This MG-SI scheme is considerably superior and robust and has permitted efficient calculations with a uniform fine grid of (81×81) points. For the square-duct configurations tested, results have been obtained for K as large as 900, which corresponds to Re = 9000. This scheme may prove to be very useful in the solution of viscous internal flows with large cross-flow velocities. The detailed structure of the eddying motion shows that one-dimensional stretching functions may not be quite suitable for these flows; some form of adaptive grid may be desired to resolve the various boundary layers and shear layers. The phenomenon of Dean's instability has been observed to occur for square ducts at K = 125, and the additional pair of secondary vortices persists up to K = 900. The corresponding polar-duct configuration does not exhibit this phenomenon. Recalling that Re = 10K in the present work, it should be observed that, for K > 300, the flow would, in reality, be turbulent and the associated Reynolds-stress driven motions could modify the flow patterns presented.

The present solutions obtained using a fine grid should aid in partially verifying the solution of other formulations for curved-duct flows. Furthermore, the fully developed curved-duct flow constitutes an excellent model problem for testing new formulations and new numerical solution techniques. It is a 2-D problem involving more than two unknowns and, unlike the driven-cavity problem which is a commonly used model problem, it is free of singularities.

Acknowledgment

This research was supported, in part, by AFOSR Grant No. 80-0160 and, in part, by NASA Grant No. NSG 3267.

References

Austin, L. R., and Seader, J. D. (1973), "Fully Developed Viscous Flow in a Coiled Circular Pipe," *AIChE Journal*, Vol. 19, No. 1, pp. 85–94.

Benjamin, T. B. (1978), "Bifurcation Phenomena in Steady Flows of a Viscous Fluid," *Proceedings of Royal Society of London*, A, Vol. 359, pp. 1–43.

Brandt, A. (1980), "Multi-Level Adaptive Computations in Fluid Dynamics," *AIAA Journal*, Vol. 18, pp. 1165–1172.

Cheng, K. C., Lin, R., and Ou, J. (1976), "Fully Developed Laminar Flow in Curved Rectangular Channels," ASME JOURNAL OF FLUIDS ENGINEERING, Vol. 98, pp. 41–48.

Cheng, K. C., Nakayama, J., and Akiyama, M. (1977), "Effect of Finite and Infinite Aspect Ratios on Flow Patterns in Curved Rectangular Channels," In *Flow Visualization*, Editor: T. Asunuma, Hemisphere Publishing Corp., pp. 181–186.

Dennis, S. C. R., and Ng, M. (1982), "Dual Solutions for Steady Laminar Flow Through a Curved Tube," *Quarterly Journal of Mechanics and Applied Mathematics*, Vol. 35, Part 3, pp. 305–324.

Ghia, K. N., and Davis, R. T. (1974), "Corner Layer Flow: Optimization of Numerical Method of Solution," *Computers and Fluids*, Vol. 2, pp. 17–34.

Ghia, K. N., Hankey, W. L., and Hodge, J. K. (1977), "Study of Incompressible Navier-Stokes Equations in Primitive Variables Using Implicit Numerical Technique," *AIAA Paper* No. 77-648; also *AIAA Journal*, Vol. 17, No. 3, pp. 298–301, (1979).

Ghia, K. N., and Sokhey, J. S. (1977), "Laminar Incompressible Viscous Flow in Curved Ducts of Regular Cross-Sections," ASME JOURNAL OF FLUIDS ENGINEERING, Vol. 99, No. 4, pp. 640–648.

Ghia, K. N., Ghia, U., Reddy, D. R., and Shin, C. T. (1980), "Analysis and Computation of Internal Viscous Flows," presented at *Workshop on Application of Advanced Computational Methods*, NASA-Lewis Research Center, Cleveland, Ohio, November 13–19.

Ghia, K. N., Ghia, U., Shin, C. T., and Reddy, D. R. (1981), "Multi-Grid Computations of Asymptotic Three-Dimensional Flow in Curved Ducts Using a Semi-Implicit Numerical Technique," *Computers in Flow Prediction and Fluid Dynamics Experiments*, ASME Publication.

Ghia, U., Ghia, K. N., and Goyal, R. K. (1979), "Three-Dimensional Viscous Incompressible Flow in Curved Polar Ducts," *AIAA Paper* No. 79-1536.

Ghia, U., Ghia, K. N., and Shin, C. T. (1982), "High-Re Solutions for Incompressible Flow Using the Navier-Stokes Equations and a Multigrid Method," *Journal of Computational Physics*, Vol. 48, No. 3, pp. 387–411.

Humphrey, J. A. C., Taylor, A. M. K. P., and Whitelaw, J. H. (1977), "Laminar Flow in a Square Duct of Strong Curvature," *Journal of Fluid Mechanics*, Vol. 83, pp. 509–527.

Joseph, B., Smith, E. P., and Adler, R. J. (1975), "Numerical Treatment of Laminar Flow in Helically Coiled Tubes of Square Cross-Section," *AIChE Journal*, Vol. 21, No. 5, pp. 965–973.

Mikhail, A. G., and Ghia, K. N. (1978), "Viscous Compressible Flow in the Boundary Region of an Axial Corner," *AIAA Journal*, Vol. 16, No. 9, pp. 931–939.

Mori, Y., Uchida, Y., and Ukon, T. (1971), "Forced Convective Heat Transfer in a Curved Channel with a Square Cross Section," *International Journal of Heat and Mass Transfer*, Vol. 14, pp. 1787–1805.

Nandakumar, K., and Masliyah, J. H. (1982), "Bifurcation in Steady Laminar Flow Through Curved Tubes," *Journal of Fluid Mechanics*, Vol. 119, pp. 475–490.

Rubin, S. G., and Khosla, P. K. (1981), "Navier-Stokes Calculations with a Coupled Strongly Implicit Method - I: Finite Difference Solutions," *Computers and Fluids*, Vol. 9, pp. 163–180.

Taylor, A. M. K. P., Whitelaw, J. H., and Yianneskis, M. (1981), "Measurements of Laminar and Turbulent Flow in a Curved Duct with Thin Inlet Boundary Layers," *NASA CR*-3367.

Vinokur, M. (1980), "On One-Dimensional Stretching Functions for Finite-Difference Calculations," *NASA CR*-3313.

APPENDIX

Use of Multi-Grid Technique for System of Equations

The differential equation to be solved is represented as

$$LU = F \quad \text{where} \quad U = \tilde{w} \quad \text{or} \quad (\zeta, \psi). \tag{A1}$$

This is to be discretized using a finite-difference approximation scheme with order of accuracy p. A sequence of grids G^k is defined with step size h_k, $k = 1, 2, \ldots, M$, such that as k increases, the mesh becomes finer. Adopting the Full Multi-Grid-Full Approximation Scheme (FMG-FAS) of Brandt (1980), a converged numerical solution u^k is first obtained on a coarse grid. This is interpolated to provide an approximation to the finer-grid solution as

$$u_{k+1} = I_k^{k+1}\, u^k. \tag{A2}$$

A couple of iterations performed on the finer grid serve to reduce the high-frequency components of the error in this solution. This is tested by comparison of the actual convergence rate of the solution with the theoretical convergence rate η of the iterative solver employed (e.g., ADI or SI procedure). Convergence rate is defined as the factor by which one iteration of the solver reduces the error in the solution of the given equation. Accordingly, the observed convergence rate of the solution on grid $(k+1)$ may be expressed as $e_{k+1}^{u^{n+1}}/e_{k+1}^{u^n}$, where n and $(n+1)$ denote two consecutive iterations and e_{k+1}^{u} represents the residual norm, taken to be the root-mean-square error in the solution of equation (A1). Hence, the procedure continues to iterate the solution in grid $(k+1)$ so long as

$$e_{k+1}^{u^{n+1}}/e_{k+1}^{u^n} \le \eta^u \tag{A3}$$

for all three of the solution variables $(\tilde{w}, \zeta, \psi)$. If condition (A3) is not satisfied for any one of the problem variables, then the computation proceeds to a subsequently coarser grid. The smoothed solution of equation (A1) on grid $(k+1)$ is then corrected by a coarse-grid correction using an approximate solution $\bar{u}^k$ of the equation

Downloaded 02 Jun 2010 to 171.66.16.66. Redistribution subject to ASME license or copyright; see http://www.asme.org/terms/Terms_Use.cfm

$$L^k \bar{u}^k = L^k (I_{k+1}^k u^{k+1}) + I_{k+1}^k (f^{k+1} - L^{k+1} u^{k+1}) \equiv f^k \tag{A4}$$

so that

$$u_{\text{new}}^{k+1} = u_{\text{old}}^{k+1} + I_k^{k+1} (\bar{u}^k - I_{k+1}^k u_{\text{old}}^{k+1}). \tag{A5}$$

where I_{k+1}^k is a restriction operator. If $(k+1)$ denotes the finest level in a multi-grid cycle, then f^{k+1} in equation (A4) is exactly F^{k+1}. Actually, the difference $(f^k - F^k)$ represents the local truncation error τ_k of the grid G^k relative to the finer grid G^{k+1}. This relative local truncation error is used to control the switching between grids and, hence, in defining convergence for the multi-grid method. Thus, if G^{k+1} is the finest grid in the current multi-grid cycle, then convergence to within the estimated truncation error requires that

$$e_{k+1} < \epsilon_{k+1} = \left(\frac{h_{k+1}}{h_k} \right)^{pq} \tau_k \tag{A6}$$

with $q = 1$. However, the present computations employed $q = 4$; this value was arrived at on the basis of numerical experimentation and comparison of the computed results with earlier results of non-MG computations that employed convergence criteria of the form given in equation (19) in the text, with ϵ typically of the order of 10^{-4}.

Convergence on intermediate grids in the multi-grid cycle is defined to occur when

$$e_k < \epsilon_k = \delta \, e_{k+1} \tag{A7}$$

where $\delta < 1$. The value used was $\delta = 0.125$.

Some of the symbols introduced in the preceding description of the FMG-FAS scheme are further described below. The interpolation operator I_k^{k+1} used in equation (A2) corresponds to locally one-dimensional linear interpolation except when $k = 1$ in which case locally 1-D cubic interpolation is employed. Equations (A4) and (A5) make use of the operator I_{k+1}^k to transfer the solution and the residuals from a fine grid to a coarse grid. This operator is, therefore, termed the restriction operator. In view of the nonlinearity of the governing equations (8), (9), and (13), the restriction operator employed was a 5-point averaging operator which is equivalent to the optimal weighted averaging defined by Brandt (1980).* The operator L^k in equation (A4) governing the coarse-grid correction $\bar{u}^k$ is simply the finite-difference operator, corresponding to the given differential operator in equation (A1) discretized on grid k, with coefficients determined according to the operator I_{k+1}^k.

The residual norm e_{k+1}^u for each governing equation of the form of equation (A1) is the root-mean-square of the residuals and was defined as

$$e_{k+1}^u = \left[\sum_{i,j} (\bar{R}_{k+1})_{i,j}^2 / h_{k+1}^2 \right]^{1/2} \tag{A8}$$

where $\bar{R}$ is the residue in the governing equation, so that $\bar{R} = (Lu - f)$, and the summation extends over all points of the computation.

For the strongly implicit scheme used to perform the iterations, the convergence rate η was taken to be 0.5 for all three variables in the problem. Although convergence rate was tested separately for each of the governing equations of the system, convergence was tested for the overall procedure as a whole. Hence, the symbol e in equations (A6) and (A7) was defined as

$$e = (e^w + e^\zeta + e^\psi)/3 \tag{A9}$$

where $e^w = e^{\bar{w}} (\partial p / \partial \phi)$.

---

*After the present computations had been completed, the present authors have determined, in a related study [U. Ghia et al. (1982)] that 9-point averaging or full-weighted averaging is more suitable for high-Re flow and also for the Neumann boundary-value problem in general stretched orthogonal coordinates.

Downloaded 02 Jun 2010 to 171.66.16.66. Redistribution subject to ASME license or copyright; see http://www.asme.org/terms/Terms_Use.cfm

W. Schneider
Professor.

E. Zauner
University Assistant.

Institut für Strömungslehre und
Wärmeübertragung

H. Böhm
University Assistant,
Institut für Leicht- und Flugzeugbau.

Technische Universität Wien,
A-1040 Vienna, Austria

The Recirculatory Flow Induced by a Laminar Axisymmetric Jet Issuing From a Wall*

The laminar, axisymmetric, submerged jet issuing from a plane, infinite wall perpendicular to the jet axis is considered at very large distance from the nozzle. Based on previous results of an asymptotic analysis, an approximate analytical solution for the complete flow field is obtained. The structure of the far field is discussed by considering various regions the size of which depends strongly on the Reynolds number. The main region is a toroidal eddy in which both inertial and viscous forces are of importance. Closer to the nozzle there is a slender jet flow with slowly varying momentum flux together with a self-similar viscous outer flow. At larger distances, the flow resembles the creeping flow due to point sources of momentum and mass, with the former decaying more rapidly than the latter as infinity is approached. Analytical predictions of the location of the eddy center compare favorably with experimental and numerical results.

Introduction

Recent investigations on the momentum flux in jets [1] indicated that the far-field structure of a laminar axisymmetric jet issuing from a nozzle in a plane, infinite wall perpendicular to the jet axis is significantly different from the picture commonly presented in textbooks. Since the outer flow, which is a viscous and rotational one [2], has a velocity component towards the origin, the entrainment of mass into the jet is coupled with an entrainment of negative momentum. Furthermore, pressure and viscous stresses act on a control surface surrounding the slender jet. Summing up the various contributions to the momentum balance results in a slow but significant reduction of the momentum flux in the jet. Thus applying classical boundary-layer theory to a laminar axisymmetric jet issuing from a wall is correct only for moderately large distance from the orifice (cf. below for an estimate of the limits of applicability).

In attempts to enlarge the regime of applicability of boundary layer theory, the method of matched asymptotic expansions was applied to find second-order boundary layer solutions [3, 4]. In the presence of walls, the asymptotic behavior at large distance (r) from the orifice turned out to be essentially different for plane and axisymmetric jets, respectively. While for plane jets the expansion is regualr as $r \to \infty$[3], the second-order terms in the axisymmetric problem grow beyond bounds as $r \to \infty$[4].

Therefore, analyzing the axisymmetric far field requires an approach that is capable of accounting for the slow variation of the momentum flux in the jet. In [1], an asymptotic analysis was performed by combining the method of matched asymptotic expansions and the method of multiple scales. As a result, a peculiar flow field was predicted. As the momentum flux in the jet decreases with increasing distance from the nozzle, the spreading rate of the jet is enhanced, and eventually the jet develops into a toroidal eddy with closed streamlines in the meridian plane. In terms of spherical coordinates r, θ, where r is referred to the nozzle exit diameter d_0 (cf. Fig. 1), the center of the toroidal eddy was found to be located at

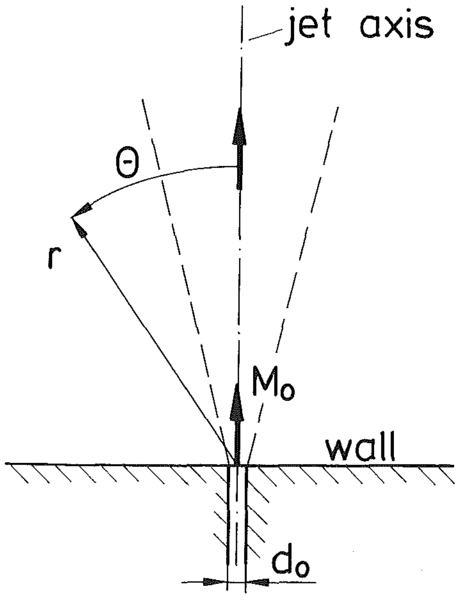

Fig. 1 Coordinate system and parameters

---

*Dedicated to Prof. Dr. K. Oswatitsch on the occasion of his 75th birthday.

Contributed by the Fluids Engineering Division of THE AMERICAN SOCIETY OF MECHANICAL ENGINEERS and presented at the International Symposium on Jets and Cavities, Winter Annual Meeting, Miami Beach, Fla., November 17-21, 1985. Manuscript received by the Fluids Engineering Division, July 17, 1985.

Copyright © 1987 by ASME

Downloaded 02 Jun 2010 to 171.66.16.66. Redistribution subject to ASME license or copyright; see http://www.asme.org/terms/Terms_Use.cfm

$$\theta_c=45.0°, \quad r_c=Ar^* \tag{1a}$$

with

$$r^*=\exp[\mathrm{Re}_0^2/(8C^2)]. \tag{1b}$$

Here, Re_0 is the Reynolds number of the jet at the orifice. It is defined according to the relation

$$\mathrm{Re}_0=M_0^{1/2}\nu^{-1}=(\overline{u_0^2}/8)^{1/2}d_0\nu^{-1} \tag{2}$$

where $2\pi M_0$ and $(\overline{u_0^2})^{1/2}$ are, respectively, the kinematic momentum flux and the mean square velocity at the orifice. The constant C^2 depends on the presence of a wall. For a plane wall (perpendicular to the jet axis) one obtains $C^2=1.91$ [2]. The constant A cannot be determined from the asymptotic analysis. This is, however, a relatively small uncertainty as compared with the exponential growth of r_c with increasing Reynolds number.

The existence of a toroidal eddy as well as the exponential dependence according to equation (1*b*) have already been confirmed by experimental data [5] (cf. also below). However, the asymptotic analysis is not completely satisfactory. At a distance about twice as large as r_c, the momentum flux in the jet becomes zero, and the spreading rate of the jet grows beyond bounds. Thus the jet is no more slender and the asymptotic analysis ceases to be valid. It is the purpose of the present investigation to determine size and shape of the recirculatory flow region and to study the structure of the flow field as the distance from the nozzle tends to infinity.

Approximate Analysis of the Eddy

As the asymptotic analysis is not strictly applicable in the eddy region and, furthermore, cannot adequately describe the far-field structure, recourse is taken to an ad hoc approximation. The basic idea is to approximate the Stokes stream function $\psi(r, \theta)$, which is referred to νd_0 with kinematic viscosity $\nu=\text{const}$, by a function that satisfies all boundary conditions and, furthermore, shows the correct limiting behavior for small and large ratios r/r_c, respectively. A free constant that is related to the unknown radial coordinate of the eddy center, r_c, is then determined such as to satisfy the global momentum balance.

If r/r_c is sufficiently small to satisfy the condition $\ln r \ll \mathrm{Re}_0^2$ (while $r \gg 1$) it follows from the asymptotic analysis [1] that the kinematic momentum flux in the jet at a distance r from the orifice can be replaced by $2\pi M_0$, and the stream function becomes

$$\psi=4rf_\times(\xi)+\ldots \tag{3a}$$

where

$$f_\times(\xi)=f(\xi)[1+(8/3)\mathrm{Re}_0^{-2}\xi^{-1}]^{-1}, \quad \xi=(1-\cos\theta)/2 \tag{3b}$$

The function $f(\xi)$ is a nondimensional stream function of the self-similar outer flow induced by a slender jet of constant momentum flux. This solution has been given previously [2], with the function $f(\xi)$ determined from a numerical integration of a first-order ordinary differential equation.

If, on the other hand, $r/r_c \gg 1$, the fluid motion has become so slow that the creeping flow approximation is applicable. The creeping motion due to a point source of momentum near a plane, infinite wall was studied in [6] and [7]. A viscous toroidal eddy was found, but the assumption of creeping motion does not apply in the present eddy region as can be seen by comparing the orders of magnitudes of the inertial term and the viscous term in the vorticity transport (or Navier-Stokes) equation with $r/r_c=\mathrm{O}(1)$. However, expanding the solution given in [6] and [7] yields

$$\psi=(Kr^*)^2r^{-1}\sin^2 2\theta+\ldots \quad \text{as} \quad r/r_c\to\infty \tag{4}$$

with a constant (Kr^*) that remains to be determined.

A simple interpolation function that satisfies the limiting conditions (3*a*) and (4) is the following:

$$\tilde{\psi}=\frac{\tilde{r}f_\times(\xi)\sin^2 2\theta}{\sin^2 2\theta+\tilde{r}^2 f_\times(\xi)} \tag{5}$$

with

$$\tilde{\psi}=\psi/(2Kr^*), \quad \tilde{r}=2r/(Kr^*). \tag{6}$$

Applying the momentum balance requires knowledge of the normal stress (pressure p and viscous normal stress $\sigma_{\theta\theta}$, both referred to $\rho\nu^2 d_0^{-2}$ with constant density ρ) at the wall. Expressing $\sigma_{\theta\theta}$ in terms of the velocity components and their derivatives, and applying the Navier-Stokes equations to determine $\partial p/\partial r$, it can be shown that the following relation holds at the wall $\theta=\pi/2$:

$$\frac{d}{dr}(p-\sigma_{\theta\theta})=\frac{1}{r^4}\frac{\partial^3\psi}{\partial\theta^3}. \tag{7}$$

To obtain the normal stress at the wall, equation (7) can be integrated with respect to r subject to the boundary condition $p-\sigma_{\theta\theta}=0$ at infinity. Evaluation of $\partial^3\psi/\partial\theta^3$ from equation (5) requires knowledge of $f'_\times(\xi)$, $f''_\times(\xi)$, and $f'''_\times(\xi)$ at the wall $\theta=\pi/2$, i.e., at $\xi=1/2$. It is obvious, and can also be deduced from equation (3*b*), that the composite solution $f_\times(\xi)$ may be replaced by the outer solution $f(\xi)$ to determine the derivatives at the wall without loss of accuracy. From the boundary value problem defining $f(\xi)$, cf. [2], one then obtains $f'(1/2)=0$, $f''(1/2)=8C^2$, and $f'''(1/2)=32C^2$.

The law of momentum, applied to the whole flow field, requires that the force acting on the wall be balanced by the

Nomenclature

A = ratio r_c/r^*
C^2 = constant in equation (1*b*). ($C^2=1.91$ according to asymptotic analysis [1][2])
d_0 = nozzle diameter
$f(\xi)$ = nondimensional stream function of self-similar outer flow induced by slender jet of constant momentum flux [2]
$f_\times(\xi)$ = composite solution, cf. equation (3*b*)
M_0 = momentum flux, divided by $2\pi\rho$, at nozzle exit (jet origin)
p = pressure at wall (referred to $\rho\nu^2 d_0^{-2}$)
Re_0 = jet Reynolds number, cf. equation (2)
r = radial coordinate (referred to nozzle diameter)
$\tilde{r}$ = reduced radial coordinate, cf. equation (6)
r^*, r^{**} = characteristic dimensionless radii, cf. equations (1*b*) and (11)
r_c = radial coordinate of eddy center (referred to nozzle diameter)
$(\overline{u_0^2})^{1/2}$ = mean square value of nozzle exit velocity
V_0 = volume flux through nozzle
θ = angular coordinate
θ_c = angular coordinate of eddy center
λ = volume flux coefficient, cf. equation (10)
ν = kinematic viscosity of fluid ($\nu=\text{const}$)
ξ = $(1-\cos\theta)/2$
ρ = density of fluid ($\rho=\text{const}$)
$\sigma_{\theta\theta}$ = normal viscous stress at wall (referred to $\rho\nu^2 d_0^{-2}$)
ψ = stream function (referred to νd_0)
$\tilde{\psi}$ = reduced stream function, cf. equation (6)
$\tilde{\psi}_0$ = value of $\tilde{\psi}$ corresponding to nozzle volume flux, cf. equation (13)

Downloaded 02 Jun 2010 to 171.66.16.66. Redistribution subject to ASME license or copyright; see http://www.asme.org/terms/Terms_Use.cfm

momentum flux through the orifice. In terms of dimensionless variables, this may be written as follows:

$$\mathrm{Re}_0^{-2}\int_{1/2}^{\infty}(p-\sigma_{\theta\theta})r\,dr=-1+O(\mathrm{Re}_0^{-2}) \qquad (8)$$

where the term $O(\mathrm{Re}^{-2})$ expresses an uncertainty due to the fact that the solution does not apply near the orifice, i.e., for $r=O(1)$.

Performing the analysis as described above with the stream function approximated according to equation (5), equation (1*b*) is reobtained for r^*, while K remains an undetermined constant of order 1. This lends further support to the results of the asymptotic analysis as far as the size of the viscous eddy and the location of its center is concerned. However, the approximate solution given here, as well as the modification to be given below, predict an eddy extending to infinity (Fig. 2), whereas the asymptotic analysis, when formally applied beyond its limits of applicability, yields a closed recirculatory flow region [1].

Far-Field Structure

Based on the assumption of large Reynolds numbers, various regions of the flow field can now be distinguished. Near the orifice, i.e., for $r=O(1)$, there is a free shear layer that separates the jet core from the surrounding fluid. At a distance $r=O(\mathrm{Re}_0)$ the shear layer has penetrated to the axis of the jet and transition to the self-similar jet flow takes place. This is the inner boundary of what will be called the "far-field," to be analyzed in the present work.

It follows from the results of the asymptotic analysis [1] that the momentum flux in the jet varies but little up to distances r that satisfy the condition $\ln r \ll \mathrm{Re}_0^2$. This, therefore, is the (rather limited) regime where the classical theories of a slender jet with constant momentum flux [8, 9] apply. The outer flow that is induced by entrainment into the jet is a viscous, rotational one [2].

As the distance from the nozzle further increases, the jet flow is modified due to the slow variation of the momentum flux as given in [1]. The jet remains slender as long as $r \ll r^*$, despite a substantial decrease in the momentum flux. Furthermore, since the entrainment rate of a slender axisymmetric jet does not depend on the momentum flux, the outer flow is not yet affected.

The structure of the flow field changes drastically when r is increased up to magnitudes of the order r^*. The jet widens and eventually develops into a recirculatory flow region, in which viscous and inertial forces are of equal importance, cf. equation (5).

With a further increase of r, the flow decays to a creeping motion, which is, in the first instance, controlled by the source of momentum in (or near) the origin of the jet. This has been discussed in the preceding section. At extremely large distances from the orifice, however, a further effect has to be taken into account. Equation (4) shows that the stream function due to the momentum source vanishes at infinity as $1/r$. There is, however, also a mass flux from the orifice. While it is true that the momentum source dominates the mass source up to distances that are of the order of r^*, the stream function due to the mass source does, of course, not vanish as $r\to\infty$. For a point source of mass located at $r=0$, an exact solution of the creeping motion equation, subject to the nonslip condition at the wall $\theta=\pi/2$, is the following [10]:

$$\psi=\lambda\mathrm{Re}_0(1-\cos^3\theta) \qquad (9)$$

where the coefficient

$$\lambda=V_0/(2\pi d_0 M_0^{1/2}) \qquad (10)$$

contains the volume flux V_0 from the orifice and depends on the shape of the velocity profile in the orifice. For a parabolic velocity profile one obtains $\lambda=(3/32)^{1/2}=0.306$.

Comparing now the stream function due to the momentum source, equation (4), with that due to the mass source, equation (9), we see that both sources are of equal importance if r is of the order of r^{**}, with

$$r^{**}=\mathrm{Re}_0^{-1}r^{*2}. \qquad (11)$$

From equation (1*b*) it follows that $r^{**}\gg r^*$.

If, finally, r is increased such that $r\gg r^{**}$, the influence of the momentum source has vanished, and the creeping flow is governed by the point source of mass. Equation (9) applies in this region, extending to infinity.

The approximate solution (5) can now be modified such as to account for the mass source effect. First it is noticed that the mass source makes a substantial contribution to the stream function in the creeping flow region only. Since the creeping motion equation is linear, this permits additive superposition. Secondly, the contribution to the force acting on the wall due to the mass source is negligible small. This can be seen from the following estimate. Equation (7) together with equation (9) show that p is of the order of $\mathrm{Re}_0 r^{-3}$. Integrating over the surface region of the wall, where the mass source is of importance, i.e., from $r=O(r^{**})$ to infinity, the force due to the mass source can be estimated. The result is a contribution of order $(r^*)^{-2}$ to the momentum balance (8), which is negligible.

Thus the modification of the approximate solution consists in a superposition of the stream functions given in equations (5) and (9). The result is

$$\tilde{\psi}=\frac{\tilde{r}f_\times(\xi)\sin^2 2\theta}{\sin^2 2\theta+\tilde{r}^2 f_\times(\xi)}+\tilde{\psi}_0(1-\cos^3\theta), \qquad (12)$$

where

$$\tilde{\psi}_0=\lambda\mathrm{Re}_0/(2Kr^*). \qquad (13)$$

A typical stream line pattern calculated from equation (12) is shown in Fig. 2. Note that there is a limiting stream line $\tilde{\psi}=\tilde{\psi}_0$ that separates the recirculatory flow region (closed stream lines) from the region in which the net mass transport to infinity takes place. The predicted structure of the flow field is in agreement with the stream line pattern obtained from flow-visualization experiments, cf. Fig. 3. The experiments have been described in [5]. The eddy can be observed in a region that is several times as large as the distance r_c from the orifice to the center of the eddy. With increasing distance the injected field occupies a growing part of the flow field. This confirms the increasing influence of the mass source on the far-field.

Numerical Investigation

The algorithm used for the numerical computations is a modified version of the TEAM finite volume code for steady

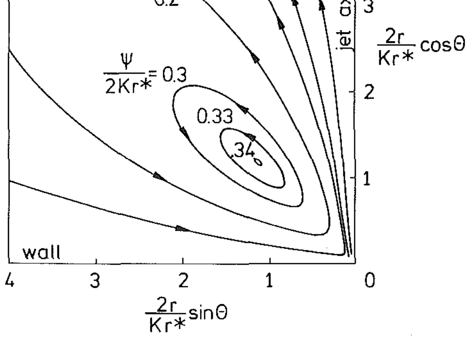

Fig. 2 Streamlines $\psi=$ const - Approximate analysis equation (12), $\mathrm{Re}_0=5.5$, parabolic exit velocity profile ($\lambda=(3/32)^{1/2}$), $K=2(\tilde{\psi}_0=0.0581)$

Downloaded 02 Jun 2010 to 171.66.16.66. Redistribution subject to ASME license or copyright; see http://www.asme.org/terms/Terms_Use.cfm

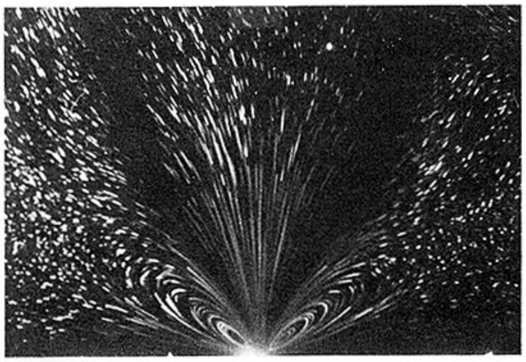

Fig. 3 Flow visualization: $Re_0 = 5.4$, $d_0 = 1.1$ mm, jet issuing from bottom

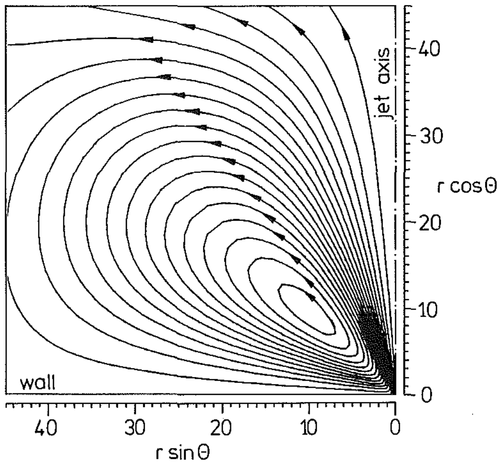

Fig. 4 Streamlines $\psi = \text{const}$ - Numerical solution, $Re_0 = 5.5$

elliptic flows [11], which, itself, is a development of the well known TEACH programs originating from the Imperial College [12]. The Navier-Stokes equations are discretized on a staggered grid and Leonard's QUICK interpolation scheme [13] is employed for the convective terms in order to minimize numerical diffusion. Continuity is enforced by a pressure correction equation of the SIMPLE type [11]. The finite volume equations are solved iteratively using the TDMA line solver.

In order to achieve, on the one hand, a good resolution of the jet velocity profile and, on the other hand, a sizeable computational domain without excessive cost in computer resources, a graded mesh was selected. The mesh gradient was kept small in order to keep down the truncation errors, and care was taken to avoid excessive length-to-width ratios of the grid cells.

A two-dimensional axisymmetric model was used in the computations. The inlet boundary conditions were chosen in such a way that the integrated momentum flux in each of the four grid cells within the orifice radius was equal to the corresponding value for a parabolic inlet profile.

The required mesh size precluded the use of outlet boundary conditions corresponding to the conditions at infinity and thus the flow's far-field behavior was approximated by that of a creeping flow due to a point source of mass situated in the jet orifice, cf. equation (9). Numerical experiments, in which such boundaries were placed at different distances from the orifice, showed this approximation to be self-consistent and acceptable for describing the flow in the vicinity of the eddy center, provided the boundaries were at a sufficient distance from the orifice. Due to the rapid rise of r_c with increasing Reynolds numbers, this limitation precluded computations for Reynolds numbers exceeding $Re_0 = 5.5$. Note that, according to equations (1*a*, *b*), r_c grows by more than two decades when Re_0 increases from 5.5 to 10.

The discretization error was checked to a limited degree by using grids with partially changed cell sizes. Hardware limitations, however did not allow to carry out a series of computations on refined grids in order to obtain some approximate value for the error, the computations having been rather closely taylored to the available resources from the start. Coarser meshes were not used because they were felt to introduce too many additional errors to be of much use for checking numerical accuracy.

A typical result of the calculations is given in Fig. 4. *Qualitative agreement with the experimental findings and the* analytical results is obvious. For a quantitative comparison cf. below. A more detailed description of the numerical investigation is given in [14].

Comparison of Results

The coordinates (θ_c, r_c) of the center of the viscous eddy are certainly the quantities that are both most interesting and most suitable for a quantitative comparison of analytical, numerical and experimental results. Plots of θ_c and ln r_c, respectively, versus Re_0^2 are shown in Figs. 5(*a*) and 5(*b*).

Two analytical solutions are available. The ad hoc approximation according to equation (12) can easily be evaluated for a maximum value of the stream function. Also shown in Figs. 5(*a*), (*b*) is the solution obtained from an asymptotic expansion in terms of large Reynolds numbers according to [1], cf. equations (1*a*, *b*).

Experimental data for θ_c and r_c are taken from [5]. To estimate side-wall effects, nozzles of two different diameters (0.5 and 1.1 mm, respectively) were used in a vessel with fixed geometry. If the distance of the eddy center from the nozzle exit was sufficiently small in comparison with the vessel half-width (less than about 0.25), the results turned out to be independent of the nozzle diameter. This was taken as an indication of negligible side-wall effects, and results from data above this limit were omitted. Furthermore, to make sure that buoyancy does not falsify the results, data were obtained with the jet issuing from the bottom and from the top of the vessel, respectively. Taking into account all the experimental uncertainties, i.e. errors in nozzle diameter, flow rate measurement and viscosity measurement, the accuracy in determining the Reynolds number is estimated to be better than 10 percent. The evaluation of the flow visualization photographs regarding the location of the eddy center is accurate within about ±1 mm, i.e., $r_c \pm 1$ for $d_0 = 1.1$ mm, and $r_c \pm 2$ for $d_0 = 0.5$ mm.

Regarding numerical data, some problems were experienced in evaluating the results for the coordinates of the eddy center, as the flow variables exhibit rather flat slopes in this area. Graphic evaluation from velocity and streamline plots yielded uncertainties of typically 5 percent, and interpolation between mesh points using point output data gave comparable error margins. Taking into account modelling and round-off errors, the total error in r_c and θ_c was estimated to be less than 10 percent.

Comparing the results, we find good agreement for the angular coordinate θ_c of the eddy center (Fig. 5(*a*)). Slight deviations for the lowest Reynolds number shown in the figure may be attributed to a violation of the basic assumption of large Reynolds number. Regarding the radial coordinate r_c of the eddy center (Fig. 5(*b*)), the data can be approximated by a straight line in the ln r_c versus Re_0^2 plot, i.e., the experiments confirm the exponential growth of r_c with Re_0^2 predicted by the asymptotic analysis, cf. equation (1*b*). For the constant C^2 in the exponent, a value $C^2 = 2.58$ is obtained from experimental data by least square linear regression, which is somewhat larger than the theoretical value $C^2 = 1.91$. The few numerical results also appear to confirm the exponential relation, with

Downloaded 02 Jun 2010 to 171.66.16.66. Redistribution subject to ASME license or copyright; see http://www.asme.org/terms/Terms_Use.cfm

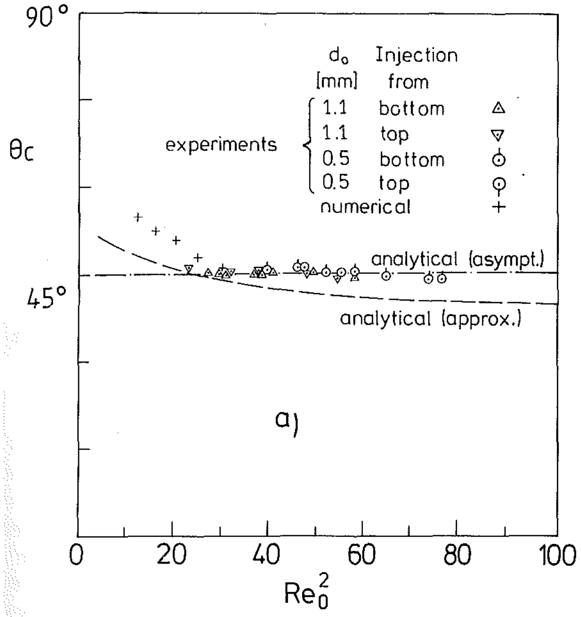

Fig. 5(*a*) Angular coordinate θ_c

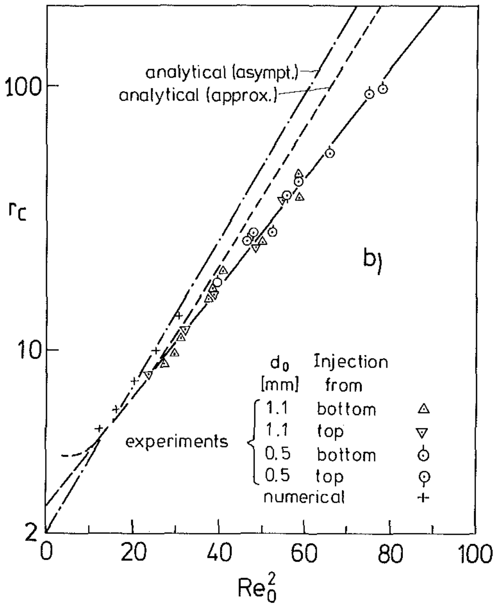

Fig. 5(*b*) Radial coordinate r_c (referred to nozzle diameter d_0) Asymptotic analysis: equations (1*a*, *b*), $A = 2$.

Approximate analysis: $\tilde{\psi}(r_c,\ \theta_c) = \tilde{\psi}_{max}$ from equation (12), $\lambda = (3/32)^{1/2}$, $K = 2$.

Experimental data: Estimated uncertainty $Re_0 \pm 10$ percent; $\theta_c \pm 2$ percent; $r_c \pm 1$(for $d_0 = 1.1$ mm), ± 2(for $d_0 = 0.5$ mm).

Numerical results: Estimated uncertainty ± 10 percent.

Fig. 5 Location of the center of the viscous eddy versus jet Reynolds number Re_0.

an exponent in between the experimental findings and the analytical value.

Conclusions

The analysis shows that, depending on the jet Reynolds number $Re_0 = M_0^{1/2}\nu^{-1}$, the following far field regions can be distinguished (radial distance r referred to nozzle diameter d_0, with $r \gg 1$).

(*a*) $\ln r \ll Re_0^2$: Classical slender jet with constant momentum flux; self-similar viscous, rotational outer flow.

(*b*) $r \ll r^* = \exp\ [Re_0^2/(8C^2)]$, with $C^2 = \text{const} = O(1)$: Modified jet flow with slowly varying momentum flux; outer flow as in (*a*).

(*c*) $r = O(r^*)$: Recirculatory flow region (toroidal eddy); viscous and inertial forces of equal importance.

(*d*) $r^* \ll r = O(r^{**})$, with $r^{**} = r^{*2}/Re_0$: Creeping flow due to point sources of momentum and mass.

(*e*) $r \gg r^{**}$: Creeping flow due to point source of mass.

According to the analysis, the center of the viscous eddy (region *c*) is located at a distance $r_c = Ar^*$ where $A = \text{const} = O(1)$, while r^* depends exponentially on the square of the Reynolds number. These analytical predictions are confirmed by the experimental data obtained from flow visualization and also by numerical solutions of the Navier-Stokes equations. The quantitative agreement, however, is not completely satisfactory, and further work toward a sufficiently accurate description of the complete flow field seems to be desirable.

Acknowledgments

The authors are grateful to Mr. J. Berger, Dr. K. Mitsotakis, and Dr. U. Schaflinger for their assistance in performing the computations. The investigations have been supported by the Fonds zur Förderung der wissenschaftlichen Forschung, Project No. P5716.

References

1 Schneider, W., "Decay of Momentum Flux in Submerged Jets," *Journal of Fluid Mechanics*, Vol. 154, 1985, pp. 91-110.

2 Schneider, W., "Flow Induced by Jets and Plumes," *Journal of Fluid Mechanics*, Vol. 108, 1981, pp. 55-65.

3 Rubin, S. G., and Falco, R., "Plane Laminar Jet," *AIAA J.*, Vol. 6, 1968, pp. 186-187.

4 Mitsotakis, K., Schneider, W., and Zauner, E., "Second-Order Boundary-Layer Theory of Laminar Jet Flows," *Acta Mechanica*, Vol. 53, 1984, pp. 115-123.

5 Zauner, E., "Visualization of the Viscous Flow Induced by a Round Jet," *Journal of Fluid Mechanics*, Vol. 154, 1985, pp. 111-119.

6 Blake, J. R., "A Note on the Image System for a Stokeslet in a Nonslip Boundary," *Proc. Camb. Phil. Soc.*, Vol. 70, 1971, pp. 303-310.

7 Blake, J. R., "On the Generation of Viscous Toroidal Eddies in a Cylinder," *Journal of Fluid Mechanics*, Vol. 95, 1979, pp. 209-222.

8 Schlichting, H., "Laminare Strahlausbreitung," *Z. Angew. Math. Mech.*, Vol. 13, 1933, pp. 260-263.

9 Schlichting, H., *Boundary-Layer Theory*, 7th Ed., McGraw-Hill, 1979.

10 Happel, J., and Brenner, H., *Low Reynolds Number Hydrodynamics*. 2nd Ed., Noordhoff Intl. Publ., Leydon, 1973, p. 138.

11 Huang, P. G., and Leschziner, M. A., "An Introduction to the Computer Code TEAM," UMIST, Univ. of Manchester, 1983.

12 Gosman, A. D., and Pun, W. M., "Calculation of Recirculating Flows," Report HTS/74/2, Imperial College, 1973.

13 Leonard, B. P., "A Stable and Accurate Convective Modelling Procedure Based on Quadratic Upstream Interpolation," *Comp. Meths. Appl. Mech. Eng.*, Vol. 19, 1979.

14 Böhm, H., Zauner, E., and Schneider, W., "Numerical Investigation of Viscous Flow Induced by an Axisymmetric Laminar Jet Issuing From a Plane Wall. In: *Numerical Methods in Laminar and Turbulent Flow* (C. Taylor et al., Eds.), Pineridge Press, Swansea, 1985, pp. 96-106.

Downloaded 02 Jun 2010 to 171.66.16.66. Redistribution subject to ASME license or copyright; see http://www.asme.org/terms/Terms_Use.cfm

Velocity Fluctuations at the Walls of a Packed Bed of Spheres for Medium Re-Numbers

R. H. Bahnen

C. G. Stojanoff

Institut fuer Thermodynamik,
RWTH Aachen,
Schinkelstr, 8,
5100 Aachen, FRG

A packed bed which is uniformly filled with equally large spheres is subjected to transpiration flow. The velocity component perpendicular to its surface was measured by means of Laser-Doppler-Velocimetry. Special attention is paid to the velocity fluctuations occurring at the wall of the cylindrical container and at the convex surface of rods of different diameters inserted in the bed center. The Re-numbers were between 800 and 1500. The experimental results are compared with results obtained from the literature.

1 Introduction

Transpiration cooled packed beds of spheres are of considerable interest for many technical applications, such as a catalytic chemical reactors, regenerative heat exchangers and gas-cooled nuclear reactors. The german gas-cooled high temperature nuclear reactor (HTGR) operates with spherical fuel elements which form a randomly packed bed of spheres. Achenbach [1] and Morales et al. [2] describe extensively the effect of the fluid velocities on the heat and mass transfer rates in packed beds. Buchlin et al. [3] investigated the occurrence of "hot spots" in active packed beds and the influence of the velocity profile on the temperature field. Photographic studies of the flow pattern in the voids of a packed bed of spheres conducted by Kubo et al. [4] revealed the correlation of the critical Reynolds-number with the porosity of the packed bed. In most technical applications one encounters randomly packed beds with significant structural perturbations of the fill due to containing or separating wall and/or protruding rods. Knowledge of the porosity distribution alone is not sufficient for the prediction of the velocity profile across the packed bed. Velocity distributions for a number of randomly packed beds of spheres were obtained by Price [5] using flow separators and Pitot-tube. Morales et al. [2] and Schwartz et al. [6] used hot-wire-anemometer with circular sensor and determined that the velocity in packed beds decreases near the wall of the containing vessel. The comparatively low spatial resolution of these methods and the flow disturbance introduced by the instrument preclude, however, an accurate measurement of the velocity near the wall. Vortmeyer and Schuster [7] used a variational method for the calculation of the velocity profile inside the packed bed for low Reynolds-numbers. However, their computation of the velocity field for a smoothed porosity function does not agree with the experimental results presented here.

In order to circumvent these problems and obtain an accurate velocity profile in the proximity of the concave container wall and of the convex surface of a protruding rod, the present investigation uses a Laser-Doppler-Velocimeter for high resolution measurements of the velocity component prependicular to the surface of the packed bed. The velocity measurements were conducted with a number of inserted rods of various diameters and covered a flow regime spanning the range of medium Reynolds numbers.

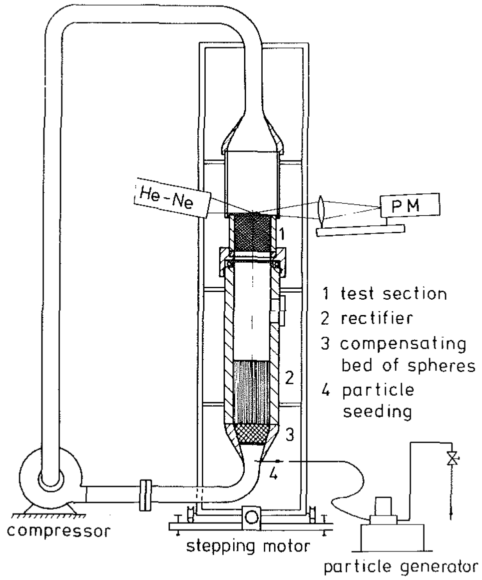

Fig. 1 Experimental setup

2 Experimental Technique

Marivoet et al. [8] and Buchlin et al. [3] reported significant spatial fluctuations of the velocity in cylindrical packed beds subjected to forced transpiration. In addition, large spatial variations of the velocity field are expected near the wall of the containing vessel and in the vicinity of convex surfaces, such as heat exchanger tubes and control rods protruding through

---

Contributed by the Fluids Engineering Division for publication in the JOURNAL OF FLUIDS ENGINEERING. Manuscript received by the Fluids Engineering Division, August 15, 1985.

Copyright © 1987 by ASME

Downloaded 02 Jun 2010 to 171.66.16.66. Redistribution subject to ASME license or copyright; see http://www.asme.org/terms/Terms_Use.cfm

the packed bed and perturbing the uniform void fraction distribution. In order to fulfill the requirements for high temporal and spatial resolution in the experimental determination of the velocity field, the experimental technique employed here was a single channel Laser-Doppler-Velocimeter (LDV). The complex nature of this technique requires a high level of experimental efforts; however, the following advantages more than compensate for this:

- high spatial resolution
- measurement of the individual velocity components
- velocity measurements are performed without flow perturbation
- calibration of the system is not necessary
- measured frequencies are linearly proportional to velocities

The experimental setup consisted of a cylinder with a diameter of 96 mm and 100 mm height, which was filled with polished steel spheres of 4 mm diameter. The experimental setup is depicted in Fig. 1. In this arrangement the cylinder is placed in the air stream and is rotated about its axis. The air stream enters the packed bed from below. Before entering the fill, the air stream passes through a compensating fill and a rectifier in order to ensure that the air flow entering the test bed has a uniform velocity profile. The light scattering particles (TiO_2), required for the LDV measurements are injected into the air stream before it passes through the compensating fill. Since the air flow is recycled, the loss of scattering particles is due to a particle adhesion to the walls and particles escaping through the opened measuring orifice positioned at the upper surface of the packed bed. This arrangement is necessary in order to avoid laser beam perturbation caused by particle adhesion at the wall of the glass enclosure. Rods of different diameters were introduced into the center of the packed bed. The rods were inserted to the bottom of the bed in order to simulate "in-core convex surfaces," such as the controlling rods of a nuclear pebble bed reactor or heat exchanger tubes in chemical reactors.

The laser beam of the 15 mW He-Ne-laser is split into two beams of equal intensity by means of a beam splitter and the emerging beams are focussed by a convex lens with a focal length of 130 mm. The two beams intersect to form a LDV sample volume in the focal point of the lens which has the following dimensions:

- diameter: 0.1 mm
- length: 0.5 mm
- fringe spacing: 1.7 μm

The scattered light from the sample volume is collected in the forward direction and transmitted to a photomultiplier. The resulting LDV signals are processed by a counter.

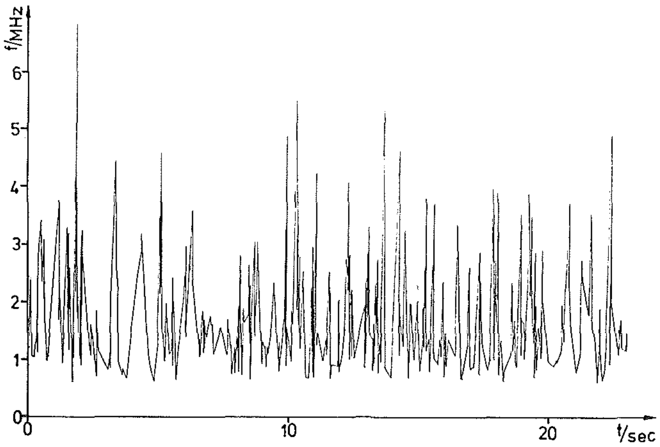

Fig. 2 Frequency versus time record for a rotating bed of spheres

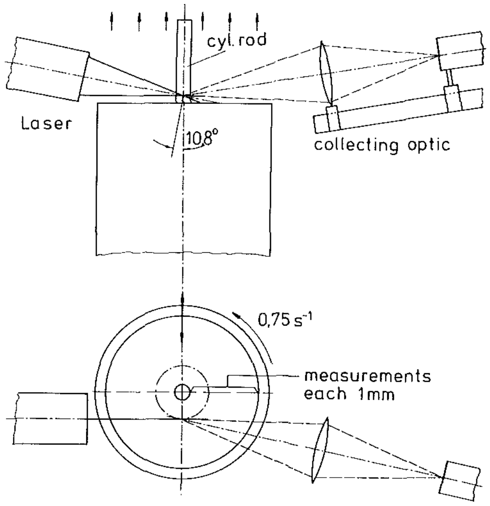

Fig. 3 Measuring points

In order to facilitate the measurement of the velocity directly above the surface of the packed bed it was necessary to position the transmitting optics at an angle which is equal to the half of the intersection angle of the two beams. This ensured that even in the center of the packed bed, the sample volume was directly above the surface of the fill. The resulting systematic measurement error was lower than 2 percent. In order to obtain the mean velocity for each radius, the packed bed was rotated and 4000 data points were registered during nearly 20 rotations. Measurements involving larger number of data points produced the same mean values, therefore all subsequent measurements were performed with 4000 data points. A portion of the resulting time signal is shown in Fig. 2.

The rotation of the bed facilitates a simple measurement of the mean values for a given radius, as this was demonstrated by Wang et al. [11]. The measurements do not provide information about the degree of turbulence because of the superposition of temporal and spatial fluctuations during the experiment with the spinning bed. Previous measurements performed on a non-rotating field yielded a 20 percent degree of turbulence for all radii. The speed of rotation was small enough, so that the influence of the centrifugal forces could be neglected ($n < 0.8\ s^{-1}$). The circumferential mean velocity for given radius is then obtained from the temporal record of the velocity signal which is integrated and multiplied with the fringe spacing.

Nomenclature

d_s = sphere diameter
f_i = burst frequency
K = fringe spacing
n = number of measurements used for calculating mean values
T_i = time between two measurements ("Sample Time")
v_1 = velocity above spheres
v_h = velocity above voids
w = velocity of air stream before entering the fill
w_v = velocity inside the voids
ϵ = porosity
ν = kinematic viscosity

Downloaded 02 Jun 2010 to 171.66.16.66. Redistribution subject to ASME license or copyright; see http://www.asme.org/terms/Terms_Use.cfm

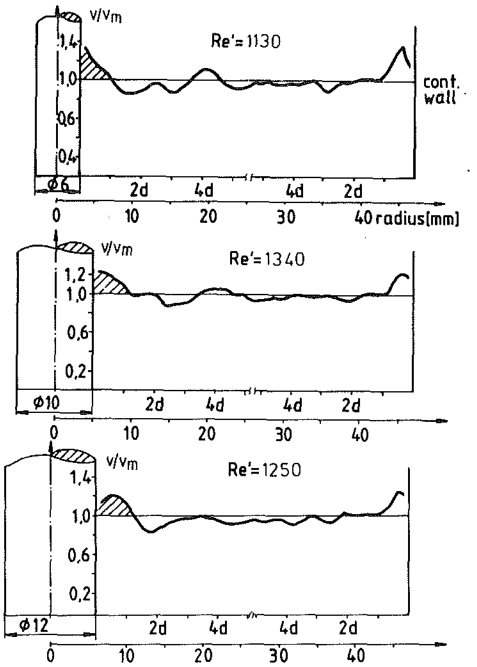

Fig. 4 Velocity distribution versus radius for different rod diameters

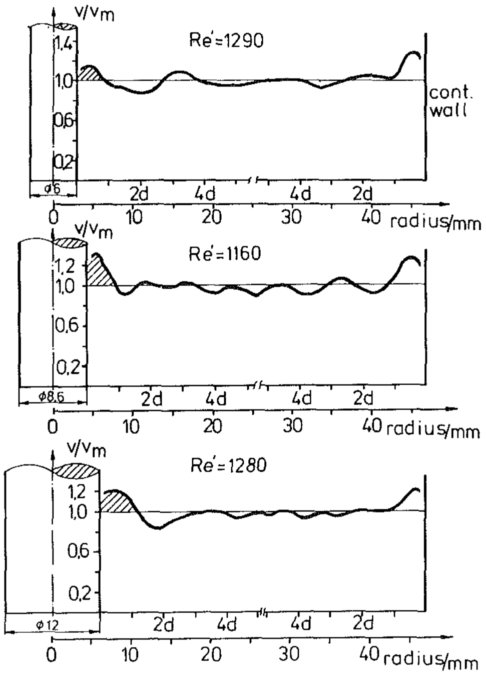

Fig. 5 Velocity distribution versus radius for different rod diameters

$$v = K\frac{\sum_{i=2}^{4000} \frac{f_{i-1}+f_i}{2} T_i}{\sum_{i=2}^{4000} T_i}$$

The measurements were performed over the entire surface of the packed bed for various Re′-numbers and diameters of the incore rods at 1 mm radial increments. Top and side views of the packed bed and the respective position of the LDV sample volume are presented in Fig. 3.

The corresponding Re′-numbers are calculated using the sphere diameter.

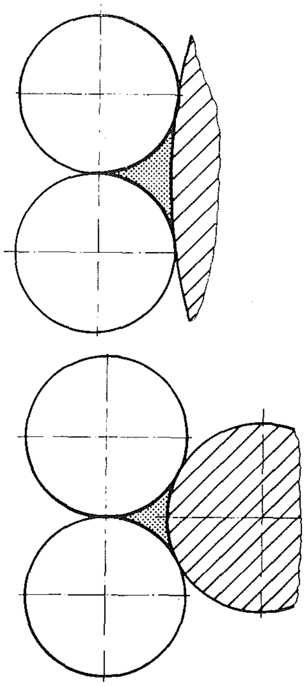

Fig. 6 Void cross-section variation between spheres and convex walls

$$\mathrm{Re}' = \frac{\epsilon}{1-\epsilon}\,\frac{w_v d_s}{\nu}$$

$$\mathrm{Re}' = \frac{1}{1-\epsilon}\,\frac{w d_s}{\nu}$$

3 Experimental Results

Initial measurements were performed in order to determine the optimum position of the height of the sampling volume above the packed bed. These results showed, that all measurements should be performed directly above the surface of the packed bed because the velocity profile becomes smoother as the vertical position of the LDV sampling volume is increased. This smoothing effect is a result of the thorough mixing of the free jets emerging from the voids of the packed bed. The mixing effect increases with increasing height of the sampling volume above the packed bed surface. The measurements depicted in Figs. 4, 5, 7, and 8 were all performed at a height of 4 mm above the surface in order to ensure a good registration of the velocity fluctuations and yet avoid local disturbances due to individual spheres protruding above the mean surface of the packed bed. The velocity profiles in Figs. 4, 5, 7, and 8 are scaled with the mean velocity obtained for the entire cross-section of the packed bed.

Figures 4 and 5 show a velocity maximum occurring at a distance of 0.5 d_s from the container wall. A smooth velocity profile is observed at larger distances. The influence of the rod diameter on the velocity distribution for various rods placed in the center of the packed bed is also depicted. In the vicinity of the container wall the rod does not influence the velocity profile. However, near the rod one clearly observes a maximum at a distance of 0.5 d_s from its convex surface, followed by a minimum at a distance of 1.5 d_s.

It should be noted that the area under the first maximum in the proximity of the rod wall, which is a measure for the volumetric flux, increases for larger rod diameters while the sphere diameter remains constant. This is due to the change in the cross-section of the void formed by the inserted rod and the surrounding spheres as depicted in Fig. 6.

The change in the cross-section produces a change in the position of the first maximum near the rod surface (Fig. 4 and

Downloaded 02 Jun 2010 to 171.66.16.66. Redistribution subject to ASME license or copyright; see http://www.asme.org/terms/Terms_Use.cfm

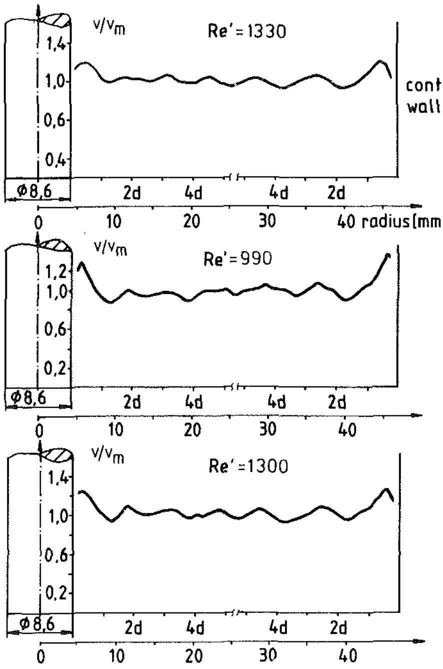

Fig. 7 Velocity distribution versus radius for different Re'-numbers

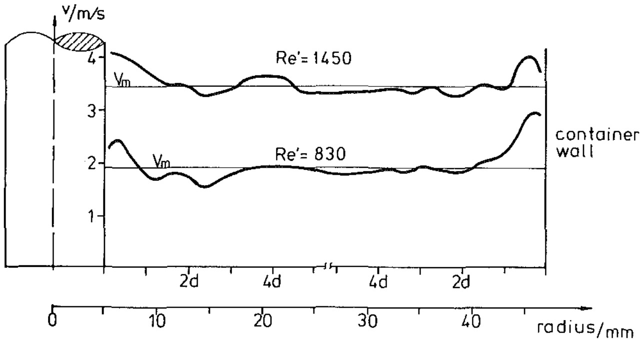

Fig. 8 Velocity distribution versus radius for low and high Re'-numbers

Fig. 5). The position of the maximum is located at a distance smaller than 0.5 d_s for small rod diameters and is close to 0.5 d_s for larger ones.

Figure 7 shows the dependence of the velocity profile from the Re'-number for a constant diameter rod. With increasing Re'-number, the velocity profile becomes smoother. This can be explained by a better mixing between the air streams above the surface of the packed bed of spheres (the Re'-number is in the transition region laminar/turbulent).

The velocity profile presented in Fig. 8 is not scaled (rod diameter of 10 mm) and one clearly sees the flattening of the velocity profile across the unperturbed surface of the packed bed—especially at the container wall.

A characteristic quantity for the smoothening of the velocity profile is, for example, the ratio of the maximum velocity at the container wall to the mean velocity, where the mean velocity is defined over the entire surface of the packed bed.

This quantity is plotted as a function of the Re'-number and is presented in Fig. 9, where $v_{\max}$ is the velocity near the container wall. However, one should point out that the assessment of the Re'-number influence is based on four sets of data available at present for a given rod diameter. A comparison of the measured velocity profiles with the porosity plot measured by Benanati and Brosilow [9], for a similar bed of spheres containing a central post, indicates that the velocity oscillations are damped more strongly as one would expect from the appearance of the porosity profile.

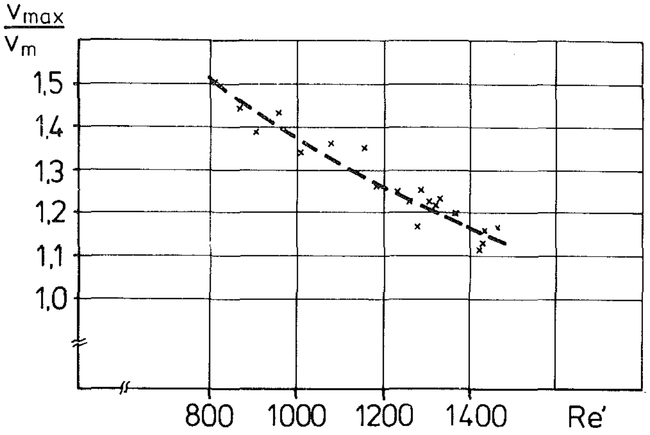

Fig. 9 Ratio of maximum velocity to mean velocity versus Re'-number

Table 1 Experimental uncertainty

Method	caused by	% Uncertainty
1-channel LDV-system	Instrument	0.5 percent (1 Digit)
	declination of optical system	2.0 percent
	calculation of mean values	2.0–5.0 percent

For example, the veloctiy profile shows one pronounced maximum only which is followed by a smooth velocity distribution. The maximum is displaced towards the center of the packed bed. Only for a rod diameter of 8.6 mm one sees an oscillation in regions away from the wall and for all Re'-numbers (Fig. 7). However, the period of the oscillation is greater than the sphere diameter which is significant departure from the regularity of the porosity variation. The stronger damping of the velocity is an expected effect because the packed bed is not composed of channels which are separated from one another. The interconnected porosity of a typical packed bed causes the separate streams of the fluid to mix. Hence, the apparent discrepancy between the two profiles may be explained when measurement of the radial component of the velocity are performed. Such measurements were outside the scope of the present investigation.

4 Uncertainty of Measured Data and Remarks on the Evaluation Procedure

For every measured point, 4000 data were registered. The measuring uncertainty in the determination of the mean values is shown in Table 1.

For regions away from the wall ($>2d_s$) the uncertainty between measurements for *different fills* is in the order of 10–15 percent due to the different surface structures of each fill, with a lower value applying to the outer regions of the field. The variations due to the structural differences of the various fills could be eliminated if mean values are obtained from a number of measurements using different fills.

The LDV signal processing by a counter supplies information on the velocity and on the time elapsed between two measurements so that one obtains a frequency-time diagram (Fig 2) which corresponds to the velocity-circumference plot for the rotated bed of spheres. The mean of this plot deviates strongly from the mean obtained from the frequency distribution of the measured signals and from subsequent correction of the mean according to Mcloughlin and Tiederman [10]. An

Downloaded 02 Jun 2010 to 171.66.16.66. Redistribution subject to ASME license or copyright; see http://www.asme.org/terms/Terms_Use.cfm

example of such correction procedure and a comparison with the mean obtained from the time-velocity record are presented in Fig. 10. For the rotating fill one observes several maxima for all distributions (Fig. 10). Due to this fact, one obtains a skewed distribution as the one presented schematically in Fig. 11, where v_l and v_h represent the velocities above the spheres and above the voids respectively.

The correction method of Mcloughlin and Tiederman [10] is based on the assumption that the density of scattering particles in the fluid is constant; therefore, the mean is shifted towards higher values of the velocity. The correction shifts back the mean value of the velocity.

The mean value in the case of a packed bed is shifted also toward higher velocities but by a different amount due to the variation in particle densities (Fig. 10). It is, therefore, absolutely necessary to determine the mean values by integrating the temporal velocity signals. The determination of the variance should also be performed in this manner. For stationary measurements above a fixed location, the frequency distributions are symmetric.

The achievable Re′-number was limited upwards by 1500, since the top layers of the packed bed were displaced at higher air flow velocities (fluidization point).

5 Comparisons With Other Measurements

Table 2 shows a comparison of measurements performed in this paper with measurements of Price [5], Morales et al. [2] and Schwartz et al. [6]. The missing dependence of the maximum values of the velocity at the wall as a function of Re-number by Price [5] is explained by the higher Re-numbers used. The spatial resolution in the papers of Morales et al. [2] and Schwartz et al. [6] was low so that it is possible that the above mentioned dependence could not be observed. Besides

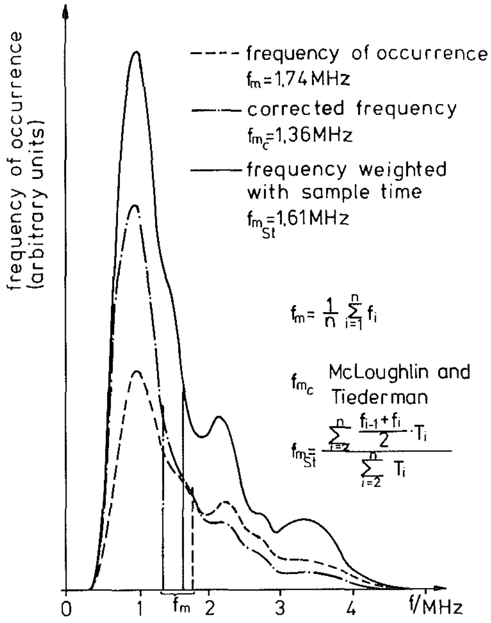

Fig. 10 Comparison of corrected and uncorrected frequency distributions for a rotating bed of spheres

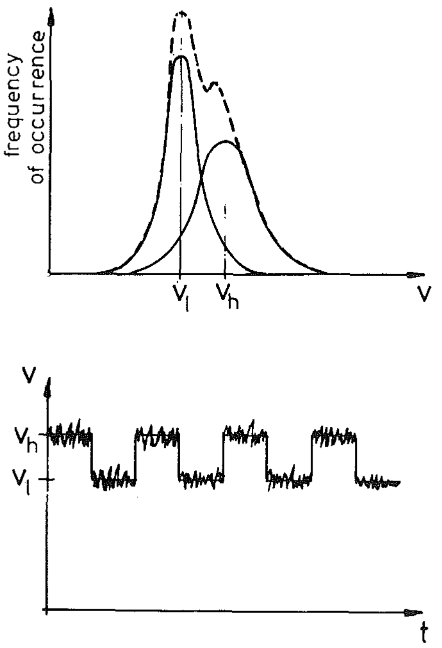

Fig. 11 Frequency distribution versus velocity

Table 2 Comparisons of different velocity measurements

Author and Measurement method	Container diameter	Size of filling	Dist. to surface	Container height	Re-number	Results
Price 1967 Flow separator and Pitot-tube	0.3 m $D/d_s = 12.5$-50	6 mm 12 mm 25 mm spheres		11.5-45 cm $H/d_s = 9$-36	1470-4350	measurements on container wall 350-1000 measurements per cross-section v_r/v_m independent from Re-number v_r independent from porosity (0.38-0.40) $v_{\max}$ in a distance of 0.5 d_s from wall $v_{\min}$ following $v_{\max}$ (damped oscillation) $v_{\max}/v_{\min}$ falls with decreasing D/d_s
Morales et al. 1951 *Schwartz, et al. 1953* Circular hot-wire-anemometer	0.05 m $D/d_c = 5 - 15$	3 mm 6 mm 9 mm cylinders	0.6 cm -75 cm	15-45.6 cm	25-332	measurements on container wall $v_{\max}$ in a constant distance from wall for each D/d_c no oscillating velocity over radius $v_{\max}/v_m$ falls with increasing Re-number $v_{\max}/v_m$ falls with decreasing h/d_c $v_{\max}/v_m$ falls with increasing D/d_c
Present measurements Laser-doppler-velocimeter and rotating packed bed of spheres containing central posts	0.096 m $D/d_s = 24$	4 mm spheres	0.4 cm	10 cm	480-850-	measurements on container and rod walls high spatial resolution 4000 measurements for each point, exact mean velocity $v_{\max}$ at a distance of 0.5 d_s from walls $v_{\min}$ following $v_{\max}$ (rod only) $v_{\max}/v_m$ falls with increasing Re-number $v_{\max}$ (container) $> v_{\max}$ (rod) (see Fig. 9)

Downloaded 02 Jun 2010 to 171.66.16.66. Redistribution subject to ASME license or copyright; see http://www.asme.org/terms/Terms_Use.cfm

the hot-wire anemometer registers also the radial component of the velocity. For the volume flow used, this is not essential.

The Re-number in Table 2 is determined using the flow velocity of the air steam before entering the fill and the sphere diameter.

$$\mathrm{Re}=\frac{wd_s}{\nu}$$

In conclusion, one could say that the velocity profile in the laminar/turbulent transition region becomes flatter with increasing Re-numbers. For higher Re-numbers, the velocity plot is probably independent from the Re-number as shown by Price [5]. A maximum of the velocity was observed at a distance of 0.5 d_s from the wall. For a rod placed at the center of the packed bed, the velocity maximum increases with increasing rod diameter. In order to clarify the period of the observed oscillation of the velocity profile (the period is greater than the sphere radius), additional measurements of the radial component of the velocity are necessary.

6 Conclusions

A Laser-Doppler Velocimeter was used for the measurement of the velocity profiles near the surface of a randomly packed bed of spheres subjected to forced fluid transpiration. The flow velocity was accurately determined across the surface of the packed bed and in the proximity of the containing wall and at the convex surface of cylindrical rods of various diameters protruding through the center of fill. The results for the velocity distributions are presented as radial profiles across the surface of the packed bed in terms of mean velocity obtained for a given radius which is normalized with the mean velocity defined for the cross section of the packed bed. These results are compared with literature data and they confirm the results of Morales et al. [2] that the normalized velocity decreases with increasing Re-number and exhibits a drop in the proximity of the concave surface of the retaining wall.

New results are presented for the velocity profiles in the vicinity of the convex surface of a protruding rod. These results are compared with the porosity measurements of Benenati and Brosilow [9] for a large bed of uniform spheres containing a central post. The comparison is facilitated by the similarity of the experimental conditions in terms of rod to sphere diameter ratio and rod to wall distance. It should be pointed out, however, that the spatial variation of the velocity measured in this investigation does not correlate well with the variation of void fraction as measured by Benenati and Brosilow [9]. The major reason for this discrepancy is seen in the radial flow component that would point away from the container wall and was not measured in the framework of this investigation. This leads to the conclusion that the porosity distribution alone is not sufficient for the determination of the velocity profile.

Acknowledgments

Financial assistance for this investigation was provided by the "Landesamt fuer Forschung, NRW," Federal Republic of Germany. The assistance of Dipl.-Ing. V. Schneider who performed many of the measurements is gratefully acknowledged.

References

1 Achenbach, E., "Forced Convective Heat Transfer and Pressure Drop in a Randomly Packed HTGR Core," *Proc. of the ANS/ASME/NRC Int. Topical Meeting on Nuclear Reactor Thermal-Hydraulics*, New York, Oct. 5-8, 1980, pp. 1-12.

2 Morales, M., Spinn, C. M., and Smith, J. M., "Velocities and Effective Thermal Conductivities in Packed Beds," *Ind. Eng. Chem.*, Vol. 43, 1951, pp. 225-232.

3 Buchlin, J. M., Lapthorn, J. C., and Ginoux, J. J., "Hot Spots in Active Packed Beds," *Verfahrenstechnik*, Vol. 11, 1977, pp. 620-624.

4 Kubo, D., Aratani, T., Mishima, A., and Yano, T., "Photographic Observation of Flow Pattern in Voids of Packed Beds of Spheres," *Journal of Chemical Eng. of Japan*, Vol. 11, 1978, pp. 405-407.

5 Price, J., "Velocity Distribution and Pressure Losses for Randomly Packed Beds of Spheres," Australian Atomic Energy Commission Research Establishment, Lucas Heights, 1967, pp. 1-11.

6 Schwartz, C. E., and Smith, J. M., "Flow Distribution in Packed Beds," *Indust. and Eng. Chemistry*, Vol. 45, 1953, pp. 1209-1218.

7 Vortmeyer, D., and Schuster, D., "Evaluation of Steady Flow Profiles in Rectangular and Circular Packed Beds by a Variational Method," *Chem. Eng. Sci.*, Vol. 38, pp. 1691-1699.

8 Marivoet, P., Teodororu, P., and Waje, S. T., "Porosity, Velocity and Temperature Profiles in Cylindrical Packed Beds," *Chem. Eng. Sci.*, Vol. 29, 1974, pp. 1836-1840.

9 Benenati, R. F., and Brosilow, C. B., "Void Fraction Distribution in Beds of Spheres," *AICHE Journal*, Vol. 8, 1962, pp. 359-361.

10 Mcloughlin, D. K., and Tiederman, W. G., "Biasing Correction for Individual Realization of Laser Anemometer Measurements in Turbulent Flows," *The Physics of Fluids*, Vol. 16, 1973, pp. 2082-2088.

11 Wang, C. P., Bernard, J. M., and Lee, R. H., "Feasibility of Velocity Field Measurement in a Fluidized Bed with a Laser Anemometer," *Proc. of the Int. Workshop on Laser Velocimetry*, July 11-13, 1978, West Lafayette, Ind.

Downloaded 02 Jun 2010 to 171.66.16.66. Redistribution subject to ASME license or copyright; see http://www.asme.org/terms/Terms_Use.cfm

T. A. Trabold
Research Assistant.

E. B. Esen
Research Assistant.

N. T. Obot
Associate Professor.
Mem. ASME

Fluid Mechanics, Heat and
Mass Transfer Laboratory,
Department of Chemical Engineering,
Clarkson University,
Potsdam, NY 13676

Entrainment by Turbulent Jets Issuing From Sharp-Edged Inlet Round Nozzles

Experiments were carried out to determine entrainment rates by turbulent air jets generated with square-edged inlet round nozzles. A parametric study was made which included the effects of Reynolds number, nozzle length, partial confinement and geometry of the jet plenum chamber. Measurements were made for the region extending from the nozzle exit to 24 jet hole diameters downstream. There is a large difference in the rate of fluid entrainment between jets generated with relatively short nozzles and those discharged through long tubes.

Introduction

The entrainment process in free turbulent jets has attracted the attention of researchers for a long time. The problem is of fundamental importance in virtually all industrial design involving free and impinging jets. Although there are numerous practical situations (e.g., mixing, combustion, etc.) where engineers are interested in finding ways to increase the rate of entrainment by turbulent jets, the desired effect is exactly the opposite for many applications such as impingement heating, evaporation and drying. For the latter processes, which usually involve use of heated jets, the negative effect of entrainment arises from the fact that it lowers the jet temperature and heat content for locations downstream from the nozzle (Obot et al., 1986).

For a circular jet, the mass flow rate at any downstream location is given by the area integral over the axial component of mean velocity:

$$m = 2\pi \int_0^\infty \rho\, U(r, z) r\, dr \qquad (1)$$

The mass flow rate (m_e) of surrounding fluid entrained by a jet then becomes

$$m_e = m - m_{j0} \qquad (2)$$

or in nondimensional form:

$$\psi = m_e/m_{j0} = (m/m_{j0}) - 1 \qquad (3)$$

where m_{j0} is the corresponding value at the nozzle exit.

It is well known that m or m_e increases with distance from the nozzle. In the developing jet region, which encompasses the potential and transition regions, there is no agreement among the various experimental results on the nature of the variation of m or m_e (i.e., linear or nonlinear) with axial distance. By contrast, in the fully developed flow region of a round jet, it is widely observed that the mass flow rate may be given by

$$dm/dz = C_0(m_{j0}/d)\,(\rho_\infty/\rho_0)^{1/2} \qquad (4)$$

where C_0 is a constant, the numerical value of which could well be expected to depend on several parameters, such as, nozzle configuration (beveled, square-edged, long tubes, etc.), turbulence, Reynolds number and confinement. It appears that Crow and Champagne (1971) were probably the first to show that the entrainment coefficient for circular jets may depend on the initial conditions at the nozzle exit. As will be evident from the discussion which follows, there has been very little investigation of the effects of a wide range of variables on entrainment characteristics for axisymmetric turbulent jets.

A summary of some of the previous results is presented in Table 1 from which several important observations can be made. First, all but three of these studies involved use of jets generated with convergent nozzles as these produce nearly uniform velocity and low turbulence levels at the nozzle exit. Second, there is, in general, satisfactory agreement among the results obtained by the various investigators who used convergent nozzles. In fact, for this nozzle configuration C_0 could be stated as 0.302 ± 0.024, which is about an 8 percent variation around the mean value. Since most of the convergent nozzle results were obtained by integration of the axial velocity data, this degree of concurrence establishes that this method

Table 1 Summary of previous studies

Author (s)	C_0(Range)	Nozzle Configuration
Crow and Champagne (1971)	0.292 ($\bar{Z} \geq 6$)	Convergent
Albertson et al. (1950)	0.32 ($\bar{Z} \geq 8$)	Convergent
Taylor et al. (1951)	0.26 ($\bar{Z} \geq 10$)	Convergent
Ricou and Spalding (1961)*	0.32 ($\bar{Z} > 0$)	Convergent
Hill (1972)*	0.32 ($\bar{Z} \geq 14$)	Convergent
Kleis and Foss (1974)	0.31 ($\bar{Z} \geq 6$)	Convergent
Sforza and Mons (1978)	0.28 ($\bar{Z} > 10$)	Convergent
Boguslawski and Popiel (1979)	0.183 ($\bar{Z} < 12$)	$L/d = 50$
Wall et al. (1980)*	$m_e/m_{j0} = 0.128\bar{Z} + 0.004\bar{Z}^2$	Long Tubes
Obot et al. (1984)	$m_e/m_{j0} = 0.13[\bar{Z} - 0.07]$ ($\bar{Z} \leq 10$)	$L/d = 12$

*Direct Method

Contributed by the Fluids Engineering Division of The American Society of Mechanical Engineers and presented at the Winter Annual Meeting, Miami Beach, Fla., November 11-17, 1985. Manuscript received by the Fluids Engineering Division *August 15, 1985.*

Copyright © 1987 by ASME

Downloaded 02 Jun 2010 to 171.66.16.66. Redistribution subject to ASME license or copyright; see http://www.asme.org/terms/Terms_Use.cfm

of determining entrainment rates is quite satisfactory, at least for axial locations up to 60 jet hole diameters (Albertson et al., 1950), depending of course on the range of Reynolds numbers of interest.

Another observation concerns the results for nonuniform jets which were generated with long tubes. Although there are quantitative differences between the results of Boguslawski and Popiel (1979) and those of Wall et al. (1980) or Obot et al. (1984), there is however one common feature, and that is, the entrainment coefficient (C_0) is substantially lower than for convergent nozzles. In this regard it is important to note that Wall et al. used the porous wall technique of Ricou and Spalding (1961). From our review of the three studies (Table 1) that involved use of the so-called direct method, it was concluded that this discrepancy is entirely the result of the difference in the geometry of the nozzles used. This observation has been verified experimentally by Obot and co-workers for limited experimental conditions (Obot et al., 1984; 1986). From the results of our exploratory studies and the literature, the conjecture was that entrainment characteristics of turbulent round jets may follow two distinct trends; one for long tubes with small differences between such results with increasing tube length, and the other for relatively short nozzles. For the latter, the entrainment rate can be quite susceptible to changes in nozzle inlet configuration (beveled or square-edged). In view of the limited range of variables (two Reynolds numbers and two nozzle lengths) covered in the aforementioned preliminary study and the large effect of nozzle configuration reported therein, it was considered worthwhile to extend the scope of that investigation.

In this paper the effects of a number of variables on entrainment rate of turbulent air jets issuing from square-edged inlet nozzles are presented. The air temperature at the nozzle exit was essentially the same as that of the entrained laboratory air and neither varied by more than 1°C during an experiment. Five different nozzles and two values of upstream contraction of the nozzle were tested. The jet Reynolds number was varied between 6000 and 42,000, while the range of axial locations extended from the nozzle exit to about 24 jet hole diameters.

Experimental Apparatus and Procedures

The apparatus was essentially the same as that described in detail in the papers referred to in the previous section. It consisted basically of a blower which delivered room temperature air through a calibrated rotameter and through interchangeable plenum chamber and nozzle plates. Internal diameter for the three type 'a' nozzles was 19.05 mm while that for the two type 'b' was 12.7 mm. All nozzles had inlet and exit sections that were square-edged. Sketches of the plenum and nozzle blocks are given in Fig. 1: the 'a' plenum was cylindrical with a length and diameter of 0.46 and 0.102 m, respectively while the other was of a square cross-section, 0.254 m inside and 0.28 m long. In addition to the differences in plenum and jet hole dimensions, an important feature of the present design is the presence of a flanged section, structurally an extension of the nozzle plate, at the jet exit of all but the two type 'a' long tubes (Fig. 1).

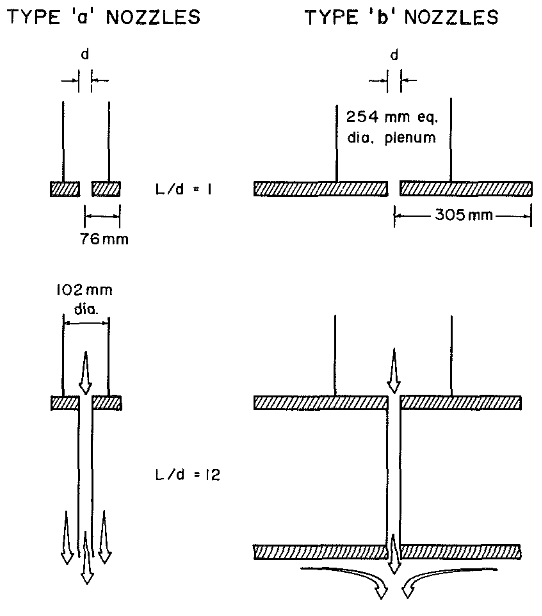

Fig. 1

Velocities were calculated from readings made with a 1.7 mm diameter cylindrical Pitot-static tube. The traversing mechanism was the same as described in Obot et al. (1984) and hence will not be repeated here. The Pitot-static tube was connected to a Statham unbonded strain gauge differential pressure transducer having a range of ±1 kPa (±0.15 psi). The output was recorded on a Hewlett Packard 3466A digital voltmeter, the smallest digit of which was 1 μV. For Reynolds number larger than 22,000, the dynamic head was measured using a Wihl-Lambrecht 655 micromanometer having various inclinations. The working fluids for the micromanometer had values of specific gravity of 0.82 and 1.0. This unit, which gives direct readings in Pascals, could be read with the help of a vernier scale to as low as 0.1 Pa with 1:2 inclination, the resolution being much lower for other inclinations.

For most axial locations, measurement of axial velocity covered both halves of the jet: the fine resolution provided by the recorders permitted accurate determination of the jet axis which was taken to coincide with the location of maximum dynamic head. Radial distances were measured in increments

Nomenclature

A = nozzle area, m^2
d = nozzle diameter, m
f = forcing frequency, Hz
$K = 2\pi\int_0^\infty \rho\, U^2 r dr$, integral of momentum
L = nozzle length, m
m = mass flow rate, kg/s
Re = Reynolds number, $m_{j0}d/A\mu$
r = radial distance from jet axis, m
$r_{0.1}$ = distance from jet axis to location where $U = 0.1U_0$, m
St = Strouhal number, fd/U_{j0}
U = local mean velocity, m/s
u = R. M. S. value of fluctuating component of velocity, m/s
X = nondimensional distance, r/d
z = axial distance from nozzle, m
$\bar{Z}$ = nondimensional axial distance, z/d
μ = fluid viscosity, Pa s
ρ = fluid density, kg/m^3
ψ = nondimensional entrainment

Subscripts

e = entrained fluid
$j0$ = centerline or average value at nozzle exit
0 = centerline value downstream from nozzle
∞ = value at ambient condition

Downloaded 02 Jun 2010 to 171.66.16.66. Redistribution subject to ASME license or copyright; see http://www.asme.org/terms/Terms_Use.cfm

ranging from 0.5 to 2 mm, depending of course on the axial location, as this provided quite detailed profiles from which data for entrainment and momentum were computed by numerical integration using Simpson's rule.

A very important comment concerns the format used in calculation of the results. The approach adopted in all of our calculations was to evaluate the integrals for the region bounded by $r=0$ and $r=r_{0.1}$, where $U(r_{0.1})=0.1U_0$. This arbitrary procedure minimizes the effect of unreliable velocity data near the jet boundaries and provides a consistent basis for comparison of results that were obtained with different nozzle configurations. It should also be mentioned that fairing the profiles to zero before integration gives results that are not significantly different from those determined using the $r_{0.1}$ arbitrary limit. The interested reader can refer to the discussion of our results (Obot et al., 1984; 1986).

Concerning uncertainties in measured velocities, it is pertinent to note that the instrumentation was designed to permit very reliable measurement of the dynamic head of the jet. The worst possible error for velocity measurements was estimated to be ±0.25 m/s. Since any particular profile for velocity, with its maximum value at the jet axis, drops off with increasing distance from the axis, it is inevitable that the largest errors in velocities occur in the vicinity of the jet periphery, regardless of the measurement technique. This knowledge was one of the underlying reasons for the choice of $r_{0.1}$. Also, although the Pitot-static tube readings are affected by the high turbulence levels in jets generated with square-edged inlet nozzles, the magnitudes of this effect are indeterminate because of lack of quantitative data on jet turbulence for similar nozzles. This obvious shortcoming, a general reflection upon the use of Pitot-static tubes in highly turbulent flows, does not detract from the usefulness of the present results; and that is, they demonstrate that entrainment rate depends to a marked degree on the nozzle details.

It should also be mentioned that the numerically calculated values of mass flow rate were checked against those determined by the rather time consuming graphical technique; the differences between the two sets of results being, on an average basis, no more than 3 percent. For example, for $L/d=1$ ($d=19.05$ mm) and $\mathrm{Re}=20{,}360$, the ψ values determined numerically for $\bar{Z}=4$, 6, 8, 12, 16, 20 and 24 were 1.0, 1.44, 2.0, 3.23, 3.83, 5.09, and 5.93 successively, which may be compared with the graphically deduced values of (in the same order) 1.03, 1.47, 1.90, 3.23, 3.80, 5.10, and 5.90. In terms of ψ, the present results for $\mathrm{Re}=6{,}500$ and $\mathrm{Re}>12{,}000$ are reproducible within 7 and 4 percent, respectively. The basis for this statement will be considered during subsequent presentation of entrainment results.

Results and Discussion

Results for entrainment are presented in Figs. 2–7 where, in each case, ψ is plotted against the nondimensional location $\bar{Z}$. In the first three figures results are shown for $L/d=1$, 5 and 12: also included in each are the calculated values of momentum ratio (K/K_0) from which it can be inferred that the basic requirement of a constant momentum flux at consecutive cross-sections is approximately satisfied. For the 'a' nozzles the effects of Re and L/d are displayed on Figs. 5 and 6, respectively. Comparison of the present results with some of the published data is given in Fig. 7. The differences in Re between the 'a' and 'b' nozzles arose naturally from the requirement that the exit momentum remains about the same. This condition was invoked with the objective of suppressing residual effects of nozzle diameter. The effects of these nozzle geometric details on velocity profiles, centerline velocity decay and spreading characteristics are contained in the paper from which this work was drawn (Trabold et al., 1985), while the corresponding effects on free jet heat transfer are documented in a recent publication (Obot et al., 1986).

Prior to discussion of the results, an important comment concerns the reproducibility of the data reported herein. In this connection it is important to note that, during the course of this work, more than seventy-five percent of the results on Figs. 2 through 6 were repeated at least once. Since the results for these replicate runs were, for the most part, indistinguishable from the original data, such data are shown only for locations where differences are discernible. Also, because of the large amount of information included on each plot, indicating the actual number of experimental points associated with each data point would have resulted in highly complex graphical presentations that would confuse rather than clarify the trends and, hence, was considered unnecessary. The limits of reproducibility given in the previous section were determined from these replicate experiments, as this was clearly more reliable than the alternative method which would involve use of the estimated uncertainty on measured velocities.

Another comment deals with the momentum ratios (K/K_0) which are shown on Figs. 2–4. It will there be observed that, whereas Fig. 2 indicates a mean value of nearly unity, the ratios for the long tubes (Figs. 3 and 4) are slightly greater than one, at variance with the expected gradual decreasing trend with axial location. For any downstream location, the difference in K between that calculated using the $r_{0.1}$ limit and fairing the profile to zero did not exceed 2 percent, validating the use of this arbitrary limit for computation of m or K. However, countering this resolution was the fact that the nozzle exit mass flow rates determined by integration of the profiles were about 3–6 percent lower than those deduced from the calibrated rotameter (Obot et al., 1986), the latter being the basis for the Reynolds number calculations. This resulted in K_0 values that were also lower than those determined from the rotameter data by 4–12 percent, the lower and larger percentage deviations being associated with short and long nozzles respectively; as the latter were characterized by fuller shapes for exit profiles. It is quite clear that, if values of K_0 were determined from the rotameter data, the general trend would be one of nearly constant values that are slightly lower than one, in line with the observations of Schneider (1985). This was not done because the resolution in m_{j0} was quite satisfactory combined with the fact that precise knowledge of momentum ratio was of little practical significance for the present application.

Examination of Figs. 2–7 reveals linear and nonlinear variation of ψ with $\bar{Z}$ depending, of course, on the conditions at the moment of discharge. For $L/d=1$, it can be seen from Fig. 2 that, for either plenum geometry, the entrainment rate is essentially the same in both the initial and fully developed regions of the jet for a given Re. This is clearly a unique feature of jets having relatively short lengths for the potential core zone and will be explored in detail later. Consistent with the trend for centerline velocity decay, use of a small cylindrical plenum reduces the mass flow rate at downstream locations and, hence, the rate of entrainment. Also, it will be observed that the absolute effect of Re, a consequence of the difference in plenum geometry, is larger for the 'a' than the 'b' configuration. The Re dependence is of course consistent with the trend for velocity distribution (Trabold et al., 1985). It should, however, be noted that in both cases the nozzle block extended beyond the plenum cross-section. Although the dimensions of the extended surface were unequal (Fig. 1), this is clearly not responsible for the trends in Fig. 2 because the streamlines for the entrained surrounding fluid are approximately similar in both cases, at least for the first two diameters.

The claim in the preceding paragraph that the dominant

Downloaded 02 Jun 2010 to 171.66.16.66. Redistribution subject to ASME license or copyright; see http://www.asme.org/terms/Terms_Use.cfm

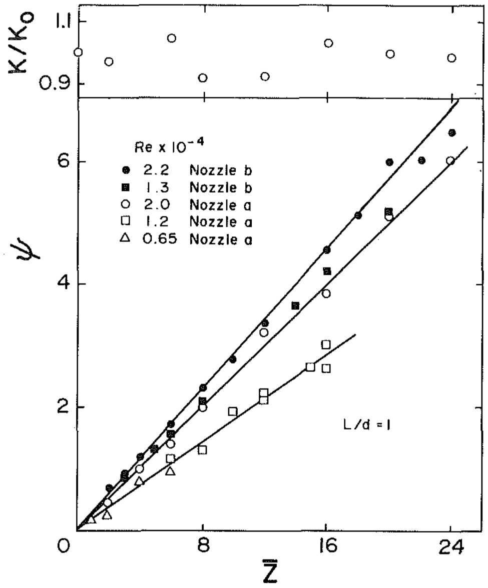

Fig. 2

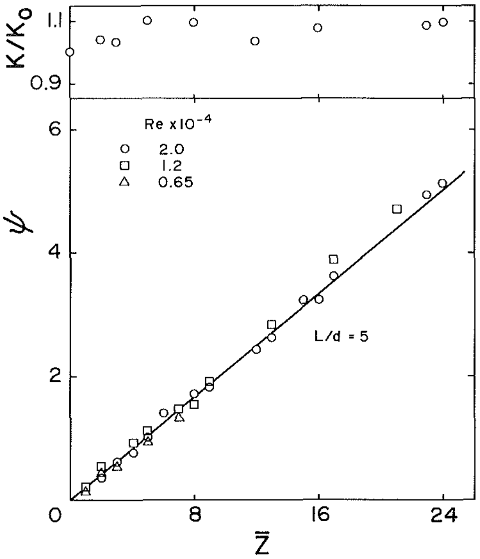

Fig. 3

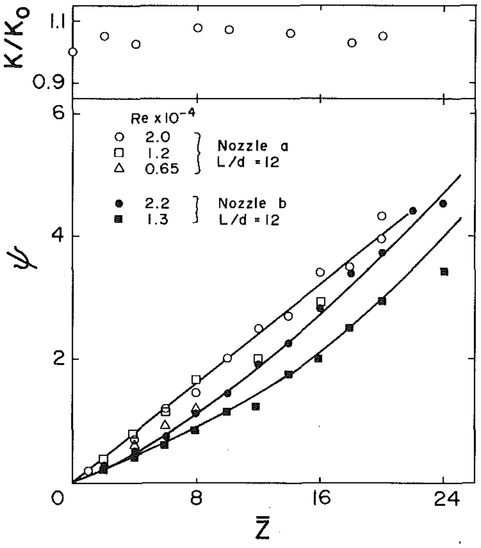

Fig. 4

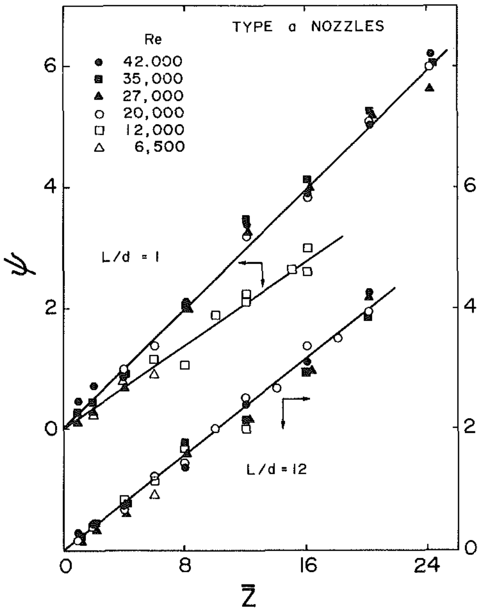

Fig. 5

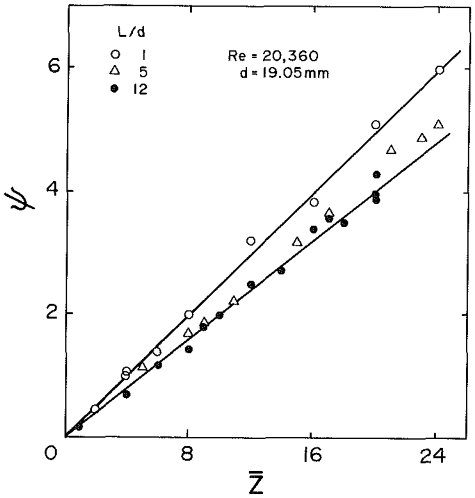

Fig. 6

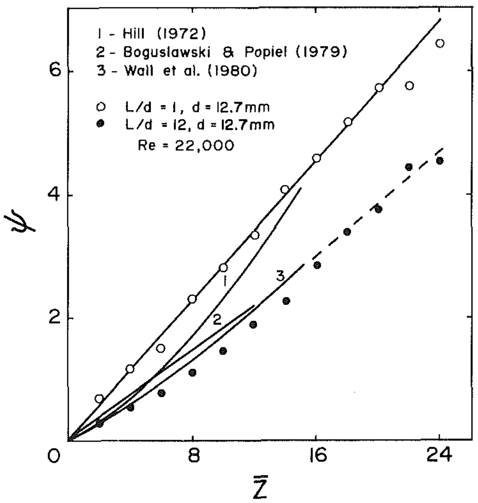

Fig. 7

Downloaded 02 Jun 2010 to 171.66.16.66. Redistribution subject to ASME license or copyright; see http://www.asme.org/terms/Terms_Use.cfm

feature is the plenum geometry (or contraction ratio) and not the difference in the relative sizes of the flanged section requires further elaboration. First, for a given Re, nozzle inlet geometry and for relatively short nozzles, it is well known that the boundary layer thickness at the nozzle exit and the maximum turbulence intensity in the vicinity of the nozzle walls, both of which affect the initial jet development, depend on the contraction ratio (Bradshaw, 1966; Hill et al., 1976; Crow and Champagne, 1971; to mention but a few). For mean velocity, the exit profiles measured 3 mm upstream of the nozzle exit provided confirmation of this observation. Second, numerical solutions of the complete Navier-Stokes equations for Re up to 1960 indicated that, although fluid entrainment was reduced with a 2.5d flanged section, changing this diameter from 7.9d to 15d did not alter the positions of the free streamline (Saad, 1975). Third, in a related study (Bakke, 1957), a flanged section of about the same relative dimension as the 'a' arrangement was used to prevent generation of large scale disturbances at the nozzle exit. Since the effect of having an extended wall at the nozzle exit is to reduce the initial rate of entrainment, it would seem then that this may be accomplished with a diameter of about 4d - 8d. A precise value for the required diameter must await results of subsequent experiments.

The Re effect noted earlier for the $L/d=1$ ('a') nozzle can be seen more clearly in Fig. 5, where results are presented for six values of Re. The straightforward conclusion is that ψ is essentially independent of Reynolds number for Re>20,000. This observation is equally valid for the type 'b' ($L/d=1$) nozzle configuration. Also, there are indications that the differences between the 'a' and 'b' results are significant only for Re<20,000.

If comparisons are made from figure to figure among Figs. 2–6, it may be observed that, although the 'a' nozzle results for $L/d=5$ and 12 are very close, a consistent trend is that jets issuing from long tubes entrain comparatively less surrounding fluid. Also, it may be noted that, relative to the $L/d=1$ results, the absolute effect of nozzle length is larger for the type 'b' than for the 'a' configuration. This observation, which can be seen more clearly in Figs. 6 and 7, may be explained as follows. Unlike relatively short nozzles which are susceptible to changes in upstream contraction, such entrance effects are almost damped out for long tubes (Obot et al., 1979) and entrainment rate depends on whether there is a flanged section at the jet exit. For the long 'a' nozzles, entrainment takes place with the streamlines of the surrounding flow field almost parallel to the jet axis (Fig. 1). This results in immediate entrainment of the stagnant fluid above the nozzle exit plane. On the other hand, with the confining surface, the streamlines for the entrained fluid change sharply from parallel to the flanged plate to parallel to the jet axis, since the entrained fluid must flow past almost the entire width of the flanged surface before it is absorbed by the jet. In other words, immediately after discharge, the effect of the flanged section is exactly the opposite of that noted above in that it restricts entrainment of the fluid above the nozzle exit plane. Consequently, for comparable nozzle exit momentum or Reynolds number, entrainment in the initial region is higher for the 'a' than 'b' nozzles.

Another important difference between flanged and unflanged exit conditions concerns the variation of ψ with $\bar{Z}$. In the case of the latter, for which the absence of a flanged section favors generation of large scale disturbances in the initial region due to interaction and mixing of the jet with the fluid drawn in from above the nozzle exit plane, these detailed measurements show a linear variation for the $0<\bar{Z}<24$ region, in agreement with the trend reported for unconfined jets (Boguslawski and Popiel, 1979). It is especially noticeable that this linear trend occurs for all Re tested (Figs. 3–5). For $L/d=12$, the experimental data can be described by the linear relation:

$$\psi=0.2\bar{Z} \tag{5}$$

This equation, which also represents all data for $L/d=5$ with average error of no more than 5 percent, is not significantly different from that given in Table 1 for unconfined jets generated with a long tube of $L/d=50$. These differences of no more than 10 percent between our results and those of Boguslawski and Popiel provide support for an observation made in the introductory section of this paper, i.e., for long nozzles or tubes entrainment rate is less sensitive to changes in the L/d ratio. By contrast, Figs. 4 and 7 establish that, due to the reduction in entrainment for the initial region, a nonlinear variation of ψ with $\bar{Z}$ prevails for the $\bar{Z}<15$ region with a flanged exit. This is precisely the trend that has been reported by many researchers who used comparable exit geometry. Thus, two seemingly similar experimental facilities can yield linear or nonlinear variation for ψ depending on the details of the nozzle; specifically on the nature of the streamlines for the surrounding fluid at the moment of discharge.

It is also of some interest to compare the effect of Re for the two sets of long nozzles. In general, for either plenum geometry, the results are essentially independent of Re for $\bar{Z}<10$, and thereafter, are almost unaffected by Re for the 'a' nozzle (Fig. 5), but the influence of Re is more pronounced when the jet is partially confined (Fig. 4).

Comparison of the present data with the results of other investigators, some of which were discussed in the introductory section of this paper, is illustrated graphically in Fig. 7. The bases for the comparison are the results obtained with the 'b' nozzle configuration for Re = 22,000, as this geometry provides exit conditions that are comparable to those for the direct method. It is pertinent to note that, with the latter approach, the jet usually discharges into a chamber having porous side walls and an impermeable wall that is structurally an extension of the nozzle plate. Also, all but two (Taylor et al., 1951; Boguslawski and Popiel, 1979) of the studies summarized in Table 1 involved use of partially confined jets similar in design to our 'b' nozzles. For $L/d=12$, the present results are closely approximated by the correlation of Wall et al. for long tubes. Since this correlation is valid for Re>23,000, it may be inferred from this close agreement that there are negligible effects of Reynolds number for Re>22,000. Judging by the trend in this figure it appears that, at larger $\bar{Z}$, there should be almost no difference between the $L/d=1$ and convergent nozzle results. In this connection, it is useful to note that, for Re>22,000, the $L/d=1$ results are adequately represented by

$$\psi=0.313\ \bar{Z} \tag{6}$$

It should be emphasized that, for $L/d=1$, the entrainment coefficient depends on both the plenum geometry and Reynolds number. Support for the above observation for large $\bar{Z}$ comes from the previous results which show that, for $\bar{Z}>10$ and at a given Re, there are only small differences in centerline velocity and velocity fluctuations between the $L/d=1$ square-edged and a comparable convergent nozzle (Obot et al., 1979).

It is of interest to note that, despite the marked effect of entrance configuration on exit profiles for mean velocity and turbulence between the short square-edged and convergent nozzles, the initial development of turbulence is very similar for both nozzles: the axial velocity fluctuations rise quite appreciably to about the same maximum and, after confluence of the two profiles, fall off with axial distance, with very small quantitative differences between such results (Fig. 8). By contrast, when jets are discharged through long tubes, the axial velocity fluctuations and shear stress rise very slowly in the potential core region, suggesting that the mixing process is less

Downloaded 02 Jun 2010 to 171.66.16.66. Redistribution subject to ASME license or copyright; see http://www.asme.org/terms/Terms_Use.cfm

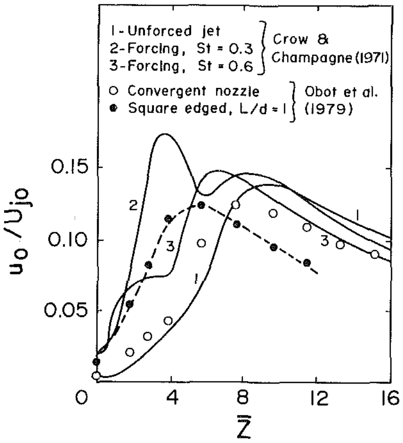

Fig. 8

intense than that for short convergent or sharp-edged inlet nozzles. Consequently, jets discharging from long tubes possess centerline velocities that are, even as far as 24 jet hole diameters downstream, about 20 percent higher than for relatively short nozzles and, hence, entrain much less fluid.

From the aforegoing presentation and discussion of results, it is clear that, in so far as entrainment is concerned, the entrance configuration is significant for the shortest nozzle and only for the $\bar{Z} < 10$ region. Although there is very little information on the structure of turbulence for jets generated with square-edged nozzles, an attempt will be made here to provide useful insight on the nature of such flows. Except for the difference in inlet geometry, the length of the present $L/d = 1$ nozzle is comparable to those of convergent nozzles used in previous studies, in particular that of Crow and Champagne (1971). The conjecture is that this inlet shape produces highly coherent motion similar to that due to periodic surging (or forcing) of the convergent nozzle jet, as in the study cited above. Since forcing reduces the potential core length, increases the rate of decay and enhances entrainment in the interval $\bar{Z} = 0$ and 6, it is not altogether surprising to note that the $\bar{Z} \geq 4$ results of Crow and Champagne for forcing under conditions $u_{j0}/U_{j0} = 2$ percent, St = 0.3 are effectively coincident with the $L/d = 1$ data of Fig. 7. Conceivably, with increasing forcing variables, conditions would eventually have been obtained for which the enhancement in entrainment would be such that a constant rate occurred in both the initial and fully developed regions of the jet.

To shed further light on the above discussion of the similarity in jet behavior between that generated with the square-edged nozzle and a nearly uniform jet which is subjected to periodic surging, relative centerline velocity fluctuations of Crow and Champagne for an unforced jet (curve 1), for forcing conditions $u_{j0}/U_{j0} = 2$ percent, St = 0.30 (i.e., $f = 185$ Hz, curve 2) and $u_{j0}/U_{j0} = 2$ percent, St = 0.6 (i.e., $f = 337$ Hz, curve 3), are reproduced here in Fig. 8. The Reynolds number in these experiments was held near 10^5. Also included in Fig. 8, for purposes of comparison, are the Re = 80,000 results of Obot et al. (1979) for a convergent nozzle designed according to ASME standards (open circles) and a square-edged nozzle of $L/d = 1$ (dark circles). The U_{j0} values were 62.7 and 79.3 m/s, the higher being for the square-edged inlet nozzle. The fact that the contoured nozzle profile of Obot et al. does not rise to the same level as that of Crow and Champagne and the one jet hole diameter shift in the location of the maximum are attributed to the well known effects of nozzle diameter and upstream contraction.

Judged solely on the basis of Fig. 8, it appears that the turbulence characteristics for the square-edged nozzle jet are closely approximated by curve 3 for St = 0.6, at least for the $0 \leq \bar{Z} < 6$ region. Consistent with this observation, the results of Crow and Champagne (c.f. Fig. 23) show about a 2d reduction in potential core length beyond that for St = 0.3, similar to that documented for $L/d = 1$, and their centerline velocity decay profile for this forcing condition is almost indistinguishable from that presented in our paper for $L/d = 1$ (Trabold et al., 1985). Also, it can be seen in Fig. 8 that, in sharp contrast with the trend for unforced jets, the absolute magnitude of the centerline velocity fluctuations (since u_0 is normalized with respect to the constant nozzle exit centerline velocity) reach a maximum around $\bar{Z} = 5$, which is probably the location where the eddies also attain their maximum intensity. For reasons given previously for the case without forcing, there is also one diameter difference in the location of this peak between St = 0.6 and the sharp-edged inlet nozzle.

Although Crow and Champagne provided no entrainment data for St = 0.6, all of the above observations together with the St = 0.3 trend in their Fig. 29 suggest that a constant rate of entrainment would prevail in all flow regions for St = 0.6. It would seem then that one method for maintaining a constant entrainment rate for all regions of the flow is to cause a significant reduction in potential core length and, for relatively short nozzles, use of a square-edged inlet would suffice.

The most obvious conclusion that can be inferred from the above discussion amounts to this: a square-edged entry produces a jet with amplitude and frequency of oscillation that are considerably larger than those for conventional convergent nozzles. This results in a higher rate of decrease of velocity with increasing distance from the nozzle, very rapid spreading and entrainment, and in significant increase in turbulent intensity over the initial region of the flow.

Conclusion

An experimental investigation of the entrainment characteristics by turbulent round jets generated with square-edged inlet nozzles was made for the region extending from the nozzle exit to 24 jet hole diameters downstream. The parametric study which included the effects of nozzle length, Reynolds number and partial confinement also considered the influence of the geometric configuration of the jet plenum chamber.

The finding is that entrainment rate depends to a marked degree on nozzle details, the highest and lowest rate being associated with the relatively short and long nozzles, respectively. For any particular nozzle, entrainment rate is essentially independent of Reynolds number in the initial region, but moderate Reynolds number effect is in evidence in the fully developed region.

The use of two contrasting geometries for the jet plenum produces mild effect on velocity decay and on entrainment for the shorter nozzle. The presence of a flanged secton at the nozzle exit lowers entrainment in the initial region of the jet.

References

Albertson, M. L., Dai, V. B., Jenson, R. A., and Rouse, H., 1950, "Diffusion of Submerged Jets," *Trans. ASCE*, Vol. 115, pp. 639–697.

Bakke, P., 1957, "An Experimental Investigation of a Wall Jet," *J. Fluid Mech.*, Vol. 2, pp. 462–472.

Boguslawski, L., and Popiel, Cz. O., 1979, "Flow Structure of the Free Round Turbulent Jet in the Initial Region," *J. Fluid Mech.*, Vol. 90, pp. 531–539.

Bradshaw, P., 1966, "The Effect of Initial Conditions on the Development of a Free Shear Layer," *J. Fluid Mech.*, Vol. 26, pp. 225–236.

Crow, S. C., and Champagne, F. H., 1971, "Orderly Structure in Jet Turbulence," *J. Fluid Mech.*, Vol. 48, pp. 547–591.

Hill, B. J., 1972, "Measurement of Local Entrainment Rate in the Initial Region of Axisymmetric Turbulent Air Jets," *J. Fluid Mech.*, Vol. 51, pp. 773–779.

Downloaded 02 Jun 2010 to 171.66.16.66. Redistribution subject to ASME license or copyright; see http://www.asme.org/terms/Terms_Use.cfm

Hill, W. G., Jenkins, R. C., and Gilbert, B. L., 1976, "Effects of the Initial Boundary-Layer State on Turbulent Jet Mixing," *AIAA Journal*, Vol. 14, pp. 513-514.

Kleis, S. J., and Foss, J. F., 1974, "The Effect of Exit Condition on the Development of an Axisymmetric Turbulent Free Jet," NASA Lewis Res. Center, Third Year Tech. Report, Grant NGR 23-004-068.

Obot, N. T., Trabold, T. A., Graska, M. L., and Gandhi, F., 1986, "Velocity and Temperature Fields in Turbulent Air Jets Issuing From Sharp-Edged Inlet Round Nozzles," *Ind. Eng. Chem. Fundam.*, Vol. 25, pp. 425-433.

Obot, N. T., Graska, M. L., and Trabold, T. A., 1984, "The Near Field Behavior of Round Jets at Moderate Reynolds Numbers," *Can. J. Chem. Eng.*, Vol. 62, pp. 587-593.

Obot, N. T., Mujumdar, A. S., and Douglas, W. J. M, 1979, "The Effects of Nozzle Geometry on Impingement Heat Transfer Under a Round Turbulent Jet," ASME Paper 79-WA/HT-53.

Ricou, F. P., and Spalding, D. B., 1961, "Measurements of Entrainment by Axisymmetric Turbulent Jets," *J. Fluid Mech.*, Vol. 11, pp. 21-32.

Saad, N. R., 1975, "Simulation of Flow and Heat Transfer under a Laminar Impinging Round Jet," M. Eng. thesis, McGill University, Montreal, Canada.

Schneider, W., 1985, "Decay of Momentum Flux in Submerged Jets," *J. Fluid Mech.*, Vol. 154, pp. 91-110.

Sforza, P. M., and Mons, R. F., 1978, "Mass, Momentum, and Energy Transport in Turbulent Free Jets," *Int. J. Heat Mass Transfer*, Vol. 21, pp. 371-384.

Taylor, J. F., Grimmett, H. L., and Comings, E. W., 1951, "Isothermal Free Jets of Air Mixing With Air," *Chem. Eng. Prog.*, Vol. 47, pp. 175-180.

Trabold, T. A., Esen, E. B., and Obot, N. T., 1985, "Entrainment by Turbulent Jets Issuing from Sharp-Edged Inlet Round Nozzles," Jets and Cavities - International Symposium, J. H. Kim et al., ed., American Society of Mechanical Engineers, New York, N.Y., FED-Vol. 32, pp. 101-109.

Wall, T. F., Nguyen, H., Subramanian, V., Mai-Viet, T., and Howley, P., 1980, "Direct Measurements of the Entrainment by Single and Double Concentric Jets in the Regions of Transition and Flow Establishment," *Trans. Inst. Chem. Eng.*, Vol. 58, pp. 237-241.

Downloaded 02 Jun 2010 to 171.66.16.66. Redistribution subject to ASME license or copyright; see http://www.asme.org/terms/Terms_Use.cfm

Steady Flow Structures and Pressure Drops in Wavy-Walled Tubes

M. E. Ralph
Post-Doctoral Research Assistant,
Department of Applied Mathematics
and Theoretical Physics,
University of Cambridge,
Cambridge, CB3 9EW, England

Solutions of the Navier-Stokes equations for steady axisymmetric flows in tubes with sinusoidal walls were obtained numerically, for Reynolds numbers (based on the tube radius and mean velocity at a constriction) up to 500, and for varying depth and wavelength of the wall perturbations. Results for the highest Reynolds numbers showed features suggestive of the boundary layer theory of Smith [23]. In the other Reynolds number limit, it has been found that creeping flow solutions can exhibit flow reversal if the perturbation depth is large enough. Experimentally measured pressure drops for a particular tube geometry were in agreement with computed predictions up to a Reynolds number of about 300, where transitional effects began to disturb the experiments. The dimensionless mean pressure gradient was found to decrease with increasing Reynolds number, although the rate of decrease was less rapid than in a straight-walled tube. Numerical results showed that the mean pressure gradient decreases as both the perturbation wavelength and depth increase, with the higher Reynolds number flows tending to be more influenced by the wavelength and the lower Reynolds number flows more affected by the depth.

1 Introduction

A number of problems has motivated the study of viscous flows in periodically constricted ducts. After Petersen modelled a porous medium as a set of wavy-walled tubes in parallel, in order to predict porous diffusion rates [1], several authors have used similar models to obtain relationships between pressure drops and flow rates. The results have usually been obtained experimentally or by numerical solution of the Stokes or Navier-Stokes equations [2–10]. Other workers have aimed to model physiological or biomedical flows, and although most studies with such applications have considered flow at an isolated constriction (as in [11] for example), a number have dealt with periodically-perturbed conduits. Sobey [12] modelled flows in furrowed membrane artificial lungs, while Savvides and Gerrard [13] were concerned with flows in arterial prostheses.

The present paper is concerned with axisymmetric flows in tubes with sinusoidal walls. Analytic solutions for this problem have been obtained [14–17], and while the value of these is undeniable, their range of applicability is necessarily limited by the restrictions of certain problem parameters to "small" or "large" values. Deiber and Schowalter's results [10] apply for sinusoidal wall perturbations of arbitrary magnitude although these were obtained using a highly novel numerical technique which was only verified experimentally for a mildly perturbed tube. The results of other workers who have considered different wall shapes may be expected to have some qualitative relevance, but the effects of geometry on the pressure drop have been the subject of some controversy (see [4]–[6], for example). The present work attempts to clarify these effects, as well as to give new insight into the problem of wavy-walled tube flow, with more attention focused on the underlying physical processes.

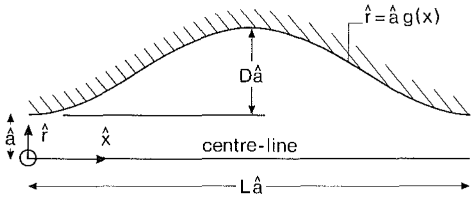

Fig. 1 The geometry of a single wavelength of the wavy-walled tube

2 Mathematical Formulation and Numerical Solution Methods

2.1 Formulation. The problem has been formulated in order to be solved by time-marching solutions from an initial state with zero velocity everywhere, and further details of the solution method are given in Ralph [18]. The axial and radial coordinates are $\hat{a}(x, r)$ (see Fig. 1), the corresponding velocity components are $\hat{U}_0(u, v)$ and the time from the initial state, density, pressure and kinematic viscosity are $\hat{T}t$, $\hat{\rho}$, $\hat{\rho}\,\hat{U}_0^2 p$, and $\hat{\nu}$, respectively. $\hat{T}$ is the time scale for the increase of the flow rate to its final value $\hat{Q}_0$, and $\hat{U}_0$ is given by

$$\hat{U}_0=\hat{Q}_0/\pi\hat{a}^2. \tag{1}$$

The instantaneous flow rate $\hat{Q}$ varies as

Contributed by the Fluids Engineering Division for publication in the JOURNAL OF FLUIDS ENGINEERING. Manuscript received by the Fluids Engineering Division August 8, 1986.

Copyright © 1987 by ASME

Downloaded 02 Jun 2010 to 171.66.16.66. Redistribution subject to ASME license or copyright; see http://www.asme.org/terms/Terms_Use.cfm

$$\hat{Q}=\hat{Q}_0 \sin 2\pi t \qquad t \leq 1/4 \tag{2a}$$

$$\hat{Q}=\hat{Q}_0 \qquad t \geq 1/4. \tag{2b}$$

Two dimensionless parameters arise when the governing equations, the Navier-Stokes equations for axisymmetric flow with zero swirl, are expressed in dimensionless form: these are a Strouhal number, St, defined by

$$\mathrm{St}=\frac{\hat{a}\hat{f}}{\hat{U}_0} \tag{3}$$

and a frequency parameter, α^2, defined by

$$\alpha^2=\frac{\hat{a}^2\hat{f}}{\hat{\nu}}. \tag{4}$$

The steady-state solution does not depend on St and α^2 independently but on their ratio $\alpha^2/\mathrm{St} = \hat{U}_0\hat{a}/\hat{\nu}$, which represents a Reynolds number and will be denoted by Re.

Following a standard procedure in computational fluid dynamics (see [19], for example), the stream function ψ is defined by

$$u=\frac{1}{r}\frac{\partial\psi}{\partial r} \tag{5a}$$

$$v=-\frac{1}{r}\frac{\partial\psi}{\partial x} \tag{5b}$$

and the vorticity, ζ, by

$$\zeta=\frac{\partial v}{\partial x}-\frac{\partial u}{\partial r}. \tag{6}$$

The problem then reduces to the solution of a vorticity transport equation and a Poisson equation for the stream function. Before a solution is attempted, however, a Prandtl-type transformation of the flow field is made, as in Sobey [12], which greatly simplifies application of the boundary conditions. We put

$$z=\frac{r}{g(x)} \tag{7}$$

where $g(x)$ is a function representing the shape of the wall (see Fig. 1). $g(x)$ is of the form

$$g(x)=1+\frac{D}{2}\left[1-\cos\frac{2\pi x}{L}\right] \tag{8}$$

with the variable parameters D and L representing the hollow depth and wall wavelength, respectively. The coordinates are further transformed by defining

$$y=z^2 \tag{9}$$

so that for equal increments in y, the z and r increments are smaller near the wall than near the tube axis. Numerical experiments showed that the calculated pressure drop converged more rapidly with decreasing mesh size when this second transformation was incorporated than when it was omitted.

The final system of governing equations is as follows.

$$\frac{\partial\zeta}{\partial t}=-\frac{1}{\mathrm{St}}\left\{u\frac{\partial\zeta}{\partial x}+2\left[y\left(\frac{h'}{h}\right)u+h\,y^{1/2}v\right]\frac{\partial\zeta}{\partial y}-\frac{h}{y^{1/2}}v\zeta\right\}$$

$$+\frac{1}{\alpha^2}\left\{\nabla^2\zeta-\frac{h^2}{y}\zeta\right\} \tag{10}$$

and

$$\nabla^2\psi=4h^2\frac{\partial\psi}{\partial y}-\frac{y^{1/2}}{h}\zeta, \tag{11}$$

where a prime denotes differentiation with respect to x, $h(x)$ is defined by

$$h(x)=\frac{1}{g(x)}, \tag{12}$$

$$\nabla^2\equiv\frac{\partial^2}{\partial x^2}+4y\left(\frac{h'}{h}\right)\frac{\partial^2}{\partial x\partial y}+4y\left[y\left(\frac{h'}{h}\right)^2+h^2\right]\frac{\partial^2}{\partial y^2}$$

$$+\left[4h^2+4y\left(\frac{h'}{h}\right)^2+2y\left(\frac{h'}{h}\right)'\right]\frac{\partial}{\partial y}, \tag{13}$$

and u and v are given by

$$u=2\,h^2\frac{\partial\psi}{\partial y} \tag{14}$$

and

$$v=-\frac{h}{y^{1/2}}\left[\frac{\partial\psi}{\partial x}+2y\left(\frac{h'}{h}\right)\frac{\partial\psi}{\partial y}\right]. \tag{15}$$

The boundary conditions are

$$\psi|_{y=0}=0 \tag{16}$$

$$\psi|_{y=1}=1/2\sin 2\pi t \qquad t\leq\frac{1}{4} \tag{17a}$$

$$\psi|_{y=1}=1/2 \qquad t\geq\frac{1}{4} \tag{17b}$$

$$\zeta|_{y=0}=0 \tag{18}$$

$$\zeta|_{y=1}=-4h\left[h^2+\left(\frac{h'}{h}\right)^2\right]\frac{\partial^2\psi}{\partial y^2}\bigg|_{y=1} \tag{19}$$

Nomenclature

Symbols with "^" are dimensioned, others are dimensionless.

$\hat{a}$ = radius of minimum tube cross-section
D = depth of wall perturbations
$\hat{f}$ = frequency characterising the start-up time in the computations
$g(x)$ = function describing the wall shape
$h(x)$ = $1/g(x)$
L = wavelength of wall perturbations
p = pressure
$\hat{Q},\hat{Q}_0$ = instantaneous and steady volumetric flow rate
r = radial coordinate
Re = a Reynolds number, $\hat{U}_0\hat{a}/\hat{\nu}$
Re_s = critical Reynolds number for separation
St = a Strouhal number, $\hat{a}\hat{f}/\hat{U}_0$
t = time
$\hat{T}$ = characteristic start-up time in the computations
u = axial velocity component
$\hat{U}_0$ = characteristic velocity, $\hat{Q}_0/(\pi\hat{a}^2)$
v = radial velocity component
x = axial coordinate
y = transformed radial coordinate, z^2
z = transformed radial coordinate, $r/g(x)$
α^2 = a frequency parameter, $\hat{a}^2\hat{f}/\hat{\nu}$
Δp_L = pressure drop per wall wavelength
ζ = vorticity
$\hat{\nu}$ = kinematic viscosity
$\hat{\rho}$ = fluid density
ψ = stream function
$\psi_{\max}$ = maximum value of the stream function
ψ_w = value of stream function at the wall

Downloaded 02 Jun 2010 to 171.66.16.66. Redistribution subject to ASME license or copyright; see http://www.asme.org/terms/Terms_Use.cfm

$$\psi|_{x=x_0+L} = \psi|_{x=x_0} \tag{20}$$

and

$$\zeta|_{x=x_0+L} = \zeta|_{x=x_0} \tag{21}$$

where x_0 denotes an arbitrary axial position. Equations (20) and (21) represent conditions of periodicity, it being assumed that the flow has the same axial wavelength, L, as the wall, so that solutions are only valid at some distance from the ends of the tube. Entrance effects on the pressure drop are discussed in Section 3.

Finally, if the axisymmetric Navier-Stokes equations are transformed using (7) and (9), and the pressure gradient with respect to y eliminated between them, we obtain

$$\left.\frac{\partial p}{\partial x}\right|_{y=1} = -\frac{1}{\mathrm{Re}}\left\{h\zeta + 2\left[h + \frac{1}{h}\left(\frac{h'}{h}\right)^2\right]\frac{\partial \zeta}{\partial y} + \frac{1}{h}\left(\frac{h'}{h}\right)\frac{\partial \zeta}{\partial x}\right\}_{y=1} \tag{22}$$

This equation gives the axial pressure gradient at the wall in terms of the vorticity field, and can be integrated numerically to give the reduction in pressure between any two points on the wall. If the axial separation of these points is L, the pressure drop will be denoted by Δp_L, which, because of the axial periodicity of the radial pressure gradient, represents the pressure drop per wall wavelength for all axial stations.

2.2 Numerical Solution. The above problem was represented in finite difference form and a standard time-marching solution strategy adopted, as described in [19], for example. The stream function equation (11) was represented by central (second order) differences and the resulting finite difference equation was solved at each time step by successive over-relaxation. The vorticity at the wall was computed from a one-sided finite difference form of equation (19), and then centred-time, centred-space differences, with the Dufort-Frankel substitution, were used in the vorticity transport equation to update the vorticity at internal points. These techniques are very similar to those used in [13, 20, 21], for example, where more detailed descriptions can be found.

The results given below were obtained using a mesh with 40 axial and 16 radial increments (41 × 17 nodes). However, in order to assess the accuracy of these computations, additional results were obtained using either 31 × 13 nodes (for Reynolds numbers less than 100) or 61 × 25 nodes (for Reynolds numbers of 100 or greater), and quadratic Richardson extrapolation used to obtain values accurate to fourth order. The differences between the fourth order values and those obtained on the 41 × 17 mesh were taken to be measures of the uncertainty of the results presented.

The Strouhal number was arbitrarily set to a value of 0.01. The size of the time step was determined by stability considerations, and values used were in the range $5 \times 10^{-4} - 1 \times 10^{-3}$. Finally, the dimensionless time required for the establishment of steady flow was between 0.5 and 3, depending on the Reynolds number.

3 Experimental Measurement of Pressure Drops

A test section was constructed in two pieces, each formed by pressing a stainless steel male mould, with a minimum diameter of 2 mm, into heat-softened Perspex blocks. In order to guarantee uniformity of the cross sections of minimum area, the diameter of the constrictions was enlarged by 0.1 mm, using a long drill of 2.1 mm diameter, and hence the wall shape was not precisely sinusoidal, but contained very short straight sections at the constrictions. The dimensionless geometric parameters were $L = 10$ and $D = 2$ (to within about 5 percent). The effect of the imperfect wall shape was estimated numerically to lead to an uncertainty of about ±3 percent in the mean pressure gradient. The overall length of the model was 230 mm, with thirteen complete wavelengths and a 50 mm section of uniform 2 mm bore pipe at each end. Pressure tappings of 0.5 mm bore were drilled at the points of greatest cross-sectional area of the 2nd, 5th, 7th, 9th, and 12th wavelengths.

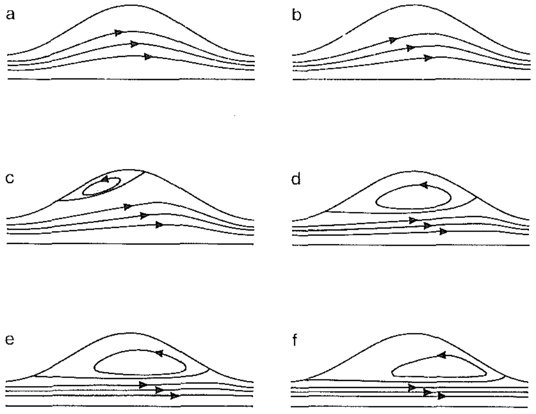

Fig. 2 Computed streamlines for flows in which the geometrical parameters are $L = 10$, $D = 2$: (*a*) Re = 5; (*b*) Re = 10; (*c*) Re = 15; (*d*) Re = 40; (*e*) Re = 100; (*f*) Re = 500. (Uncertainty in position of vortex center is ±0.3 in x and ±0.06 in r.)

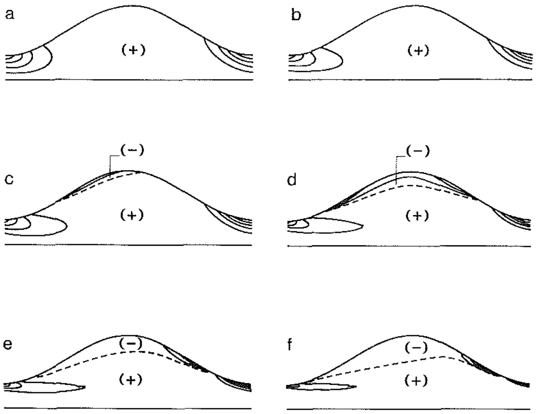

Fig. 3 Vorticity contour plots for flows in which the geometrical parameters are $L = 10$, $D = 2$: (*a*) Re = 5 ($\Delta\zeta_+ = 0.94$); (*b*) Re = 10 ($\Delta\zeta_+ = 1.02$); (*c*) Re = 15 ($\Delta\zeta_+ = 1.09$, $\Delta\zeta_- = -0.036$); (*d*) Re = 40 ($\Delta\zeta_+ = 1.36$, $\Delta\zeta_- = -0.091$); (*e*) Re = 100 ($\Delta\zeta_+ = 1.70$, $\Delta\zeta_- = -0.30$); (*f*) Re = 500 ($\Delta\zeta_+ = 2.38$, $\Delta\zeta_- = -0.63$). (Uncertainty in maximum value of vorticity is ±2 percent.)

Solutions of glycerol were used for the working fluid, and dynamic viscosities in the approximate range 1–50 centipoise were obtained. Viscosity was measured using a rotary viscometer (Brookfield Synchro-Lectric LVT model with UL adapter), and repeat measurements were made frequently during a series of experiments. Comparison of measured viscosities with tabulated values, for known concentrations under standard conditions, showed the measurements to be about 3 percent accurate.

An overhead reservoir and constant head tank supplied the flow, and flow straighteners and a contraction of 9:1 area reduction were incorporated upstream of the test-section. Flow rate was held constant by clamping a length of flexible tubing with a long clamp, and was measured by collecting, in a measured time, a sample of fluid in a graduated cylinder.

The pressure drops were determined by measuring the difference in the heights of columns of working fluid maintained above two pressure tappings. Typical differences in liquid level were 10–40 cm, with liquids of relative density 1.0–1.2.

Downloaded 02 Jun 2010 to 171.66.16.66. Redistribution subject to ASME license or copyright; see http://www.asme.org/terms/Terms_Use.cfm

Most pressure measurements were conducted using the pressure tappings at the 2nd and 12th hollows in order to maximise the difference in the liquid column heights. The error due to entrance effects was estimated, using the other pressure tappings, to be less than 3 percent for Reynolds numbers up to about 300, but rising to as large as 50 percent for Reynolds numbers of 1500. All the experimental pressure drop results given below were calculated from measurements made at the 2nd and 12th hollows, and thus reflect fully developed values only for Reynolds numbers up to 300.

4 Reynolds Number Effects on the Flow Structure

Figure 2 shows computed streamline plots for flows at various Reynolds numbers with geometrical parameters $L = 10$ and $D = 2$. These are qualitatively similar to the plots obtained by Sobey [12] for the analogous two-dimensional problem. At the lower Reynolds numbers [Figs. 2(*a*) and (*b*)], the flows are unseparated, although the effects of inertia are visible in Fig. 2(*b*) as streamlines are not symmetrical with respect to the flow direction. At a Reynolds number of about 12, separation occurs near the point of greatest rate of tube divergence. The separation region grows rapidly with Reynolds number at first [Figs. 2(*c*) and (*d*)], but then more slowly [Figs. 2(*e*) and (*f*)], as it becomes constrained by the size of the hollow.

Vorticity contour plots, for the same set of parameters as in Fig. 2, are given in Fig. 3. Zero vorticity contours are shown as dashed lines (but note that the voriticity is also zero on the axis), and the signs of the vorticity in adjacent regions are indicated on the figures. Magnitudes of contour increments are denoted by $\Delta\zeta_+$ and $\Delta\zeta_-$ in the positive and negative vorticity regions respectively. In every case vorticity is generated most rapidly at the tube contractions and is transported from there by the actions of convection and diffusion. At low Reynolds number, diffusion is predominant and there is a high rate of vorticity transport normal to the direction of flow, but as the Reynolds number increases, convection becomes more important, and the vorticity contours become increasingly aligned with the flow. Reversed flow then leads to the generation of negative vorticity [Figs. 3(*c*)-(*f*)]. The distribution of vorticity at the wall is of particular interest, and the present results have shown qualitative resemblance to those given in [12]. At all Reynolds numbers, the wall vorticity in each central quarter wavelength is about two orders of magnitude smaller than the peak value attained near the contractions, a rather larger difference than was found in the two-dimensional case [12]. As the Reynolds number increases, the vorticity peaks become taller and narrower and shift to positions just upstream of the points of minimum cross-sectional area. Accompanying the growth of each positive peak, a lesser negative peak develops upstream of the reattachment point, and an even smaller minimum is found downstream of the separation point. These phenomena, which have also been observed previously [12, 17], have not been adequately explained. Presumably, the flow near the reattachment point is like two-dimensional viscous stagnation point flow (see [22], for example), for which the similarity solution possesses a wall vorticity distribution antisymmetric about the reattachment point. In the present case, the minimum is less pronounced than the maximum because the analogy with stagnation point flow is not perfect. In particular, the incident "jet" is highly sheared, with fluid elements passing downstream of the reattachment point having greater velocities than those within the separation region.

Finally, velocity profiles are given in Fig. 4, showing axial and radial components at the points of minimum and maximum cross-sectional area. The axial profile at a contraction has a nearly parabolic form at low Reynolds number which becomes flattened near the axis as the Reynolds numbers increases. This is characteristic of an entry flow effect, which would be expected to increase in importance at higher Reynolds number. At the highest Reynolds number considered, however, the profile reverts to an approximately parabolic shape near the centre-line, with rapid velocity variation near the wall. Physically, this can be explained by arguing that at such high Reynolds numbers, the velocity profile does not have time to adjust to the larger flow area as it passes between constrictions and there is no separate entrance effect at each constriction. Some adjustment must take place near the wall, but otherwise the velocity profile has the shape appropriate to fully developed flow.

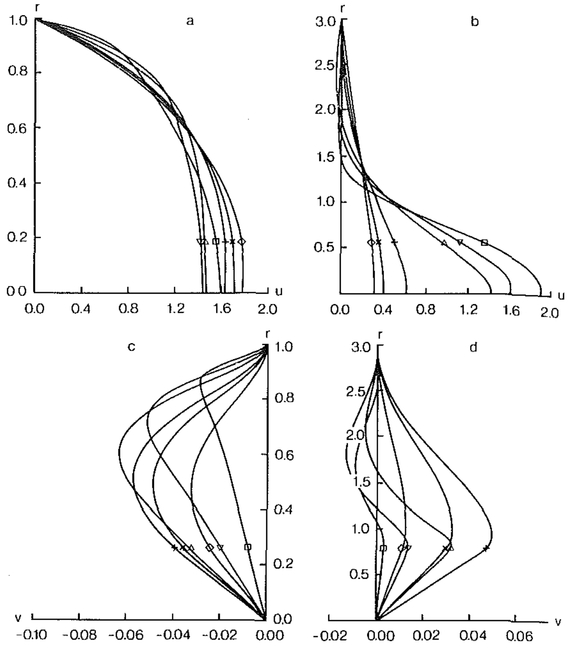

Fig. 4 Velocity profiles for flows in which the geometrical parameters are $L = 10$, $D = 2$: (*a*) axial component at a constriction; (*b*) axial component at an enlargement; (c) radial component at a constriction; (*d*) radial component at an enlargement. Re = 5 (◇); Re = 10 (×); Re = 15 (+); Re = 40 (△); Re = 100 (▽); Re = 500 (□). (Uncertainty in *u* is ±0.01; uncertainty in *v* is ±0.004.)

The axial velocity profiles at an enlargement show the development of a point of inflexion and the onset of reverse flow as the Reynolds number increases. The large difference in the magnitudes of the forward and backward velocities is striking. Because the flow is approximately parallel to the axis at the contractions and enlargements, the radial velocity profiles are plotted on a smaller scale than the axial profiles. An interesting trend shown in Figs. 4(*c*) and (*d*) is that the maximum radial velocity first increases and then decreases as the Reynolds number increases. At low Reynolds number, the flow is almost unaffected by inertia and the streamlines are nearly symmetrical with respect to the sense of the flow: perfect symmetry would imply zero radial velocity where the wall is parallel to the axis. At high Reynolds number on the other hand, inertia forces fluid particles to travel in straight lines, which results in nearly parallel flow except in the separation regions. Where neither of these effects is very strong, at intermediate values of the Reynolds number, the greatest radial velocity reaches a maximum.

5 Geometric and Interacting Reynolds Number Effects on Separation

Sobey [12] has shown that the boundary layer theory of

Downloaded 02 Jun 2010 to 171.66.16.66. Redistribution subject to ASME license or copyright; see http://www.asme.org/terms/Terms_Use.cfm

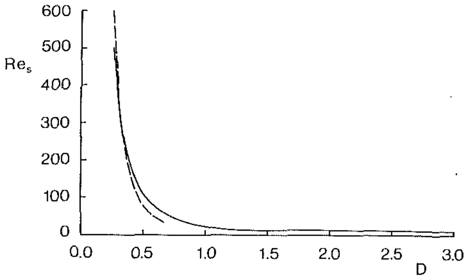

Fig. 5 Variation of the critical Reynolds number for separation with D (for L = 10). Solid curves denotes numerical results; dashed line represents equation (23). (Uncertainty in numerical value of Re_S is the greatest of ±0.5 and ±4 percent.)

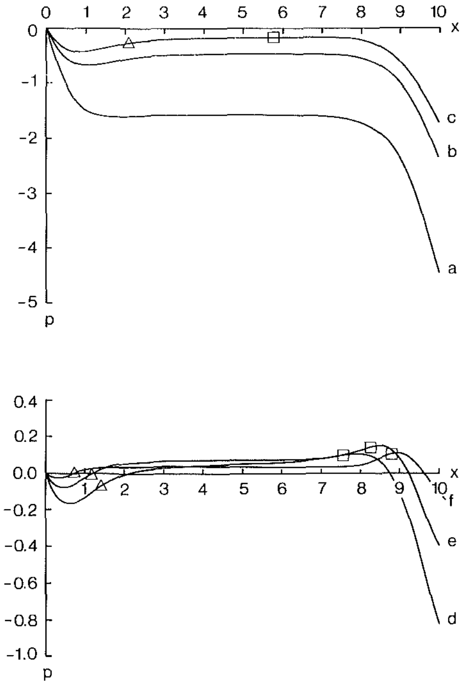

Fig. 6 Variation of the pressure at the wall with axial position: (L = 10, D = 2) (a) Re = 5; (b) Re = 10; (c) Re = 15; (d) Re = 40; (e) Re = 100; (f) Re = 500. Triangle and square symbols show positions of separation and reattachment where appropriate. (Uncertainty in p is ±0.5 in a–c, and ±0.01 in d–f. Uncertainty in x-coordinates of separation and reattachment points is ±0.04.)

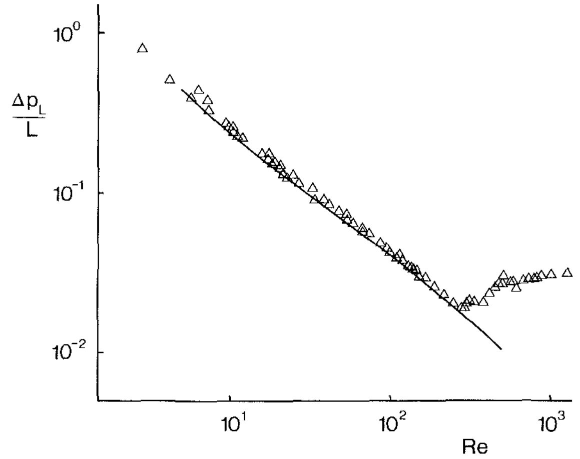

Fig. 7 Variation of the mean pressure gradient per wall wavelength of tube with Reynolds number (L = 10, D = 2). Solid curve represents numerical results; triangle symbols show experimental measurements. (Numerical uncertainty in $\Delta p_L/L$ is ±2 percent. Experimental uncertainty in $\Delta p_L/L$ is ±5 percent and in Re is ±3 percent.)

Smith [23] is applicable to flow in two-dimensional wavy-walled channels, provided that certain limitations on the parameters are obeyed. The results of this analysis apply to the axisymmetric case, if an appropriate length scale is chosen in defining the Reynolds number (the boundary layer thickness being assumed small compared with the tube radius). The boundary layer problem is governed by a single parameter, $\mathrm{Re}^{1/3} L^{-1/3} D$, and Sobey obtained that value which divided separated and unseparated flows. For the present problem this result becomes

$$\mathrm{Re}_s^{1/3} L^{-1/3} D \approx 1.0 \qquad (23)$$

where Re_s is the critical Reynolds number for separation. It is required that $D \ll 1$, $L \gg 1$ and $\mathrm{Re} \gg L$ for validity of the boundary layer solution.

In Fig. 5, critical Reynolds numbers obtained by numerical solution of the full Navier-Stokes equations (solid curve) are compared with those given by boundary layer theory (dashed curve) for a fixed wall wavelength, $L = 10$. The curves are seen to be in close agreement for values of D less than about 0.4. The extremely rapid (approximately inverse cubic) variation of Re_s with D for small D contrasts with the very slow rate of change for values of D greater than about 1.

Indeed, as the hollow depth increases, streamline plots for marginally separated flows show that separation is initiated near the tips of the hollows rather than in the rapidly diverging sections of the tube. This fact, and the weak Reynolds number dependence imply that inertial effects are not the cause of flow reversal in such cases, and numerical experiments in which the inertial terms have been set identically to zero have shown the existence of very weak recirculations. The vortex strength can be represented by $(\psi_{\max} - \psi_w)$, the difference between the maximum value of the stream function and its value at the wall, and in Stokes flow, with $L = 10$ and $D = 5$, $(\psi_{\max} - \psi_w)$ is of order 10^{-4}. By contrast, in the moderate Reynolds number flow of Fig. 2(e), in which $L = 10$, $D = 2$, and $\mathrm{Re} = 100$, the vortex strength is about 10^{-1}. Calculations on a number of refined meshes gave no indication that the Stokes flow vortex strength was tending to zero. Finally, we note that if the hollow is deep enough and the Reynolds number is fairly large, secondary separation may occur, as in the case with $L = 10$, $D = 4$, and $\mathrm{Re} = 200$, for example.

6 Pressure Drop Results

The calculated variation of the pressure at the wall is shown in Fig. 6, for tubes with geometry given by $L = 10$, and $D = 2$, for several Reynolds numbers. The arbitrary pressure datum is taken to be at $x = 0$ and the figure is split into two parts because of the widely-differing pressure drop magnitudes. In each case, the pressure gradient is much smaller where the bore is enlarged than at the constrictions, because the low velocities in the hollow (see Fig. 4) give rise both to low values of wall shear and small inertial pressure changes. Positive values of $\partial p/\partial x$ are expected in the separated regions where the wall vorticity is negative, but pressure recovery also occurs when $\mathrm{Re} = 10$, representing an unseparated flow, and upstream of the separation points in the separated flows. This is due to the inviscid pressure rise associated with flow deceleration in a diverging tube. At high enough Reynolds number, a pressure maximum is found near the reattachment point and both the viscous stagnation point flow solution and simple potential flow ideas would lead us to expect this.

For the same geometry, the variation with Reynolds number of the mean pressure gradient, $\Delta p_L/L$, is shown in Fig. 7. The

Downloaded 02 Jun 2010 to 171.66.16.66. Redistribution subject to ASME license or copyright; see http://www.asme.org/terms/Terms_Use.cfm

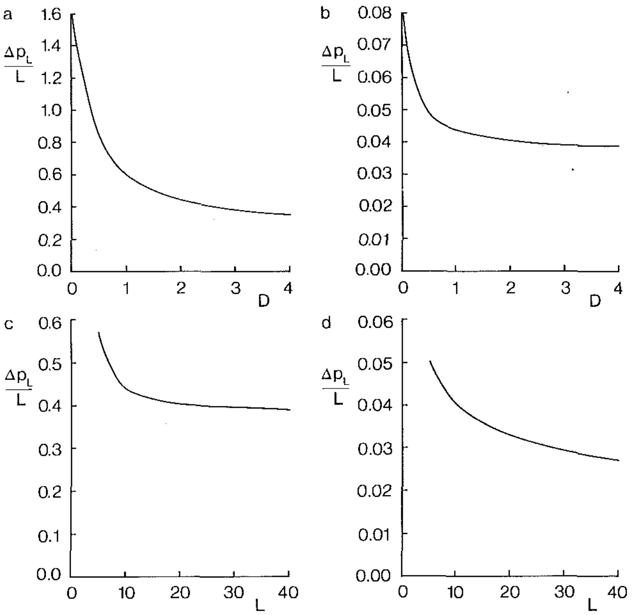

Fig. 8 The effects of the geometric parameters on the mean pressure gradient: (*a*) effect of varying *D* with *L* = 10, Re = 5; (*b*) effect of varying *D* with *L* = 10, Re = 100; (*c*) effect of varying *L* with *D* = 2, Re = 5; (*d*) effect of varying *L* with *D* = 2, Re = 100. (Uncertainty in $\Delta p_L/L$ is ±1 percent in *a* and *c*, and ±5 percent in *b* and *d*.)

axes are logarithmic in Re_0 and $\Delta p_L/L$, and the solid curve denotes the numerical results. The slope of the curve is approximately -1 for large and small values of Re, as it is in the case of a pipe of uniform bore, but is smaller in magnitude for Reynolds numbers between about 10 and 25. This is associated with the increasing size of the separation zone in this Reynolds number range.

The triangle symbols in Fig. 7 show the results of experimental measurements of mean pressure gradient, and are seen to be in good agreement with the numerical results over most of the Reynolds number range. Typically, measured values were 5 percent greater than corresponding predicted values. This can be accounted for by the experimental errors due to the imperfect wall shape, entrance effects and viscosity measurement, and by the numerical discretisation error.

As the Reynolds number increased to values greater than about 300, the measured mean values of $\Delta p_L/L$ increased dramatically. Corresponding to this change, the pressure drops across the downstream half of the test section became larger than those in the upstream half, and hence it can be deduced that the "entrance-length" effect was in fact a transition-length effect, with the flow becoming turbulent downstream of some axial position. For Reynolds numbers greater than about 500, the dimensionless pressure gradient became less Reynolds number dependent, as would be expected in fully turbulent flow.

The effects on the pressure drop of varying the geometrical parameters are shown in Fig. 8, for low and intermediate Reynolds numbers, Re = 5 and Re = 100. Figures 8(*a*) and (*b*) show how $\Delta p_L/L$ varies with D for L fixed at a value of 10. In both cases the pressure is a decreasing function of D, since an increase in D at a fixed Reynolds number corresponds to maintaining the same flow rate in a conduit of increasing mean bore. At large values of D, the pressure drop decreases less rapidly with D, because a smaller proportion of the pressure change occurs in the enlarged parts of the tube. This effect is particularly marked in the higher Reynolds number case, because the velocities near the wall in a hollow are a smaller fraction of the mean velocity than in the lower Reynolds number case.

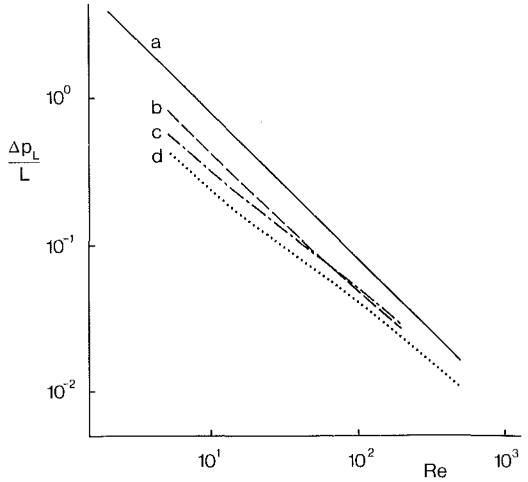

Fig. 9 The differing effects of Reynolds number on the mean pressure gradient for different sets of geometrical parameters: (*a*) *D* = 0; (*b*) *L* = 10, *D* = 0.5; (*c*) *L* = 5, *D* = 2; (*d*) *L* = 10, *D* = 2. (Uncertainty in $\Delta p_L/L$ is ±3 percent in *b*, ±5 percent in *c* and ±2 percent in *d*.)

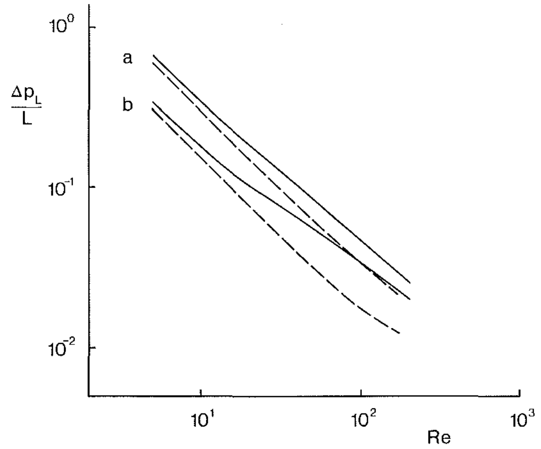

Fig. 10 Comparison of numerical results obtained using the present scheme (solid curves) with those given in [10] (dashed curves) for two sets of geometrical parameters: (*a*) *L* = 8.98, *D* = 0.857; (*b*) *L* = 15.7, *D* = 3. (Uncertainty in present values of $\Delta p_L/L$ is ±2 percent.)

Figures 8(*c*) and (*d*) show the effects of varying the wall wavelength, L, with D fixed at a value of 2. Increasing the wavelength is seen to result in a reduction of the pressure drop, and the dependence on L remains strong for larger values of L in the higher Reynolds number case. It has been found that the length of the separation region, as a fraction of the wall wavelength, decreases as L increases, implying that less energy dissipation per unit length occurs as a result of the reversed flow. There is also a reduction in the wall vorticity maximum as L increases, consistent with a reduced energy dissipation per unit length due to the forward flow. In the low Reynolds number flow on the other hand, the dependence of the pressure drop on L is weak for wavelengths greater than about 10. This is because the flow at any axial position becomes a close approximation to a Poiseuille form at the local tube bore. Hence, the pressure drop is primarily determined by the mean bore, with variations in L having little effect. As L increases, the pressure gradient in Fig. 8(*c*) appears to be approaching the value which can be calculated under the assumption of a parabolic axial velocity profile everywhere.

Finally, Fig. 9 shows the interacting effects of Reynolds number and geometry on the pressure drop. The solid curve (*a*) represents the well-known solution for steady flow in a tube of uniform bore, and is a straight line with gradient -1.

Downloaded 02 Jun 2010 to 171.66.16.66. Redistribution subject to ASME license or copyright; see http://www.asme.org/terms/Terms_Use.cfm

The dashed curve (b), the dash-dotted curve (c), and the dotted curve (d) denote numerical results for wavy-walled tubes with geometrical parameters $L = 10$ and $D = 0.5$; $L = 5$ and $D = 2$; and $L = 10$ and $D = 2$, respectively. Note that, as expected from Figs. 8(a) and (b), the pressure drop is smaller for any wavy-walled tube than for the uniform tube. The slopes of curves 9(c) and (d) are significantly smaller in magnitude than those of curves (a) and (b), indicating that dimensional mean pressure gradients in severely distorted tubes are more strongly Reynolds number dependent than those in more mildly distorted tubes. This is because the inertial terms of the governing equations are identically zero in a uniform tube, but their importance increases as the wall becomes increasingly perturbed.

7 Discussion and Conclusions

7.1 Flow Structure. In the limit of very large or very small Reynolds number, it has been shown that certain numerical solutions of the Navier-Stokes equations can be related to analytical theories. Good agreement with Smith's boundary layer theory [23], in the prediction of a critical Reynolds number for separation has been demonstrated for mildly perturbed walls. Further striking evidence of the applicability of Smith's ideas to the present problem is shown by the axial velocity profile in Fig. 4(a), for a flow at a Reynolds number of 500, which exhibits a distinct boundary layer character, although the experiments showed that this flow could become unstable in practice. Previous authors have also noted the onset of transition at relatively low Reynolds numbers in periodically constricted conduits [2, 24].

Flow reversal in Stokes flow has been theoretically predicted to occur in sharp corners of sufficiently small included angle by Moffatt [25] and subsequently by other workers ([26], for example). Viscous flow reversal can also occur when point sources of momentum, or other singularities, are placed near a plane boundary, as described in [27] and [28]. In the present problem there are no singularities, either on the boundary or within the fluid, but the Stokes flow separation which takes place has similarities with both of these theoretical mechanisms: a certain minimum wall curvature is necessary, in that there is a lower bound on D, and a source of momentum is present in the form of the driving flux.

7.2 Pressure Drop. The Reynolds number effects on laminar pressure drops, as determined in the present work, are in qualitative agreement with those of other workers, [4, 5, 7, 13], in that there is departure from a linear dependence on the flow rate for Reynolds number greater than some critical value. Quantitative comparison with the work of Deiber and Schowalter [10] is possible, and certain of their calculated results, as given in their Fig. 5 and expressed in the present notation, are shown in Fig. 10. Results from [10] are shown as dashed curves and those obtained by the present author for identical parameter values are represented as solid curves. The agreement is fair for curves (a), corresponding to flows in the mildly perturbed tube, for which there is experimental verification in [10]. For curves (b), representing flows in which the wall perturbation is severe ($L = 15.7, D = 3$, in the present notation), the agreement is poor and there is no experimental verification in [10]. The present author believes this to be due to errors arising from the numerical scheme used by Deiber and Schowalter: this method entails an iteration in geometry rather than time, and is, to this author's knowledge, unique; the present scheme has been used successfully in several related studies ([13], [20], and [21], for example), and the time-marching philosophy is very well established. Furthermore, the experimental verification in the present work has been carried out for a more severely perturbed tube (with $D = 2$) than was used in [10] (where $D = 0.857$), providing a more rigorous test of the treatment of the nonlinear terms.

Comparison of the predicted geometrical effects on pressure drop with those of other authors is complicated by the different definitions of Reynolds number used. However, with results recast to conform to the present definitions, an almost universal conclusion (of [4], [5], [7–10], [13] and [15]) is that increasing D or L, at constant Reynolds number, reduces the pressure drop, a result which is perhaps obvious intuitively. In [2] it is argued that the wall wavelength is the sole geometric determinant of pressure drop, but in view of the evidence to the contrary this is unlikely to be true in general. The present results would, however, suggest that this conclusion is substantially correct for deep hollows at high Reynolds number.

Finally, it is believed that the present definition of Reynolds number, based on conditions at a constriction, is superior to the more usual definition in terms of conditions at the cross-section of mean flow area, unless the Reynolds number is small. With the Reynolds number fixed under the present definition, the pressure drop is less sensitive to changes in geometry than if the "mean cross-section" Reynolds number were held constant, except when Re is less than about 10. The present Reynolds number is a more fundamental determinant of the nature of the flow, reflecting the fact that most of the pressure drop and vorticity generation occurs at the constrictions.

Acknowledgments

I am greatly indebted to Dr. I. J. Sobey of Schlumberger Research, Cambridge for many invaluable discussions. I would also like to thank members of the Medical Engineering Unit of Oxford University, where this work was carried out, including Drs. B. J. Bellhouse and J. W. Stairmand for useful advice and M. A. L. Stevenson and J. Greenford for technical assistance. I acknowledge receipt of a Science and Engineering Research Council postgraduate studentship.

References

1 Petersen, E. E., *AIChE J.*, Vol. 4, 1958, p. 343.
2 Batra, V. K., Fulford, G. D., and Dullien, F. A. L., *Can. J. Chem. Eng.*, Vol. 32, 1970, p. 622.
3 Dullien, F. A. L., and Azzam, M. I. S., *AIChE J.*, Vol. 19, 1973, p. 222.
4 Payatakes, A. C., Tien, C., and Turien, R. M., *AIChE J.*, Vol. 19, 1973a, p. 67.
5 Payatakes, A. C., Tien, C., and Turien, R. M., *AIChE J.*, Vol. 19, 1973b, p. 1036.
6 Azzam, M. I. S., and Dullien, F. A. L., *Chem. Eng. Sci.*, Vol. 32, 1977, p. 1445.
7 Fedkiw, P., and Newman, J., *AIChE J.*, Vol. 23, 1977, p. 255.
8 Franzen, P., *Rheol. Acta*, Vol. 16, 1977, p. 548.
9 Neira, M. A., and Payatakes, A. C., *AIChE J.*, Vol. 24, 1978, p. 43.
10 Deiber, J. A., and Schowalter, W. R., *AIChE J.*, Vol. 25, 1979, p. 638.
11 Lee, J-S, and Fung, Y-C, ASME *J. Appl. Mech.*, Vol. 37, 1970, p. 9.
12 Sobey, I. J., *J. Fluid Mech.*, Vol. 96, 1980, p. 1.
13 Savvides, G. N., and Gerrard, J. H., *J. Fluid Mech.*, Vol. 138, 1984, p. 129.
14 Belinfante, D. C., *Proc. Camb. Phil. Soc.*, Vol. 58, 1962, p. 405.
15 Burns, J. C., and Parkes, T., *J. Fluid Mech.*, Vol. 29, 1967, p. 731.
16 Dodson, A. G., Townsend, P., and Walters, K., *Rheol. Acta*, Vol. 10, 1971, p. 508.
17 Chow, J. C. F., and Soda, K., *Phys. Fluids*, Vol. 15, 1972, p. 1700.
18 Ralph, M. E., *D. Phil. thesis*, Univ. of Oxford, 1985.
19 Roache, P. J., *Computational Fluid Dynamics*, 2nd Edition, Hermosa Press, 1976.
20 Cheng, L. C., Clark, M. E., and Robertson, J. M., *J. Biomech.*, Vol. 5, 1972, p. 467.
21 Cheng, L. C., Robertson, J. M., and Clark, M. E., *J. Biomech.*, Vol. 6, 1973, p. 521.
22 Schlichting, H., *Boundary-Layer Theory*, 7th Edition, McGraw-Hill, 1979.
23 Smith, F. T., *Quart. J. Mech. Appl. Math.*, Vol. 29, 1976, p. 127.
24 Stephanoff, K. D., D. Phil. thesis, Univ. of Oxford, 1981.
25 Moffatt, H. K., *J. Fluid Mech.*, Vol. 18, 1964, p. 1.
26 O'Neill, M. E., *J. Fluid Mech.*, Vol. 133, 1983, p. 427.
27 Blake, J. R., *J. Fluid Mech.*, Vol. 95, 1979, p. 209.
28 Liron, N., and Blake, J. R., *J. Fluid Mech.*, Vol. 107, 1981, p. 109.

Downloaded 02 Jun 2010 to 171.66.16.66. Redistribution subject to ASME license or copyright; see http://www.asme.org/terms/Terms_Use.cfm

I. K. Tsanis
Visiting Fellow,
National Water Research Institute,
Canada Centre for Inland Waters,
Burlington, Ontario, L7R 4A6 Canada

H. J. Leutheusser
Professor,
Department of Mechanical Engineering,
University of Toronto,
Toronto, Ontario, M5S 1A4 Canada

An Example of Transient Laminar Countercurrent Flow

This paper presents a numerical and experimental study of transient laminar countercurrent flow in which the pressure gradient is time-dependent. An explicit finite-difference scheme is used to solve numerically the governing equations. Experimental results are obtained with a new kind of apparatus and are found to verify the numerical predictions.

Introduction

Laminar plane countercurrent flow is a generalized plane Couette flow in which an imposed adverse pressure gradient ensures zero net mass flux, see Fig. 1(*a*). In a practical context, this motion occurs in hydrodynamic bearings [1], and in a number of environmental flows such as slow wind-driven water currents [2], and boom-contained oil slicks in rivers [3]. There do not appear to exist any published data, especially on the transient behavior of this important fluid motion, and it is the intention of the present paper to close this information gap. To this end, the whole problem of laminar plane countercurrent flow of an incompressible Newtonian fluid is dealt with both analytically and experimentally. In particular, the classical exact solution of the Navier-Stokes equation for the steady case is complemented by a numerical solution of the governing equations for a more general case of motion, viz. the establishment-in-time of flow starting from an initially quiescent state. The theoretical predictions so obtained are verified experimentally using a novel experimental facility [2].

Theoretical Considerations

Steady Laminar Countercurrent Flow. With reference to the definition diagram of Fig. 1(*a*) which may be interpreted as representing, for instance, a water body subject to wind shear, the applicable form of the equation of motion is

$$\frac{dP}{dx} = \mu \frac{d^2u}{dz^2} \tag{1}$$

subject to the boundary conditions and continuity requirement

$$u = 0 \quad at \quad z = 0 \tag{1a}$$

$$u = u_s \quad at \quad z = h \tag{1b}$$

$$\int_0^h u dz = 0 \tag{1c}$$

Integration of equation (1) with respect to z between 0 and h yields

$$\frac{dx}{dP} = \frac{\tau_s - \tau_b}{h} \tag{2}$$

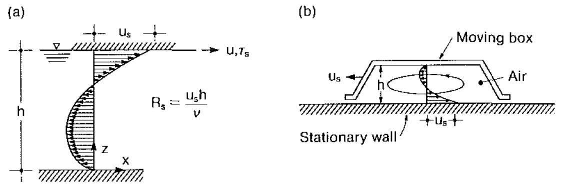

Fig. 1 Definition diagrams of countercurrent flow (*a*), and laboratory simulation (*b*)

which gives the pressure gradient as a function of the shear stresses acting over the periphery of an infinitely long and infinitely wide fluid volume, and the depth h of the flow field. The flow itself consists of a drift current in direction of the applied surface shear stress τ_s near the moving surface, and a pressure-induced return current near the bottom. Because the pressure gradient is constant, equation (2) can be generalized to give the shear-stress distribution in the vertical, $\tau = \tau(z)$,

$$\tau = \tau_b + (\tau_s - \tau_b)\frac{z}{h} \tag{3}$$

The linear shear-stress distribution of equation (3) holds for both laminar and turbulent motions. However, the corresponding velocity distribution $u = u(z)$ depends on the applicable constitutive relationships. In particular, for laminar flow, it is

$$\frac{u}{u_s} = 3\left(\frac{z}{h}\right)^2 - 2\left(\frac{z}{h}\right) \tag{4}$$

where

$$u_s = \frac{h^2}{6\mu}\frac{dP}{dx} \tag{5}$$

The shear stress distribution corresponding to equation (4) is

$$\tau = 2\mu \frac{u_s}{h}\left(3\frac{z}{h} - 1\right) \tag{6}$$

whence

$$\eta = \frac{\tau_b}{\tau_s} = -0.50 \tag{7}$$

This indicates that, for laminar flow, the bottom shear is 50 percent of the surface shear. Moreover, the shear stress is zero at $z/h = 1/3$, and the velocity $u = 0$ occurs at $z/h = 0$ and $z/h = 2/3$. Finally, the nondimensional surface-shear coefficient,

---

Contributed by the Fluids Engineering Division for publication in the Journal of Fluids Engineering. Manuscript received by the Fluids Engineering Division, April 29, 1986.

Copyright © 1987 by ASME

Downloaded 02 Jun 2010 to 171.66.16.66. Redistribution subject to ASME license or copyright; see http://www.asme.org/terms/Terms_Use.cfm

$$c_f = \frac{\tau_s}{\rho u_s^2/2} \tag{8}$$

becomes

$$c_f = \frac{8}{R_s} \tag{9}$$

$$R_s = \frac{u_s h}{\nu} \tag{10}$$

is the bulk Reynolds number of the shear-induced flow in terms of the kinematic viscosity.

Transient Laminar Countercurrent Flow. The equation of motion for unsteady motion is

$$\frac{\partial u}{\partial t} = -\frac{1}{\rho}\frac{dP}{dx}(t) + \nu \frac{\partial^2 u}{\partial z^2} \tag{11}$$

For the case of interest herein, i.e., the establishment-in-time of flow in consequence of a time-varying surface velocity $u_s(t)$, the applicable initial and boundary conditions are the following:

$$u(0, t) = 0 \tag{11a}$$

$$u(z, 0) = 0 \tag{11b}$$

$$u(h, t) = f(t)u_s \quad f(t) < 1 \text{ for } t < t_o \text{ and } f(t) = 1 \text{ for } t \geq t_o \tag{11c}$$

in which $f(t)$ is a specified function of time. Equation (11*a*) denotes the no-slip condition at the stationary boundary, equation (11*b*) is the initial condition of the problem, and equation (11*c*) expresses the variation of the surface velocity with time. Because of the parabolic character of equation (11), both the velocity and the pressure gradient tend toward the steady-state solution of equations (4) and (5) at $t = \infty$. The surface velocity starts at $t = 0$ when $u(h, 0) = 0$, and increases to u_s = constant at $t = t_o$. The continuity requirement which has to be satisfied is given by equation (1*c*).

Introducing the following dimensionless variables

$$z_h = \frac{z}{h} \tag{12a}$$

$$u_h = \frac{u}{u_s} \tag{12b}$$

$$t_h = \frac{\nu t}{h^2} \tag{12c}$$

$$p_h = \frac{h^2}{\mu u_s}\frac{dP}{dx} \tag{12d}$$

into the equation of motion yields

$$\frac{\partial u_h}{\partial t_h} = -p_h(t) + \frac{\partial^2 u_h}{\partial z_h^2} \tag{13}$$

Similarly, the initial and boundary conditions (11*a*) to (11*c*), and the continuity requirement (1*c*) become, respectively,

$$u_h(0, t_h) = 0 \tag{13a}$$

$$u_h(z_h, 0) = 0 \tag{13b}$$

$$u_h(1, t_h) = f(t_h)$$

$$f(t_h) < 1 \text{ for } t_h < t_{oh} = \frac{\nu t_o}{h^2} \text{ and } f(t_h) = 1 \text{ for } t_h \geq t_{oh} \tag{13c}$$

$$\int_0^1 u_h \, dz_h = 0 \tag{13d}$$

and equations (4) and (5) become

$$u_h(z_h, \infty) = 3z_h^2 - 2z_h \quad \text{and} \quad p_h(\infty) = 6 \tag{13e}$$

Integration of equation (13) with respect to z_h between 0 and 1 gives

$$\frac{\partial}{\partial t_h}\int_0^1 u_h \, dz_h = -p_h + \left.\frac{\partial u_h}{\partial z_h}\right|_1 - \left.\frac{\partial u_h}{\partial z_h}\right|_0 \tag{14}$$

By inspection, the left-hand side of equation (14) is zero. This yields

$$p_h = \left.\frac{\partial u_h}{\partial z_h}\right|_1 - \left.\frac{\partial u_h}{\partial z_h}\right|_0 \tag{15}$$

Equations (13) and (15) form a coupled system with the two unknowns of pressure p_h and velocity u_h, respectively. This system of equations, with conditions (13*a*) to (13*d*), can be solved numerically for the general case of any given function $f(t_h)$.

In the following, an explicit finite-difference scheme is used in which the time derivative is approximated by a forward difference, and the spatial second derivative is approximated by a central difference. Time is indicated by the upper index

Nomenclature

$c_f = \frac{\tau_s}{\rho u_s^2/2}$ = nondimensional surface-shear coefficient
d = width of the moving air volume
$f(t)$ = function of time
g = acceleration due to gravity
h = depth of the moving air volume
n = time index
i = space index
L_e = length of flow establishment
$N = i_{\max}$ = total number of nodes
$R_s = \frac{u_s h}{\nu}$ = bulk Reynolds number
P = piezometric pressure
$P_h = \frac{h^2}{\mu u_s}\frac{dP}{dx}$ = nondimensional pressure gradient
t = time
t_o = time required by the carriage to reach constant velocity
$t_h = \frac{\nu t}{h^2}$ = nondimensional time
$t_{oh} = \frac{\nu t_o}{h^2}$ = nondimensional time t_o
u = velocity component in streamwise x-direction
u_s = velocity of the moving surface
$u_h = \frac{u}{u_s}$ = nondimensional velocity
$u_{h_i}, u_{h_{i+1}}$ = nodal values of mean velocity
x, z = length coordinates
$z_h = \frac{z}{h}$ = nondimensional transverse length coordinate
$z_{h_i}, z_{h_{i+1}}$ = nodal distances
Δt = time step
Δx = space step
$\eta = \frac{\tau_b}{\tau_s}$ = bottom to surface shear stress ratio
μ = dynamic viscosity
$\nu = \frac{\mu}{\rho}$ = kinematic viscosity
ρ = density
τ = shear stress

Subscripts

s = surface
b = bottom
∞ = terminal

Downloaded 02 Jun 2010 to 171.66.16.66. Redistribution subject to ASME license or copyright; see http://www.asme.org/terms/Terms_Use.cfm

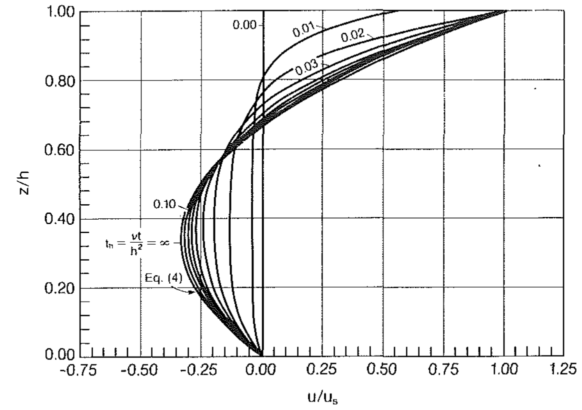

Fig. 2 Developing laminar shear-induced countercurrent flow for linearly increasing surface velocity

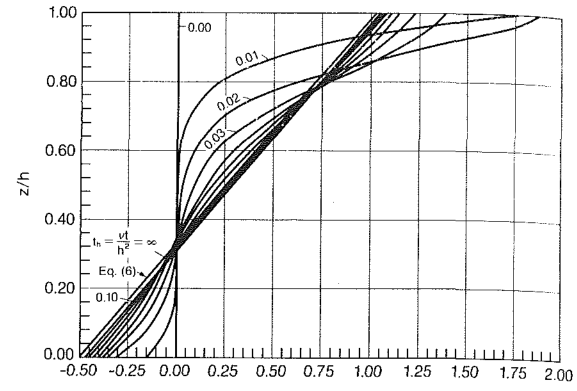

Fig. 3 Shear-stress distribution in developing laminar shear-induced countercurrent flow for linearly increasing surface velocity

$n(t_n = n\Delta t$, where Δt is the time step used for the discretization of time), and the position along the z_h axis is indicated by the lower index $i(z_i = i\Delta z$, where Δz is the space step), and $N = i_{\max}$ is the total number of nodes. In this terminology, equations (13) and (15) become, respectively,

$$u_{hi}^{n+1} = u_{hi}^{n} - \Delta t_h p_h{}^n + \frac{\Delta t_h}{\Delta z_h{}^2}\,(u_{hi+1}^{n} - 2u_{hi}^{n} + u_{hi}^{n-1}) \tag{16}$$

and

$$p_h{}^n = \frac{u_{hN}^{n} - u_{hN-1}^{n}}{\Delta z_h} - \frac{u_{h2}^{n} - u_{h1}^{n}}{\Delta z_h} \tag{17}$$

In order to have a stable solution, the following criterion [4] has to be satisfied, i.e.,

$$\frac{\Delta t_h}{\Delta z_h{}^2} \leq 0.5 \tag{18}$$

and which, hence, determines the time step of the numerical scheme.

To apply the numerical scheme to the problem at hand, the space between the stationary and moving boundaries is discretized by 40 unequal elements, with closer spacing used near the boundaries where the velocity gradients are large. For this case the finite-difference forms of the equations (13) and (15) are, respectively,

$$u_{hi}^{n+1} = u_{hi}^{n} - \Delta t_h p_h{}^n + \frac{2\Delta t_h}{\Delta z_{h_i} + \Delta z_{h_{i-1}}}\left(\frac{u_{hi+1}^{n} - u_{hi}^{n}}{\Delta z_{h_i}} - \frac{u_{hi}^{n} - u_{hi-1}^{n}}{\Delta z_{h_{i-1}}}\right) \tag{19}$$

and

$$p_h{}^n = \frac{u_{hN}^{n} - u_{hN-1}^{n}}{\Delta z_{h_{N-1}}} - \frac{u_{h2}^{n} - u_{h1}^{n}}{\Delta z_{h_1}} \tag{20}$$

The smallest elements are the ones right on the moving boundary $\Delta z_{h_{N-1}}$, and on the stationary boundary Δz_{h_1}, with a value of 0.002. The largest elements are in the core of the flow with a value of 0.04. In order to satisfy the stability criterion (18), the time step Δt_h used is 1.25×10^{-6}. The numerical scheme tends to give lower than the expected value for the pressure gradient, and causes a violation of continuity (see Appendix). In order to minimize this effect in the present instance to less than 1 percent, the scheme corrects for continuity at each step according to equation (14). This can be written in finite-difference form as follows

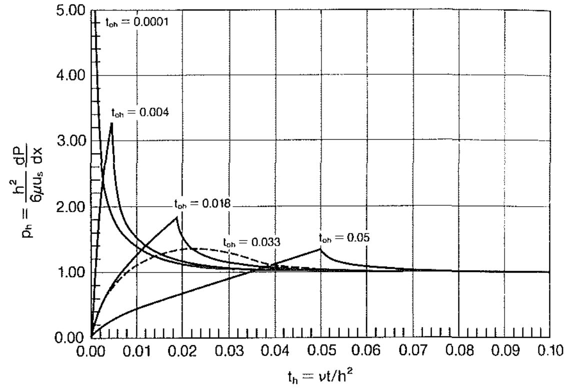

Fig. 4 Time-wise variation of pressure gradient in shear-induced laminar countercurrent flow for various cases of linearly increasing surface velocity. The dashed curve corresponds to the case of smoothly developing flow which is dealt with in Figs. 6 and 7

$$\frac{\displaystyle\sum_{i=1}^{i=N-1} \frac{u_{hi}^{n} + n_{hi+1}^{n}}{2}\,\Delta z_{h_i} - \sum_{i=1}^{i=N-1} \frac{u_{hi}^{n+1} + u_{hi+1}^{n+1}}{2}\,\Delta z_{h_i}}{\Delta t_h} = -p_h{}^n + \frac{u_{hN}^{n} - u_{hN-1}^{n}}{\Delta z_{h_{N-1}}} - \frac{u_{h2}^{n} - u_{h1}^{n}}{\Delta z_{h_1}} \tag{21}$$

For the special case of a linearly increasing surface velocity from zero to u_s in time $t_o = 3$s, or $t_h = 0.018$, typical of the experimental apparatus used herein, the velocity profiles at different nondimensional times t_h are depicted in Fig. 2. The time-wise evolution of the velocity tends toward the steady state, i.e., equation (4), at theoretically infinite time. According to the analysis, the velocity reaches 99 percent of its final value at time $t_h \approx 0.10$. This means that for a laboratory flow with $R_s = 1330$, reaching $u_s = 0.40$ m/s in $t_o = 3$s, and with $h = 5$ cm and $\nu = 1.5 \times 10^{-5}$ m²/s, a traveling time of $t \approx 16.66$ s is required for the flow to become essentially developed. The corresponding distance is $L_e \approx 5.90$ m and, hence, the nondimensional length of flow development is

$$\frac{L_e}{h} \approx 118 \tag{22}$$

The nondimensional shear-stress distribution for different times t_h is depicted in Fig. 3. The shear-stress distribution is deduced from the numerically calculated velocity profiles. The pressure gradient p_h as a function of time t_h is calculated internally in each step of the computer program. The nondimensional pressure gradient increases from zero to a maximum value at the time when the surface velocity reaches its final

Downloaded 02 Jun 2010 to 171.66.16.66. Redistribution subject to ASME license or copyright; see http://www.asme.org/terms/Terms_Use.cfm

value, and then decreases quickly tending toward the steady state value which, at $t=\infty$, is equal to 6, cf. equation (5). Variation of the time t_o leads to different pressure distributions. A number of these, including the relevant case of $t_{oh}=0.018$, is presented in Fig. 4. In the case of a suddenly applied constant surface velocity, the pressure gradient has an infinite value at $t_h=0$, whence it decreases towards the steady-state value of 6.

Experimental Apparatus

The facility used in the present work is an existing experimental apparatus for the study of plane Couette flow [5] which was modified to suit the needs of the present experiment. In the apparatus, the moving wall is propelled by the carriage of towing-tank installation, and the fixed wall is the surface of a stationary bench which is constructed alongside the towing channel proper. The sheared fluid medium is air.

The velocity of the propelling carriage can be varied continuously from zero up to a maximum of about 3 m/s, and the maximum acceleration is 0.80 m/s^2. The speed of the carriage is monitored by means of wheel-driven tachometer, and is separately timed over a precisely measured base distance. The resulting mean carriage velocity is estimated to be accurate to be within 0.01 m/s.

In order to induce an adverse pressure gradient in the sheared fluid layer sandwiched between the two solid boundaries in motion relative to each other, the moving wall of the existing facility is closed on all sides with plexiglass plates, thus forming a moving air-filled cavity, see Fig. 1(*b*). Clearances between box sidewalls and the stationary bench are carefully closed by flexible seals to prevent the air from escaping and, thus, to keep the box pressurized during its motion.

The moving box is a 2.40-m long and 0.95-m wide plexiglass container, which straddles with its longitudinal side walls the 0.71-m wide stationary plate. The clear height of the box, and its inclination relative to the stationary wall can be adjusted between a minimum of 0.01 m and a maximum of 0.15 m with the aid of four cranking mechanisms.

The stationary wall of the apparatus is composed of panels of plate glass situated on top of a 31-m long aluminum bench. The top surface of the glass panels is co-planar with the horizontal plane of the carriage track. The 31-m long glass-covered bench begins and terminates 14.5 m away from the two end points of the 60 m long towing channel. The required distances for accelerating and decelerating the carriage to and from its maximum velocity of 3 m/s are less than 14.5 m. Based on this, the whole 31-m length of the stationary bench is available for testing purposes under steady-state conditions over the whole range of carriage velocities. The maximum Reynolds number R_s attainable with the apparatus, i.e., for $u_s=3.0$ m/s and $h=0.15$ m, is 30,000.

The determination of velocity and position of the towing carriage is crucial in the experimental investigation. An electronic device connected to two identical interrupt-type light sensors, spaced 10 m apart, and a stopwatch are used for the speed determination of the carriage. The position of the carriage is established with the aid of a reflect-type light sensor in conjunction with 63 stainless steel strips equally spaced every 0.50 m along the 31-m long stationary bench.

Flow properties are measured with standard hot-wire velocimetry equipment which is stored aboard the towing carriage. Single wire probes are used for measuring the velocity. Calibration of the hot-wire sensors is accomplished with the apparatus itself. In particular, for velocities greater than 0.2 m/s the probe to be calibrated is fixed to the carriage and towed inside a protective sleeve attached to the stationary bench [6]. For velocities smaller than 0.2 m/s, with the carriage at rest, the probe is moved horizontally inside the stationary box by a traversing mechanism [7].

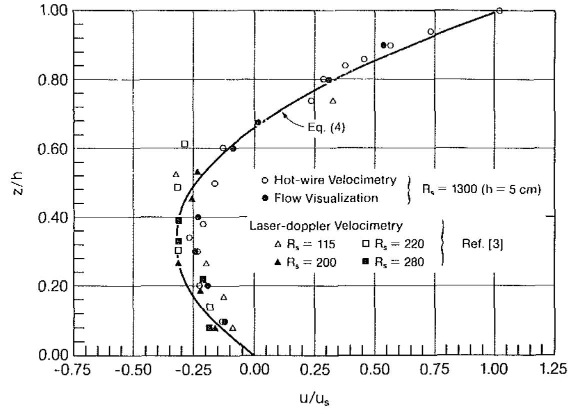

Fig. 5 Comparison between experimentally determined and analytically predicted velocity profiles for steady laminar shear-induced countercurrent flow

Because of the low velocities involved in the experiments, the hot-wire measurements are complemented, where appropriate, by flow visualization using the smoke-wire technique [8]. Its principle of operation is that a fine wire, coated with liquid paraffin and heated by the passage of an electric current pulse, vaporizes the liquid and thus forms a dense white smoke. The traveling distance of the smoke particles is proportional to the local flow velocity. Ancillary instruments used in the application of the smoke-wire method include a video system, and a still camera for photographing the monitor screen.

Results and Discussion

Transition from laminar to turbulent flow begins at some value of Reynolds number R_{cr} below which even strong disturbances do not cause the flow to become unstable. This Reynolds number varies between flows.

The critical Reynolds number for the shear-induced countercurrent flow under investigation herein is obtained by observing the oscilloscope display of a hot-wire signal. From this it appears that turbulence begins at a critical Reynolds number $R_{cr}=1750\pm150$ which is in excellent agreement with Keulegan's observations of wind-induced water currents in an air-sea interaction tunnel [9]. These findings compare with $R_{cr}\approx1200$ for plane Couette flow [10] and, thus, identify countercurrent flow as the clearly more stable one (i.e., it is less susceptible to the development of an inflection point in the laminar velocity profile) of these two related fluid motions.

Steady Laminar Countercurrent Flow. In addition to hot-wire measurements, the smoke-wire technique for flow visualization is used in the quantitative analysis of this case.

Experimental results obtained by both techniques (for $R_s=1300$ and $h=5$ cm) and data from reference [3], together with the analytically predicted velocity profile, equation (4), are compiled in Fig. 5. Notwithstanding possibly incomplete flow development, the findings are in generally good agreement with the theory. The up to 15 percent difference between the experimental and theoretically predicted results in the return portion of the flow is likely due to some inadvertent air leakage from the moving cavity.

Transient Laminar Countercurrent Flow. A hot-wire anemometer, a position counter, a signal conditioner, a digital voltmeter, and a video system are used to study developing laminar countercurrent flow. The output voltage of the hot-wire sensor is displayed simultaneously with the reading of the position counter indicating the instantaneous location of the carriage. The voltages are converted to velocities using the

Downloaded 02 Jun 2010 to 171.66.16.66. Redistribution subject to ASME license or copyright; see http://www.asme.org/terms/Terms_Use.cfm

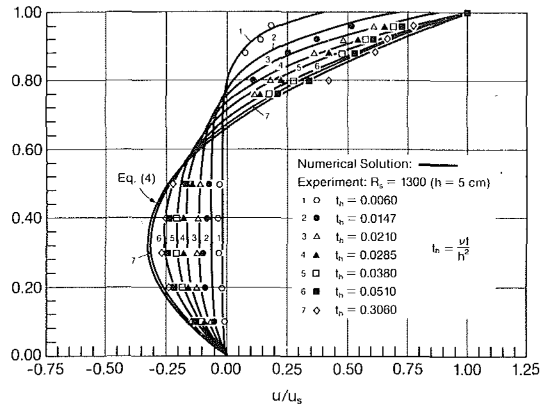

Fig. 6 Experimental verification of numerically predicted velocity profiles for smoothly developing laminar countercurrent flow: $t_{oh} = 0.033$

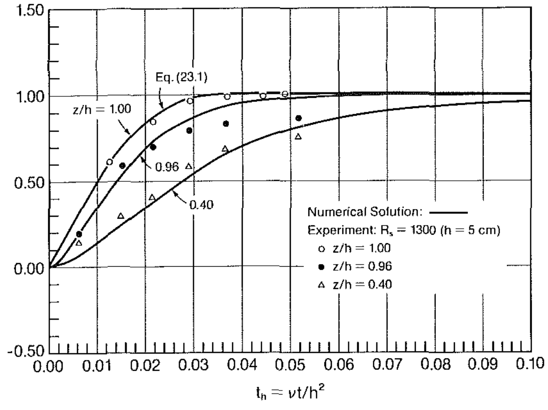

Fig. 7 Experimental verification of numerically predicted time-wise variation of selected local velocities in smoothly developing laminar countercurrent flow: $t_{oh} = 0.033$

hot-wire calibration, and are plotted as functions of non-dimensional position z_h and time t_h.

At the beginning of the experimental runs, the moving box is located above the leading end of the stationary bench, providing a quiescent environment for the hot-wire sensor. The voltmeter reading at this instant corresponds to zero velocity. The towing channel carriage, to which the moving box is attached, is then accelerated from zero velocity, tending asymptotically toward the maximum velocity in nondimensional time $t_{oh} = 0.033$ in accordance with the following,

$$u_h(1, t_h) = -918.27\, t_h^2 + 60.60\, t_h \qquad \text{for } t_h < 0.033 \qquad (23.1)$$

$$u_h(1, t_h) = 1 \qquad \text{for } t_h \geq 0.033 \qquad (23.2)$$

The pressure distribution corresponding to these conditions is included as a dashed line in Fig. 4. Its pattern reflects the smooth time-wise variation of the surface velocity which reaches its maximum value at $t_h = 0.022$ gradually. Fig. 6 depicts the experimental verification of the numerically predicted velocity profiles for transient laminar countercurrent flow with $R_s = 1300$, $h = 5$ cm, and subject to conditions (23). Despite an up to 15 percent difference between predictions and experimental velocity points in the return portion of the flow at large times, the agreement is very good and thereby confirms the validity of the numerical solution. Figure 7 illustrates the corresponding experimental verification of the numerically predicted time-wise variation fo some local velocities. In this, the curve for $z/h = 1.00$ represents a plot of equation (23.1).

Conclusions

An explicit finite-difference scheme is developed for the numerical solution of the governing equations of transient laminar countercurrent flow of incompressible Newtonian fluids. Distributions of velocity, shear stress and pressure gradient are presented for the case of time-wise flow establishment. Numerically predicted velocity profiles are found to be in a good agreement with corresponding experimental results for both steady and unsteady conditions of flow.

Acknowledgments

The work described herein was made possible through Grant A-1541 of the Natural Sciences and Engineering Research Council of Canada.

References

1 Schlichting, H, *Boundary Layer Theory*, 6th edition, McGraw-Hill, New York, NY, 1968.

2 Tsanis, I. K., *"Characteristics of Shear-induced Countercurrent Flow,"* Ph.D. thesis, University of Toronto, Toronto, Ontario, Canada, 1986.

3 Berry, B. A., and Rajaratnam, N., "Oil Slicks in Ice Covered Rivers," *Journal of Hydraulic Engineering*, ASCE, Vol. 111, No. HY3, 1985, pp. 369-379.

4 Koutitas, C., *Elements of Computational Hydraulics*, Pentech Press, London, UK., 1983.

5 Aydin, M., and Leutheusser, H. J., "Novel Experimental Facility for the Study of Plane Couette Flow," *Review of Scientific Instruments*, Vol. 50, No. 11, 1979, pp. 1362-1366.

6 Aydin, M., and Leutheusser, H. J., "Very Low Velocity Calibration and Application of Hot-wire Probes," *DISA Information*, No. 25, 1980, pp. 17-18.

7 Tsanis, I. K., "A Hot-wire Anemometer Calibration Technique at Very Low Velocities," *Dantec Information*, No. 4, Feb. 1987, pp. 13-14.

8 Torri, k., "Flow Visualization by Smoke-wire Technique," *Proceedings of the International Symposium on Flow Visualization*, Tokyo, 1977, pp. 175-180.

9 Keulegan, G. H., "Wind Tides in Small Closed Channels,"*Journal of Research*, National Bureau of Standards, Vol. 46, No. 5, 1951.

10 Leutheusser, H. J., and CHu, V. H., "Experiments on Plane Couette Flow," *Journal of the Hydraulics Division* (ASCE), Vol. 97, No. HY9, 1971, pp. 1269-1284.

APPENDIX

Uncertainty Estimates

Experimental Uncertainty. In Figs. 5 through 7, the uncertainty of the authors' plotted experimental data in u/u_s is ± 0.03 at 20:1 odds. In the area of flow reversal, the error may be larger due to observed, very slow fluctuations of the position of zero-velocity about $z/h \approx 0.67$ which affect the hot-wire voltage output.

Numerical Uncertainty. The numerical scheme used for the solution of equations (19) and (20), or (21), uses Taylor-series expansions of the involved derivatives. The forward difference, i.e.,

$$\left.\frac{\partial u_h}{\partial z_h}\right|_i = \frac{u_{hi+1} - u_{hi}}{\Delta z_h} + 0(\Delta z_h) \approx \frac{u_{hi+1} - u_{hi}}{\Delta z_h} \qquad (24)$$

neglects terms of the order of Δz_h. Thus, it has a truncation error of order Δz_h and is first-order accurate.

The central-difference form of the second derivative, i.e.,

$$\left.\frac{\partial^2 u_h}{\partial z_h^2}\right|_i = \frac{\dfrac{u_{hi+1} - u_{hi}}{\Delta z_h} - \dfrac{u_{hi} - u_{hi-1}}{\Delta z_h}}{\Delta z_h} \qquad (25)$$

is second-order accurate. Although the central difference offers this advantage, it has some shortcomings with respect to stability. For example, in order to minimize the numerical error the elements Δz_h have to be very small. However, by reducing the element Δz_h, the time step shrinks in the order of Δz_h^2 according to the stability criterion of equation (18). This results in an increase of computational time.

To test the accuracy estimation, different grids with equally and unequally spaced Δz_h are used in the following. For the

Downloaded 02 Jun 2010 to 171.66.16.66. Redistribution subject to ASME license or copyright; see http://www.asme.org/terms/Terms_Use.cfm

case of ultimately steady flow, i.e., for $t_h \rightarrow \infty$, $p_h(\infty) = 6$ and $u_h(\infty) = 3z_h^2 - 2z_h$, the velocity areas of the drift and return currents have opposite signs, but are of equal magnitude, viz.

$$-\int_0^{2/3} u_h dh = \int_{2/3}^{1} u_h dh = 0.1481.$$

Thus, by direct integration it is readily found that drift and return currents are perfectly balanced and, hence, that the net area under the velocity distribution is exactly zero. Things are different under conditions of numerical integration. Close inspection of equation (20) shows that the evaluation of the nondimensional pressure gradient p_h depends solely on the elements right next to the flow boundaries. Taking into consideration that in these areas the velocity gradients are high, it can be concluded that the size of the elements Δz_{h_1} and $\Delta z_{h_{N-1}}$ are critical for the accuracy of the numerical scheme.

The first test is between equally and unequally spaced elements. For $\Delta z_{h_1} = \Delta z_{h_{N-1}} = 0.0025$, 400 equally spaced elements are required. In order to have a stable solution, a time step of 2.5×10^{-6} is used, and the required computational time by VAX11-780 for $t_h = 0.10$, i.e., at approximately 99 percent of the ultimately steady state, is found to be 1540 seconds. The corresponding nondimensional pressure gradient $p_h/6$ is 0.99188 instead of unity, and the mass balance is 0.002836 in lieu of zero. As a consequence, the drift current amounts to only 99.6 percent, and the return current to only 96.8 percent, of their respective exact values. On the other hand, unequally spaced elements yield the same, or better accuracy with less computational time. Typical numerical results, for 40 unequal elements, are as follows:

Δz_{h_1}	$\Delta z_{h_{N-1}}$	$p_h/6$	$\int_0^1 u_h dz_h$	Comp'l Time (seconds)	Error in p_h(%)	Error in Continuity (%)
0.0050	0.0025	0.988994	0.004296	155	1.11	1.45
0.0025	0.0020	0.994568	0.002393	260	0.55	0.81
0.0020	0.0020	0.995220	0.002198	316	0.50	0.74

The values in the 7th column are obtained by dividing the values in the 4th column by the absolute theoretical value of the areas under the drift and return currents, i.e., 0.2962.

The truncation error has an effect on both the mass balance and the pressure term. In the following an attempt is made to reduce this error. In particular, equation (21) is used instead of equation (20), and the pressure term is corrected according to the non-zero value of the mass-balance time derivative. To test if there is an improvement, the correction is applied every $\Delta t_h = 0.005$ up to $t_h = 0.100$. Numerical results, for 40 unequal elements, are as follows:

Δz_{h_1}	$\Delta z_{h_{N-1}}$	$p_h/6$	$\int_0^1 u_h dz_h$	Error in p_h (%)	Error in Continuity (%)
0.0050	0.0025	0.992200	0.004291	0.78	1.448
0.0025	0.0020	0.996487	0.002384	0.35	0.800
0.0020	0.0020	0.997248	0.002190	0.27	0.739

It can be seen that the correction yields an improvement in the value of the pressure term, and a slight reduction in the violation of the mass balance. In particular, at $t_h = 0.10$, and with $\Delta z_{h1} = \Delta z_{h_{N-1}} = 0.002$, the drift current reaches 99.6 percent, and the return current 97.4 percent of their exact values. Corresponding percentages, for $t_h = 0.125$, are, respectively, 99.9 and 98.4. The precise instant at which the velocity reaches 99 percent of its final value is difficult to determine due to the inherent numerical error, but it seems to lie between 0.100 and 0.125. Accordingly, the nondimensional length of flow development L_e/h is somewhere 118 and 168. Further improvement of this solution can be achieved by reducing Δz_{h_1}. This, however, would increase the required computational time.

Downloaded 02 Jun 2010 to 171.66.16.66. Redistribution subject to ASME license or copyright; see http://www.asme.org/terms/Terms_Use.cfm

Resistance to the Flow of Fluids Through Simple and Complex Porous Media Whose Matrices Are Composed of Randomly Packed Spheres

R. M. Fand

B. Y. K. Kim

A. C. C. Lam

R. T. Phan

Department of Mechanical Engineering,
University of Hawaii at Manoa,
Honolulu, Hawaii 96822

Experimental data relating to the flow of fluids through simple and complex porous media whose matrices are composed of randomly packed spheres have been obtained. In this context the term "simple" refers to porous media whose matrices are composed of spheres of uniform diameter, while "complex" refers to matrices composed of spheres having different diameters. It was found that Darcy's law is valid for simple media within a range of the Reynolds number, Re, whose upper bound is 2.3. The upper bounds of Darcy flow for complex media were found to be consistent with this value. It is shown that the resistance to flow in the Darcy regime can be characterized by taking the Kozeny-Carman constant equal to 5.34 if the characteristic dimension is taken equal to the weighted harmonic mean diameter of the spheres that comprise the matrix. Forchheimer's equation was found to be valid for simple media within the range $5 \leq Re \leq 80$. The corresponding bounds for complex media were found to be consistent with this range. It is shown that the resistance to flow in the Forchheimer regime for both simple and complex media can be characterized by adopting the following values of the Ergun constants: $A = 182$ and $B = 1.92$. Finally, it is shown that fully developed turbulent flow exists when $Re > 120$ and that the resistance to flow in the turbulent regime can be calculated using Forchheimer's equation by adopting the following values of the Ergun constants: $A' = 225$ and $B' = 1.61$. A simple method for characterizing the behavior of porous media in the transition regions between Darcy and Forchheimer and between Forchheimer and turbulent flow is presented.

Objective

The objective of the study reported in this paper was to obtain useful correlation equations that relate the pressure gradient to the velocity of flow of fluids through simple and complex porous media whose matrices are composed of randomly packed spheres. These equations were to be determined by analyzing a new set of accurate experimental data obtained for this specific purpose. In this context the term "simple" refers to porous media whose matrices are composed of spheres of uniform diameter, while "complex" refers to matrices composed of spheres having different diameters. The range of the Reynolds number was sufficiently broad as to encompass the so-called Darcy, Forchheimer and turbulent flow regimes. It is anticipated that the results presented herein will be applicable in a general way to fluid flows through naturally occurring porous media such as sand; and also, more specifically, to flows through porous media whose matrices are composed of fabricated smooth pellets.

Review of the Literature

General Discussion: Regimes of Flow. Dybbs and Edwards [1] have published a comprehensive review paper in which they present the results of laser anemometry and flow visualization studies of the flow of liquids in porous media. The porous media consisted of plexiglass spheres in a hexagonal packing and glass and plexiglass rods arranged in a complex, fixed three dimensional geometry. Various liquids, including water, were employed. The Reynolds number, Re, based on average pore size and average pore velocity ranged from 0.16 to 700.

The results in [1] indicated the existence of four regimes of flow in porous media: (1) The Darcy regime where the flow is dominated by viscous forces and the exact nature of the flow is determined by local geometry. This type of flow occurs at $Re < 1$ and Darcy's law, which states that the pressure gradient is directly proportional to the flow rate, holds. At $Re = 1$, boundary layers begin to develop near the solid boundaries of the pore. (2) The inertial flow regime, which begins at Re between 1 and 10, wherein the boundary layers become more pronounced and an "inertial core" appears. The development of

---

Contributed by the Fluids Engineering Division for publication in the JOURNAL OF FLUIDS ENGINEERING. Manuscript received by the Fluids Engineering Division, February 5, 1986.

Copyright © 1987 by ASME

Downloaded 02 Jun 2010 to 171.66.16.66. Redistribution subject to ASME license or copyright; see http://www.asme.org/terms/Terms_Use.cfm

these "core" flows outside the boundary layers causes a nonlinear relationship between the pressure gradient and the flow rate. This steady nonlinear flow regime persists to $\mathrm{Re} = 200$. (3) An unsteady laminar flow regime in the range $200 < \mathrm{Re} < 350$, which is characterized by laminar wake oscillations for $200 < \mathrm{Re} < 300$ followed by the formation of vortices in the range $300 < \mathrm{Re} < 350$. (4) A highly unsteady and chaotic regime for $\mathrm{Re} > 350$ that qualitatively resembles turbulent flow.

Bear [2] points out that, in addition to the flow regimes described above, there exists a value of Re *below* which Darcy's law does not hold. The flow in this lowest range of Re will be referred to hereinafter as "pre-Darcy flow." If the lower bound of Re for which Darcy's law holds is designated by Re_{DL}[1], then the pre-Darcy regime corresponds to $\mathrm{Re} < \mathrm{Re}_{DL}$. The existence of pre-Darcy flow is attributed to non-Newtonian behavior of fluids and the fact that the streaming potential generated by the flow, particularly in fine-grained media, can produce small countercurrents along the pore walls in a direction opposite to that of the main flow [2]. An important aspect of pre-Darcy flow is that within this region a finite value of the pressure gradient exists below which the Darcian velocity (defined below) is zero. There is no available precise information concerning the magnitude of Re_{DL}, but published data on Darcy flow indicate that $\mathrm{Re}_{DL} < 10^{-5}$. The pre-Darcy regime was not studied in the present investigation because the sensitivity of available instrumentation was not sufficient to measure the extremely low pressure gradients and velocities pertaining thereto.

The experiments conducted by Dybbs and Edwards differ from those reported herein with respect to the configuration of the porous matrices employed; thus, Dybbs and Edwards employed spheres in a *regular* hexagonal packing, whereas in the present investigation the packing of spheres was random. Furthermore, Dybbs and Edwards based Re on the average pore size, whereas in the present study Re is based upon the particle (sphere) diameter. Thus, although the several regimes of flow described by Dybbs and Edwards are consistent with the results of the present investigation, the reported ranges of Re that delineate these regimes must differ in the two studies.

Quantitative Information: Darcy and Pre-Darcy Flow. In 1856 Henry Darcy performed experiments on the flow of water through a pipe packed with sand and discovered that, under certain conditions, the volume rate of flow through the pipe was proportional to the negative of the pressure gradient. This relationship, which is called Darcy's law and was subsequently modified to include the fluid viscosity, can be stated as follows:

$$P' = \frac{\mu}{K}\, v,$$

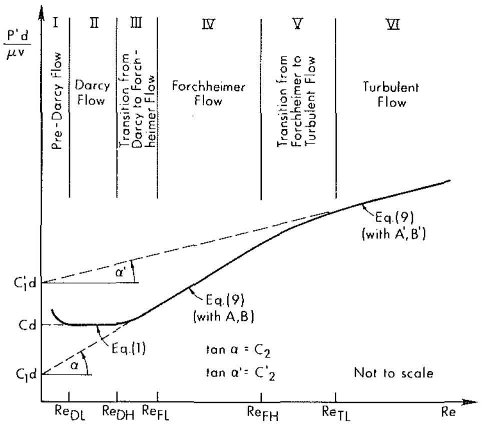

Fig. 1 Zones of flow through porous media

where P' represents the negative of the pressure gradient in the direction of flow, v is the volume rate of flow per unit area (called the Darcian speed or simply speed[2]), μ is the dynamic viscosity of the fluid, and K is a constant of proportionality called the permeability. It will be found convenient to divide the preceding equation by $\mu v d^{-1}$, where d is a characteristic dimension of the porous matrix (sphere diameter in the present case), with the following result:

$$\frac{P'd}{\mu v} = Cd, \tag{1}$$

where $C = K^{-1}$. The Reynolds numbers corresponding to the lower and upper bounds of the Darcy regime will be designated by Re_{DL} and Re_{DH}, respectively.

The pre-Darcy and Darcy regimes of flow are shown in Fig. 1 (zones I and II, respectively). In this figure the dashed horizontal line labeled equation (1) represents Darcy's law, and the solid curve represents (qualitatively) the actual variation of $P'd/\mu v$ versus Re for a porous medium. Obviously, equation, equation (1) represents actual behavior only for $\mathrm{Re}_{DL} < \mathrm{Re} \leq \mathrm{Re}_{DH}$.

A great deal of analytical and experimental effort has been expended upon the determination of K in Darcy's law for various porous media. The following semi-empirical equation has been found to accurately represent many experimental data:

$$K = (\kappa s_0^2 \alpha)^{-1}; \quad \alpha = \frac{(1-\epsilon)^2}{\epsilon^3} \tag{2}$$

where ϵ is the porosity, s_0 is the specific surface of the particles (surface area per unit volume) and κ is an experimentally determined dimensionless constant called the Kozeny-Carman constant. For a porous medium composed of spheres of uniform diameter d, $s_0 = 6/d$, and hence

---

[1] The subscript *DL* is a mnemonic device which refers to the lowest value (*L*) of the Reynolds number for which Darcy (*D*) flow occurs. Similar subscripts will be used to refer to the highest value (*H*) of the Reynolds number for which a particular kind of flow occurs.

[2] The term "velocity" will be used in this connection when the context makes the intended meaning clear.

Nomenclature

A, B = first and second Ergun constants for Forchheimer (laminar) flow
A', B' = first and second Ergun constants for turbulent flow
C = inverse of K
d = diameter of sphere
d_h = mean diameter of spheres, per equation (4)
D = diameter of test section of water tunnel
K = permeability
P' = negative of the pressure gradient
Re = Reynolds number
v = Darcian speed
α = a function of ϵ, per equation (2)
β = a function of ϵ, per equation (8)
ϵ = porosity
κ = Kozeny-Carman constant
μ = dynamic viscosity
ρ = fluid density

Downloaded 02 Jun 2010 to 171.66.16.66. Redistribution subject to ASME license or copyright; see http://www.asme.org/terms/Terms_Use.cfm

$$K = \frac{d^2}{36\kappa\alpha}. \tag{3}$$

For porous media composed of particles that are not uniform in size, Irmay [3] has suggested that d in equation (3) be replaced by the weighted mean harmonic diameter d_h defined as follows:

$$d_h = \left(\sum_{i=1}^{n} \frac{f_i}{d_i}\right)^{-1}, \tag{4}$$

where f_i is the mass fraction for particles having diameter d_i. Equation (4) presumes that all particles have the same density.

Quantitative Information: Non-Darcy Flow. The literature abounds with references to "non-Darcy flow," which is an umbrella term that refers to all flows for which $\mathrm{Re} > \mathrm{Re}_{DH}$ and encompasses all the various phenomena described by Dybbs and Edwards in their second, third and fourth differentiated flow regimes. Inertia forces and turbulence effects come into play in non-Darcy flow, in addition to the viscous forces that are solely responsible for Darcy flow. Forchheimer [4] is widely regarded as being the first to suggest a nonlinear relationship between the pressure gradient and fluid velocity for $\mathrm{Re} > \mathrm{Re}_{DH}$. In 1901 he proposed a second order, and later a third order equation to fit experimental data as follows:

$$P' = av + bv^2, \tag{5}$$

$$P' = av + bv^2 + cv^3, \tag{6}$$

where a, b, and c are empirical constants. In 1930 Forchheimer suggested that experimental data could be represented better by the following correlation:

$$P' = av + bv^m, \tag{7}$$

where $1.6 \leq m \leq 2$. A major shortcoming of Forchheimer's equations is that none of them can adequately account for the combined effects of geometry and viscosity and hence the empirical constants contained therein must be redetermined for each specific porous medium.

In 1952 Ergun [5] generalized equation (5) by examining the phenomenon from the point of view of its dependence upon the flow rate and properties of the fluid, and upon the fractional void volume, orientation, size and shape of the porous matrix. He concluded that P' can be equated to the sum of two terms as follows:

$$P' = \left(\frac{A\alpha\mu}{d^2}\right)v + \left(\frac{B\beta\rho}{d}\right)v^2;$$

$$\alpha = \frac{(1-\epsilon)^2}{\epsilon^3} \quad \text{and} \quad \beta = \frac{(1-\epsilon)}{\epsilon^3} \tag{8}$$

where A and B are dimensionless constants, μ is the dynamic viscosity and ρ the density of the fluid, d is the mean equivalent diameter of the particles comprising the porous matrix and ϵ is the porosity of the matrix. A and B will be referred to hereafter as the first and second Ergun constants for Forchheimer flow. In 1958 Irmay [6] derived equation (8) for steady flow by averaging the Navier-Stokes equations. If equation (8) is divided by $\mu v d^{-1}$ the following convenient form is obtained:

$$\frac{P'd}{\mu v} = C_1 d + C_2 \mathrm{Re} \tag{9}$$

where

$$C_1 d = \frac{A\alpha}{d}, \quad C_2 = \frac{B\beta}{d} \quad \text{and} \quad \mathrm{Re} = \frac{dv\rho}{\mu}.$$

A graph of equation (9) is shown in Fig. 1; it is valid in the Forchheimer regime, labeled Region IV, for which $\mathrm{Re}_{FL} < \mathrm{Re} \leq \mathrm{Re}_{FH}$.

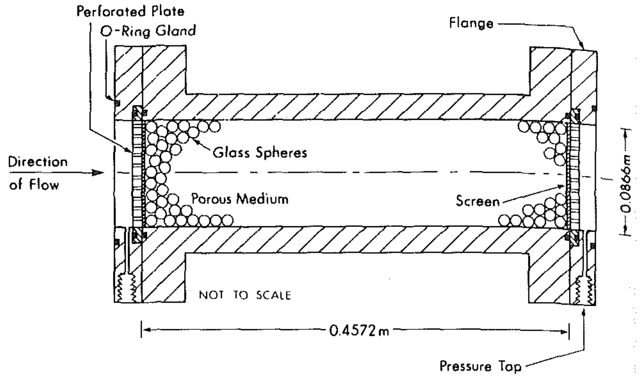

Fig. 2 Test section of water tunnel

The applicability of equation (8) depends upon the universality and accuracy of the constants A and B. Ergun concluded that $A = 150$ and $B = 1.75$, but subsequent experimental data have shown that these values are not definitive. Thus, Macdonald et al. [7] have compared equation (8) with data obtained by Rumpt and Gupta [8] and they have found that these data indicate a weak functional dependence of A and B upon the porosity. Furthermore, they claim that a better fit to the data can be obtained by using $\alpha = \epsilon^{-5.5}$ instead of $(1-\epsilon)^2/\epsilon^3$; however, this dependence upon porosity was found to be inaccurate over the wide range of porosity from 37 to 64 percent. Macdonald et al. recommend that for engineering applications the values of A and B be taken equal to 180 and 1.8, respectively, for smooth particles.

Experimental Apparatus and Procedures

The primary piece of apparatus used in the present study was the stainless steel water tunnel described in [9], subsequently modified. Through this tunnel, water can be either pumped with a variable speed drive or gravity-fed through a loop into which any one of a series of calibrated orifice plates can be inserted to measure the rate of flow. Gravity feed, in conjunction with a constant head tank, was used to create low speed flows (less than 0.0004 m/s) and the variable speed pump was used for higher rates of flow (from 0.004 to 0.13 m/s). An electrically heated section and water cooled concentric tube heat exchanger are incorporated into the loop to permit temperature control.

The tunnel contains a stainless steel cylindrical test section into which the glass spheres comprising the porous matrices were inserted. The glass spheres were held in place by means of a pair of circular perforated retaining plates as shown in Fig. 2. Thin stainless steel screens were interposed between the glass spheres and the perforated retaining plates in order to prevent clogging of the perforations. A thermocouple placed 7 cm downstream from the test section was used to measure the temperature of the flowing water from which the experimental values of ρ and μ could be determined. The temperature of the water ranged from 19.0 to 22.7 °C in the present study.

The pressure drop across the test section was measured by means of a Foxboro Differential Pressure Cell for low pressure differences (less than 1.25 kPa) and by means of a series of manometers for higher pressure differences (from 1.25 to 62 kPa). The relatively small pressure drop across the perforated plates was determined experimentally as a function of velocity by performing tests in the absence of glass spheres in the test section, and this quantity was subtracted from the overall pressure drop across the test section in the presence of glass spheres in order to obtain the pressure drop across the porous medium. The pressure drop across the porous medium

Downloaded 02 Jun 2010 to 171.66.16.66. Redistribution subject to ASME license or copyright; see http://www.asme.org/terms/Terms_Use.cfm

Table 1 Results

	d, d_h (mm)	ϵ	κ	A	B	A'	B'
Simple Media	2.098	0.357	5.33	184.2	1.925	198.8	1.892
	3.072	0.360	5.28	177.8	1.902	218.3	1.638
	4.029	0.359	5.12	174.0	1.811	216.8.	1.545
Complex Media	3.690	0.348	5.33	180.6	1.920	237.1	1.593
	3.276	0.344	5.38	183.5	1.935	227.6	1.690
	2.759	0.342	5.28	179.5	1.882	223.8	1.616
U*	±0.001d, d_h	±0.004	±0.23	±9.0	±0.095	±11.2	±0.080
Mean value (excluding 2.098 mm)						224.7	1.612

*Uncertainty at 20:1 odds

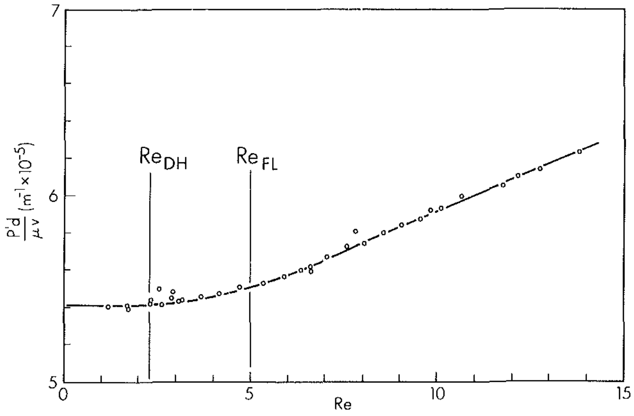

Fig. 3 Graph of data for Darcy flow (Uncertainty in Re = ±0.03 Re and in $P'd/\mu v$ = ±0.042 $P'd/\mu v$ at 20:1 odds)

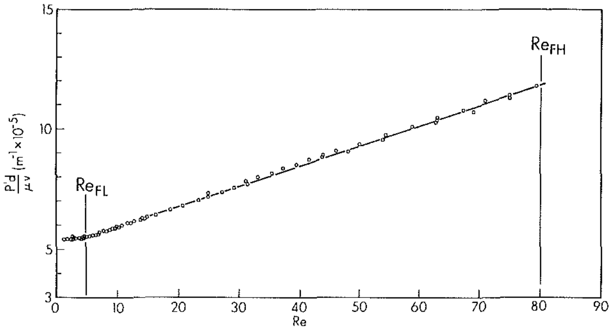

Fig. 4 Graph of data for Forchheimer flow (Uncertainty in Re = ±0.03 Re and in $P'd/\mu v$ = ±0.042 $P'd/\mu v$ at 20:1 odds)

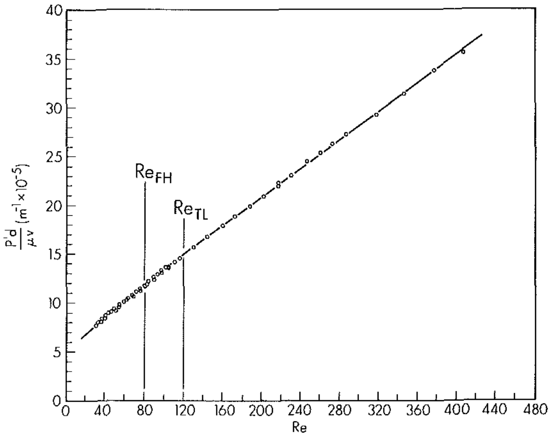

Fig. 5 Graph of data for Turbulent flow (Uncertainty in Re = ±0.03 Re and in $P'd/\mu v$ = ±0.042 $P'\mu\partial\mu v$ at 20:1 odds)

divided by the axial length of the porous medium yielded experimental values of P′ corresponding to arbitrarily imposed values of v. All reported measurements of velocity in the test section and pressure drop across the test section are estimated to be correct to within 1 and 2 percent, respectively.

The porous media used in the present study consisted of matrices of small soda-lime glass spheres saturated with water. The nominal diameters of the glass spheres were 2, 3, and 4 mm. By carefully measuring the density of the spheres[3] and weighing individually a statistically large number (100 or more) of each size on a high precision balance, it was determined that the average equivalent mean diameters, d, of the three sizes were 2.098, 3.072, and 4.029 mm, respectively. So-called "simple" porous media were created by filling the test section of the tunnel with the preceding three sizes of glass spheres, and three "complex" media were created by mixing the 2 and 4 mm spheres in the following proportions by mass of former to latter: 10/90 percent; 25/75 percent; 50/50 percent. The harmonic mean diameter, d_h, for these complex media are equal to 3.690, 3.276, and 2.759 mm, respectively (see equation (4)). Hereafter, the simple media will be designated by citing their values of d, and the complex media will be designated by their values of d_h.

The glass spheres were loaded into the test section of the tunnel in a "random" fashion, by which is meant the following: The test section was removed from the tunnel, dried and stood on end with one perforated plate and screen in place at the bottom. Then the (dry) glass spheres were poured into the test section in small pre-mixed, weighed batches. Each batch was gently pressed down with the flat end of a circular rod, in order to create a firm and stable matrix. When the test section was completely full, the second screen was installed and the second perforated plate was attached, and this whole assembly was then reinserted into the tunnel. The porosities, ϵ, of the porous matrices were easily calculated from the known weights of the porous matrices and known volume of the test section. The values of ϵ for the six media employed are listed in Table 1. A total of 640 experimental data points were obtained in the range $0.18 \leq Re \leq 408$.

Analysis of the Data and Results

Darcy and Forchheimer Flow. The data sets for each value of d and d_h (six in all) were plotted using the coordinates indicated in Fig. 1 and shown, by way of example, piece-meal in Figs. 3, 4, and 5. A total of 513 data points were taken with Darcy and Forchheimer flow, including transition regions. The plotted points were sufficiently dense as to determine, with little uncertainty, a set of six smooth representative "data curves."

Determination of Re_{DH}, Re_{FL}, and Re_{FH}. By ascertaining the values of Re at which changes occurred in the slopes of the data curves for the three simple porous media, it was determined that $Re_{DH} = 2.3 \pm 0.1$, $Re_{FL} = 5.0 \pm 0.5$ and $Re_{FH} = 80 \pm 5$. To determine these bounds for the complex media it was found necessary to consider two different Reynolds numbers that coexist for a given fluid bulk velocity, namely, Re_{d_ℓ} and Re_{d_s}, where the subscripts d_ℓ and d_s designate Reynolds numbers that are based upon the diameters of the largest and smallest spheres comprising the complex porous matrix, respectively.

Now, if it is hypothesized that the upper bounds of the Darcy and Forchheimer flow regimes for complex media are determined by the *largest* spheres in the matrix, because transition from one flow regime to the next higher is *initiated* by the largest spheres, then it follows that the upper bounds for a

---

[3] This was done by first accurately weighing an empty graduated flask and then weighing the same flask when filled with a known mass of glass spheres plus water.

Downloaded 02 Jun 2010 to 171.66.16.66. Redistribution subject to ASME license or copyright; see http://www.asme.org/terms/Terms_Use.cfm

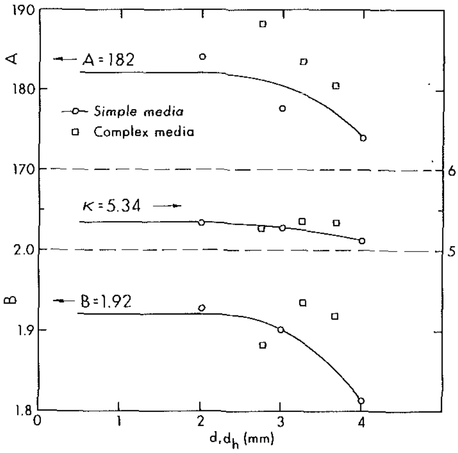

Fig. 6 Graphs of κ, A, and B (Uncertainties listed in Table 1)

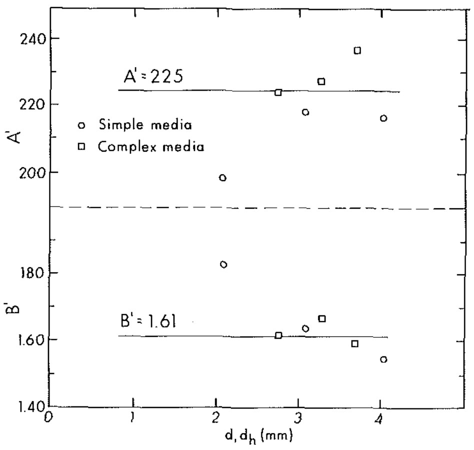

Fig. 7 Plots of A' and B' (Uncertainties listed in Table 1)

complex medium with known d_h can be calculated by multiplying the upper bounds determined for simple media by the ratio d_h/d_ℓ. When this is done for the three values $d_h = 3.690$, 3.276, and 2.759 mm utilized in the present study, the corresponding Reynolds numbers *based upon* d_h are 2.1, 1.9 and 1.6, respectively. These values agreed well with the Reynolds numbers *based upon* d_h at which the data curves for the complex media diverge from Darcy theory (that is, from horizontality), and this agreement is considered to be a confirmation of the validity of the original hypothesis. A similar argument was found to yield consistent results with respect to Re_{FH}. Finally, the converse of the argument, namely, that the lower bounds of flow regimes (in particular, Re_{FL}) for complex media can be determined by multiplying Re_{FL} for simple media by the ratio d_h/d_s was also found to be consistent with the experimental data curves.

Determination of κ. By inserting the value for κ obtained from equation (1) into equation (3) it follows that

$$\kappa = \frac{d^2 P'}{36 \mu v \alpha}\,; \quad \alpha = \frac{(1-\epsilon)^2}{\epsilon^3}\,, \tag{10}$$

which is a formula for the Kozeny-Carman constant, κ, in terms of the measured experimental quantities d, P', μ, v, and ϵ. Table 1 lists the measured values of κ for the six media studied here, and Fig. 6 shows a plot of these values versus d or d_h.

The measured values of κ listed in Table 1 incorporates an unavoidable experimental error due to the so-called "wall effect." This "wall effect" is a consequence of the fact that the glass spheres which contact the *wall* of the containing test section do so at discrete points of tangency, and hence the porosity of the medium near the containing wall is not uniform; in fact, the porosity approaches unity as the wall is approached. The increased porosity near the wall has the spurious effect of diminishing the measured value of κ and the error becomes more pronounced as the particle size (sphere diameter, d) increases (relative to the test section diameter D). The curve in Fig. 6 which passes through the plotted values of κ for the simple media droops with increasing d because of the wall effect. The shape of this curve suggests that the wall effect is nearly negligible for sphere diameters less than 2 mm ($d/D = 0.023$). Since all three complex media contain appreciable numbers of 2 mm spheres, the wall effects for all three complex media are nearly negligible, which is consistent with the nearly-equal values of κ for complex media listed in Table 1 and plotted in Fig. 6. It was concluded on the basis of the six data points in Fig. 6 that the best estimate for the value of κ is 5.34.

Determination of A and B. The values of A and B were calculated by first determining the equation of the line fitted to the data points as shown, by way of example, in Fig. 4 and then using the fact that $C_1 d$ and C_2 represent the intercept and slope of this line, per equation (9). From this it follows that $A = C_1 d(d/\alpha)$ and $B = C_2\ (d/\beta)$. The experimentally determined values of A and B for the six media studied are listed in Table 1 and plotted in Fig. 6. The influence of the wall effect was taken into account in the same manner as was done in the case of κ and it was determined that $A = 182$ and $B = 1.92$.

Post Forchheimer Flow: Turbulence. The term "post Forchheimer flow" refers to flows for which $\mathrm{Re} > \mathrm{Re}_{FH}$, that is, for Reynolds numbers higher than those for which Forchheimer flow occurs. As stated earlier, there is a transition from laminar to turbulent flow as Re increases beyond Re_{FH}. There has not been published heretofore a correlation for the resistance to flow in porous media that differentiates between the *laminar* Forchheimer and turbulent regimes of flow, and hence this part of the present investigation is considered to be particularly interesting.

A sample plot of the experimental data for $\mathrm{Re} > \mathrm{Re}_{FH}$ is shown in Fig. 5. These plots reveal that for $\mathrm{Re} > 120$ (based upon d or d_h) the data fall on a straight line for every medium studied. The region defined by $80 < \mathrm{Re} \leq 120$ in Fig. 5 corresponds to the transition Region V in Fig. 1 from which it follows that the minimum Reynolds number for turbulent flow, Re_{TL}, equals 120. The region $\mathrm{Re} > \mathrm{R}_{TL}$ in Fig. 5 corresponds to Region VI in Fig. 1. It is interesting and consistent with the general characteristics of turbulence to note that $\mathrm{Re}_{TL} = 120$ for simple media (where Re is based on d) and also for complex media (where Re is based on d_h). Thus, when turbulent eddies occur the fluid "sees" a complex porous matrix as though it were a simple matrix composed of uniform particles having diameters equal to d_h.

The fact that the experimental data plotted in Fig. 5 fall on a straight line for $\mathrm{Re} > \mathrm{Re}_{TL}$ leads to the conclusion that equation (8) can be used to represent the data for turbulent flow exactly as it was for Forchheimer flow—the only difference in the two cases is in the values of the Ergun constants, which, for turbulent flow, will be represented by A' and B'.

The experimentally determined values of A' and B' for the six media studied are listed in Table 1 and plotted in Fig. 7. The plot of the data reveal two facts graphically: 1) the results for 2 mm glass spheres are significantly different from those for the other five media, and 2) the latter five values of A' and B' cluster in a random fashion around means from which they differ by less than 5.6 and 4.2 percent, respectively. The reason for the divergence of A' and B' for the 2 mm spheres is doubtlessly due to the fact that the porous matrix composed of

Downloaded 02 Jun 2010 to 171.66.16.66. Redistribution subject to ASME license or copyright; see http://www.asme.org/terms/Terms_Use.cfm

2 mm spheres was structurally unstable under conditions of turbulent (relatively high speed) flow. In this context "structurally unstable" means that the glass spheres *moved* under the action of the fluid stream. This was ascertained experimentally by measuring the permeability of the porous medium (with Darcy flow) after each set of turbulent experiments. It was observed that the permeability of the 2 mm matrix was generally *reduced* after the 2 mm matrix had been subjected to turbulent flow tests. Thus, the relatively high speed turbulent flow *compacted* the 2 mm matrix. This was not observed to occur with any other of the media studied. For this reason the values of A' and B' for the 2 mm matrix were discarded, and the final values of A' and B' were taken to be the averages for the five remaining media, as indicated in Table 1. It should also be noted that no consistent "wall effect" was observed with turbulent flow. This does not imply that no wall effect was present, but rather that its influence when turbulence flow occurs is relatively small, as might be expected when the enhancement of momentum transfer (and consequent flattening of the velocity profile) due to turbulence is considered. After disregarding the turbulence data for the 2 mm matrix, the values of A' and B' based on the average values for the remaining five media are $A' = 225$ and $B' = 1.61$, respectively.

Discussion of Errors

Darcy and Forchheimer Flow. A total of 67 data points were collected in the Darcy regime ($\mathrm{Re} \leq 2.3$) and 362 data points were collected in the Forchheimer regime ($5 < \mathrm{Re} \leq 80$). The values of $P'd/\mu v$ for each datum in these two regions of flow calculated by using equations (1) and (8) together with the values of $\kappa = 5.34$, $A = 182$, and $B = 1.92$ differ from the corresponiding experimental values by less than 2.8 percent.

The transition region between Darcy and Forchheimer flow ($2.3 < \mathrm{Re} \leq 5$), (see Region II in Fig. 1) is difficult to characterize mathematically. However, this difficulty can be overcome by making an approximation that will incur negligible error for most applications. The approximation consists of defining an artificial *point of transition* (instead of *region of transition*) at which an abrupt change from Darcy to Forchheimer flow is assumed to occur. The Reynolds number corresponding to this artificial transition point will be designated by Re_{DF}. If, now, Re_{DF} is taken equal to 3, then the experimental data points in the transition region are represented by Darcy's law for $2.3 < \mathrm{Re} \leq 3$ and by Ergun's equation for $3 < \mathrm{Re} \leq 5$ (with appropriate values of the constants κ, A and B, as the case may be) with less than 2.8 percent error. This level of error is acceptable for most applications. The preceding technique for representing the transition region from Darcy to Forchheimer flow was used successfully in [10].

Turbulent Flow. A total of 82 data points were collected in the turbulent flow regime ($\mathrm{Re} > 120$). The highest value of Re achieved was 408. The values of $P'd/\mu v$ for each data point in the turbulent regime calculated by using Ergun's equation with $A' = 225$ and $B' = 1.61$ differ from the corresponding experimental values by less than 3.5 percent.

The complex transition region between Forchheimer and turbulent flow can be treated in a manner analogous to that between Darcy and Forchheimer flow. Thus, if Re_{FT} represents the artificial *point of transition* from Forchheimer to turbulent flow, and if Re_{FT} is taken equal to 100, then Ergun's equation with appropriate constants A and B or A' and B' represents the experimental transition data with errors less than 7 percent. This level of error may not always be negligible, but the advantage of having a simple mathematical representation for this transition region may outweigh the disadvantages associated with the error.

Conclusions

The present experimental investigation leads to six conclusions as listed below. Conclusions 1 and 3 report the magnitudes of certain limits and the values of κ, A, and B with an accuracy that is greater than has been available heretofore. Conclusions 2 and 4 indicate how the limits of Darcy and Forchheimer flow can be determined for complex porous media. Conclusions 5 and 6 indicate how the resistance to flow in the turbulent regime and in the transition regions can be characterized.

1. For simple media, Darcy flow occurs for $\mathrm{Re}_{DL} < \mathrm{Re}_{DH} \leq 2.3$ and the Kozeny-Carman constant, κ, equals 5.34. R_{DL} is less than 10^{-5}.
2. For complex media, Darcy flow occurs for $\mathrm{Re} \leq 2.3(d_h/d_\ell)$ and the Kozeny-Carman constant, κ, equals 5.34 if the characteristic dimension of the complex porous medium is taken to be d_h.
3. For simple media, Forchheimer flow occurs for Reynolds numbers between $\mathrm{Re}_{FL} = 5$ and $\mathrm{Re}_{FH} = 80$ and the Ergun constants are $A = 182$ and $B = 1.92$. These values are close to those recommended by MacDonald, et al. [7], namely, $A = 180$ and $B = 1.8$. Forchheimer flow spans the second and third regimes of flow described by Dybbs and Edwards (see review of the literature).
4. For complex media, Forchheimer flow occurs for Reynolds numbers between 5 (d_h/d_s) and 80 (d_h/d_ℓ) and the Ergun constants are $A = 182$ and $B = 1.92$.
5. Turbulent flow occurs for both simple and complex media when the Reynolds number exceeds 120. The resistance to flow in the turbulent regime can be characterized by Ergun's modification of Forchheimer's equation, if the constants therein are taken to be $A' = 225$ and $B' = 1.61$. This finding is particularly interesting and may explain why Forchheimer proposed equation (7) for "non-Darcy flow" subsequent to his original proposal per equation (5)—he was probably attempting to account for the diminished slope of the curve in Fig. 5 in the turbulent regime.
6. The transition regions between Darcy and Forchheimer flow and between Forchheimer and turbulent flow can be described in simple mathematical terms if the transitions are assumed to occur at particular points. This assumption will result in negligible error in most applications.

Acknowledgment

This research was supported by National Science Foundation Grant No. CBT83-12095.

References

1 Dybbs, A., and Edwards, R. V., Department of Fluid, Thermal and Aerospace Sciences report, FTAS/TR (Case Western Reserve University) No. 75-117, Workshop on Heat and Mass Transfer in Porous Media (PB-252 387) (NTIS: Springfield, VA) 1975, 228 pp.

2 Bear, J., *Dynamics of Fluids in Porous Media*, American Elsevier Pub. Co., Inc., 1972, pp. 125–127.

3 Irmay, S., "On the Theoretical Derivation of Darcy and Forchheimer Formula," *Transaction American Geographical Union*, Vol. 39, No. 4, 1958, pp. 702–707.

4 Forchheimer, P., Wasserbeweguing durch Boden, *Z. Ver. Deutsch Ing.*, Vol. 45, 1901, pp. 1782–1788.

5 Ergun, S., "Fluid Flow through Packed Column," *Chemical Engineering Progress*, Vol. 48, No. 2, 1952, pp. 89–94.

6 Irmay, S., "Theoretical Model of Flow through Porous Media," RILEM Symp. Transfer of Water in Porous Media, Paris, 1964; *Bull. RILEM*, Vol. 29, Dec. 1965, pp. 36–43.

7 Macdonald, I. F., El-Sayed, M. S., Mow, K., Dullien, F. A. L., "Flow through Porous Media—the Ergun's Equation Revisited," *American Chemical Society*, 1979.

8 Rumpt, H., and Gupta, A. R., *Chem. Ing. Tech.*, Vol. 43, 1971, p. 367.

9 Fand, R. M., "Heat Transfer by Forced Convection from a Cylinder to Water in Crossflow," *Int. J. of Heat and Mass Transfer*, Vol. 8, 1965, pp. 995–1010.

10 Fand, R. M., Steinberger, T. E., Cheng, P., "Natural Convection Heat Transfer from a Horizontal Cylinder Embedded in a Porous Medium," *Int. J. of Heat and Mass Transfer*, Vol. 29, 1986, pp. 119–133.

Downloaded 02 Jun 2010 to 171.66.16.66. Redistribution subject to ASME license or copyright; see http://www.asme.org/terms/Terms_Use.cfm

DISCUSSION

E. Guyon[1], A. Hansen[2], and S. Roux[1]

The comparison between the transport properties of monodisperse arrays of spheres and bidisperse ones is a first step toward an understanding of the effect of a moderate dispersion of pore sizes in a well characterized random geometry. It was found that both the Formation Factor (normalized resistance of the fluid filling the pores) and Darcy permeability were similar in both cases (with a proper averaging of the sphere radii in the latter case [11]. Dispersion measures a distribution of the transit times across the porous medium and was expected to reveal the distribution of currents coming from that of the channel radii. But, again, experiments in carefully prepared bidisperse packup could be fit with data on single size ones by the same averaging of sphere radii as above [12].

The article of Fand et al. offers an alternative approach to study the effect of the distribution of local hydrodynamic currents. It consists in following the transition of the linear Darcy flow variation (D) to a nonlinear one given by a law of the type:

$$p' = av + bv^m$$

p' is the pressure gradient along the flow, v is the average flow rate. In this study results obtained on binary mixtures of spheres ($d=2$ and 4 mm) are compared to single size ones ($d=2,3,4$ mm).

The linear coefficient a is well described by the classical Kozeny-Carman relation. The nonlinear term is due to inertia for intermediate flow rates and to turbulence at higher Reynolds numbers. The article introduces 3 critical values for Re which can be identified as changes of slope in a p'/v versus v plot for *single size* spheres:

$\mathrm{Re}_{DH} = 2.3 \pm 0.1$, $\mathrm{Re}_{FL} = 5.05 \pm 0.5$ which give the lower and upper limit for the transition from linear to nonlinear (F for Forscheimer) regime,

$\mathrm{Re}_{FH} = 80 \pm 5$ for the lower limit of the turbulent one.

The original result is the observation that, in a *bidisperse* array ("complex" medium), the upper bounds of the two regimes (D and F) are controlled by the radii of the largest spheres (in the evaluation of the Reynolds number) whereas, conversely, the lower bound is controlled by the smallest ones. This is consistent with the idea that the largest pores and, consequently, the largest flow rates in this well connected geometry control the onset of nonlinearities and turbulence. The broader range of the transition regime for bidisperse arrays is an indication of the width of the distribution of currents.

This original result can be put in the more general and fundamental framework of nonlinear effects in random lattices. If the local characteristics of an individual bond of such a lattice is piecewise linear with well defined and random thresholds (this randomness being related to the width of the pore size distribution in the above case) the overall characteristics has also a threshold whose nature can be related to that of a percolation problem. Above this threshold, one expects a power law dependence of the variation in a transition regime where one has a progressive increase of bonds going from one state (one linear regime) to the other one (another linear regime). Numerical simulations of such problems using classical methods of statistical physics are under way [13]. On the experimental side the extension of the above work on porous media to the flow of nonlinear fluids (such as Bingham threshold fluid studied in our laboratory) should reinforce the transition region problem considered here. But applications to other problems of random matter physics are also considered, such as hyperelasticity of packed arrays [14], nonlinear electrical behavior of lattices of diodes . . .

Additional References

11 Guyon, E., Oger, L., and Plona, T., to appear in *J. Phys. D.*

12 Hulin, J. P., Charlaix, E., Plona, T., Oger, L., and Guyon, E., to appear in *AIChEJ.*

13 Roux, S., and Herrmann, H., S. Roux, H. J. Hermann, A. Hansen, and E. Guyon, C. R. Acad. Sci. Paris, 1987.

14 Stauffer, D., Herrmann, H. J., Roux, S., *J. Physique*, Vol. 43, 1987, p. 347.

Authors' Closure

The discussors' remarks are much appreciated by the authors. We agree that the comparison between the transport properties of monodisperse and bidisperse arrays of spheres, which constitutes one facet of the present study, is merely a first step toward obtaining an understanding of the effect of a dispersion of pore sizes in a well characterized random geometry. We further agree that the experimental results reported here, particularly those concerning transition, can be related to the more general and fundamental framework of nonlinear effects in random lattices. We look forward with interest to the publication of the numerical simulations of such problems using the classical theory of statistical physics to which the discussors refer. We hope that the relatively accurate experimental data presented in the present paper will be useful for testing the validity of such theoretical studies.

---

[1] Laboratoire d'Hydrodynamique et de Mécanique Physique ESPCI, Paris, France.

[2] Groupe de Physique des Solides, ENS, 75231 Paris, France.

Copyright © 1987 by ASME

Downloaded 02 Jun 2010 to 171.66.16.66. Redistribution subject to ASME license or copyright; see http://www.asme.org/terms/Terms_Use.cfm

Flow Characteristics of Swirling Coaxial Jets From Divergent Nozzles

T. Mahmud

J. S. Truelove

T. F. Wall

Department of Chemical and
Materials Engineering,
University of Newcastle,
N. S. W. 2308
Australia

The aerodynamic characteristics of free, swirling, coaxial jets issuing from an air model of a typical burner for pulverized bituminous coal have been studied. Detailed measurements of mean velocity and static pressure have been obtained in the region near the nozzle exit. The boundary of the reverse-flow zone has been mapped and the recirculated-mass flowrate measured in order to quantify the effects of velocity ratio and swirl in the primary and secondary jets. The influence of burner geometry (divergent-nozzle length and centre-line blockage) has also been studied. The type of flow pattern is found to depend upon the level of swirl in the primary and secondary jets. The recirculated-mass flowrate is predominantly influenced by secondary swirl. The measurements have been compared with predictions obtained by numerical solution of the governing conservation equations in orthogonal curvilinear co-ordinates. The general features of the flows are adequately predicted although discrepancies in detail seem to indicate deficiencies in the turbulence model.

1 Introduction

Swirl is used in industrial burners to promote mixing between fuel and hot recirculated combustion products and thereby achieve stable, high-intensity flames.

Early experimental studies [1] at the International Flame Research Foundation (IFRF) on swirling air jets reported the formation of an internal reverse-flow zone due to vortex breakdown at high levels of swirl (swirl numbers greater than 0.6). A divergent nozzle increased the size and strength of the reverse-flow zone. Later studies [2] identified the type-1 and type-2 flow patterns illustrated in Fig. 1: the former at high primary-jet velocity and the latter at low primary-jet velocity. Recent cold flow studies [3] on a brown-coal burner showed that relatively low levels of primary swirl favoured type-2 flows and also identified the type-3 flow pattern illustrated in Fig. 1. Preliminary aerodynamic studies [4] on a model of a typical black-coal burner showed the formation of the three flow patterns previously observed and also, in the presence of an on-axis bluff body simulating an oil gun, the formation of an attached type-2 flow (type-2A in Fig. 1) with a large reverse-flow zone anchored to the bluff body.

In the present experimental and theoretical investigations, the aerodynamics of unconfined isothermal air jets issuing from a laboratory-scale model of a typical black-coal burner are studied. Detailed meausrements of mean velocity and static pressure in the near-burner region are reported. The effects of nozzle flow (jet velocity and swirl) and burner geometry (bluff body and quarl length) on the flow pattern and recirculated mass flowrate are examined. The measurements are used to evaluate a theoretical model for predicting turbulent flows. The measurements and calculations are intended to give an improved understanding of the aerodynamics of isothermal swirling flows and provide a basis for understanding the mechanism of flame stabilization in related combusting flows.

2 Flow Configuration and Instrumentation

2.1 Swirl Burner. The experiments were performed on a 1/9th-scale air model of a black-coal burner. The air distribution and swirl generation apparatus was the same as that described previously [3]. The burner nozzle, shown schematically in Fig. 2, consisted of two coaxial pipes with a divergent exit, or quarl. A cylindrical bluff body was inserted on the axis for some of the experiments. Swirl in the primary and secondary flows was generated by tangential-entry swirlers located well upstream of the burner nozzle. The flow at the burner throat was turbulent and substantially axisym-

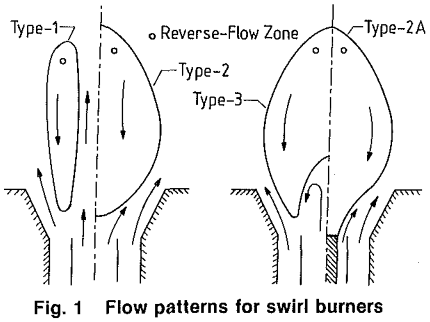

Fig. 1 Flow patterns for swirl burners

Contributed by the Fluids Engineering Division for publication in the JOURNAL OF FLUIDS ENGINEERING. Manuscript received by the Fluids Engineering Division March 21, 1986.

Copyright © 1987 by ASME

Downloaded 02 Jun 2010 to 171.66.16.66. Redistribution subject to ASME license or copyright; see http://www.asme.org/terms/Terms_Use.cfm

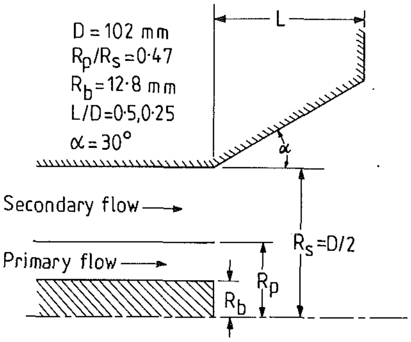

Fig. 2 Nozzle geometry for model black-coal burner

metric (velocity asymmetry along a diameter less than 4 percent).

2.2 Flow Conditions. The flows are characterized by the type of flow pattern (Fig. 1), the levels of swirl in the primary and secondary flows, S_p and S_s respectivley, and the momentum flux ratio, M_R.

The swirl numbers were calculated from the integration of measured time-mean velocity and static gauge pressure distributions at the nozzle exit. The momentum flux ratios were calculated using average nozzle velocities determined from the measured (orifice flowmeter) flowrates.

Detailed distributions of velocity and static pressure have been measured for type-2, type-2A and type-3 flows at two levels of secondary swirl ($S_s = 1.0$, 0.84) with two quarls ($L/D = 0.5$, 0.25). The results are numerous, and space limitations dictate that only those at high swirl with the long quarl (the base flows) can be reported in detail. Further information may be found in [10]. For convenient reference, the operating conditions for the three base flows are summarized in Table 1.

2.3 Instrumentation and Measurement Errors. The pitotmeters were the same as those described previously [3]. The boundary of the reverse-flow zone ($U = 0$ contour) was determined with a two-hole pitotmeter. Spatial resolution was typically ±1mm. The three components of mean velocity and static pressure were measured with a calibrated [3] spherical five-hole pitotmeter. Measurement errors are to be expected due to probe interference, and the high levels of turbulence and strong shear in some regions of the flow. Flow perturbation due to probe interference is difficult to quantify. However, a recent study [5] suggests that for curved probes of the type used here the perturbation in mean velocity (as measured by laser anemometry) is not large, typically less than 10 percent. Little information is available about the effect of turbulence on five-hole pitotmeters, but the effect is known to be significant at high turbulence intensities and can be expected to result in high values for the magnitude of the velocity, with an error proportional to the square of the turbulence

Table 1 Operating conditions for base flows

Operating Conditions	FLOW TYPE Type-3	Type-2	Type-2A
Geometry			
L/D	0.5	0.5	0.5
α,deg	30	30	30
R_p/R_s	0.47	0.47	0.47
R_b/R_p	0	0	0.53
Flow			
$\bar{U}_s$,m/s	18	18	18
$\bar{U}_p$,m/s	11	11	11
S_s	1.0	1.0	1.0
S_p	0	0.42	0
S_s'	0.78	0.78	0.78
S_p'	0	0.25	0
S_t	1.55(1.00)+	1.25(0.94)+	1.32(0.95)+
S_t'	0.73	0.70	0.71
M_R	0.11	0.11	0.092

+ A small but significant contribution to the total axial momentum flux, G_x, is derived from the pressure integral along the quarl wall. Values in parentheses obtained when pressure integral along quarl wall neglected.

Nomenclature

a = scale-factor ratio
A = nozzle cross-sectional area
D = burner nozzle diameter
G_x = axial momentum flux,

$$2\pi\int_0^\infty (\rho U^2 + P) r\, dr$$

G_x' = axial momentum flux excluding static pressure
G_θ = tangential momentum flux,

$$2\pi\int_0^\infty \rho U W r^2 dr$$

h = scale factor
H = coordinate variation term
k = turbulence energy
ℓ = mixing length
L = quarl length
$\dot{m}$ = mass flow rate
M_R = momentum flux ratio, $(\rho\bar{U}^2A)_p/(\rho\bar{U}^2A)_s$
P = mean static gauge pressure
PI = pressure-integral contribution to G_x
r = radial coordinate
R = nozzle radius
S_p = primary swirl number,

$$\int_{R_b}^{R_p} \rho U W r^2 dr \Big/ \left(R_p \int_{R_b}^{R_p} (\rho U^2 + P) r dr\right)$$

S_s = secondary swirl number,

$$\int_{R_p}^{R_s} \rho U W r^2 dr \Big/ \left(R_s \int_{R_p}^{R_s} (\rho U^2 + P) r dr\right)$$

S_t = total swirl number, $G_\theta/(R_s G_x)$
S' = swirl number excluding static pressure
U = mean velocity in x or axial direction
$\bar{U}$ = space-average axial velocity
V = mean velocity in y or radial direction
W = mean tangential velocity
x = x or axial coordinate
y = y coordinate
α = quarl half angle
ϵ = dissipation rate of turbulence energy
ρ = density
θ = tangential coordinate
ψ = streamfunction,

$$2\pi\int_0^r \rho U r dr / \dot{m}_t$$

Subscripts

b = blockage
max = maximum
p = primary
r = recirculation
s = secondary
t = total

Downloaded 02 Jun 2010 to 171.66.16.66. Redistribution subject to ASME license or copyright; see http://www.asme.org/terms/Terms_Use.cfm

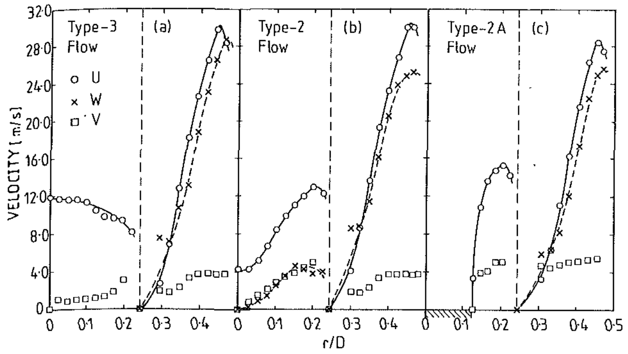

Fig. 3 Radial profiles of velocity at the burner nozzle exit. Radial components determined by continuity. Maximum error 10 percent for U and 15 percent for W as discussed in Section 2.3.

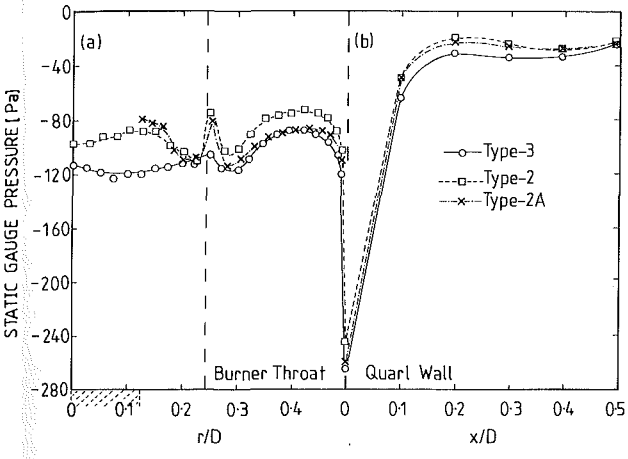

Fig. 4 Profiles of static gauge pressure (a) across the nozzle exit, and (b) along the divergent quarl wall. Errors estimated to be ± 10 percent at the nozzle exit and 2 percent along the quarl wall.

intensity. Nevertheless, remarkably good measurement accuracy is frequently achieved by pressure probes, even in regions of recirculating flow where turbulence intensities exceed 100 percent [6, 7]. The effect of shear on five-hole pitotmeters is significant in regions of high velocity gradient and can be expected to result in an error for the direction of the velocity vector proportional to the shear parameter [8]. A simple theoretical analysis of shear flow past a sphere [9] was used to estimate the measurement error. The effect of shear was small except in a narrow region of the flow adjacent to the quarl. At the nozzle exit, the axial component of velocity was estimated to be about 10 percent (2m/s) high and the tangential component 15 percent (3m/s) low at the point of maximum shear (shear parameter around 0.7). Along the quarl, the maximum error in axial velocity was estimated to be about 15 percent (3 m/s) and in tangential velocity about 5 percent (1 m/s). The radial component of velocity is small throughout most of the flow and consequently subject to larger errors (up to 100 percent low in the shear layer adjacent to the quarl). As a check on the precision of the probe, the mass flowrate calculated by integrating the measured axial velocity profile at the nozzle exit was compared with that measured directly by an orifice flowmeter: the discrepancy was less than 5 percent.

The static pressure in the secondary nozzle at the exit plane (throat) was measured by the a disk probe. These measurements are more accurate than those obtained by the five-hole pitotmeter. The static pressure along the quarl wall was measured by pressure tappings on the wall. The turbulence intensity at the nozzle exit (required for input to the theoretical model) was estimated by a single hot-wire probe aligned with the radial direction. In this orientation, the probe effectively measures the intensity of turbulent fluctuations in the main flow direction. The rms velocity fluctuations normal to the main flow direction were assumed to be 0.6 times that in the main flow direction [12].

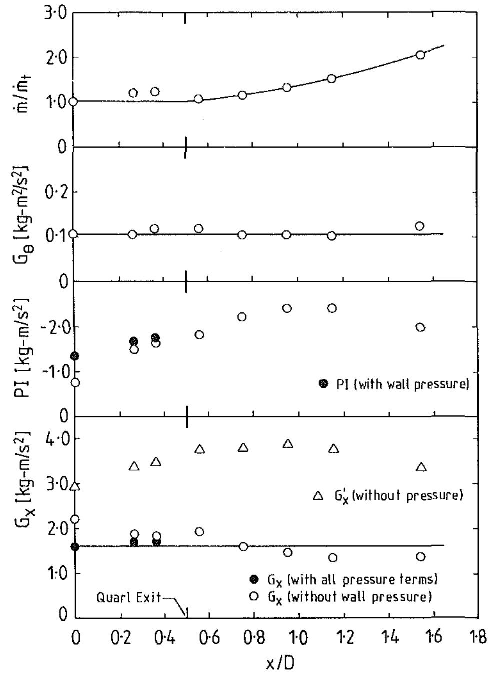

Fig. 5 Variation of mass flowrate and momentum flux along the jet for type-2A flow. Errors estimated to be ± 10 percent for mass flowrate and ± 12 percent for momentum flux.

3 Results

3.1 Exit-velocity and Static Pressure Profiles. Figure 3 shows the radial profiles of axial and tangential components of mean velocity at the nozzle exit for the three base flows. In the secondary nozzle, the axial and tangential velocity profiles are highly peaked, with velocity maxima near the outer edge of the annulus. In the primary nozzle, the axial velocity profiles in the absence of swirl conform to the well-known profiles for fully developed flow in pipes (Fig. 3 (a)) and annuli (Fig. 3 (c)). With primary swirl, the peak in the axial velocity profile is displaced from the axis (Fig. 3(b)). As noted in Section 2.3, the radial component of velocity is subject to rather large measurement errors and consequently the nozzle-exit values were determined by continuity from measured profiles of axial velocity at two axial locations close to the nozzle exit.

Figure 4 shows the profile of static gauge pressure at the nozzle-exit plane, comprising the radial profile across the nozzle exit and the axial profile along the divergent quarl wall. The static gauge pressure within the quarl is negative with a minimum on the quarl wall at the throat of the nozzle. Atmospheric pressure is approached at the end of the divergent quarl. The general features of the pressure profile are similar to those observed previously for strongly-swirled jets from divergent nozzles [1].

3.2 Mass Flowrate and Momentum Conservation. Figure 5 shows the mass flowrate and the axial fluxes of axial momentum (G_x) and tangential momentum (G_θ) at a number of axial positions along the jet for the type-2A flow. The mass flowrate is constant within the divergent quarl and increases beyond the quarl due to entrainment of the surrounding fluid. The axial flux of tangential momentum is conserved along the jet. The axial flux of axial momentum is also conserved along the jet but only when all pressure contributions are included; omitting the contribution from the pressure integral along the quarl wall leads to high values of momentum flux within the quarl.

Downloaded 02 Jun 2010 to 171.66.16.66. Redistribution subject to ASME license or copyright; see http://www.asme.org/terms/Terms_Use.cfm

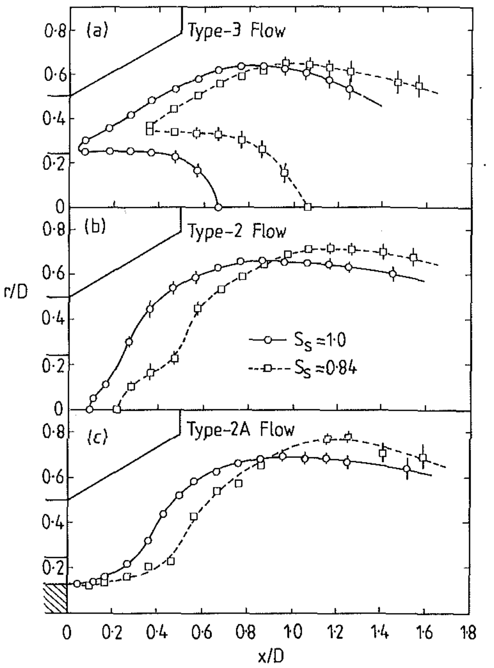

Fig.6 Reverse-flow boundary ($U=0$ contour) for the three base flows and the variation with secondary swirl. Error bars indicate degree of asymmetry. Spatial resolution ± 1mm.

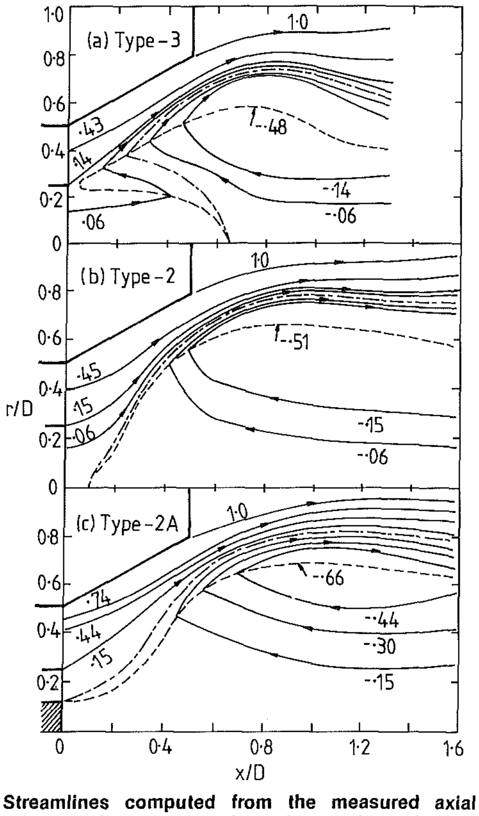

Fig. 7 Streamlines computed from the measured axial velocity distribution. Errors in streamfunction values estimated to be ±10 percent. $U=0$ contour, - - -; $\psi=0$ contour, - • • • -.

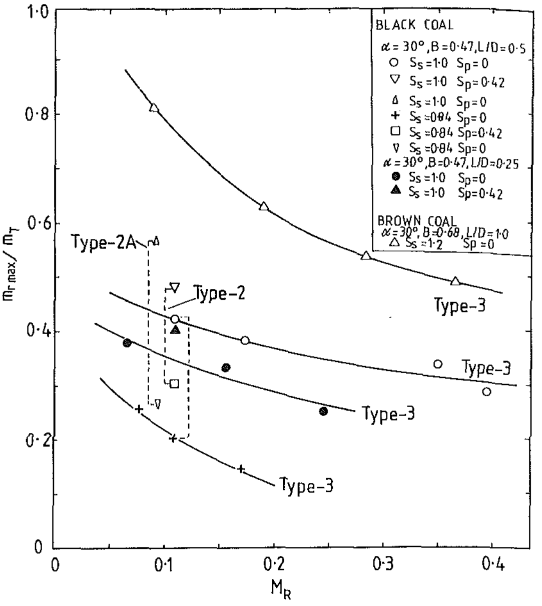

Fig. 8 Recirculated-mass flowrate as a function of momentum flux ratio for various flow conditions. Errors estimated to be ± 10 percent.

3.3 Boundary of the Reverse-Flow Zone. Figure 6 depicts the boundary of the reverse-flow zone ($U=0$ contour) for the three base flows and also shows the influence of secondary swirl on the reverse-flow zone. For the base type-3 flow (Fig. 6(*a*)) the unswirled primary jet penetrates partially the reverse-flow zone. The previous measurements [4] show that the reverse-flow zone is penetrated completely (type-1 flow) at a momentum flux ratio of about 0.8. Swirl in the primary jet results in type-2 flow with a large reverse-flow zone (Fig. 6(*b*)). The addition of a cylindrical bluff body on the axis (extending to the throat of the nozzle) produces type-2A flow with the reverse-flow zone anchored to the bluff body (Fig. 6(*c*)) as a result of the coalescence of the reverse-flow zone induced by swirl and that created by the bluff body. However, for small bluff bodies the reverse-flow zones do not coalesce and separate zones of reverse flow are formed. The critical blockage ratio for an anchored reverse-flow is around 0.05 at a momentum flux ratio of about 0.1.

At the lower secondary swirl level ($S_s=0.84$) the gross features of the reverse-flow boundary are essentially unchanged, although the front stagnation point for the type-2 and type-3 flows is located further from the burner nozzle.

The boundary of the reverse-flow zone at axial distances beyond 2D could not be measured precisely due to the low mean velocities and high levels of turbulent fluctuations.

3.4 Streamline Pattern. The streamline patterns for the three base flows are shown in Fig. 7.

The boundaries of the reverse-flow zone ($U=0$ contour) and the recirculation zone ($\psi=0$ contour) are also shown in the figure.

Figure 7(*a*) shows the streamlines for the type-3 flow. Approximately 90 percent of the primary flow penetrates the reverse-flow zone. The eye of the recirculation zone is located at an axial distance of 0.7D.

Figure 7(*b*) depicts the streamlines for the type-2 flow and illustrates the effect of swirl on the primary flow near the nozzle exit. The eye of the recirculation zone is at an axial location of 0.85D.

Figure 7(*c*) shows the streamlines for the type-2A flow and illustrates the effect of an on-axis bluff body on the flow pattern. The eye of the recirculation zone is located at an axial distance of 0.95D.

For all three flow types, the central reverse-flow zone occupies a considerable volume of the flow. The recirculated mass flowrates are 0.48 $\dot{m}_t$, 0.51 $\dot{m}_t$ and 0.66 $\dot{m}_t$ for the type-3, type-2 and type-2A flows respectively.

The streamlines at the lower secondary swirl number of 0.84 are similar to those shown in Fig. 7, the principal difference being in the mass flowrate of recirculated fluid, as discussed in the following section.

3.5 Recirculated-Mass Flowrate. Figure 8 shows the

Downloaded 02 Jun 2010 to 171.66.16.66. Redistribution subject to ASME license or copyright; see http://www.asme.org/terms/Terms_Use.cfm

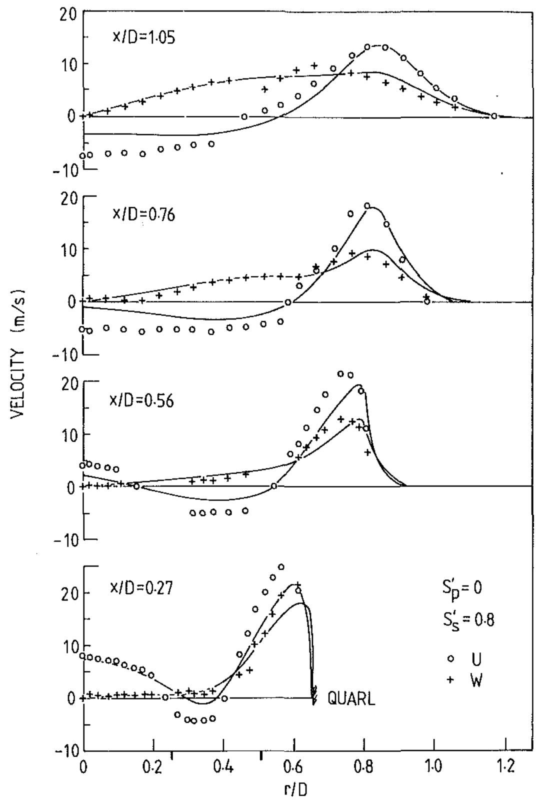

Fig.9 Predicted and measured radial profiles of velocity for the type-3 flow. Errors in velocity estimated to be ± 5 percent. Predictions ——; measurements *o U*, *+ W*.

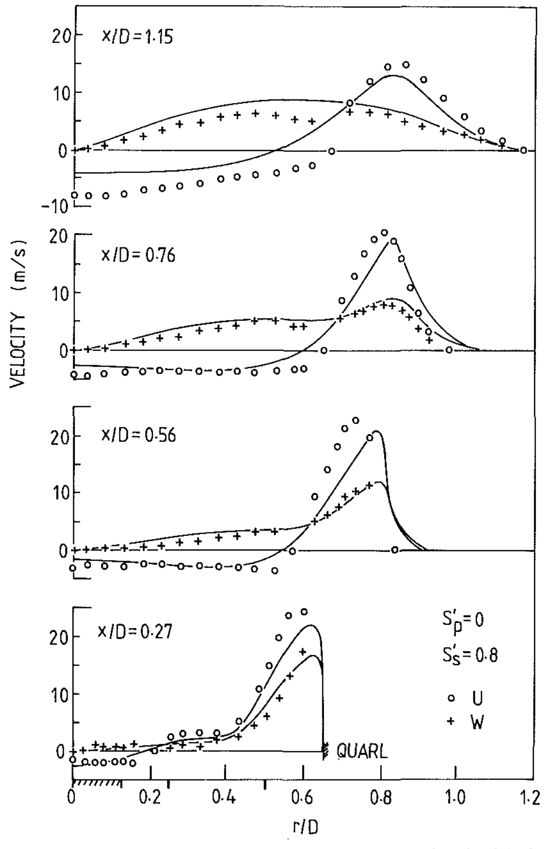

Fig. 10 Predicted and measured radial profiles of velocity for the type-2A flow. Errors in velocity estimated to be ± 5 percent. Predictions ——; measurements *o U*, *+ W*.

maximum recirculated-mass flowrate normalized with the total mass flowrate at the nozzle exit (ψ at the eye of the recirculation zone) as a function of the momentum flux ratio for various flow conditions. As can be seen, the recirculated-mass flowrate decreases with increasing momentum flux ratio. An increase in secondary swirl, from swirl number 0.84 to 1.0, substantially increases the recirculated-mass flowrate, typically by a factor of about 2.0, as indicated by the broken lines joining points which differ only in the level of secondary swirl. The effect of primary swirl is less than that of secondary swirl but is still considerable, especially at low secondary swirl where the addition of primary swirl (swirl number 0.42) increases the recirculated-mass flowrate by a factor of about 1.5. As primary swirl has little effect on the total swirl number the increase in recirculation with primary swirl is presumably a result of the change in flow pattern, from type-3 to type-2. An on-axis bluff body also effects a change in flow pattern, from type-3 to type-2A, and increases the recirculation, by a factor of about 1.2 with the present blockage ratio. A decrease in quarl length, from 0.5D to 0.25D, decreases recirculation by a factor of about 1.2.

Also shown in Fig. 8 are the recirculated-mass flowrates for the brown-coal burner studied previously [3]. The higher swirl, longer quarl and larger nozzle-radius ratio of the brown-coal burner compared to the black-coal burner result in substantially more recirculation.

4 Calculations

The predictions were obtained by numerical solution of the time-mean equations governing conservation of mass and momentum, supplemented by the k-ϵ effective viscosity turbulence model. The general form of the equations for axisymmetric flow formulated in orthogonal curvilinear coordinates is given in Appendix 1.

The boundary conditions were obtained from the measurements wherever possible. Thus, the inlet velocities and turbulence energy were taken from meausrements at the nozzle exit. The turbulence energy dissipation rate at the inlet was estimated as $k^{3/2}/\ell$ with the mixing length, ℓ, taken to be 0.33 times the supply duct dimension (radius for the primary nozzle and annulus width for the secondary nozzle). The turbulence length scale can reasonably be related to the supply duct dimension because the swirlers are located well upstream of the nozzle exit. At the entrainment boundary ($y/D=4.3$), the static pressure was assumed to be constant, U, W, and k were taken as zero and V was calculated from the V-momentum equation with the continuity condition $rV=$const. At the outflow boundary, which was located well beyond the recirculation zone in a region of forward flow ($x/D=10.5$), the axial derivative of static pressure was assumed to be zero and U was calculated from the U-momentum equation. In practice, the calculations of the near-nozzle flow proved to be insensitive to the conditions imposed at the entrainment and outflow boundaries. At walls the velocity was set to zero and so-called wall functions, based on logarithmic velocity profiles, used to bridge the turbulent boundary layer [3, 14].

The differential equations were reduced to a conservative finite-difference form using the control-volume method over an orthogonal curvilinear grid covering one half-plane of the axisymmetric flow domain. Third-order (quadratic) upwind-weighted convective differencing was used to minimize numerical diffusion [13]. The finite-difference equations were solved by well-established computational methods [14].

The computations were carried out on a non-uniform 30×30 grid constructed by matching an orthogonal curvilinear grid in the near-nozzle region to a rectilinear grid in the far field. The grid-generation procedure is outlined in Appendix 2. Grid lines were concentrated in regions of high gradient, for example adjacent to the quarl wall. The final grid was selected after computations with other grids revealed an

Downloaded 02 Jun 2010 to 171.66.16.66. Redistribution subject to ASME license or copyright; see http://www.asme.org/terms/Terms_Use.cfm

acceptable degree of grid independence. Results were also obtained for a 22 × 22 grid and a second 30 × 30 grid with a more uniform distribution of lines in the radial direction. The difference in the calculated velocities was typically less than two percent of the maximum velocity.

Figures 9 and 10 show the calculated and measured radial profiles of axial and tangential components of mean velocity at various axial locations near the quarl for the type-3 and type-2A flows. As can be seen, the general features of the flows are correctly predicted. The axial location of the forward stagnation point and the maximum width of the reverse-flow zone are within 10 percent of the measurements. However, in regions of high velocity gradient and within the reverse-flow zone the predicted and measured axial velocities differ significantly. By comparison, the predicted and measured tangential velocities are in much better agreement. In the reverse-flow zone the axial velocity is consistently underpredicted and as a consequence the calculated maximum recirculated mass flowrates, 0.20 $\dot{m}_t$, 0.21 $\dot{m}_t$ and 0.26 $\dot{m}_t$ for the type-3, type-2 and type-2A flows, respectively, are only about one half of those measured.

The discrepancies between predictions and measurements can be attributed to measurement errors and deficiencies in the turbulence model. In the regions of high velocity gradient adjacent to the quarl wall the pitotmeter yields axial velocities that are high (by around 3 m/s) and tangential velocities that are slightly low (by around 1 m/s). Thus, measurement errors would seem to account for most of the discrepancy in the high-shear region, although the turbulence model cannot be ruled out conclusively. In the reverse-flow zone the pitotmeter may be influenced by the high levels of turbulence (predicted to exceed 100 percent) and yield axial velocities that are too high. However, as noted in section 2.3, good precision is frequently achieved by pitotmeters in recirculation regions where the turbulence intensity is high. Discrepancies have also been observed for the recirculating flow in an annular jet [15] and behind a surface-mounted rib [16]. In the former case the data were obtained by laser anemometry. Thus, the large discrepancy in axial velocity in the reverse-flow zone is unlikely to be due to measurement errors alone and can probably be attributed to deficiencies in the turbulence model.

Eddy-viscosity turbulence models are known to be deficient for swirling recirculating flows due to neglect of anisotropy in the turbulent viscosity. In particular, entrainment and recirculation are not predicted correctly by the k-ϵ turbulence model. A number of corrections to the k-ϵ model have been proposed, generally involving ad-hoc modifications to the turbulence-model constants and/or the generation term in the dissipation equation. Three corrections to the k-ϵ model were examined; the Richardson-number modification to the ϵ-generation term [17]; the streamline-curvature modification to the eddy viscosity [15]; and the preferential-dissipation modification to the ϵ-generation term [18]. However, none was found to reduce the discrepancy in axial velocity in the reverse-flow zone.

The discrepanices may also be due, in part, to errors in the inlet conditions. In particular, the radial velocity is not known very precisely from the measurements and the turbulence dissipation rate in merely estimated from an assumed mixing length. Decreasing the dissipation rate (increasing the mixing length) leads to improved agreement in the reverse-flow zone but at the expense of the agreement elsewhere in the flow. Also, as a result of the shear-induced bias in the axial and tangential velocities at the nozzle exit (see Section 2.3) the swirl number of the inlet flow is probably around 10 percent low, and consequently the axial velocity in the reverse-flow zone is likely to be unpredicted.

5 Conclusions

Several types of stable, symmetric recirculating flows can be produced by swirling coaxial jets issuing from a divergent nozzle. Partial penetration of the reverse-flow zone by the primary jet (type-3 flow) is found in the absence of primary swirl, the degree of penetration being increased by an increase in primary velocity. At high primary velocity the reverse-flow zone is penetrated completely resulting in type-1 flow. However, this (undesirable) flow type is not expected for operating conditions typical of coal burners. The jet flow is deflected around the reverse-flow zone (type-2 flow) when the primary flow is swirled beyond a certain minimum level. An anchored type-2A flow is produced when a bluff body (simulating an oil-gun igniter) is inserted on the axis of the primary nozzle.

The reverse-flow zone is located closer to the nozzle exit as the level of secondary swirl is increased. The location of the reverse-flow zone within the divergent quarl is relatively insensitive to the quarl length (for quarls of length 0.25D and 0.5D) but beyond the quarl the zone is narrower the shorter the quarl.

The recirculated-mass flowrate is increased by an increase in swirl level and a decrease in momentum flux ratio, but is predominantly influenced by secondary swirl. Relatively small levels of primary swirl increase recirculation through a change in flow from type-3 to type-2. The recirculation rate is also increased by an increase in the quarl length and by insertion of a bluff body on the axis of the primary nozzle.

The general features of the flows are adequately represented by a calculation procedure based on numerical solution of the mass and momentum conservation equations supplemented by an eddy-viscosity turbulence model. Unexplained discrepancies between the measurements and calculations are thought to be attributable to the turbulence model. Corrections to the turbulence model, including the well-known Richardson number modification, showed no improvement. Further development of turbulence models for strongly swirling flows is desirable.

Acknowledgments

The continuing support of the National Energy Research Development and Demonstration Program of Australia is gratefully acknowledged.

References

1 Chigier, N. A., and Beer, J. M., "Velocity and Static-Pressure Distributions in Swirling Air Jets issuing from Annular and Divergent Nozzles," ASME *Journal of Basic Engineering*, Vol. 86, 1964, pp. 788–796.

2 Leuckel, W., and Fricker, N., "The Characteristics of Swirl-Stabilized Natural Gas Flames, Part 1: Different Flame Types and their Relation to Flow and Mixing Patterns," *J. Inst. Fuel*, Vol. 49, 1976, pp. 103–112.

3 Dixon, T. F., Truelove, J. S., and Wall, T. F., "Aerodynamic Studies on Swirled Coaxial Jets from Nozzles with Divergent Quarls," ASME JOURNAL OF FLUIDS ENGINEERING, Vol. 105, 1983, pp. 197–203.

4 Mahmud, T., Wall, T. F., and Truelove, J. S., "Aerodynamic Studies on Jets issuing from Swirled Double-Concentric Nozzles with Divergent Exits," *Proc. of Eighth Australasian Fluid Mechanics Conference*, University of Newcastle, Australia, 1983, pp. 1B.10–13.

5 LaRue, J. C., Samuelsen, G. S., and Seiler, E. T., "Momentum and Heat Flux in a Swirl-Stablized Combustor," *Twentieth Symposium (International) on Combustion*, The Combustion Institute, 1984, pp. 277–285.

6 Habib, M. A., and Whitelaw, J. H., "Velocity Characteristics of Confined Coaxial Jets with and without Swirl," ASME JOURNAL OF FLUIDS ENGINEERING, Vol. 102, 1980, pp. 47–53.

7 Vu, B. T., and Gouldin, F. C., "Flow Measurements in a Model Swirl Combustor," *AIAA Journal*, Vol. 20, 1982, pp. 642–651.

8 Davies, P. O. A. L., "The Behaviour of a Pitot Tube in a Transverse Shear," *Journal of Fluid Mechanics*, Vol. 3, 1958, pp. 441–456.

9 Cousins, R. R., "A Note on Shear Flow Past a Sphere," *Journal of Fluid Mechanics*, Vol. 40, 1970, pp. 543–547.

10 Mahmud, T., "Aerodynamic and Combustion Characteristics of Swirl Burners for Pulverized Coal," PhD thesis, The University of Newcastle, Australia, 1986.

11 Pope, S. B., "The Calculation of Turbulent Recirculating Flows in

Downloaded 02 Jun 2010 to 171.66.16.66. Redistribution subject to ASME license or copyright; see http://www.asme.org/terms/Terms_Use.cfm

General Orthogonal Coordinates" *Journal of Computational Physics*, Vol. 26, 1978, pp. 197–217.

12 Habib, M. A., and Whitelaw, J. H., "The Calculation of Turbulent Flow in Wide-Angle Diffusers," *Numerical Heat Transfer*, Vol. 5, 1982, pp. 145–164.

13 Leonard, B. P., "A Stable and Accurate Convective Modelling Procedure Based on Quadratic Upstream Interpolation," *Computer Methods in Applied Mechanics and Engineering*, Vol. 19, 1979, pp. 59–98.

14 Gosman, A. D., and Pun, W. M., "Calculation of Recirculating Flows," Imperial College, Mechanical Engineering Department Report HTS/74/2, 1974.

15 Leschziner, M. A., and Rodi, W., "Calculation of Annular and Twin Parallel Jets using Various Discretization Schemes and Turbulence-Model Variations," ASME JOURNAL OF FLUIDS ENGINEERING, Vol. 103, 1981, pp. 352–360.

16 Benodekar, R. W., Goddard, A. J. H., Gosman, A. D., and Issa, R. I., "Numerical Prediction of Turbulent Flow Over Surface-Mounted Ribs," *AIAA Journal*, Vol 23, 1985, pp. 359–366.

17 Rodi, W., "Influence of Bouyancy and Rotation on Equations for the Turbulent Length Scale," *Proc. Second Symposium on Turbulent Shear Flows*, Imperial College, London, 1979, pp. 10.37–10.42.

18 Hanjalic, K., and Launder, B. E., "Sensitizing the Dissipation Equation to Irrotation Strains," ASME JOURNAL OF FLUIDS ENGINEERING, Vol. 102, 1980, pp. 34–40.

APPENDIX 1

Equations in Orthogonal Curvilinear Coordinates

The transport equations for axisymmetric flow in orthogonal coordinates can be expressed in the general form [11, 12]

$$\nabla_x\left(\rho U\phi-\Gamma_\phi\frac{\partial\phi}{\partial x}\right)+\nabla_y\left(\rho V\phi-\Gamma_\phi\frac{\partial\phi}{\partial y}\right)=S_\phi$$

where the divergence operators are defined by

$$\nabla_x\equiv\frac{1}{rh_y}\frac{\partial}{\partial x}rh_y$$

$$\nabla_y\equiv\frac{1}{rh_x}\frac{\partial}{\partial y}rh_x$$

and h_x and h_y are the scale factors for physical displacements along the curvilinear grid lines in the x and y directions, respectively. The scale factor for the θ direction, h_θ, is equal to the radial distance from the axis of symmetry, r. U, V, and W are the components of mean velocity in the directions x, y, and θ, respectively. The coordinate variation terms $H_{\alpha,x}$ and $H_{\alpha,y}$ are defined by

$$H_{\alpha,x}=\frac{1}{h_\alpha}\frac{\partial h_\alpha}{\partial x}$$

$$H_{\alpha,y}=\frac{1}{h_\alpha}\frac{\partial h_\alpha}{\partial y}$$

where α stands for x, y, or θ. The H's represent the curvature of the coordinate surfaces, for example, $H_{\alpha,x}$ represents the curvature of the surface $\alpha=$const. in the direction of the x-coordinate line. Values of Γ_ϕ and S_ϕ for each variable ϕ are given below.

Continuity:

$\phi=1,\ \Gamma_\phi=0,\ S_\phi=0.$

U-Momentum:

$$\phi\ =\ U,\ \Gamma_\phi=\mu_{\text{eff}}$$

$$\begin{aligned}S_\phi\ =\ &-\frac{\partial P^*}{\partial x}+\nabla_x\left[\mu_{\text{eff}}\left(\frac{\partial U}{\partial x}+2VH_{x,y}\right)\right]\\&+\nabla_y\left[\mu_{\text{eff}}\left(\frac{\partial V}{\partial x}-UH_{x,y}-VH_{y,x}\right)\right]\\&+H_{y,x}\left[\rho V^2-2\mu_{\text{eff}}\left(\frac{\partial V}{\partial y}+UH_{y,x}\right)\right]\\&+H_{\theta,x}\left[\rho W^2-2\mu_{\text{eff}}\left(UH_{\theta,x}+VH_{\theta,y}\right)\right]\\&-H_{x,y}\left[\rho UV-\mu_{\text{eff}}\left(\frac{\partial U}{\partial y}+\frac{\partial V}{\partial x}-UH_{x,y}-VH_{y,x}\right)\right]\end{aligned}$$

V-Momentum:

Obtained from U equation by commuting U and V, and x and y.

W-Momentum

$$\phi\ =\ W,\ \Gamma_\phi=\mu_{\text{eff}}$$

$$\begin{aligned}S_\phi\ =\ &-\nabla_x\left(\mu_{\text{eff}}WH_{\theta,x}\right)-\nabla_y\left(\mu_{\text{eff}}WH_{\theta,y}\right)\\&-H_{\theta,x}\left[\rho UW-\mu_{\text{eff}}\left(\frac{\partial W}{\partial x}-WH_{\theta,x}\right)\right]\\&-H_{\theta,y}\left[\rho VW-\mu_{\text{eff}}\left(\frac{\partial W}{\partial y}-WH_{\theta,y}\right)\right]\end{aligned}$$

Here P^* is the effective pressure, $P+\frac{2}{3}\rho k$, and μ_{eff} is the effective viscosity, $\mu+\mu_t$, where the turbulent viscosity, μ_t, is given by $C_\mu\rho k^2/\epsilon$.

k-Equation:

$\phi=k,\ \Gamma_\phi=\mu_{\text{eff}}/\sigma_k$

$S_\phi=G-\rho\epsilon$

ϵ-Equation:

$\phi=\epsilon,\ \Gamma_\phi=\mu_{\text{eff}}/\sigma_\epsilon$

$$S_\phi=\frac{\epsilon}{k}(C_1G-C_2\rho\epsilon)$$

where the production of kinetic energy is given by

$$\begin{aligned}G\ =\ &\mu_{\text{eff}}\left\{2\left[\left(\frac{\partial U}{\partial x}+VH_{x,y}\right)^2+\left(\frac{\partial V}{\partial y}+UH_{y,x}\right)^2\right.\right.\\&\left.+\left(UH_{\theta,x}+VH_{\theta,y}\right)^2\right]\\&+\left(\frac{\partial U}{\partial y}+\frac{\partial V}{\partial x}-UH_{x,y}-VH_{y,x}\right)^2\\&\left.+\left(\frac{\partial W}{\partial x}-WH_{\theta,x}\right)^2+\left(\frac{\partial W}{\partial y}-WH_{\theta,y}\right)^2\right\}\end{aligned}$$

and the constants C_μ, C_1, C_2, σ_k and σ_ϵ are assigned the values 0.09, 1.44, 1.92, 1.0, and 1.22, respectively.

APPENDIX 2

Grid-Generation Procedure

The grid-generation procedure is based on a conformal mapping of the irregular solution domain in physical ($\tilde{x}$, $\tilde{y}$)-space onto a rectangular polygon in computational (ξ, η)-space. The image of an orthogonal grid inscribed in the rectangular polygon is an orthogonal curvilinear mesh in the physical space, as shown in Fig. 11.

The Cartesian coordinates of the orthogonal curvilinear grid nodes are found from a finite-difference solution of Laplace's equations [11]:

Downloaded 02 Jun 2010 to 171.66.16.66. Redistribution subject to ASME license or copyright; see http://www.asme.org/terms/Terms_Use.cfm

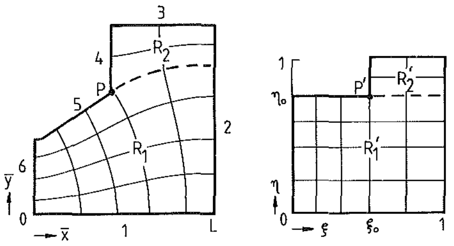

(a) (b)

Fig. 11 **Solution domain in (*a*) physical (Cartesian) space, and (*b*) computational (orthogonal) space.**

$$\frac{\partial^2 \bar{x}}{\partial \xi^2} + a^2 \frac{\partial^2 \bar{x}}{\partial \eta^2} = 0$$

$$\frac{\partial^2 \bar{y}}{\partial \xi^2} + a^2 \frac{\partial^2 \bar{y}}{\partial \eta^2} = 0$$

with the following conditions for the six-sided domain:

Side 1: $\bar{y} = 0, \ \dfrac{\partial \bar{x}}{\partial \eta} = 0$

Side 2: $\bar{x} = L, \ \dfrac{\partial \bar{y}}{\partial \xi} = 0$

Side 3: $\bar{y} = R, \ \dfrac{\partial \bar{x}}{\partial \eta} = 0$

Side 4: $\bar{x} = \bar{x}_B(\bar{y}), \ \dfrac{\partial \bar{y}}{\partial \xi} = -a \dfrac{\partial \bar{x}}{\partial \eta}$

Side 5: $\bar{y} = \bar{y}_Q(\bar{x}), \ \dfrac{\partial \bar{x}}{\partial \eta} = -\dfrac{1}{a} \dfrac{\partial \bar{y}}{\partial \xi}$

Side 6: $\bar{x} = 0, \ \dfrac{\partial \bar{y}}{\partial \xi} = 0$

and constant scale-factor ratio a $(= h_x/h_y)$ determined from

$$a = \frac{L}{\displaystyle\int_0^1 \frac{\partial \bar{y}}{\partial \eta}\bigg|_{\eta=0} d\xi}$$

The coordinates (ξ_0, η_0) of the corner point P' (the image of P) are determined so that the sub-region mappings $R_1 \leftrightarrow R'_1$ and $R_2 \leftrightarrow R'_2$ have the same scale-factor ratios. The sub-regions R_1 and R_2 are formed by extending the boundary line 5 (quarl wall) as shown by the broken line in Fig. 11. The extension is arbitary and can be chosen so that the grid follows the curved shear layer beyond the quarl. The coordinate ξ_0, and a scale-factor ratio a_1, are determined by mapping R_1 onto the unit square. A second scale-factor ratio, a_2, is determined from the mapping of R_2 onto the unit square. Equality of scale-factor ratios for the sub-region mappings is achieved by taking

$$\eta_0 = \frac{1}{1 + (1 - \xi_0) a_1 / a_2}$$

and the scale-factor ratio is given by $\eta_0 a_1$.

Downloaded 02 Jun 2010 to 171.66.16.66. Redistribution subject to ASME license or copyright; see http://www.asme.org/terms/Terms_Use.cfm

Added Mass and Damping for Cylinder Vibrations Within a Confined Fluid Using Deforming Finite Elements

R. Chilukuri

JAYCOR
San Diego, CA 92121

Added mass and fluid damping coefficients for vibrations of an inner cylinder that is enclosed by a concentric outer cylinder are determined by finite element analysis of the unsteady, laminar, incompressible flow in the annulus. Continuously deforming space-time finite elements are used to track the moving cylinder and the changing shape of the space domain. For small cylinder vibration amplitudes, the present results agree well with the work of earlier investigators who solved the linearized Navier-Stokes equations on a fixed mesh. Fluid damping coefficients are shown to increase with vibration amplitude. Added mass coefficients may either increase or decrease with increasing vibration amplitude.

1 Introduction

Forced vibration of an inner cylinder within a concentric, fluid-filled, outer cylinder is considered as shown in Fig. 1. Forced, harmonic, unidirectional, inner cylinder vibrations induce an unsteady flow field within the annulus.

Finite element analysis is used to calculate the time-dependent, oscillatory flow field and the results presented in terms of added mass and fluid damping coefficients. Continuously deforming space-time finite elements [1] are used to track the moving cylinder.

The computer program "USHA," developed and validated during the course of this project, is currently being used to study more complex fluid structure interaction problems that occur within heat exchanger tube banks.

2 Governing Equations and Solution Scheme

The governing Navier-Stokes and mass conservation equations for laminar, incompressible flow are

$$\frac{\partial u}{\partial t}+u\frac{\partial u}{\partial x}+v\frac{\partial u}{\partial y}=-\frac{1}{\rho}\frac{\partial p}{\partial x}+2\nu\frac{\partial^2 u}{\partial x^2}+\nu\left[\frac{\partial^2 u}{\partial y^2}+\frac{\partial^2 v}{\partial x\partial y}\right] \tag{1}$$

$$\frac{\partial v}{\partial t}+u\frac{\partial v}{\partial x}+v\frac{\partial v}{\partial y}=-\frac{1}{\rho}\frac{\partial p}{\partial y}+2\nu\frac{\partial^2 v}{\partial y^2}+\nu\left[\frac{\partial^2 u}{\partial x\partial y}+\frac{\partial^2 v}{\partial x^2}\right] \tag{2}$$

$$\frac{\partial u}{\partial x}+\frac{\partial v}{\partial y}=0 \tag{3}$$

The forced vibration of the inner cylinder is given by:

$$x_c(t) = A\sin(\omega t) \tag{4}$$

$$u_c(t)=\dot{x}_c = A\,\omega\cos(\omega t). \tag{5}$$

Finite element analysis of laminar, incompressible, newtonian fluid flow is well established [1, 3]. A summary of the novel features of the present solution procedure is given below.

Figure 2 shows an overview of the present algorithm. All the boxes in Fig. 2 are self-explanatory, except for the one on implicit integration of the Navier-Stokes equations, which will be elaborated on here.

Let $A(t)$ represent the spatial region occupied by the fluid at time t. Then, D^n, the region in space-time containing the fluid between times t^n and t^{n+1} is defined as

$$D^n = \{(x,y,t): (x,y)\epsilon\, A(t),\ t^n < t < t^{n+1}\} \tag{6}$$

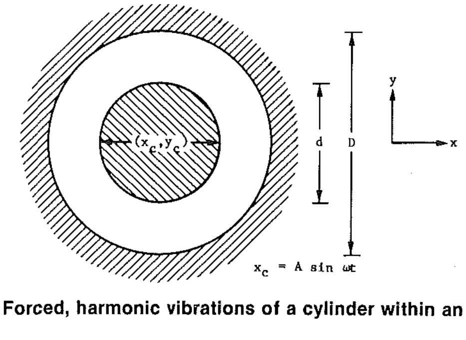

Fig. 1 Forced, harmonic vibrations of a cylinder within an annulus

---

Contributed by the Fluids Engineering Division of The American Society of Mechanical Engineers, and presented at the ASME Pressure Vessel and Piping Conference, Symposium on Flow Induced Vibrations, San Diego, Calif., June 28–July 2, 1987.

Copyright © 1987 by ASME

Downloaded 02 Jun 2010 to 171.66.16.66. Redistribution subject to ASME license or copyright; see http://www.asme.org/terms/Terms_Use.cfm

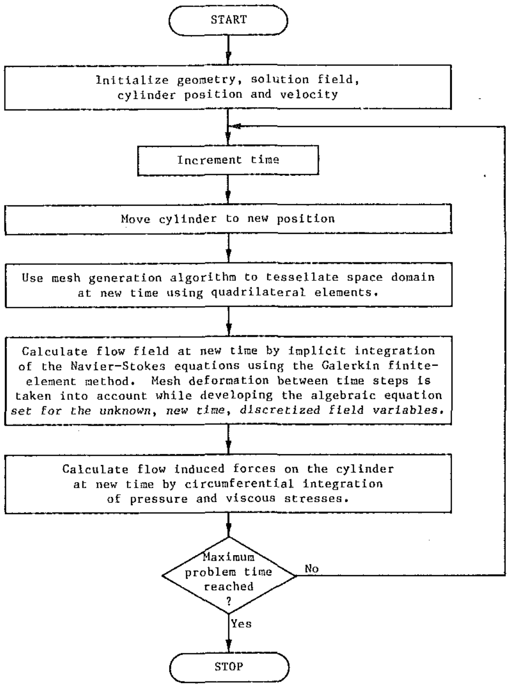

Fig. 2 Skeleton flow chart of finite element scheme for analysis of fluid-structure interaction

Let A^n represent the area at time t^n. The spatial regions A^n and A^{n+1} are tessellated by nine-node, quadrilateral (space) regions. Space-time elements (with 18 nodes each) are defined by joining corresponding nodes of the nine-node quadrilateral (space) regions at times t^n and t^{n+1} as shown in Fig. 3. Space-time element transformation and element interpolation functions are defined by relations such as:

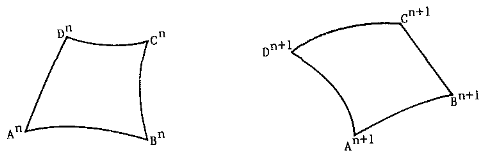

Fig. 3(*a*) Deformation of a quadrilateral region within a time step

SPACE-TIME INTERPOLATION

$$f^e = \frac{1+\zeta}{2}\sum_{j=1}^{9} N_j^e f_j^{e,n+1} + \frac{1-\zeta}{2}\sum_{j=1}^{9} N_j^e f_j^{e,n} \quad ; \qquad p^e = \frac{1+\zeta}{2}\sum_{k=1}^{4} NP_k^e p_k^{e,n+1} + \frac{1-\zeta}{2}\sum_{k=1}^{4} NP_k^e p_k^{e,n}$$

$f = u, v, x$ and y

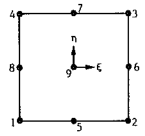

$N_1^e = \xi\eta(\xi-1)(\eta-1)/4$

$N_2^e = \xi\eta(\xi+1)(\eta-1)/4$

$N_3^e = \xi\eta(\xi+1)(\eta+1)/4$

$N_4^e = \xi\eta(\xi-1)(\eta+1)/4$

$N_5^e = (1-\xi^2)\eta(\eta-1)/2$

$N_6^e = (1-\eta^2)\xi(\xi+1)/2$

$N_7^e = (1-\xi^2)\eta(\eta+1)/2$

$N_8^e = (1-\eta^2)\xi(\xi-1)/2$

$N_9^e = (1-\xi^2)(1-\eta^2)$

$NP_1^e = (\xi-1)(\eta-1)/4$

$NP_2^e = -(\xi+1)(\eta-1)/4$

$NP_3^e = (\xi+1)(\eta+1)/4$

$NP_4^e = (\xi-1)(\eta+1)/4$

Fig. 3(*b*) Mapping of each of the quadrilateral regions of Fig. 3(*a*) to a square

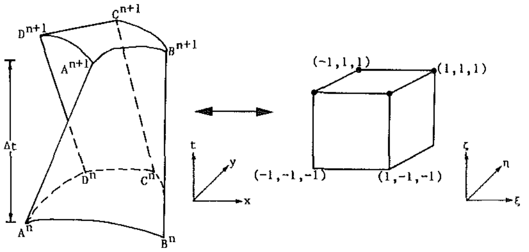

Fig. 3(*c*) Iso-parametric transformation of space-time elemental "volume" to a cube

Nomenclature

a = constant in equation (10)
A = amplitude of vibration (cm)
b = refers to elements of J^{-1}; also a constant in equation (10)
C = Courant number; $A * \omega * \Delta t/\mathrm{DRM}$
C_m = nondimensionalized added mass coefficient, see equation (12)
C_v = nondimensionalized damping coefficient, see equation (12)
d = diameter of inner cylinder (cm)
d = diameter of outer cylinder (cm)
DRM = minimum radial spacing between velocity nodes in undeformed configuration (cm)
$F_1(t)$ = instantaneous nondimensional drag force on inner cylinder
J = Jacobian matrix of elemental coordinate transformation
l = distance along circumference of inner cylinder (cm)
n_j = direction cosine of outward normal to inner cylinder surface
N_j^e = jth (biquadratic) interpolation function for u, v, x, and y within an element e
NEL = total number of elements
NP_k^e = kth (bilinear) interpolation function for pressure, within an element e
NRD = number of elements in radial direction (undeformed configuration)
NTH = number of elements in circumferential direction (undeformed configuration)
p = pressure (dynes/cm^2)
Re = Reynolds number, $\omega d^2/4\nu$
t = time (s)
u = x-direction velocity (cm/s)
v = y-direction velocity (cm/s)
x = distance along abscissa (cm)
y = distance along ordinate (cm)

Greek Symbols

ξ,η,ζ = coordinates for element transformation
μ = dynamic viscosity (gm/cm/s)
ν = kinematic viscosity (cm^2/s)
ω = angular velocity (radians/s)
ρ = fluid density (gm/cm^3)

Subscripts

c = refers to vibrating cylinder
i,j,k = indices that refer to node numbers within an element

Superscripts

e = refers to quantities within an element
n = refers to quantities at the nth time step (level)

Downloaded 02 Jun 2010 to 171.66.16.66. Redistribution subject to ASME license or copyright; see http://www.asme.org/terms/Terms_Use.cfm

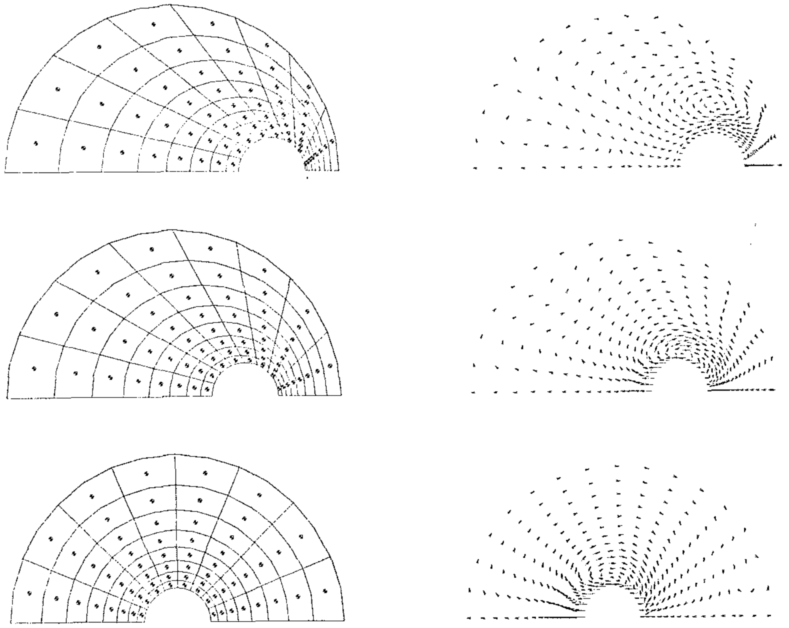

Fig. 4 Typical mesh deformation and velocity vectors on a coarse mesh. NRD = 8, NTH = 8, NEL = 64, *D/d* = 5, *A/d* = 1.5

$$\begin{aligned} x &= \frac{1-\zeta}{2}\sum_{j=1}^{9} N_j^e\, x_j^{e,n} + \frac{1+\zeta}{2}\sum_{j=1}^{9} N_j^e x_j^{e,n+1}, \\ u &= \frac{1-\zeta}{2}\sum_{j=1}^{9} N_j^e\, u_j^{e,n} + \frac{1+\zeta}{2}\sum_{j=1}^{9} N_j^e u_j^{e,n+1}, \qquad (7) \\ p &= \frac{1-\zeta}{2}\sum_{k=1}^{4} NP_k^e\, p_k^{e,n} + \frac{1+\zeta}{2}\sum_{k=1}^{4} NP_k^e p_k^{e,n+1}, \end{aligned}$$

where N_j^e and NP_k^e are element interpolation functions that "live" only within each element and x_j^e, u_j^e, etc. are nodal values. N_j^e and NP_j^e are expressed in natural coordinates as tabulated in Fig. 3.

Figure 3 also illustrates transformation of each element from (x, y, t) to a cube in (ξ, η, ζ) coordinates.

Applying the Galerkin principle to the weak (integrated) form of the governing equations, integrating by parts to reduce the order of spatial derivatives and noting that the resulting boundary integrals are equal to zero for the present problem, the following integrals corresponding to the x-momentum balance and continuity equation [equations (1) and (3)] are obtained. Similar manipulations are necessary for the y-momentum equation [equation (2)]. (Summation convention applies with $1 \le j \le 9$ and $1 \le k \le 4$.)

$$\begin{aligned} \sum_{\substack{\text{all}\\ \text{elements}}} \int_{-1}^{1} \frac{1+\zeta}{2} \int_{-1}^{1}\int_{-1}^{1} \Big\{ N_e^i \Big[b_{31}\frac{\partial N_j^e}{\partial \xi}\, u_j^{e,\zeta} \\ + b_{32}\frac{\partial N_j^e}{\partial \eta}\, u_j^{e,\zeta} + b_{33}\frac{N_j^e(u_j^{e,n+1}-u_j^{e,n})}{2} \\ + u^n \frac{\partial N_j^e}{\partial x}\, u_j^{e,\zeta} + v^n \frac{\partial N_j^e}{\partial y}\, u_j^{e,\zeta} \Big] - \frac{1}{\rho}\frac{\partial N_i^e}{\partial x} NP_k^e p_k^{e,\zeta} \\ + 2\nu \frac{\partial N_i^e}{\partial x}\frac{\partial N_j^e}{\partial x}\, u_j^{e,\zeta} + \nu \frac{\partial N_i^e}{\partial y}\frac{\partial N_j^e}{\partial y}\, u_j^{e,\zeta} \\ + \nu \frac{\partial N_i^e}{\partial y}\frac{\partial N_j^e}{\partial x}\, v_j^{e,\zeta} \Big\} \times (\det J)\, d\xi\, d\eta\, d\zeta = 0 \qquad (8) \end{aligned}$$

$$\begin{aligned} \sum_{\substack{\text{all}\\ \text{elements}}} \int_{-1}^{1}\int_{-1}^{1}\int_{-1}^{1} \frac{1+\zeta}{2} NP_k^e \Big(\frac{\partial N_j^e}{\partial x}\, u_j^{e,\zeta} \\ + \frac{\partial N_j^e}{\partial y}\, v_j^{e,\zeta} \Big) (\det J)\, d\xi\, d\eta\, d\zeta = 0 \qquad (9) \end{aligned}$$

where

$$\begin{aligned} u_j^{e,\zeta} &= u_j^{e,n+1}\frac{1+\zeta}{2} + u_j^{e,n}\frac{1-\zeta}{2} \\ v_j^{e,\zeta} &= v_j^{e,n+1}\frac{1+\zeta}{2} + v_j^{e,n}\frac{1-\zeta}{2} \\ p_k^{e,\zeta} &= p_k^{e,n+1}\frac{1+\zeta}{2} + p_k^{e,n}\frac{1-\zeta}{2} \\ b_{31} &= \frac{\partial \xi}{\partial t}, \quad b_{32} = \frac{\partial \eta}{\partial t}, \quad b_{33} = \frac{\partial \zeta}{\partial t} \end{aligned}$$

and,

$$J = \begin{bmatrix} \dfrac{\partial x}{\partial \xi} & \dfrac{\partial y}{\partial \xi} & 0 \\ \dfrac{\partial x}{\partial \eta} & \dfrac{\partial y}{\partial \eta} & 0 \\ \dfrac{\partial x}{\partial \zeta} & \dfrac{\partial y}{\partial \zeta} & \dfrac{\partial t}{\partial \zeta} \end{bmatrix}$$

The volume integral over the space-time region D^n is evaluated as the sum of the volume integrals over individual space-time elements. Again we note that interpolation functions N_j^e and NP_j^e are nonzero only within the element e.

Volume integration over each cubical space-time element

Downloaded 02 Jun 2010 to 171.66.16.66. Redistribution subject to ASME license or copyright; see http://www.asme.org/terms/Terms_Use.cfm

(Fig. 3) is carried out using an 18-point symmetric integration rule that is exact for cubic monomials in ζ and fifth power monomials in ξ and η. The integration rule is given by

$$\int_{-1}^{1}\int_{-1}^{1}\int_{-1}^{1} f\,d\xi\,d\eta\,d\zeta$$

$$\begin{aligned}
&= \frac{25}{81}\,[f(a,-a,b)+f(a,a,b)+f(-a,a,b)+f(-a,-a,b)\\
&\quad + f(a,-a,-b)+f(a,a,-b)+f(-a,a,-b)+f(-a,-a,-b)]\\
&\quad + \frac{40}{81}\,[f(a,0,b)+f(-a,0,b)+f(0,a,b)+f(0,-a,b)\\
&\quad + f(a,0,-b)+f(-a,0,-b)+f(0,a,-b)+f(0,-a,-b)]\\
&\quad + \frac{64}{81}\,[f(0,0,b)+f(0,0,-b)] \qquad (10)
\end{aligned}$$

where $a = \sqrt{3/5}$ and $b = \sqrt{1/3}$.

The banded equation set for the unknown, new time variables was solved by gaussian elimination at each time step. Nodal condensation was employed to remove equations for nodal variables associated with interior nodes (node #9 in Fig. 3) from the equation set.

3 Results

Anticipated flow symmetry allows the calculational domain to be confined to half the physical flow field. The deforming mesh, changing shape of the calculational domain and typical velocity vectors are illustrated in Fig. 4. Simple geometric scaling was used to generate a new mesh at each time step. The coarse mesh shown in Fig. 4 was chosen for clarity of display rather than accuracy. Mesh rearrangement and refinement as described in Section 3.2 were necessary to obtain quantitatively accurate results.

All meshes used in the present study are described by five parameters: NRD, NTH, DRM, RATIO, and C. NRD and NTH are the number of elements in the radial and circumferential directions. Thus the total number of elements used to tessellate the flow field is given by NEL = NRD * NTH. For example, NRD = 8, NTH = 8 and NEL = 64 for the mesh shown in Fig. 4. DRM is the radial spacing between the inner cylinder wall and the closest discrete velocity location. RATIO is the geometric progression factor used to expand the radial spacing between discrete velocities. For clarity, it should be mentioned that there are (2 * NRD + 1) discrete velocity locations along the radial direction, and (2 * NTH + 1) discrete velocity locations in the angular direction. Thus the 64 element mesh of Fig. 4 has 289 discrete u-velocity locations, 289 v-velocity locations and 81 discrete pressure locations. Uniform spacing was employed in the angular direction.

The time step is presented in terms of a nominal Courant number [$C = (A^*\omega^*\Delta t)/\mathrm{DRM}$]. The maximum, instantaneous Courant number may be larger than the nominal Courant number by as much as a factor of 2.5. The Courant number as defined above is based on the speed of the cylinder and not on the speed with which fluid particles cross element boundaries. Thus, a large Courant number is not indicative of an exceptionally stable numerical scheme.

All results are hereafter presented in terms of added mass and fluid damping coefficients [2, 4–7]. It is recognized that nonlinear fluid structure interactions are best described in terms of energy transfer. However, added mass and fluid damping coefficients evaluated as described below serve to illustrate nonlinearity.

The instantaneous drag experienced by the inner cylinder was evaluated by circumferential integration of surface stresses as follows:

$$F_i(t) = [\textstyle\int_l \sigma_{ij} n_j\, dl]/[(\rho\pi d^2 A\,\omega^2)/4] \qquad (11)$$

where

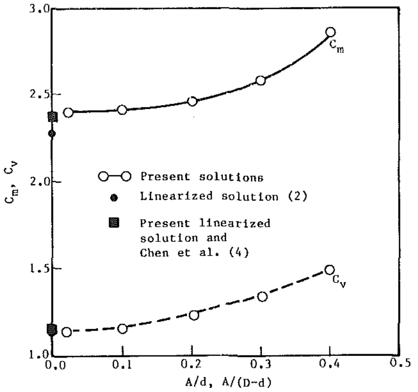

Fig. 5 Effects of vibration amplitude on added mass and damping coefficients; $D/d = 2$; Re = 50

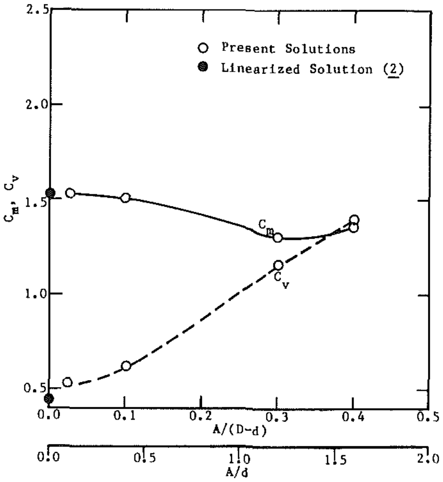

Fig. 6 Effect of vibration amplitude on added mass and viscous damping coefficients; $D/d = 5$; Re = 50

$$\sigma_{ij} = -p\delta_{ij} + \mu\left[\frac{\partial u_i}{\partial x_j} + \frac{\partial u_j}{\partial x_i}\right].$$

Added mass and fluid damping coefficients were obtained by nondimensionalizing the calculated drag at instants corresponding to maximum acceleration and maximum velocity, respectively.

$$\begin{aligned}
C_m &= \mathrm{ABS}\,F_1\ [\{t=[2n-1)\pi]/2\omega\}]\\
&\qquad\qquad n=1,2,3,\ \ldots \qquad (12)\\
C_v &= \mathrm{ABS}\,F_1\ [\{t=[(n\pi)/\omega]\}]
\end{aligned}$$

3.1 Effect of Vibration Amplitude on Added Mass and Damping. Figure 5 shows added mass and fluid damping coefficients as a function of vibration amplitude for $D/d = 2$ and Re = 50. Added mass and fluid damping coefficients increase with increasing vibration amplitude. At small vibration amplitudes, the nonlinear solutions smoothly approach linearized solutions obtained using a simplified version of USHA. Present linearized calculations of damping coefficients agree well with the analytical solutions of Chen et al. [4]. The slight discrepancy (< 5 percent), as shown in Fig. 5, between the present linearized predictions for added mass and Yang and Moran's results [2] is suspected to be a result of truncation errors. Systematic truncation error tests (grid refinement) with USHA are reported in the next section. Details on the grid used by Yang and Moran are unavailable.

Figure 6 shows that the added mass first decreases and later increases, while damping coefficient increases with vibration

Downloaded 02 Jun 2010 to 171.66.16.66. Redistribution subject to ASME license or copyright; see http://www.asme.org/terms/Terms_Use.cfm

Table 1 Numerical results and mesh details for Figs. 5 and 6 (Re = 50, NRD = 8, NTH = 8, DRM/d = 0.001)

Run no.	D/d	A/d	C	C_m	C_v
1	2	0.02	1.31	2.40	1.14
2	2	0.1	6.54	2.42	1.16
3	2	0.2	6.54	2.47	1.23
4	2	0.3	6.54	2.58	1.35
5	2	0.4	6.54	2.86	1.50
6	5	0.1	13.1	1.53	0.53
7	5	0.4	13.1	1.50	0.62
8a	5	1.2	39.3	1.28	1.28
8b	5	1.2	19.6	1.31	1.19
8c	5	1.2	13.1	1.31	1.16
9	5	1.6	13.1	1.35	1.40

Table 2 Reynolds number dependence of C_m and C_v (D/d = 2, A/d = 0.4, NRD = 8, NTH = 8, DRM/d = 0.006)

Run no.	Re	C	C_m	C_v
10	10	8.73	3.17	4.60
11	50	6.54	2.85	1.50
12	100	8.73	2.63	1.08
13	200	8.73	2.41	0.84
14	500	8.73	2.18	0.70

Table 3 Validity of approximations made in earlier studies (D/d = 2, A/d = 0.4, Re = 50, NRD = 8, NTH = 8, DRM/d = 0.006, C = 6.54)

Run no.	Nonlinear advection terms included?	Deforming mesh?	C_m	C_v
11	Yes	Yes	2.85	1.50
15	Yes	No	2.38	1.61
16	No	Yes	2.94	2.48
17	No	No	2.38	1.16

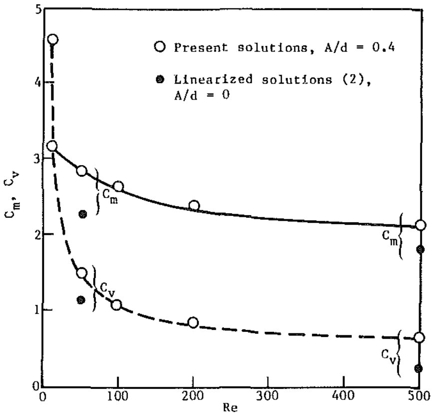

Fig. 7 Effect of Reynolds number on C_m and C_v; D/d = 2

amplitude for D/d = 5 and Re = 50. Damping coefficients are seen to be more sensitive to vibration amplitude than added mass coefficients. This geometry (D/d = 5) permits larger amplitude vibrations than the case of D/d = 2. However, the results obtained with C > 13.1 (D/d = 5 and A/d = 1.2) may not be free from numerical errors as explained under Section 3.2 and as is evident by comparing Run #8a with Run #8b in Table 1.

Miller [5] experimentally determined that added mass coefficient first decreases and then increases with increasing vibration amplitude for complex shaped bodies in an unbounded fluid.

Figure 7 and Table 2 show that added mass and damping coefficients decrease with increasing Reynolds number (D/d = 2 and A/d = 0.4). Similar behavior was noticed by Yang and Moran [2], and Miller [5].

Earlier investigators [2,4] neglected nonlinear advection terms in the governing equations and modeled inner cylinder vibration in a fixed mesh by prescribing a time dependent mass flux (periodic blowing and suction) at the surface of the inner cylinder. Thus earlier results were limited to high frequency, small amplitude vibrations. Simplified versions of the present computer program "USHA" were used to evaluate the two

Table 4 Mesh refinement study (D/d = 2, A/d = 0.4)

Run no.	Re	NRD	NTH	DRM/d	C	C_m	C_v			No. of time steps at
							$\omega t = \pi$	$\omega t = 2\pi$	$\omega t = 4\pi$	$\omega t = 2\pi$
18	50	8	8	0.002	6.54	2.85	1.44	1.50	*	192
19	50	8	12	0.002	6.54	2.86	1.44	1.50	*	192
20	50	12	8	0.001	6.54	2.84	1.44	*	*	384
14	500	8	8	0.006	8.73	2.18	0.52	0.70	*	48
21	500	12	12	0.001	6.54	2.16	0.48	0.70	0.70	384

*Not available.

Table 5 Duration of initial transient (D/d = 2, A/d = 0.4, Re = 50, NRD = 8, NTH = 8, DRM = 0.002)

Run No. 4: C = 6.54			Run No. 22: C = 25.1		
$\omega * t$	C_m	C_v	$\omega * t$	C_m	C_v
$\pi/2$	2.92		$\pi/2$	2.94	
π		1.44	π		1.44
$3\pi/2$	2.85		$3\pi/2$	2.86	
2π		1.50	2π		1.49
$5\pi/2$	2.85		$5\pi/2$	2.87	
3π		1.50	3π		1.49

Downloaded 02 Jun 2010 to 171.66.16.66. Redistribution subject to ASME license or copyright; see http://www.asme.org/terms/Terms_Use.cfm

approximations made by earlier investigators. The computer runs summarized in Table 3 demonstrate that each of the two approximations are individually invalid for large amplitude vibrations ($D/d = 2$, $A/d = 0.4$, Re = 50).

3.2 Numerical Accuracy. The number and distribution of elements in the calculated domain was chosen after several attempts. Simple geometric rules were used to generate the spatial discretization at each time step as visible in Fig. 4.

The effect of grid refinement is shown in Table 4 for the largest amplitude ($A/d = 0.4$) considered in this study for $D/d = 2$. Comparison of Run #18 with Run #19 reveals that the circumferential resolution obtained with NTH = 8 is adequate at Re = 50. Run #20 shows the negligible effect (Re = 50) of increasing NRD by 50 percent, while simultaneously reducing the minimum radial spacing DRM and time step by half as compared to Run #18. Similar checks were carried out for the case of $D/d = 5$, $A/d = 0.1$ and Re = 50. Run #21 demonstrates the effect of grid refinement at Re = 500.

All results presented in this paper were run to a nondimensional time $\omega t = 2\pi$. Table 5 demonstrates that the added mass and viscous damping coefficients evaluated at $\omega t = 3\pi/2$ and 2π, respectively, are uninfluenced by initial startup transients and are representative of oscillatory steady state values. Table 5 also shows that accurate solutions can be obtained with USHA at larger time steps.

About 41 s of CPU time on JAYCOR's Univac 1100/60 mainframe computer were required per time step for NRD = NTH = 8.

4 Conclusions

A finite element scheme and computer program (USHA) have been developed for analysis of nonlinear fluid structure interactions. USHA calculates flow induced by large amplitude structural vibrations using continuously deforming space-time finite elements to track the moving structure.

At small vibration amplitudes, USHA predictions for added mass and damping coefficients agree well with previous linearized analyses. Fluid damping coefficients were found to increase with increasing vibration amplitude. Added mass coefficient may either increase or decrease with increasing vibration amplitude.

Acknowledgments

Computer resources for the present study were provided by JAYCOR. Mesh refinement studies were performed using a grant from the San Diego Supercomputer Center. The author is grateful to Dr. J. H. Stuhmiller for his encouragement and to Ms. Patricia Faller for superb manuscript preparation.

References

1 Frederickson, C. S., and Watts, A. M., "Finite Element Method for Time-Dependent Incompressible Free Surface Flow," *Journal of Comp. Phys.*, Vol. 39, 1981, pp. 282-304.

2 Yang, C.-I., and Moran, T. J., "Finite-Element Solution of Added Mass and Damping of Oscillation Rods in Viscous Fluids," ASME *Journal of Applied Mechanics*, Vol. 46, 1979, pp. 519-523.

3 Silliman, W. J., and Scriven, L. E., "Separating Flow Near a Static Contact Line: Slip at a Wall and Shape of a Free Surface," *Journal Comp. Phys.*, Vol. 34, 1980, pp. 287-313.

4 Chen, S. S., Wambsganss, M. W., and Jendrzejczyk, J. A., "Added Mass and Damping of a Vibrating Rod in Confined Viscous Fluids," ASME *Journal of Applied Mechanics*, Vol. 43 No. 2, 1976, pp. 325-329.

5 Miller, R. R., "The Effects of Frequency and Amplitude of Oscillation on the Hydrodynamic Masses of Irregular Shaped Bodies," M. S. thesis, Mechanical Engineering, University of Rhode Island, 1965.

6 Paidoussis, M. P., Suss, S., Pustejovsky, M., "Free Vibration of Clusters of Cylinders in Liquid-Filled Channels," *Journal of Sound and Vibration*, Vol. 55, No. 3, 1977, pp. 443-459.

7 Levy, S., and Wilkinson, J. P. D., "Calculation of Added Water Mass Effects for Reactor System Components," General Electric Corporate Research and Development Report 75CRD095, 1975.

Downloaded 02 Jun 2010 to 171.66.16.66. Redistribution subject to ASME license or copyright; see http://www.asme.org/terms/Terms_Use.cfm

Spray Photographs, Poppet Lift, and Injection Pressure of an Oscillating Poppet Injector

B. Chehroudi

P. Lombardi

P. G. Felton

F. V. Bracco

Department of Mechanical Engineering
and Aerospace Engineering,
Princeton University,
Princeton, NJ 08544

Sprays from an injector with a conical oscillating poppet and supplied with fuel at injection rates similar to those used in direct-injection stratified-charge engines have been characterized. Instantaneous injection pressure and poppet lift were measured and short-exposure backlit photographs were taken at several times during injection. Spray axial tip penetration and velocity were determined from the photographs. The experiments were conducted in a constant-volume pressure vessel. The gas was nitrogen and the liquid was hexane. The gas temperature was either 25° or 55°C. The experiments included a systematic variation of the ambient pressure, pump speed and injected liquid volume. It was found that the structure of the spray was strongly affected by the chamber pressure. The hollow cone collapsed and injection duration, spray axial initial velocity and tip penetration decreased with increasing chamber pressure. Increasing pump speed decreased both injection duration and number of oscillations.

Introduction

Research on the early-injection Direct-Injection Stratified-Charge (DISC) engine in the Engine Research Department at General Motors Research Laboratories showed that the most successful injection system for this engine used a conical-oscillating-poppet injector (COPI) [1]. The General Motors studies led to the understanding of some of the factors affecting the characteristics of sprays from the COPI and also indicated the importance of several other parameters which were not studied in detail. In particular, Shearer and Groff [1] analyzed the behavior of the spray and its pulsating characteristics by high speed schlieren photography and concluded that instantaneous measurements of poppet lift and flow rate would be required for a more complete understanding of this injection system. Takagi [2] performed numerical computations of transient hollow-cone sprays without and with evaporation and with intermittent injection and discussed the effect of drop size, ambient gas pressure, injection velocity, injection mass flow rate and spray cone angle. The influence of drop coalescence and breakup on spray penetration, vaporization and mixing were investigated by Reitz and Diwakar [3] in a modelling study. For the injector conditions they used the measured line pressure and assumed a constant amplitude sin-square function for the poppet opening which was in phase with the pressure oscillations. Both studies concluded that the structure of this type of hollow-cone sprays could be analyzed with greater confidence if the instantaneous injection parameters were known.

In this work an attempt was made to remedy the lack of data on the initial conditions of the fuel injection system. To this end a detailed study of the tip pressure and poppet lift of a single design of COPI injector has been carried out and a comprehensive photographic study of the spray characteristics has been completed. The spray tip penetration was also determined using the photographs. Since the influence of the operational parameters of the injector, the fuel line, and the pump system on the behavior of the spray can be felt only through the instantaneous injection pressure and poppet opening, the direct measurements reported in the following sections allow the injection process to be better understood, and provide a data-base for the testing of numerical models. Data were obtained for a range of injection pump speeds, fuel volume flow rates, and ambient pressures, including conditions relevant to practical reciprocating engine applications.

Description of the Experimental Apparatus

The apparatus consisted of a spray chamber, a heated-pressurized gas supply, a water-cooled condenser, and a fuel injection pump. A diagram of the system is shown in Fig. 1(*a*). The gas pressurization system provided a coflow of nitrogen in the spray chamber and helped to dry the windows of the spray chamber for more efficient optical access during injection. On leaving the spray chamber, the mixture of nitrogen and fuel (hexane in this case) passed through a condenser to separate the nitrogen from the hexane which were then recirculated.

The spray chamber was made up of three cylindrical steel sections, 19 cm I.D. to give a total height of 90 cm. The central section was provided with four quartz windows 10 cm in diameter at 90 deg to each other. A water-cooled injector holder was mounted axially through the top plate of the spray chamber and the liquid was injected downwards into the chamber.

Contributed by the Fluids Engineering Division for publication in the JOURNAL OF FLUIDS ENGINEERING. Manuscript received by the Fluids Engineering Division June 19, 1986.

Copyright © 1987 by ASME

Downloaded 02 Jun 2010 to 171.66.16.66. Redistribution subject to ASME license or copyright; see http://www.asme.org/terms/Terms_Use.cfm

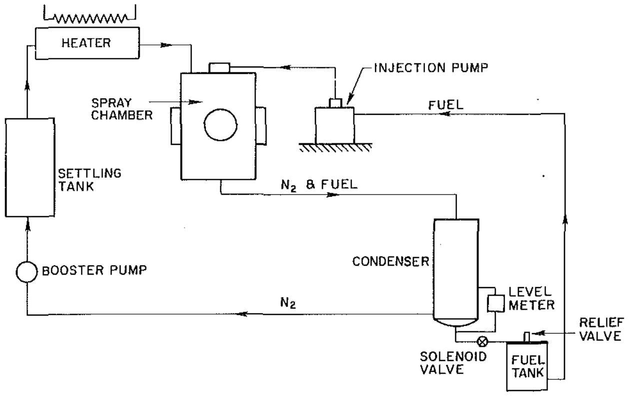

Fig. 1(*a*) Diagram of the test rig

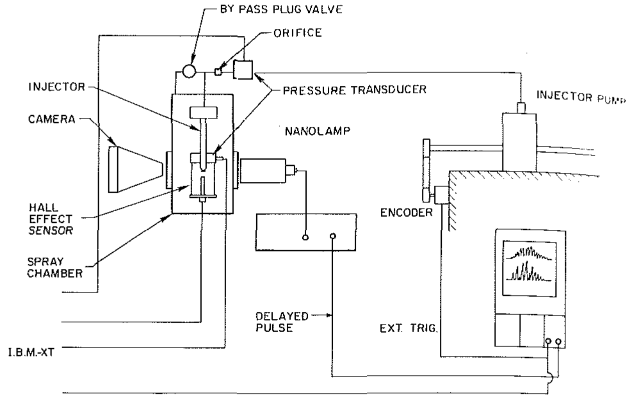

Fig. 2 Schematic of experimental setup

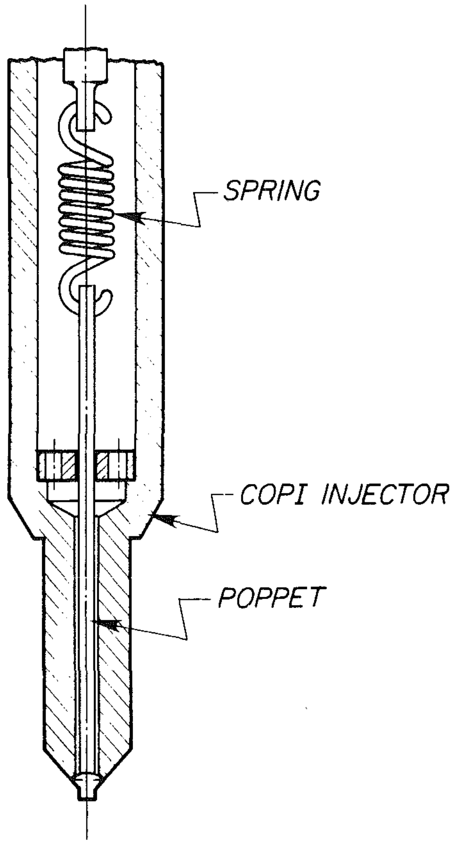

Fig. 1(*b*) Schematic of the COPI injector

The injector was a General Motors conical-oscillating-poppet injector; the total, included poppet angle was 60 deg, the poppet radius was 1.345×10^{-3} m and the nozzle opening pressure was set at 3.13 MPa. Fig. 1(*b*) shows the schematic of this injector. The main feature of this injector is that it generates a pulsating hollow-cone spray whose initial angle is roughly equal to the poppet angle. A similar injector design was also reported by Simko et al. [4]. The fuel injection pump was an American Bosch pump type APE-B1 having the following specification: 6/1 cam; PPK 1/6Z (6 mm) plunger; PVE 30/1Z (modified to 35 mm^3 retraction volume) delivery valve. The fuel pump was connected to the COPI injector by stainless steel tubing (890 mm × 3.25 mm i.d. and 1.65 mm wall thickness). The peak pumping rate was 7.3 mm^3/cam degree. The fuel used for all the experiments reported here was Hexane + 0.1 percent Oleic Acid (added to improve lubricity). A micrometer was used to control the rack position of the pump, which sets the injected fuel volume. The fuel flow rate was calibrated for all the pump speeds used and showed reproducibility to ±3 percent.

Two piezoelectric pressure transducers were used to measure the instantaneous fuel pressure. One was located in the fuel line at the entrance of the injector holder, 350 mm upstream of the tip of the fuel injector, and the other within the injector at a distance of 25 mm from the tip. As it will be explained later, a snubber orifice was used in the fuel line just upstream of the injector; the line pressure was measured upstream of this snubber orifice. The transducers were Kistler fuel injector transducers, Model No. 607f122, with a frequency response of up to 150 kHz. The pressure measurements were made relative to the chamber pressure; this was achieved by equalizing the line pressure with the chamber pressure via a bypass line and then setting the zero of the charge amplifier (Kistler Model No. 504E). A specially modified plug valve was used in order to minimize the dead volume introduced to the fuel line (see Fig. 2).

In order to measure the instantaneous poppet displacement, a Wolff Controls Corp. Hall-effect sensor, Mod. ASM201-002, was used along with a Samarium/Cobalt magnet Mod. SCM213-006 (2.2 mm diameter). The magnet was glued to the tip of the poppet of the COPI injector and

Nomenclature

A = open area of injector tip
$c_d = Q_{\text{act}}/Q_{id}$ = average discharge coefficient
N = total number of maxima observed above 10 μm in poppet lift measurements
p_{ch} = chamber gas pressure
p_l = liquid pressure at the tip of the injector
Q = volume of liquid per injection
Q_{act} = measured volume of liquid per injection
$Q_{id} = \int_0^T A(2\Delta p/p_\ell)^{1/2} dt$ = ideal volume of liquid per injection
t = time
T_i = injection duration
V_i = measured axial initial velocity
y_p = measured poppet lift
y_{st} = measured spray tip penetration
$\Delta p = p_\ell - p_{ch}$ = liquid tip differential pressure
ρ_ℓ = density of liquid

Downloaded 02 Jun 2010 to 171.66.16.66. Redistribution subject to ASME license or copyright; see http://www.asme.org/terms/Terms_Use.cfm

Table 1 Experimental conditions

Chamber pressure MPa	Pump speed rpm	Actual flow rate ml/inj	Nominal flow rate ml/inj	C_d	N
0.1	800	0.0308	0.03	0.71	2
		0.0409	0.04	0.70	4
		0.0607	0.06	0.75	5
	1200	0.0310	0.03	0.71	2
	1600	0.0302	0.03	0.6	2
		0.0394	0.04	0.72	3
		0.0593	0.06	0.81	3
0.65	800	0.0308	0.03	---	–
1.02	800	0.0308	0.03	0.72	3
		0.0409	0.04	0.73	4
		0.0607	0.06	0.73	5
	1200	0.0310	0.03	---	2
	1600	0.0302	0.03	0.80	2
		0.0394	0.04	0.80	3
		0.0593	0.06	0.75	3
1.70	800	0.0308	0.03	---	–
		0.0409	0.04	0.77	4
		0.0607	0.06	0.76	5
	1200	0.0310	0.03	---	2
	1600	0.0302	0.03	0.79	2
		0.0394	0.04	0.75	3
		0.0593	0.06	0.72	3

Uncertainty in Chamber Pressure : ±0.015 MPa
Uncertainty in Pump Speed : ±10 rpm
Uncertainty in Actual Flow Rate : ±0.001 ml/inj
Uncertainty in C_d : ±0.02

glue residues around the tip were carefully removed in order not to create obstructions at the injector exit. The typical calibration curve for the Hall-effect sensor is quadratic in shape and is sensitive to the magnet characteristics. The calibration had to be repeated whenever a new magnet was used. The mass of the magnet was approximately 1 percent of the total mass of the moving parts of the injector (30 mg as opposed to 2500 mg), thus ensuring that the presence of the magnet does not significantly affect the dynamic behavior of the poppet. An instrumentation amplifier with a gain of 1 was used to condition the signal from the Hall-effect sensor. A BEI mdoel H25D-SS-360-ABZC8830-SM18 shaft encoder mounted on the shaft of the fuel injection pump was used to send a data acquisition pulse on each shaft revolution.

Data acquisition for both the pressure and the poppet lift were via a 12-bit-A/D converter having a sampler frequency of 33 kHz interfaced to an IBM-PC/XT computer. The pulse from the shaft encoder was used both to trigger the data-acquisition cycle and to determine the speed of the fuel injection pump by means of a digital counter. A computer program was developed for acquisition and statistical analysis of data. Individual pressure and poppet lift records as well as the ensemble averages and standard deviations were obtained.

The photographic apparatus consists of two systems, allowing both large and small field of view pictures of the spray. The first system, for small-field-of-view pictures, consisted of an aluminum tube 107 cm long equipped with a Takumar 200 mm, f 13.5 lens, a mechanical shutter, and a Polaroid film back. This camera was mounted on a movable frame with a one-dimensional traversing mechanism for focusing. The magnification of this sytem was measured using a reticle at the location of the injector tip and was found to be 5.6. Polaroid type 57 (ASA 3000) black and white film was used, The light source was provided by a Xenon nanolamp model 437-A with 20 nsec half width flash duration. A Tektronix variable delay module was used to trigger the nanolamp after the pulse from the shaft encoder was received. Pictures of the spray were taken at different times during the injection cycle with a resolution of 0.05 milliseconds. The second system, for large field of view pictures, consisted of a 35 mm camera with a 100 mm lens, a General Radio Stroboslave unit, type 1539-A having 1.2 microsecond flash duration. The same digital triggering amplifier as for the first system was used and the film used was a 35 mm Kodak Plus-X pan ASA 125.

Experimental Conditions and Procedure

Table 1 summarizes all the experimental conditions. For each condition the following tests were performed: 1) simultaneous measurements of injector tip differential fuel pressure and poppet lift; 2) high magnification (small-field-of-view) photography of the spray; 3) large-field-of-view photography of the spray. (A complete set of data and photographs for these conditions is presented in reference [5]).

The ambient gas pressure experiments were performed with the optical windows of the spray chamber removed in order to prevent premature recirculation and the consequent wetting of the windows. Suction ducts were placed in the window seats in order to prevent fuel vapor from diffusing into the room. The temperature in this case was equal to the room temperature (23-27°C). For the high-gas-pressure tests the rig was gradually charged with the gaseous nitrogen until the desired chamber pressure was reached. The gas booster pump was then turned on to circulate the nitrogen through the system. In this case, the experiments were performed at a temperature of 55°C, which is the minimum temperature required to keep the windows free from fuel droplets.

The static-opening differential pressure of the COPI injector was set at 3.13 MPa by adjusting the poppet spring preload using a jerk pump with a test gage, and the maximum poppet lift was unrestrained. The rack position of the injection pump was set to the desired value, determined from the flow rate calibration of the pump. The fuel flow rate calibration was checked periodically before and after each set of tests. The injection pump speed was set by monitoring the frequency of the shaft encoder pulses on a digital counter. For the fuel tip pressure and the poppet lift tests, the pressure transducer and the Hall-effect sensor signals, along with the pulses from the shaft encoder, were sent to the A/D converter. The plug valve on the bypass line connecting the fuel line to the spray chamber was opened and the charge amplifier for the piezoelectric transducer grounded, thus setting the reference pressure to the chamber pressure. The by-pass valve was then closed and the injection pump started. After the system had stabilized, the data was acquired. A set of simultaneous differential tip pressure and poppet lift were ensemble averaged over 32 injection cycles. This data acquisition procedure was repeated for each test condition. The reproducibility of the tip pressure and poppet lift measurements is documented in Fig. 3 which presents typical ensemble means and standard deviations of the fluctuations over 32 injection cycles at two different pump speeds. The accuracy of the data is limited by the A/D converter and is ±.02 MPa for the pressure and ±2 μm for the poppet lift.

In early tests of the injection system, the tip pressure showed a bimodal behavior characterized by high amplitude pressure oscillations and low residual line pressure in one injection, followed by very low amplitude pressure oscillations and high residual pressure in the next injection. This behavior was very precise, repeatable and clearly characteristic of the injection pump, line, and injector as one system. The domain of this behavior was found to be dependent on the fuel flow rate and injection pump speed. In order to overcome this difficulty a snubber orifice was placed in the fuel line (see Fig. 2).

Downloaded 02 Jun 2010 to 171.66.16.66. Redistribution subject to ASME license or copyright; see http://www.asme.org/terms/Terms_Use.cfm

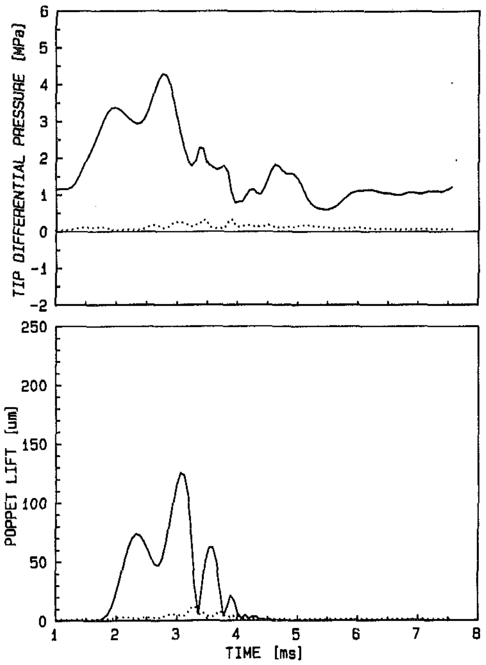

Fig. 3 Ensemble averaged mean and rms of the tip differential pressure and poppet lift at 1600 rpm (. . . : RMS of fluctuations; __: Ensemble averaged mean) (Uncertainty in $\Delta p = \pm 0.02$ MPa, $y_p = \pm 2$ μm and $t = \pm 0.03$ ms)

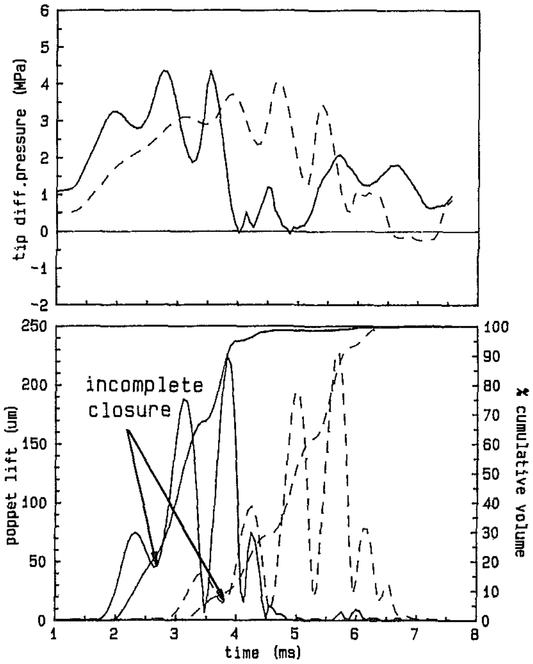

Fig. 4 Poppet lift and tip differential pressure measurements at $p_{ch} = 0.1$ MPa and $Q = 0.06$ ml/inj (---: 800 rpm, ___: 1600 rpm) (Uncertainty in $y_p = \pm 2 \mu$m, $\Delta p = \pm 0.02$ MPa, $t = \pm 0.03$ ms)

The effects of the physical location as well as the size of the orifice on the stability of the tip pressure were recorded. It was found that a snubber orifice with a diameter of 0.635 mm and a length-to-diameter ratio of about 4, at a distance of approximately 305 mm from the injector tip, caused a reasonably broad stable operating zone.

High-magnification (5.6:1) photography at the conditions shown in Table 1 were taken. In this case, the spray was backlighted using a 20ns nanolamp. A firing pulse was generated using the shaft encoder signal along with the delay module of the Tektronix Dual Time Base unit. This enabled the lamp to be fired at any desired time with respect to the fixed reference time. It should be mentioned that, due to the special mount for the Hall-effect sensor, it was not possible to measure poppet lift and take photographs simultaneously. Consequently, all the photographs were taken only after the complete set of tip pressure and poppet lift data had been gathered. For this reason tip pressure traces for each experimental condition were acquired before and after the photographs were taken and the two traces were equal within experimental uncertainty. Also, it was possible to relate each photograph to a particular time (points on the corresponding tip pressure and poppet lift plots).

Experimental Results

I. Simultaneous Tip Differential Pressure and Poppet Lift Measurements. Figure 4 is a plot of the ensemble-averaged tip differential pressure, poppet lift, and the calculated cumulative volume of liquid injected per cycle, for one of the conditions of Table 1. The general behavior of the tip pressure and poppet lift can be described as follows. The tip differential pressure always increased rapidly to a value larger than the opening pressure. At that point the pressure started to decrease as the poppet opened and reached a minimum at a point where the poppet lift was maximum. Then it started to increase again as the poppet closed. The pressure was always out of phase with the poppet lift. This behavior was repeated a number of times until the end of injection. Then the injector pressure was observed to go below the chamber pressure (this behavior could lead to injector tip fouling in an engine application). The time between successive maxima was observed to decrease from the first to the last pulse (typically: 0.82 ms, 0.77 ms, 0.58 ms, 0.37 ms). A possible explanation for this behavior is that at the beginning the time between successive maxima is related to the action of the pressure imposed by the fuel pump in the line, whereas later, it tends to assume the natural period of the oscillating system (0.37 ms). This behavior should be contrasted with the assumption by Reitz and Diwakar [3] of a constant amplitude and frequency in phase with the pressure.

The ideal volume flow rate was determined by calculating the open area of the injector from the poppet displacement and the injection velocity from the tip pressure differential. From this it has been possible to deduce an average discharge coefficient for the injector, C_d, as the ratio of the actual to the ideal volume flow rate. The discharge coefficient, the actual volumetric flow rate (from the pump calibration), and the number of major poppet oscillations are reported for each tested condition in Table 1. The line pressure profile was also measured at all conditions. It was found to be significantly different in shape and out of phase with respect to the corresponding tip pressure profile. No observations, however, are reported regarding the line pressure behavior since the tip pressure is the meaningful parameter as far as the initial conditions of the spray are concerned.

During the tests, the chamber pressure, the injection pump speed and the volume flow rate were varied according to Table 1. The influence of each of these parameters is discussed next.

(*a*) *Effect of the Chamber Pressure.* As far as the shapes of the poppet lift and of the tip differential pressure are concerned, no appreciable differences among the data at different chamber pressures were observed. Note that the plots refer to the relative fuel pressure whose general shape doesn't change with the chamber pressure. Therefore, once the opening pressure is reached, the behavior of the poppet is practically identical independently of the chamber pressure. However, the magnitude of the tip differential pressure increases by about 0.25 MPa to 0.4 MPa as the chamber pressure is in-

Downloaded 02 Jun 2010 to 171.66.16.66. Redistribution subject to ASME license or copyright; see http://www.asme.org/terms/Terms_Use.cfm

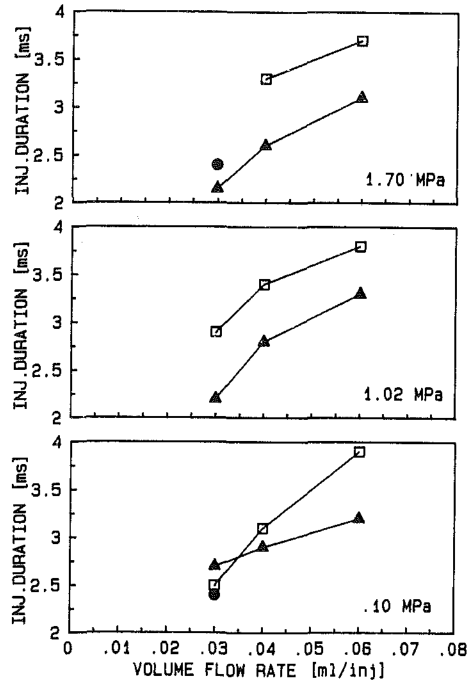

Fig. 5 Ensemble averaged injection duration as a function of fuel flow rate at three different chamber... pressures. Pump... speeds: □: 800 rpm, ●: 1200 rpm, ▲: 1600 rpm (Uncertainty in $T_i = \pm 0.1$ ms, $Q = \pm 3$ percent).

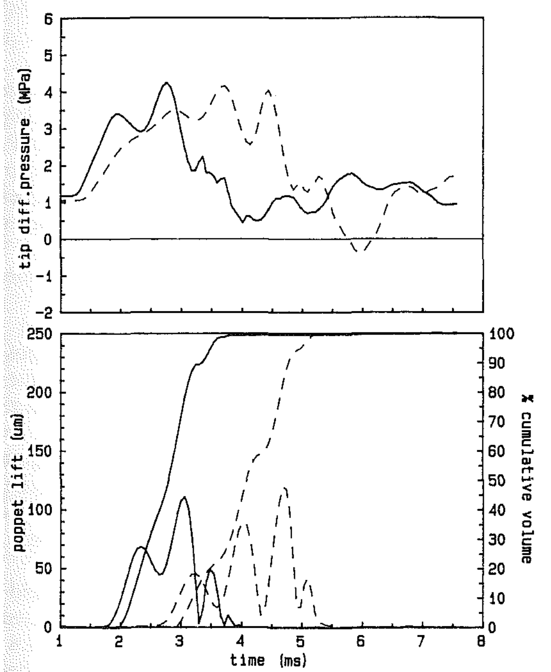

Fig. 6 Poppet lift and tip differential pressure measurements at $p_{ch} = 1.02$ MPa and Q = 0.03 ml/inj (···: 800 rpm, ___: 1600 rpm) (Uncertainty in $\Delta p = \pm 0.02$ MPa, $y_p = \pm 2\mu$m, $t = \pm 0.03$ ms)

creased. Also, the ensemble averaged injection duration seems to decrease with the increase of chamber pressure, being less sensitive at high flow rate, see Fig. 5. A similar effect is also reported in reference [1].

(*b*) *Effect of the Injection Pump Speed.* The effect of the injection pump speed is that of shifting the poppet displacement cycle. It can be observed from the poppet lift plot in Fig. 4 at $p_{ch} = 0.4$ MPa, $Q = 0.06$ ml/inj, that as the speed increases from 800 to 1600 rpm, the opening occurs about 1 ms earlier. The cumulative injected volume plots also clearly show this behavior. For all the conditions tested, except at 0.03 ml/inj and atmospheric pressure, the injection duration decreases an average of 18 percent as the pump speed is increased from 800 rpm to 1600 rpm, see Fig. 4.

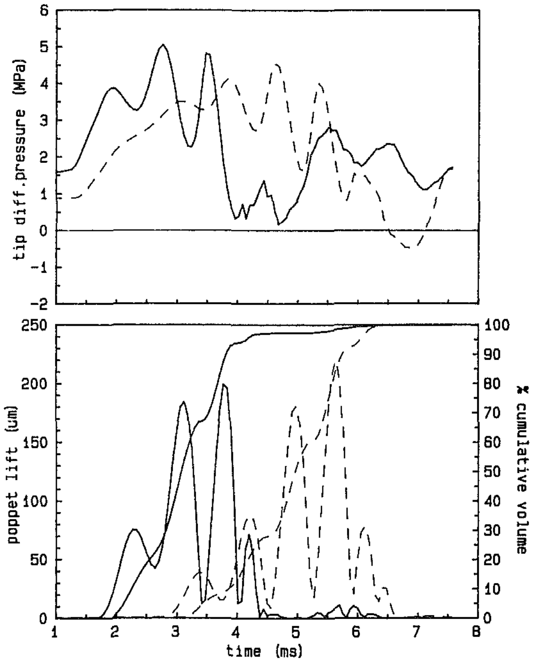

Fig. 7 Poppet lift and tip differential pressure measurements at $p_{ch} = 1.02$ MPa and Q = 0.06 ml/inj (···; 800 rpm, ___: 1600 rpm) (Uncertainty in $\Delta p = \pm 0.02$ MPa, $y_p = \pm 2\mu$m, $t = \pm 0.03$ ms)

The number of observable oscillations and their relative amplitudes also change slightly. Typically one oscillation less is observed at 1600 rpm and the one having the maximum amplitude occurs earlier. For example, in Fig. 4 there are 4 maxima at 1600 rpm the highest being the third one, while there are 5 maxima at 800 rpm the highest being the fourth one.

Another aspect is that the pressure rise at the beginning of the injection increases with increasing pump speed. At 800 rpm a slight change of slope in the tip pressure curve is observed before it reaches the first maximum value; this may be due to a small displacement of the poppet which attenuates the rate of increase in the fuel pressure prior to the actual opening. This behavior is not observed at higher rpm.

(*c*) *Effect of the Injected Volume Flow Rate.* An increase in the injected volume flow rate results in an increase in the duration of the injection (Fig. 5), the number of poppet oscillation cycles, and the amplitude of the poppet oscillations. For example, consider the test at the conditions $p_{ch} = 1.02$ MPa, speed = 800 rpm, whose results are shown in Figs. 6 and 7. For a volume flow rate of 0.03 ml/inj, one finds an injection duration of about 3 ms with a maximum poppet oscillation amplitude of 120 μm and a number of 4 observable maxima. In contrast at 0.06 ml/inj the injection duration is increased to about 4 ms with the maximum amplitude of 220 μm and the number of maxima of 5. From percent cumulative volume flow rate plots, it is seen that the last pulse has only less than 10 percent of the total fuel injected per cycle.

II. Photographs. Photographs showing the behaviour of the spray were taken at the conditions of Table 1. In general, the injector produces a 60 deg hollow-cone sheet in the near

Downloaded 02 Jun 2010 to 171.66.16.66. Redistribution subject to ASME license or copyright; see http://www.asme.org/terms/Terms_Use.cfm

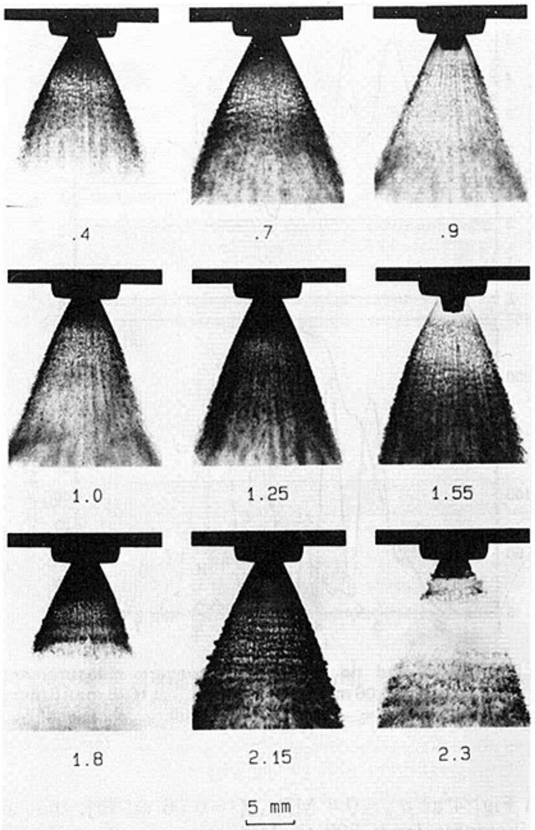

Fig. 8 High magnification photographs of the spray at $p_{ch}=0.1$ MPa, $Q=0.03$ ml/inj and pump speed = 800 rpm (the number under each photograph is the time elapsed in ms from the poppet opening)

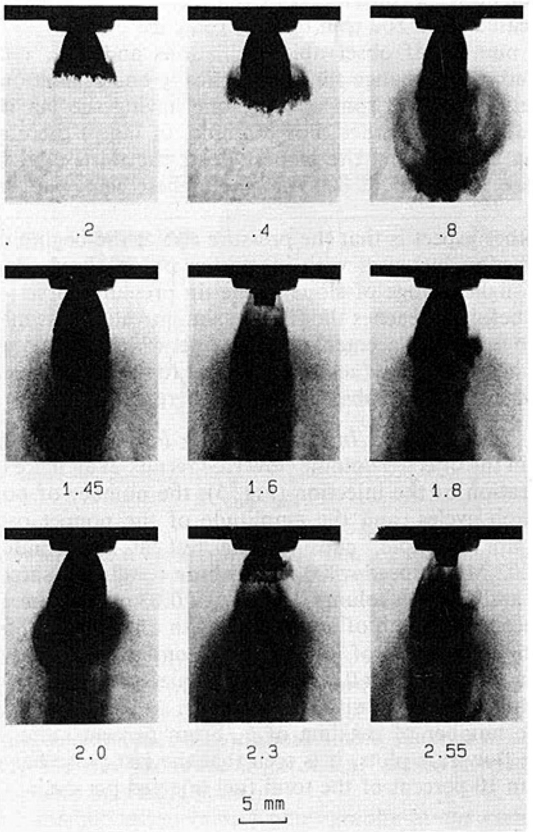

Fig. 9 High magnification photographs of the spray at $p_{ch}=1.02$ MPa, $Q=0.03$ ml/inj and pump speed = 800 rpm (the number under each photograph is the time elapsed in ms from the poppet opening)

field. The major dynamic characteristic of the resulting spray is the pulsating behavior which was selected with the intention of reducing tip penetration [1]. As stated earlier, the number of poppet oscillations is related to the injection pump speed and the volume flow rate. The number of photographed pulses varies between 3 and 5. The last pulse is not always recognizable in the photographs but is recorded in the poppet lift measurements.

In the set of photographs at atmospheric conditions (see Fig. 8 at $p_{ch}=0.1$ MPa, $Q=0.03$ ml/inj and 800 rpm, the number under each photograph being the time elapsed from the first poppet opening in ms units) an incomplete poppet closure is clearly visible after the first rise of the poppet (also visible in the poppet lift results in Figs. 4 and 6 from where it appears to be more pronounced at higher pump speeds). In fact, the liquid sheet in the near field becomes so thin that the small magnet attached to the poppet tip is visible through it (see the photograph at 0.9 ms in Fig. 8). The liquid sheet then becomes thicker again and the magnet disappears until the poppet closes completely. From the photographs at atmospheric pressure, different flow structures can be observed as the liquid leaves the injector. In the near field the liquid seems to form a continuous conical liquid sheet. At a distance of about two poppet diameters, the liquid sheet starts to disintegrate through a perforated sheet mechanism [6] and into the drops and ligaments. At the same time the amplitude of the disturbances on the spray surface seems to increase. At a distance of about 6 poppet diameters the break up of the filaments into small particles is first observed. At all conditions at atmospheric pressure the spray shape looks conical and essentially symmetric.

At higher chamber pressures (see Fig. 9 at $p_{ch}=1.02$ MPa, $Q=0.03$ ml/inj and 800 rpm) the fuel flow behavior is quite different. Just away from the exit plane of the injector, the cone angle starts to decrease and the spray tends to assume a cylindrical form and eventually collapses and loses axial symmetry. A feature of the spray at a gas pressure of 1.02 MPa is the clear evidence of a torroidal vortex at the tip of the spray which becomes visible at approximately 3 poppet diameters downstream of the injector exit. Similar flow structure was observed when the injector was rotated by 180 deg. The reproducibility of the photographs is as good as that of the tip pressure and the poppet lift measurements (Fig. 3).

Spray tip axial penetrations were measured using the photographs obtained at different magnification ratios in order to include the spray far field and, at the same time, to obtain a higher accuracy in the near field data (the penetration values are limited to less than about 20 mm for high magnification results). The results in the overlapping region of the two sets of photographs are in good agreement. Note that the time scale for these plots is the same as that for the tip differential pressure results so that direct comparisons are possible.

In the tip axial penetration plot regarding the large-field-of-view data at 800 rpm and atmospheric pressure reported in Fig. 10(*a*), one additional pulse is observed at about 0.8 ms after the first poppet opening. This is in fact due to the incomplete poppet closure explained earlier, see Fig. 8. In high magnification photographs, the light intensity and optics are optimized to detect such a behavior. But in the large-field-of-view photographs one gets the illusion that a new spray pulse is occurring. That this is an illusion is also clearly shown in the poppet lift measurements (see for example Fig. 4). Furthermore, this illusion is more pronounced at higher pump speeds and flow rates. Our convention has been to consider the second injection pulse to start after complete closure.

Looking at the high-pressure tip axial penetration plots (see for example, Fig. 11), one interesting characteristic is the different behavior of the first and second pulses at 800 rpm pump speed. The average tip velocity of the second pulse appears to

Downloaded 02 Jun 2010 to 171.66.16.66. Redistribution subject to ASME license or copyright; see http://www.asme.org/terms/Terms_Use.cfm

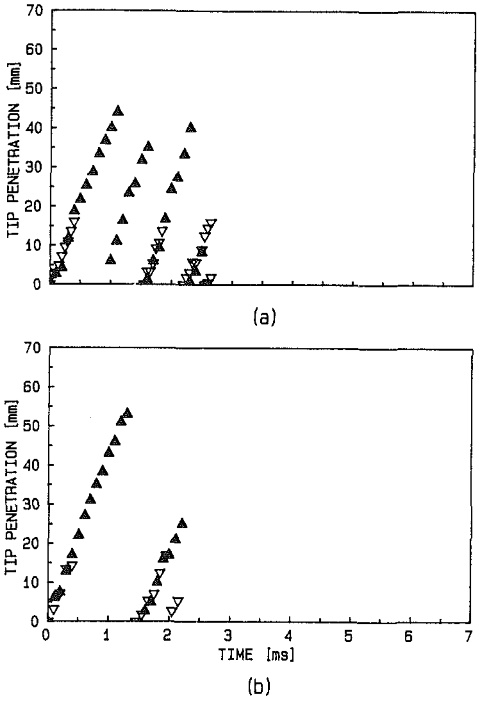

Fig. 10 Axial tip penetration measurements at $p_{ch} = 0.1$ MPa and $Q = 0.03$ ml/inj; pump speed: (*a*) 800 rpm, (*b*) 1600 rpm. Data obtained from: ▲: large field of view photographs; ▽: high magnification photographs (Uncertainty in $y_{st} = \pm 1.5$ mm for data, ±0.5 mm for data, and $t = \pm 0.03$ ms).

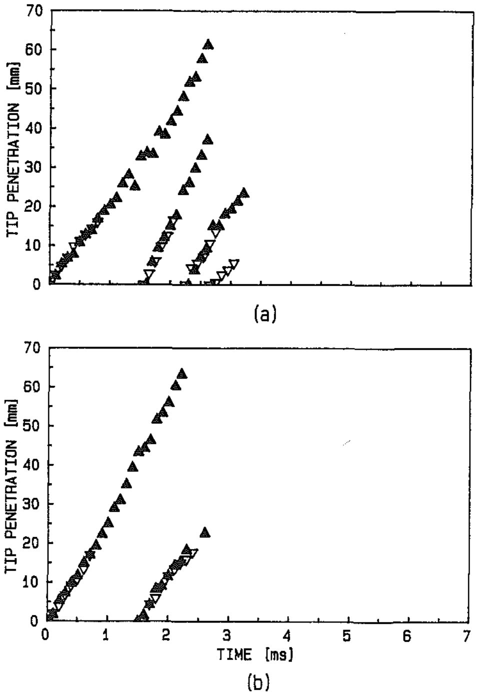

Fig. 11 Axial tip penetration measurements at $p_{ch} = 1.02$ MPa and $Q = 0.04$ ml/inj; pump speed: (*a*) 800 rpm, (*b*) 1600 rpm. Data obtained from: ▲; large field of view photographs; ▽: high magnification photographs (Uncertainty in $y_{st} = \pm 1.5$ mm for data, ±0.5 mm for data, and $t = \pm 0.03$ ms).

be larger than that of the first one, which means that the second injection pulse has a tendency to overtake the first one. Also in Fig. 11(*a*)) it seems that the average tip axial velocity of the spray for the first pulse is increased for injection time above 2 ms. This is due to the fact that the liquid injected after the incomplete closure in general penetrates faster and eventually catches up with the tip of the fuel injected prior to this partial closure. The rise of the tip penetration curve after 2 ms during the first pulse is because of this overtaking phenomenon.

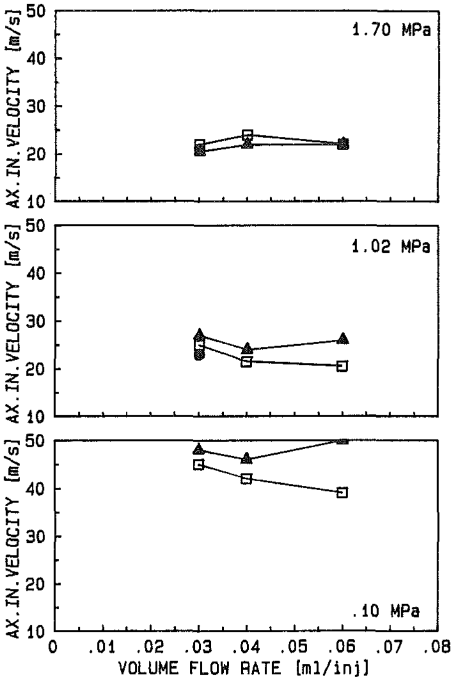

Fig. 12 Axial component of the initial velocity as a function of the fuel flow rate at three different chamber pressures. Pump speed: □ : 800 rpm, ● : 1200 rpm, ▲ : 1600 rpm (Uncertainty in $V_i = \pm 2$m/s, $Q = \pm 3$ percent).

Finally, at a given fuel flow rate and chamber pressure, (Figs. 11(*a*) and (*b*)), it seems that the first injection pulse at 1600 rpm pump speed penetrates slightly faster than the corresponding one at 800 rpm. Conversely, the second injection pulse seems to show opposite trend to the first one.

The axial component of the initial injection velocity of the liquid was calculated from the tip penetration plots. It is defined as the slope of the penetration curve of the first oscillation at the opening (time = 0). It appears from Fig. 12 that the most important parameter in determining the value of this quantity is the chamber pressure. In fact, at atmospheric chamber pressure the spray initial velocity is about 45 m/s (±13 percent) while it has fallen to about 24 m/s (±15 percent) at 1.02 MPa and finally to about 22 m/s (±9 percent) at 1.70 MPa. No significant influence of the fuel volume flow rate is observed on the initial injection velocity. On the other hand, the initial velocity is 7 percent to 28 percent higher at 1600 rpm than at 800 rpm pump speed for atmospheric and 1.02 MPa chamber pressures, the larger difference being observed at the higher fuel volume flow rate. Conversely no appreciable influence of the injection pump speed was observed at the highest chamber pressure (1.70 MPa).

Conclusions

The effects of chamber pressure, injection pump speed, and fuel flow rate on the characteristics of the spray and the COPI injector are as follows. Chamber Pressure – At atmospheric condition the liquid appears to leave the injector in the form of a continuous conical sheet which then perforates and later atomizes. As the chamber pressure is increased the cone angle decreases and a large torroidal shape recirculation zone

Downloaded 02 Jun 2010 to 171.66.16.66. Redistribution subject to ASME license or copyright; see http://www.asme.org/terms/Terms_Use.cfm

becomes clear. The spray tip axial penetration also decreases with increasing chamber pressure. The injector tip pressure was found to be different in shape and phase from the line pressure; therefore it is important for injectors of this type to measure tip pressure rather than line pressure. No effect of chamber pressure on the shape of the tip differential pressure and poppet lift traces was observed. However, the injection duration seems to decrease with increasing chamber pressure, being less sensitive at high flow rates. Injection Pump Speed – the overall behavior of the flow does not change with pump speed. However, the injection starts earlier in time and the number of observable oscillations decreases with increasing pump speed. The initial (axial) spray tip velocity is usually higher at high pump speeds and lower gas pressures. Fuel Flow Rate – There is no appreciable change in the overall structure of the spray with fuel flow rate. However, injection duration, number of poppet oscillations, and the amplitude of the poppet lift increases with increasing flow rate. Throughout this report we have referred to the gas pressure because the gas pressure was the quantity varied in the experiments. However, there is strong evidence to suggest [7] that the gas density actually is the controlling parameter as far as the breakup of the liquid sheets and penetration and shape of the spray are concerned.

Acknowledgments

Support for this work was provided by General Motors and the Department of Energy (Contract No. DE-AC-04-81AL16338). The General Motors Research Laboratories are also thanked for providing fuel injectors, and Mr. Steve DeNagel is thanked for his continuous advice.

References

1 Shearer, A. J., and Groff, E. G., "Injection System Effects on Oscillating-Poppet-Injector Sprays," The Diesel and Gas Engine Power Division, ASME, *Technical Conference*, Boulder, Colo., Oct. 7-9, 1984.

2 Takagi, T., "Computations and Analysis of Transient Hollow Cone Sprays," Report No. 1706, Department of Mechanical and Aerospace Engineering, Princeton University, June 1985.

3 Reitz, R. D., and Diwakar, R., "Effect of Drop Breakup on Fuel Sprays," GM Research Report GMR-5160. Also presented at Western States Section of Combustion Institute, University of California, Davis, CA, Oct. 1985.

4 Simko, A., Choma, M. A., and Repko, L. L., "Exhaust Emission Control by the Ford Programmed Combustion Process – PROCO," SAE-720052, Detroit, Mich., Jan. 10-14, 1972.

5 Chehroudi, B., Lombardi, P., Felton, P. G., and Bracco, F. V., Report No. 1744, Department of Mechanical and Aerospace Engineering, Princeton University, March 1986.

6 Dombrowski, N., and Fraser, R. P., *Phil. Trans. Roy. Soc.*, Series 247A, 1953, pp. 101-140.

7 Bracco, F. V., *SAE Transactions*, Vol. 94, 1985, pp. 144-167.

Downloaded 02 Jun 2010 to 171.66.16.66. Redistribution subject to ASME license or copyright; see http://www.asme.org/terms/Terms_Use.cfm

Compressor Erosion and Performance Deterioration

W. Tabakoff
Professor,
Department of Aerospace Engineering
and Engineering Mechanics,
University of Cincinnati,
Cincinnati, Ohio 45221

Aircraft engines operating in areas where the atmosphere is polluted by small solid particles are typical examples of jet engines operating under hostile atmospheric environment. The particles may be different kinds of sand, volcanic ashes or others. Under these conditions, the gas and particles experience different degrees of turning as they flow through the engine. This is mainly due to the difference in their inertia. This paper presents the results of an investigation of the solid particle dynamics through a helicopter engine with inlet particle separator. The particle trajectories are computed in the inlet separator which is characterized by considerable hub and tip contouring and radial variation in the swirling vane shape. The nonseparated particle trajectories are determined through the deswirling vanes and the five stage axial flow compressor. The results from this study include the frequency of particle impacts and the erosion distribution on the blade surfaces.

Introduction

Commercial and military airplanes are often exposed to foreign objects such as birds, hailstones, ice slabs, runway gravel, and others which are ingested into engine inlets. The ingestion of particulate matter such as sand and dust leads to the deterioration of these engines both structurally and aerodynamically. Some of the mechanisms that cause foreign object ingestion are: (*a*) vortex from engine inlet-to-ground during high power setting with the aircraft standing or moving on the runway, (*b*) sand storms transporting sand to several thousands feet altitude, (*c*) thrust reverser efflux at low airplane speed blow sand, ice and other particles into the engine inlets. Sand and salt spreading on runways in wintertime contribute to solid particle ingestion by airbreathing engines. Erosive solid particles may also be produced during the combustion process, from the burning of different types of heavy oils or synthetic fuels.

Recently several serious accidents have been related to jet engine failures due to operation in particulate environments. Examples of these accidents are by a British Airways 747 Boeing powered by four Rolls Royce RB211 engines on June 23, 1982, and by a Singapore Airline 747 Boeing powered by Pratt and Whitney engines. In addition, many reported industrial gas turbine engine failures have been connected to their exposition to particulate flows. Research efforts are still needed to provide a thorough knowledge of the various parameters which influence the extent of erosion damage. This knowledge is required to improve the life and the aerodynamic performance of aircraft engines operating in an ambient of particulate flow, and avoid such accidents in the future.

Under two-phase flow conditions, the gas and particles experience different degrees of turning through the blade channels. The degree of turning and acceleration or deceleration achieved by the particles depends on the ratio of the viscous forces to the inertial forces experienced by the particles. This leads to variations in particle concentration across the blade channels and causes a change in the properties of the gas flows which alters the engine performance during the period of particle ingestion [1].

If the particles are erosive, impingement of particles on the blade surfaces can cause severe erosion damage, leading to structural failure of the blades. This damage is manifested by pitting and cutting of the blade leading and trailing edges, and a general increase in the blade surface roughness [2]. The overall effect of the above phenomena, from the aerodynamic viewpoint, is an increase in total pressure loss across the blade row.

The erosion problems in military and commercial airplane gas turbine engines are generally recognized in industry. The operating life of helicopter engines operating in sandy areas is very short (from 50 to 250 hours). Erosion in current commercial turbofan engines primarily attacks rotor blades, stator vanes, and outer shrouds in compressors. Refurbishment of these components may be required at any time within the time frame of 3600 to 14,000 hours, depending on the axial position of airfoils within a turbomachine, the airplane route structure, and the cycle usage of an engine. A study performed on commercial jet engines estimates that a minimum of 2 percent thrust specific fuel consumption loss is caused by the performance deterioration due to erosion (NASA Conference Publication 2190, May 6–7, 1981). The application of inlet vortex dissipation devices has been shown to reduce erosion in engines. However, most of the commercial engine fleet do not have such devices.

The intensity and pattern of the compressor and turbine erosion is dependent on the locations of particle impacts and on the magnitude and direction of their impact velocity relative to the surface. It is very important to be able to accurately calculate the particle trajectories in turbomachines if

---

Contributed by the Fluids Engineering Division of The American Society of Mechanical Engineers and presented at the AIAA/ASME 4th Joint Fluid Mechanics, Plasma Dynamics and Lasers Conference, Atlanta, Ga., May 12–14, 1986. Manuscript received by the Fluids Engineering Division July 29, 1986.

Copyright © 1987 by ASME

Downloaded 02 Jun 2010 to 171.66.16.66. Redistribution subject to ASME license or copyright; see http://www.asme.org/terms/Terms_Use.cfm

one is to determine their influence on the engine life and performance.

Three dimensional particle trajectory calculations through axial flow turbines and compressors were first reported by Hussein and Tabakoff [3, 4]. They studied the effect of particle size, and particle material density on their trajectories and demonstrated their influence on particle impact locations. On the other hand, the three dimensional particle trajectories through twisted vanes were studied by Hamed [5] who demonstrated that the particle trajectories are strongly influenced by the hub and tip contouring for the different particle sizes. The erosion intensity and pattern of twisted blades were reported by Hamed and Fowler [6] and were shown to be strongly dependent on the particle size.

This paper presents the results of an investigation of the solid particle dynamics through a helicopter engine with inlet particle separator.

Analysis

The equations governing the particle motion, in the turbomachinery flow fields are written in a rotating frame of reference using cylindrical coordinates. The three components of the equations of motion in a frame rotating about the engine axis with angular velocity ω are given by:

$$\frac{d^2 r_p}{d\tau^2} = F_r + r\left[\frac{d\theta_p}{d\tau} + \omega\right]^2 \tag{1}$$

$$r_p \frac{d^2\theta_p}{d\tau^2} = F_\theta - \frac{2dr_p}{d\tau}\left(\frac{d\theta_p}{d\tau} + \omega\right) \tag{2}$$

$$\frac{d^2 z_p}{d\tau^2} = F_z \tag{3}$$

where r_p, θ_p, z_p define the particle location in cylindrical polar coordinates and ω is the blade angular velocity. The centrifugal force and Coriolis acceleration are represented by the last terms on the right-hand side of equations (1) and (2). The first term on the right-hand side of equations (1) through (3) represents the force of interaction between the two phases, per unit mass of particles. It is dependent on the relative velocity between the particles and the gas flow, as well as the particle size and shape. Under the particulate flow conditions in turbomachines, the effect of the forces due to gravity and to interparticle interactions are negligible compared to those due to the aerodynamic and centrifugal forces. In addition, the force of interaction between the two phases is dominated by the drag due to the difference in velocity between the solid particles and the flow field. The force of interaction per unit mass of solid particles is therefore given by

$$\bar{F} = \frac{3}{4}\frac{\rho}{\rho_p}\frac{C_D}{d}\left[\left(V_r - \frac{dr_p}{d\tau}\right)^2 + \left(V_\theta - \frac{d\theta_p}{d\tau}\right)^2 + \left(V_z - \frac{dz_p}{d\tau}\right)^2\right]^{1/2}(\bar{V} - \bar{V}_p) \tag{4}$$

where V_r, V_θ, V_z, represent the relative gas velocities in the radial, circumferential and axial directions, respectively, ρ, ρ_p are the gas and solid particle densities, d the particle diameter, and C_D the drag coefficient. The drag coefficient is dependent on the Reynolds number, which is based on the relative velocity between the particle and the gas. Empirical relations as shown in reference [4] are used to fit the drag curve over a wide range of Reynolds numbers.

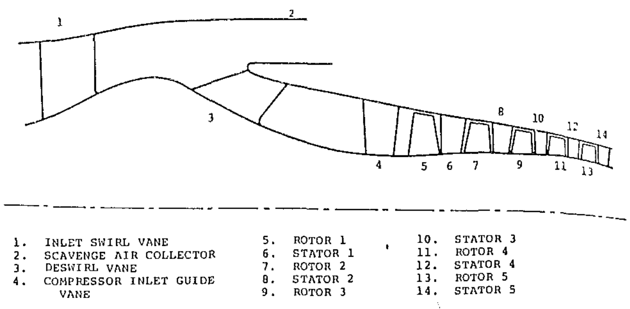

Fig. 1 Schematic of engine separator with compressor

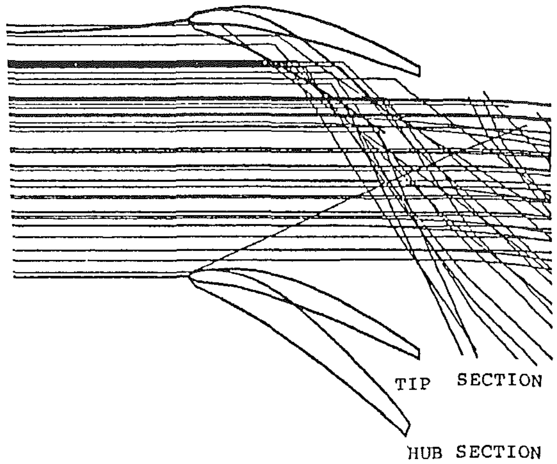

Fig. 2 Particle trajectory view, in the z-θ plane, through the inlet separator

Trajectory Calculations. The particle trajectory calculations consist of the numerical integration of the equations (1)–(4) in the flow field, up to the point of blade, hub or tip impact. The impact location can be determined from the particle trajectory calculations and the local geometry of the impacted surface. The magnitude and direction of the impact velocity relative to the surface, for a large number of particles constitute the essential data needed for the evaluation of the erosion of the various turbomachinery components. The magnitude and direction of particle rebounding velocity after these impacts are dependent on the impacting conditions and the particular particle surface material combination under consideration. Empirical correlations of the restitution parameters are used to calculate the particle rebounding conditions in the calculation of particle trajectories. These correlations [7] are based on the experimental data obtained using

Nomenclature

C_D = particle drag coefficient
d = particle diameter, m
F = force of interaction between the gas and the particle
r = radial distance from the turbomachine axis, m
V = gas relative velocity, m/s
V_p = particle relative velocity, m/s
z = axial coordinate, m
ϵ = erosion parameter, mg/m^2/gr or mg/gr
θ = angular coordinate, radians
ρ = gas density, kg/m^3
ρ_p = particle density, kg/m^3
ω = rotor speed (radians/s)
γ = frequency of particle impacts (total number of particle impacts per unit area of the blade surface per unit number of ingested particle)

Subscripts

p = particle
r = component in radial direction
z = component in axial direction
θ = component in circumferential direction

Downloaded 02 Jun 2010 to 171.66.16.66. Redistribution subject to ASME license or copyright; see http://www.asme.org/terms/Terms_Use.cfm

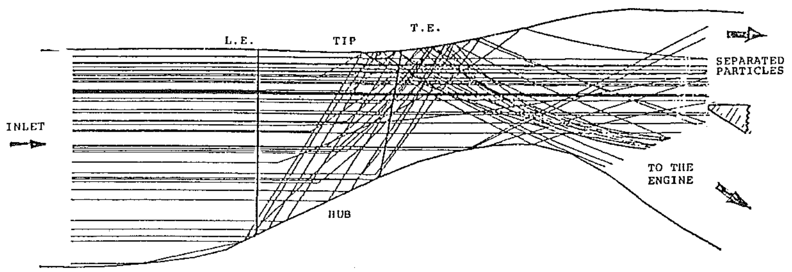

Fig. 3 Particle trajectory view, in the *z-r* plane, through the inlet separator

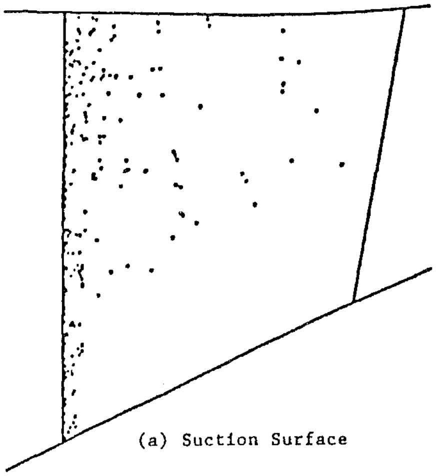

(a) Suction Surface

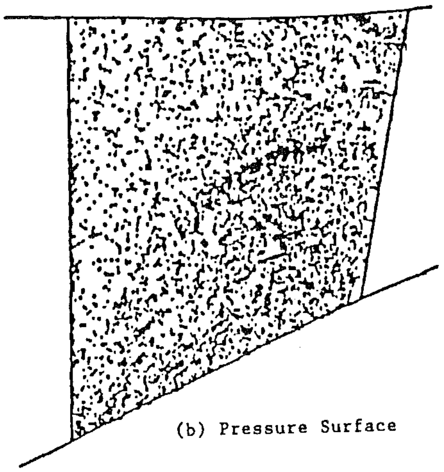

(b) Pressure Surface

Fig. 4 Particle inlet swirling vane impacts

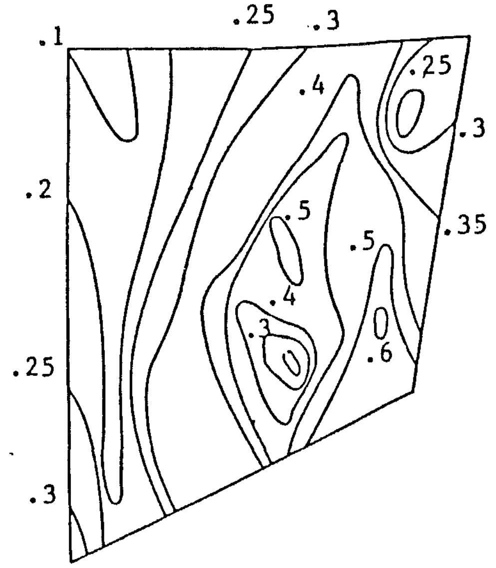

Fig. 5 Distribution of the erosion rate, ϵ, on the swirling vane pressure surface

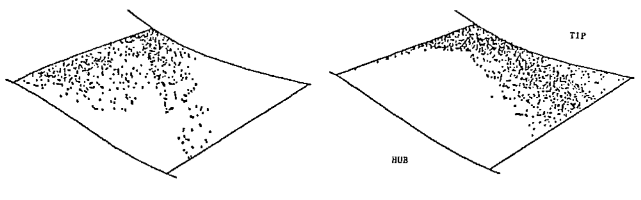

a) SUCTION SURFACE

b) PRESSURE SURFACE

Fig. 6 Particle deswirling vane impacts

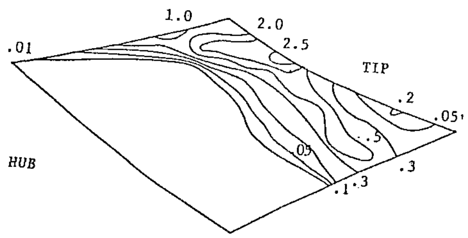

Fig. 7 Distribution of the erosion parameter on the deswirling vane pressure surface

high speed photography and Laser Doppler Velocimetry for particle laden flows over metal samples at various incidence angles and flow velocities in a special tunnel. Two correlation parameters such as the velocity and angle restitution ratios describe the particle rebound characteristics in the two dimensional tunnel. These ratios were found to be mainly dependent upon the impingement angle and not significantly influenced by the particle size and impact velocity.

The velocities and angles of impact and rebound are considered relative to the rotating blade in the case of rotor blade impacts [8]. Furthermore, in order to use these correlations in the three dimensional particle trajectories, a knowledge of the geometry of the solid surface at the impact location is required. Geometrical data describing the blade, hub and tip configuration should be therefore available during the trajectory calculations to be used in the determination of the impact location and the impingement angle relative to the surface.

Flow Field Representation in Particle Trajectory Computation. Careful consideration must be given to the flow field representation in the particle trajectory calculations [5]. The flow field solution must be chosen to represent the important flow field characteristics in any particular application. Further consideration must also be given to the computer storage re-

Downloaded 02 Jun 2010 to 171.66.16.66. Redistribution subject to ASME license or copyright; see http://www.asme.org/terms/Terms_Use.cfm

quired for this data and computer time for interpolating flow properties at each time step in the numerical integration of the particles equations of motion.

The field representation on a number of blade to blade stream surfaces [9] was used in the particle trajectory calculations through the axial flow compressor. On the other hand the flow field description on a mid channel hub to tip stream surface coupled with a blade to blade velocity gradient equation [10] was used in the particle trajectory calculations through the inlet separator and the deswirling vanes with the highly contoured hub and tip annulus. This flow modeling in the particle trajectory calculations insured the accurate representation of the three dimensional flow field in the particle trajectory calculations throughout the engine.

Blade Mass Erosion Prediction. The computation of the blade surface erosion combines the empirical correlations for the mass erosion parameter for a given particle target material combination [7, 12] with the results of the particle trajectory calculations for a large number of particle trajectories in the form of the impact velocities and impingement angles.

The experimental measurements in the erosion tunnel indicate that the target erosion was found to be dependent upon the particle impact velocity, impingement angle and on the flow and target temperatures. Experimental measurements were obtained in the erosion tunnel for quartz particles (165 micron diameter) impacting 510 stainless steel at different impacting velocities and impingement angles.

The experimental data was used to obtain the following empirical equation for the erosion mass parameter, ϵ, which is defined as the ratio of the eroded mass of the target material to the mass of impinging particles.

$$\epsilon = K_1 \left[1 + CK\left(K_{12}\sin\left(\frac{90}{\beta_0}\,\beta_1\right)\right)\right]^2 V_1^2\cos^2\beta_1(1-R_t^2)$$

$$+K_3(V_1\sin\beta_1)^4 \quad \text{(units mg/gr)} \tag{5}$$

where V_1 and β_1 are the impact velocity and impingement angle, respectively.

$R_t = 1-0.0016\,V_1\sin\beta_1$,
R_t = tangential restitution ratio
β_0 = angle of maximum erosion
$CK = 1$ for $\beta_1 \leq 2\beta_0$
$CK = 0$ for $\beta_1 > 2\beta_0$

K_1, K_{12} and K_3 are material constants which were found to be as follows:

$K_1 = 0.5225 \times 10^{-5}$
$K_{12} = 0.266799$
$K_3 = 0.549 \times 10^{-12}$

The erosion computer code was especially developed to calculate the blade surface erosion distribution. The program input consists of the blade surface geometrical data and the particle blade impact data as determined by the particle trajectory calculations. A blade surface fitted grid is generated and the impact data is then combined with the empirical equations to predict the mass erosion intensity and pattern. The mesh size was carefully selected, according to the finite number of particles trajectories, to give the most accurate representation of the blade surface erosion.

The output from this program includes the blade erosion distribution as well as the distribution of the impact velocity, impingement angles and the frequency of particle impacts on the blade surface, γ. The detailed distribution of all these significant erosion parameters over each blade surface in a multistage compressor is essential for taking specific measures to alleviate blade erosion problems.

Results and Discussion

The results of the particle trajectory analysis are presented through the inlet separator and the axial flow compressor of a helicopter engine which is shown schematically in Fig. 1. The design combines the influence of a highly contoured hub with the swirling vanes at inlet to deflect the particles in the radial direction for separation. In general, it was found that the large particle trajectories are dominated by the hub, tip and vane impacts, while the flow field influence is only pronounced on the smaller particle trajectories. More details about the particle trajectories in the inlet separator over a wide range of particle sizes can be found in reference [11].

The results of the particle trajectory calculations are presented here to show the particle impact locations with the swirling and deswirling vanes and the five stage axial flow compressor blades. The presented results for 100,000 particles entering the engine, corresponds to 0.6 grams of ingested sand of 165 micron diameter particle. The results of the particle trajectory computations for the inlet separator are presented in Figs. 2 and 3 which show the projection of the particle trajectories in the blade to blade cylindrical surface and the meridional plane through the machine axis, respectively. One can observe that the trajectories of these large particles deviate considerably from the flow streamlines because of their high inertia. These particles can be seen to continue in their axial motion uninfluenced by the flow field until they impact the blade or casing. One can see that some of the particles near the tip traverse the twisted blades without any impacts. Many of these particles are still separated however because of their outward radial location relative to the splitter between the engine and scavenged flow. The particles that impact the swirling vanes pressure surface, rebound with a smaller radially outward velocity component and a larger circumferential velocity component that causes their centrifugation. These particles impact the tip casing and acquire a radially inward velocity after rebounding which causes them to enter the engine. On the other hand, many of the particles that impact the inner casing are reflected in the radially outward direction towards the tip annulus. Many of these particles also impact the outer casing and acquire a radial inward velocity after rebounding and later enter the engine. The very few particles exempt from this behavior are those impacting the inner casing further downstream, much closer to the hump, and might miss entering the engine due to their later impact locations with the outer casing, which causes them to separate. Figure 4 shows the locations of the particle impacts with the swirling vane surface. One can see from this figure that in general the particles impact the vane pressure surface much more frequently than the suction surface. The frequency of particle impacts with the swirling vane pressure surface vary along the vane chord and span and are more intense in the inner half of the span because of the particles which are deflected by their impact with the contoured hub. Very few particles impact the vane suction surface and these impacts are generally limited to the leading edge region. The extent of particle vane suction surface leading edge impact region was found to decrease with decreased particle sizes. Figure 5 shows the distribution of the calculated erosion parameter on the pressure surface. This figure shows that maximum blade erosion is predicted at the corner of the blade between the trailing edge and the hub. The particle impact angle of 25–30 degrees in this region is close to β_0, the impact angle corresponding to the maximum erosion for this particle target material combination. Both impact velocity and frequency of particles impact are also high in this region.

The unseparated particles enter the engine with the unscavenged air which follows the inner part of the flow path. Figure 6 shows the locations of particle impacts with the deswirling vane surface. One can see from this figure that the particle impacts with the deswirling vanes pressure surface are

Downloaded 02 Jun 2010 to 171.66.16.66. Redistribution subject to ASME license or copyright; see http://www.asme.org/terms/Terms_Use.cfm

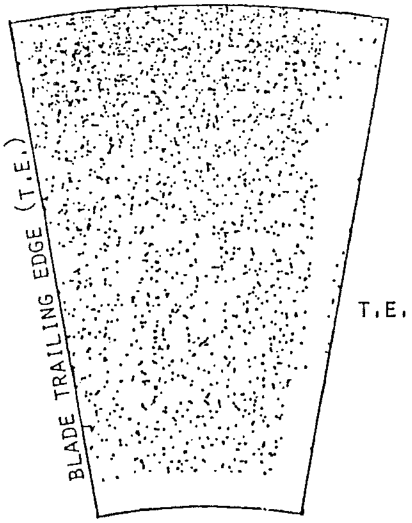

Fig. 8 Particle distribution at the vane exit

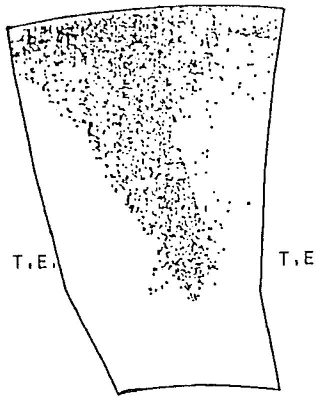

Fig. 9 Particle distribution first rotor exit

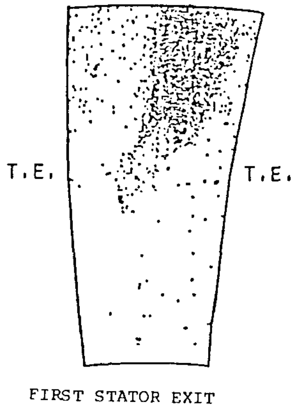

Fig. 10 Particle distribution first stator exit

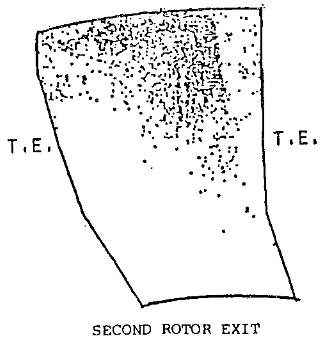

Fig. 11 Particle distribution second rotor exit

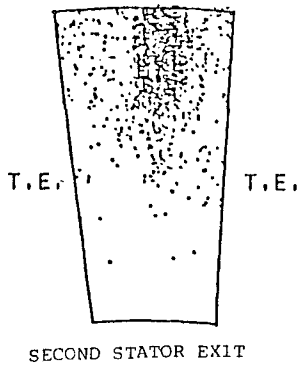

Fig. 12 Particle distribution 2nd stator exit

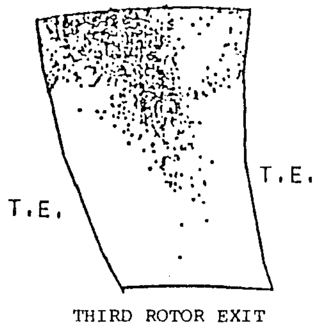

Fig. 13 Particle distribution 3rd rotor exit

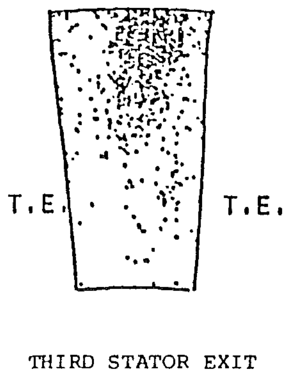

Fig. 14 Particle distribution 3rd stator exit

concentrated near the outer half of the deswirling vanes leading edge, but tend to spread over a larger portion of the vane pressure surface near the trailing edge. On the deswirling vanes suction surface, the particle impacts are more spread over the vane surface near the leading edge, but their spanwise distribution is limited to a narrower band that moves towards the humb near the vane trailing edge. The presented particle impact pattern with the deswirling vane surface is a result of the combined effect of particle distribution as they enter the vanes and the geometry of the twisted vanes and highly contoured annulus. Figure 7 shows that the erosion pattern on the pressure side of the deswirling vanes is maximum at the tip of the blade. Figure 8 shows the particles distribution after they leave the IGV vanes. As the particles travel through deswirl vanes they are redistributed in the radial inward direction

Downloaded 02 Jun 2010 to 171.66.16.66. Redistribution subject to ASME license or copyright; see http://www.asme.org/terms/Terms_Use.cfm

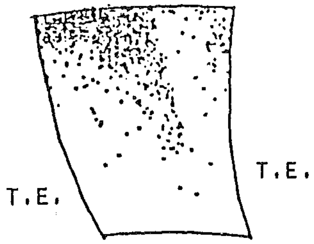

FOURTH ROTOR EXIT

Fig. 15 Particle distribution 4th rotor exit

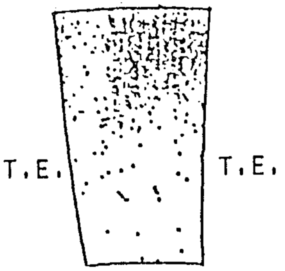

FOURTH STATOR EXIT

Fig. 16 Particle distribution 4th stator exit

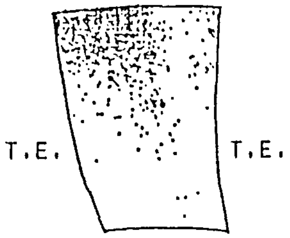

FIFTH ROTOR EXIT

Fig. 17 Particle distribution 5th rotor exit

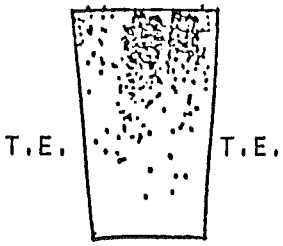

FIFTH STATOR EXIT

Fig. 18 Particle distribution 5th stator exit

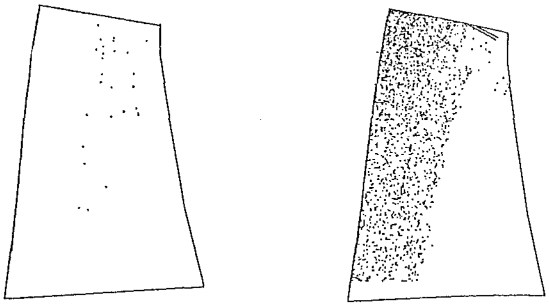

(a) Suction Surface (b) Pressure Surface

Fig. 19 Particle blade impacts—first rotor

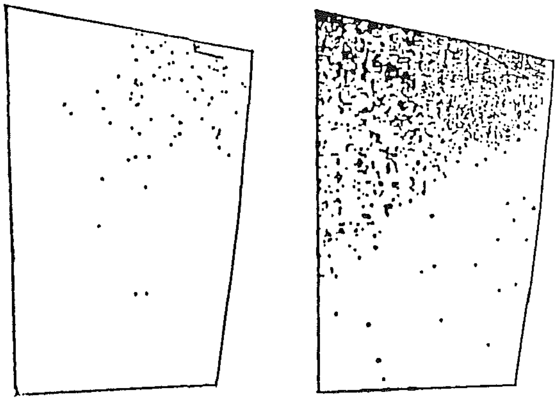

(a) Suction Surface (b) Pressure Surface

Fig. 20 Particle blade impacts—first stator

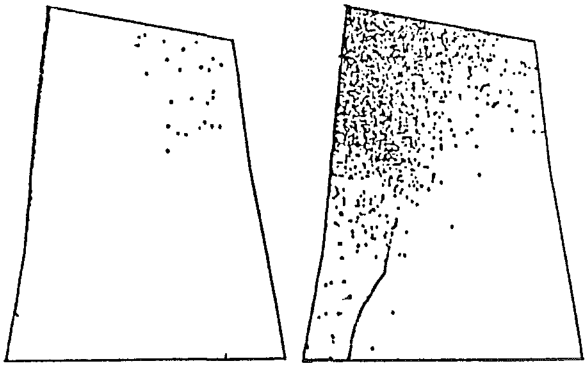

(a) Suction Surface (b) Pressure Surface

Fig. 21 Particle blade impacts—second rotor

before entering the compressor. The rest of the results demonstrate the dynamic characteristics of the particles as they are entrained by the gas through the five stage axial flow compressor. Due to the large difference in size between the compressor blades and the inlet swirling and deswirling vanes, Figs. 2 and 3 are half the scale of the rest of the presented results.

Figures 9 through 18 show the particle distribution at stations located between each two successive blade rows in the axial flow compressor. One can see from Fig. 9 that the particle distribution is very nonuniform at the station between the first rotor and stator blades. Figure 9 shows that there are very few particles in the inner quarter of the annulus, and that in the outer two-thirds, the particles are not uniformly distributed in the circumferential direction. Both distributions result from the particle impacts with the rotor pressure surface, through which the particles acquire circumferential velocities and are subsequently centrifuged to the outer annulus. Figures 10 through 18 demonstrate that these tendencies continue throughout the subsequent compressor stages, with the particles nearly absent throughout the inner half span in the latter compressor stages. The circumferential particle distribution at the blade row exits, which can be seen in Figs. 9 through 18, has no significant influence on the subsequent stages since the relative motion between the successive blade rows tend to average out this effect.

As the particles enter the compressor inlet guide vanes, they are more uniformly distributed in the radial direction. Figures 19 through 28 show the particle impact locations over the suction and pressure surfaces of the rotor and stator blades of the

Downloaded 02 Jun 2010 to 171.66.16.66. Redistribution subject to ASME license or copyright; see http://www.asme.org/terms/Terms_Use.cfm

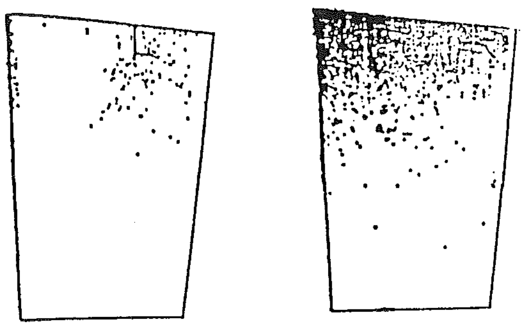

(a) Suction Surface (b) Pressure Surface

Fig. 22 Particle blade impacts—second stator

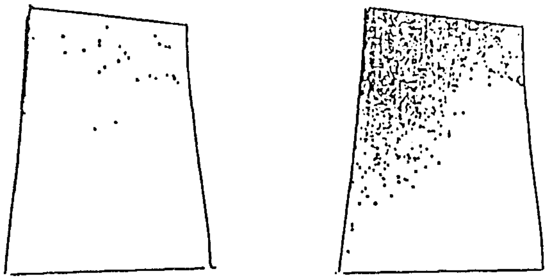

(a) Suction Surface (b) Pressure Surface

Fig. 23 Particle blade impacts—third rotor

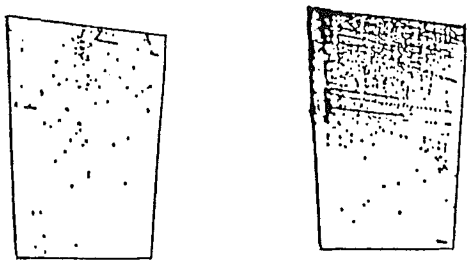

(a) Suction Surface (b) Pressure Surface

Fig. 24 Particle blade impacts—third stator

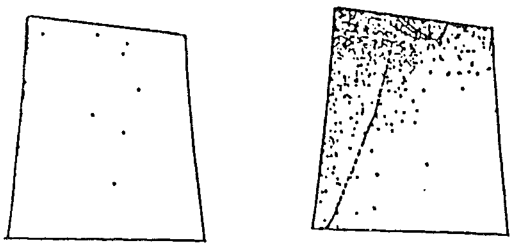

(a) Suction Surface (b) Pressure Surface

Fig. 25 Particle blade impacts—fourth rotor

five-stage axial flow compressor. An investigation of these figures reveals that a far greater number of particles impact the blade pressure surfaces, than their suction surfaces. The location and pattern of particle impacts were found to depend on the location of the compressor stage. Figure 19(*b*) shows that in the first rotor, the particle impacts extend over the blade pressure surface almost to half the chord, along most of the blade height. In the following blade rows, the particle

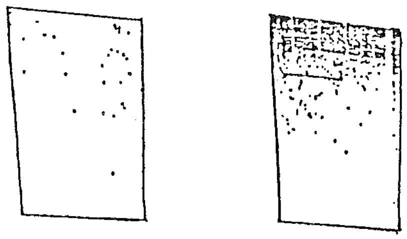

(a) Suction Surface (b) Pressure Surface

Fig. 26 Particle blade impacts—fourth stator

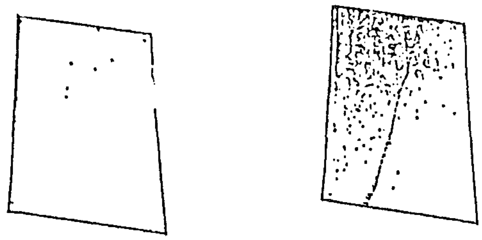

(a) Suction Surface (b) Pressure Surface

Fig. 27 Particle blade impacts—fifth rotor

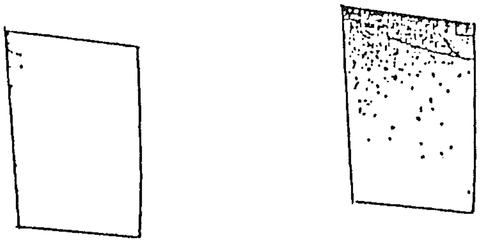

(a) Suction Surface (b) Pressure Surface

Fig. 28 Particle blade impacts—fifth stator

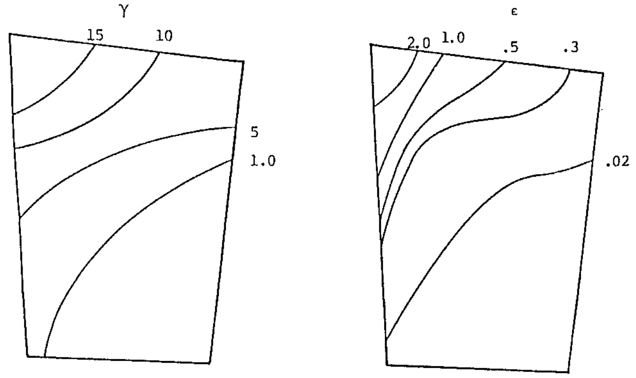

a) FREQUENCY OF PARTICLE IMPACTS

b) BLADE EROSION MASS PARAMETER

Fig. 29 Compressor IGV pressure side

blade impacts are found mostly near the outer radii and extend from the leading edge further along the blade chord. This is particularly true of the stator blade impacts, since these blades encounter the particles after acquiring very high circumferential velocities from the rotating blade impacts. The particles

Downloaded 02 Jun 2010 to 171.66.16.66. Redistribution subject to ASME license or copyright; see http://www.asme.org/terms/Terms_Use.cfm

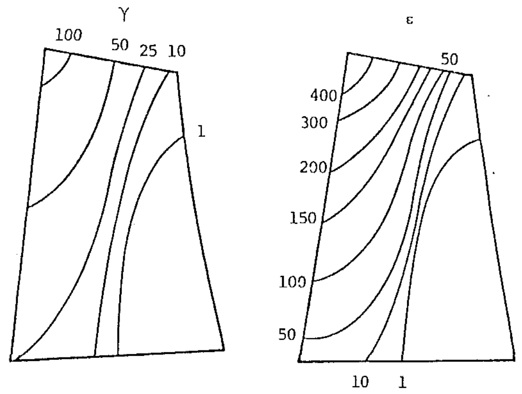

a) PARTICLE IMPACT FREQUENCY b) BLADE EROSION PARAMETER

Fig. 30 First rotor

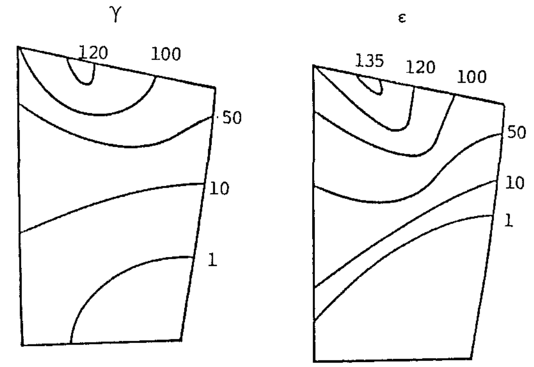

a) PARTICLE IMPACT FREQUENCY b) BLADE EROSION PARAMETER

Fig. 31 First stator

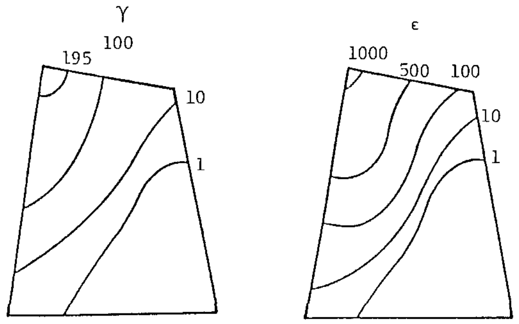

a) PARTICLE IMPACT FREQUENCY b) BLADE EROSION PARAMETER

Fig. 32 Second rotor

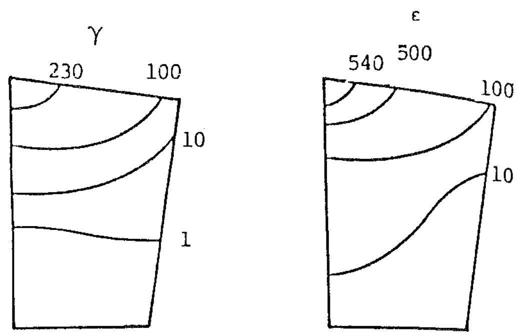

c) PARTICLE IMPACT FREQUENCY d) BLADE EROSION PARAMETER

Fig. 33 Second stator

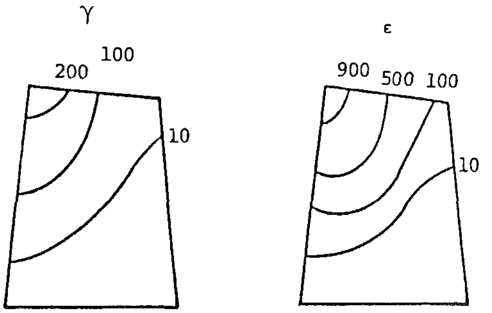

a) PARTICLE IMPACT FREQUENCY b) BLADE EROSION PARAMETER

Fig. 34 Third rotor

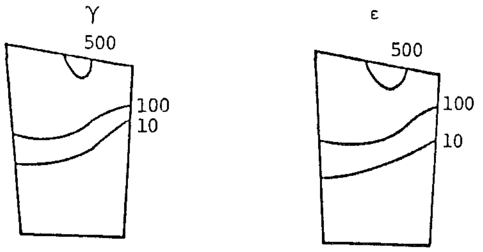

a) PARTICLE IMPACT FREQUENCY b) BLADE EROSION PARAMETER

Fig. 35 Third stator

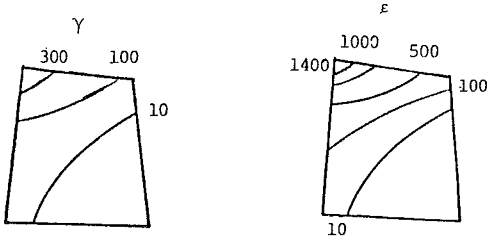

a) PARTICLE IMPACT FREQUENCY b) BLADE EROSION PARAMETER

Fig. 36 Fourth rotor

acquire much lower circumferential velocities from their stator blade impacts.

Figures 19 through 28 provide a qualitative description of the blade erosion pattern through the five-stage compressor. A quantitative description of the blade erosion can be determined according to the procedure described in references [6] and [12]. The computation of blade material erosion combines the presented data for the particle impact locations, the velocity and impingement angle relative to the blade as determined from the trajectory calculations, with the experimentally determined erosion characteristics of the stainless steel blade. From the examination of Figs. 19 through 28, one can observe that the impacts on the blade suction surfaces are insignificant. Therefore in this paper, the computation of blade material erosion is presented for only the blade pressure surfaces. Figure 29 shows the compressor inlet guide vane pressure side surface, with contours of the trajectory calculated frequency of particle impacts and erosion mass parameter. Maximum frequency of impacts and erosion are shown on the left tip corner. Figures 30 through 39 present the

Downloaded 02 Jun 2010 to 171.66.16.66. Redistribution subject to ASME license or copyright; see http://www.asme.org/terms/Terms_Use.cfm

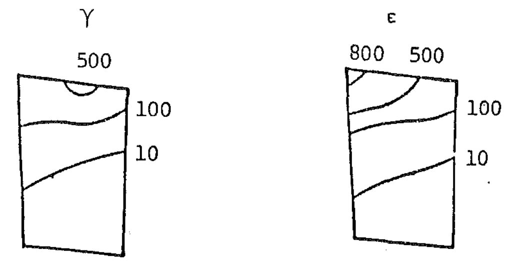

a) PARTICLE IMPACT FREQUENCY

b) BLADE EROSION PARAMETER

Fig. 37 Fourth stator

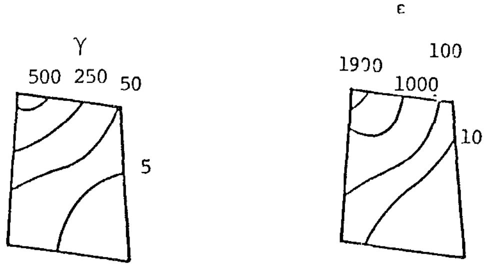

a) PARTICLE IMPACT FREQUENCY

b) BLADE EROSION PARAMETER

Fig. 38 Fifth rotor

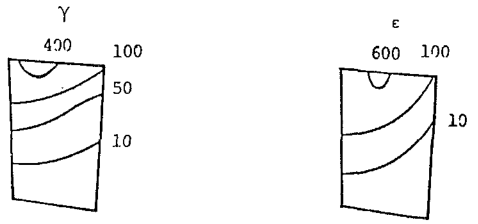

a) PARTICLE IMPACT FREQUENCY

b) BLADE EROSION PARAMETER

Fig. 39 Fifth stator

important blade erosion parameters, namely the frequency of particle impacts, and particle erosion parameter ϵ, for the five compressor stages. One can observe from the rotor blade pressure surfaces in Figs. 30, 32, 34, 36, and 38 that both particle impacts and erosion patterns are similar. The maximum erosion are shown at the blades leading edge tip corners, then diminishing towards the trailing edges hub corners. A region of the rotor blade pressure surface at the hub trailing edge corner extending diagonally over one third of the blade chord near the hub to about two-thirds of the blade span at the trailing edge is not subjected to any particle impacts and hence suffers no erosion. Figures 31, 33, 35, 37, and 39 show the variation of particle impact frequency and erosion parameters on the blade pressure surfaces of the five stators of the axial flow compressor. One can see from these figures that the stator blade pressure surface erosion pattern is very similar to the particle impact frequency pattern. The maximum stator blade erosion is always at the tip but is not necessarily near the leading edge. A small portion of the stator blade at the leading edge near the hub is not subjected to particle impacts. This is due to the effect of the preceding rotor impacts which centrifuge the particles in the radially outward direction. However, the particles are distributed more uniformly in the radial direction as they leave the stator blades. This explains the difference in the location of the nonimpacted blade surfaces in stationary and rotating blade rows. In general the erosion intensity per unit surface area increases in the latter stages due to the reduced flow path. The maximum value of stator blade erosion is generally lower than the maximum rotor blade erosion. One can observe from Figs. 19 through 28 that the erosion of the latter stages is particularly severe as the particles crowd near the outer annulus in the region with the smallest blade heights. An experimental study of the effect of erosion on the performance of a single stage axial flow compressor [13], revealed rotor and stator blade erosion patterns, which are consistent with the particle impact locations shown in Figs. 19 and 20.

There are two main consequences from the erosion damage of the blades. The first one is the change in the airfoil geometry and the quality of the surface. This is measured by the quantity of the material removed and the changes in the airfoil dimensions and the increase in the blade surface roughness. The second aspect is the change in the flow field due to the change in the airfoil geometry and the surface quality. This is measured by the changes in the pressure distribution and the total pressure loss coefficient of the blades.

The results obtained from the three dimensional analysis of the trajectories and erosion were not compared with the T700 engine. However, we believe that this analysis will agree very well with the real engine operating in such environment. During the last fifteen years of experience with similar analyses, we have found that the theory agrees well with the experimental findings. Confirmations have been performed with two General Electric helicopter engines, models 53 and 58. In addition, coal burning gas turbines, steam turbines, petrochemical turbine expenders, compressors and radial turbines have been compared and show good agreement. Most of this research work has been done for Industry. Some comparisons of trajectory calculations and erosion with experiments are reported in references [13–15].

Conclusion

The dynamics of the suspended solid particles which are entrained by the air through the engine inlet separator and its axial flow compressor were investigated. The distribution of the unseparated particles and the locations of particle-blade impacts were determined from the particle trajectory computations and presented throughout the five stage axial flow compressor. The presented results show a greater number of particle impacts with the blade pressure surfaces and very few impacts with the blade suction surfaces in the axial flow compressor rotors and stators. The results also show a nonuniform particle distribution in both the circumferential and radial directions between each pair of sequential blade rows. The trajectories of the 165 micron sand particles are dominated by their impacts with the blade pressure surfaces, after which they tend to migrate in the radial direction under the influence of the centrifugal forces. This process is initiated at the first rotor and continues throughout the five stages leading to increased particle concentration toward the outer annulus and the absence of the particle near the inner annulus. This in turn affects the blade erosion pattern in the various stages.

The maximum stator blade erosion is always at the tip, but not at the leading edge, and the maximum rotor blade erosion is near the leading edge at the tip. The maximum values of the rotor blade erosion are generally larger than the maximum stator blade erosion. In general, it may be concluded that the erosion damage can lead to significant reduction in engine efficiency as well as performance, due to the change in blades surfaces, tip leakages and blade pressure distribution.

Acknowledgment

This research was sponsored by U.S. Army Research Office-Durham, under Contact No. DAAG29-82-K-0029. We

Downloaded 02 Jun 2010 to 171.66.16.66. Redistribution subject to ASME license or copyright; see http://www.asme.org/terms/Terms_Use.cfm

gratefully acknowledge our useful discussions with Dr. Robert Singleton of Army Research Office.

References

1 Tabakoff, W., "Review – Turbomachinery Performance Deterioration Exposed to Solid Particles Environment," ASME JOURNAL OF FLUIDS ENGINEERING, Vol. 106, June 1984, pp. 125–134.

2 Tabakoff, W., "A Study of the Surface Deterioration due to Erosion," ASME *Journal of Engineering for Power*, Oct. 1983, pp. 834–839.

3 Hussein, M. F., and Tabakoff, W., "Computation and Plotting of Solid Particle Flow in Rotating Cascades," *Computers and Fluids*, Vol. 2, 1974, pp. 1–15.

4 Hussein, M. F., and Tabakoff, W., "Dynamic Behavior of Solid Particles Suspended by Polluted Flow in a Turbine Stage," *Journal of Aircraft*, Vol. 10, No. 7, July 1973, pp. 434–440.

5 Hamed, A., "Solid Particle Dynamic Behavior Through Twisted Blade Rows," ASME JOURNAL OF FLUIDS ENGINEERING, Vol. 106, Sept. 1984, pp. 251–256.

6 Hamed, A., and Fowler, S., "Erosion Pattern of Twisted Blades by Particle Laden Flows," ASME *Journal of Engineering for Power*, Vol. 105, Oct. 1983, pp. 839–843.

7 Grant, G., and Tabakoff, W., "Erosion Prediction in Turbomachinery Resulting from Environmental Solid Particles," *Journal of Aircraft*, Vol. 12, No. 5, May 1975.

8 Beacher, B., Tabakoff, W., and Hamed, A., "Improved Particle Trajectory Calculations through Turbomachinery Affected by Coal Ash Particles," ASME *Journal of Engineering for Power*, Vol. 104, Jan. 1982, pp. 64–68.

9 Katsanis, T., "Fortran Program for Calculating Transonic Velocities on a Blade-to-blade Stream Surface of a Turbomachine," NASA TND 2809, May 1965.

10 Katsanis, T., and McNally, W. D., "Revised Fortran Program for Calculating Velocities and Streamlines on the Hub-Shroud Mid Channel Stream Surface of an Axial, Radial, or Mixed Flow Turbomachine or Annular Duct, Vols. 1 and 2," NASA TND 8430, and NASA TND 8431, 1977.

11 Hamed, A., "Particle Dynamics of Inlet Flow Fields with Swirling Vanes," *Journal of Aircraft*, Vol. 19, No. 9, 1982, pp. 707–712.

12 Tabakoff, W., Hamed, A., and Ramachandran, J., "Study of Metal Erosion in High Temperature Coal Gas Stream," ASME *Journal of Engineering for Power*, Vol. 102, Jan. 1980, pp. 148–152.

13 Balan, C., and Tabakoff, W., "Axial Flow Compressor Performance Deterioration," AIAA Paper No. 84-1208, June 11–13, 1984.

14 Beacher, B., and Tabakoff, W., "Trajectories of Ash Particles Through a Coal-Burning Gas Turbine," ASME Paper 84-GT-122.

15 Beacher, B., "Investigation of Small Particle Trajectories Through Turbomachinery Environments," Ph.D. thesis, University of Cincinnati, 1983.

Downloaded 02 Jun 2010 to 171.66.16.66. Redistribution subject to ASME license or copyright; see http://www.asme.org/terms/Terms_Use.cfm

E. F. Matthys
Department of Mechanical and
Environmental Engineering
University of California,
Santa Barbara, CA 93106
Assoc. Mem. ASME

H. Ahn

R. H. Sabersky
Mem. ASME

Division of Engineering and
Applied Science
California Institute of Technology,
Pasadena, CA 91125

Friction and Heat Transfer Measurements for Clay Suspensions With Polymer Additives

Local heat transfer and friction coefficients were measured in a circular tube for suspensions of bentonite and for a combination of bentonite and polyacrylamide in water. Both the entrance and fully-developed regions were examined in laminar and turbulent regimes. A viscosity model based on rheological measurements makes it possible to represent the results obtained for the pure suspensions with newtonian relationships. The fluid combining clay and polymer, however, exhibited characteristics typical of viscoelastic solutions and was observed to display an unexpectedly high sensitivity to mechanical degradation.

Introduction

It has been suggested in the past that clay suspensions might sometimes induce unexpectedly large reductions in drag with respect to newtonian fluids. We have attempted to investigate further this claim using an experimental installation recently built by one of the authors. This installation was designed specifically for the measurement of the heat transfer and friction characteristics of various types of drag-reducing polymer solutions and suspensions.

The phenomenon of drag reduction is usually explained by interactions between the turbulence and elastic structures present in the fluid such as networks of macromolecules or fibers. Suspensions of clay particulates do not, however, appear to exhibit a similar type of strongly elastic behavior. It is therefore likely that the reduction in friction found previously for dilute clay suspensions corresponds only to the usual pseudoplastic friction reduction, and not to any fluid/turbulence interactions as in the viscoelastic drag reduction sense. This conclusion is supported by our experimental results.

A series of tests were conducted involving pure bentonite suspensions and also fluids prepared by adding polymer to these suspensions. Indeed, little information is available on this type of system which is routinely used for the drilling of oil wells. The addition of polymer to a bentonite suspension was observed to result in the flocculation of the fluid and in the development of its unexpectedly large sensitivity to mechanical degradation. This sensitivity induced important modifications of the friction and heat transfer characteristics of the fluid.

Summary of Previous Work

A large number of studies have been conducted on the subject of purely viscous non-newtonian fluids since such early work as that by Gregory [1]. The viscous behavior of bentonite suspensions, in particular, has been studied because of their pseudoplastic and thixotropic nature which is of vital importance for their use as drilling fluids [2]. Of interest, among others, is the work by Metzner and co-workers who introduced the concept of a generalized Reynolds number for the prediction of friction and heat transfer of power-law fluids [3, 4]. Another study suggested that for dilute aqueous thoria suspensions, the friction factor and the velocity profile would follow the newtonian laws if a viscosity estimated at the wall shear stress is used [5].

The addition of polymer or complex soaps to suspensions in order to reduce the friction has also been investigated in the past [6–8]. The stability and kinetics of the coagulation processes for colloids under shear [9], the various colloidal effects on the rheology of suspensions [10], and the phase separations in colloidal suspensions induced by polymer addition [11] have all been studied recently as well. The heat transfer aspects of particle suspensions were examined [4, 12, 13, 14] to a lesser extent, however, with some studies suggesting that newtonian heat transfer relationships might also be applicable for these fluids if an appropriate shear viscosity is used. A more complete literature review can be found elsewhere [15].

Experimental Installation

Some of the most important features of the experimental installation are mentioned briefly hereafter, a more detailed description being found in [15]. A schematic of this setup is also shown in Fig. 1. This installation was designed primarily for the study of polymeric solutions, and particular attention was therefore paid to the minimization of unintentional degradation of the fluids tested. Accordingly, rotating or reciprocal pumps were not adequate for our purposes, and a large single-action hydraulic cylinder (0.2545 m ID) was used for these experiments.

Such a once-through configuration also greatly enhances

Contributed by the Fluids Engineering Division for publication in the JOURNAL OF FLUIDS ENGINEERING. Manuscript received by the Fluids Engineering Division, June 24, 1986.

Copyright © 1987 by ASME

Downloaded 02 Jun 2010 to 171.66.16.66. Redistribution subject to ASME license or copyright; see http://www.asme.org/terms/Terms_Use.cfm

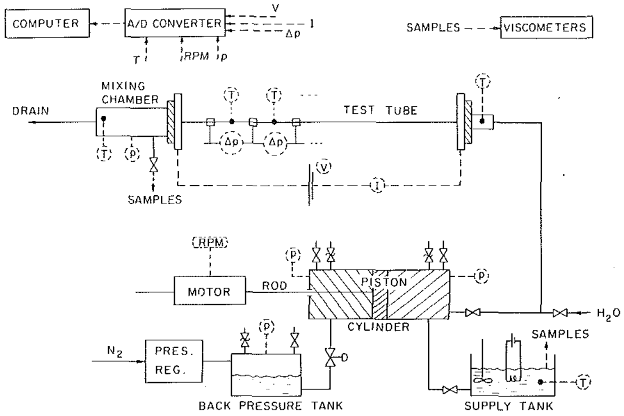

Fig. 1 Schematic of the experimental installation

the accuracy of the volumetric flow measurements which are normally difficult to conduct in-line with non-newtonian fluids. With the configuration used, the measurement of the speed of the piston via an electromagnetic transducer provided us with accurate values of the flow rate if pressurized fluid was supplied to the back of the piston in order to suppress leaks across the O-rings. Feed pipes of relatively large diameter (0.0508 m ID) were used in the system to reduce further any unintentional degradation experienced by the fluid.

The test tube used in these experiments was horizontal and of 7.86 mm ID and $L/D = 617.5$. This large L/D ratio is needed because entrance lengths of that order are necessary to achieve full development of temperature profiles in the case of many drag-reducing polymer solutions [15]. In addition, this rather long test section allows for better investigation of the degradation effects along its length. The test tube was instrumented with a number of thermocouples and differential pressure transducers to permit simultaneous measurements of friction and heat transfer at various axial locations. The measurement of both quantities at the same location is necessary if they vary significantly with distance because of degradation for example, which is indeed the case in these experiments as will be shown later.

Other measurements included the heating power as well as entrance and exit bulk temperature and pressure. A constant heat flux mode obtained by Joule heating of the tube wall was chosen for the high accuracy with which the corresponding heat fluxes can be computed from wall temperature and electric power measurements. These and all the other measurements were collected by a computerized data acquisition system. Verification runs were conducted systematically with newtonian fluids to assess the accuracy and reproducibility of the data, and both friction and heat transfer results were found in these cases to be very close to the values predicted by accepted correlations for newtonian fluids.

The degradation induced in the test tube itself being significant for some polymer solutions, it was shown that it is essential to evaluate properly the viscous characteristics of the fluid at the location of the measurements [15]. This is also true if other phenomena such as shear-thickening are of importance for the fluid in question [16]. Consequently, samples of the fluids were taken from the test tube during the measurements in order to be able to estimate the decrease in viscosity caused by the shear experienced in the test tube itself.

This viscosity was measured with custom-built capillary viscometers that were capable of operating in the laminar regime at the high shear rates observed in the test tube during the friction and heat transfer experiments (typically from 500 to 30,000 s^{-1}). One of these viscometers was of the pressurized tank type, fitted with a vertical capillary open to the atmosphere; the other was based on a horizontal piston and cylinder design with a horizontal capillary. In both cases, the pressure in the chamber was measured with pressure tranducers. The flow rates were computed from collected samples in the first case and from piston speed in the second. The capillaries used in this study for the measurement of the viscosity of the fluids ranged from an ID of 0.645 mm ($L/D = 469$) to 2.13 mm ID ($L/D = 337$). Additional factors such as temperature, degradation, aging, and concentration were also varied to evaluate their influence on the viscosity of the fluids tested.

Test Fluids

Bentonite was chosen as test material for the studies of suspensions because of its common use in the oil industry as a major component of drilling muds. The bentonite used in this study is routinely used in field operations (it satisfies API 13A specifications). It is produced by American Colloid. Published values were used for the physical properties of dry clay at 20°C: $Cp = 877$ J/(kg °K) and $k = 1.28$ W/(m °K). The properties of the suspensions were inferred from these values by simple ratio (for Cp) or using Maxwell's formula (for k). Tap water was used as suspending fluid and the pH of the suspension was monitored for variations.

Concentrations of 1 to 5 percent by weight of bentonite were chosen in order to be able to cover significant ranges of both laminar and turbulent regimes with the existing installation. The friction and heat transfer results for the 1 percent suspension were discarded, however, because of the rapid sedimentation rate it exhibited, which prevented good repeatability of the results. Indeed, sedimentation tests showed that the time needed to obtain a half-height of clear water from an homogeneous fluid would vary between a few

Nomenclature

C_F = $\tau_w/(0.5\rho V^2)$ friction coefficient
C_H = $h/(\rho\ Cp\ V)$ Stanton number
Cp = specific heat capacity [W s/kg °K]
D = tube inside diameter [m]
$f\,[x/D]$ = entrance region correction factor (equation (5))
Gz = $(\pi\ \mathrm{Re}_a\ \mathrm{Pr}_a\ D)/(4x)$ Graetz number
h = $q_w/(T_w - T_b)$ convection coefficient [W/m² °K]
j_H = $C_H \mathrm{Pr}_a^{2/3}$ apparent Colburn factor
k = thermal conductivity [W/m °K]
K = $\tau_w/(\gamma_w)^n$ consistency [N s^n/m^2]
K' = $\{(3n+1)/(4n)\}^n K$ consistency [N s^n/m^2]
n = power law exponent (see definition of K)
Nu = $(hD)/K$ Nusselt number
Pr_a = $(\eta_a\ Cp)/k$ Apparent Prandtl number
q_w = wall heat flux [W/m²]
Re_a = $(\rho VD)/\eta_a$ Apparent Reynolds number
Re′ = $(\rho V^{2-n} D^n)/(K'\ 8^{n-1})$ generalized Reynolds number
T_b = bulk temperature [°K]
T_w = wall temperature [°K]
V = bulk velocity [m/s]
x = distance from the entrance of the tube [m]
γ_n = $(8V)/D$ Newtonian laminar wall shear rate [s^{-1}]
γ_w = $\{(3n+1)\ \gamma_n\}/(4n)$ laminar wall shear rate [s^{-1}]
η_a = τ_w/γ_w apparent viscosity [N s/m²]
η_{eff} = τ_w/γ_n effective laminar viscosity [N s/m²]
ν_{eff} = η_{eff}/ρ effective laminar kinematic viscosity [m²/s]
ρ = density [kg/m³]
τ_w = wall shear stress [N/m²]

Downloaded 02 Jun 2010 to 171.66.16.66. Redistribution subject to ASME license or copyright; see http://www.asme.org/terms/Terms_Use.cfm

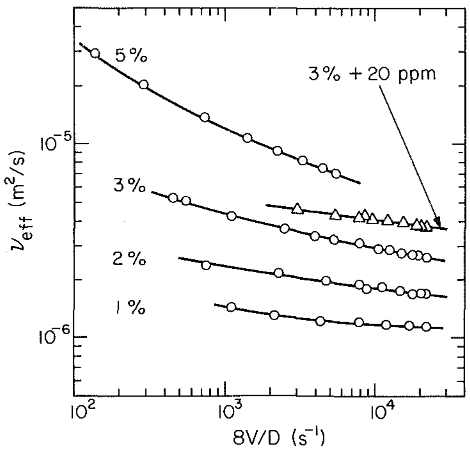

Fig. 2 **Effective laminar viscosity of pure bentonite suspensions and of an unused combination of bentonite and polyacrylamide in water. (Sample of 1 percent bentonite measured at 25.4°C, 2 percent at 25.0°C, 3 percent at 25.1°C, 5 percent at 25.2°C, and 3 percent + 20ppm polyacrylamide at 23.2°C.) [ν_{eff} ± 5 percent; 8V/D ± 1 percent].**

minutes for the 1 percent suspension and several weeks for the 5 percent one, with an abrupt jump observed around 3 percent.

The density of a 5 percent by weight bentonite suspension was measured to be

$$\rho = 1{,}174 - (0.480\ T)$$

where T is expressed in Kelvins. The density of suspensions of lower concentration was computed from this result using linear interpolations.

The polymer used in these experiments is a high-molecular weight polyacrylamide (Separan AP-273 by Dow Chemical Co.) which, at the low concentration used in this study (20 ppm by weight,) does not modify significantly the density, conductivity, and specific heat capacity of its solvent.

The effective laminar viscosity of the bentonite suspensions was measured with the capillary viscometers. Typical viscosity results are shown in Fig. 2 as a function of the corresponding newtonian laminar wall shear rate. Results are also shown for an unused combination of 3 percent bentonite and 20 ppm polyacrylamide in water. The addition of this small amount of polyacrylamide to the bentonite suspension appears to have significantly increased the viscosity of the fluid. This viscosity increase is in fact proportionally larger than if the same amount of polymer had been added to water alone (43 versus 7.5 percent). Also, considering the sensitivity to degradation exhibited by this fluid (described below), it is likely that its viscosity at low shear rates might be even proportionally larger with respect to the pure clay suspension.

The addition of polyacrylamide induced an immediate flocculation of the suspension, further characterized by a typical upper layer of clear water. This flocculation could be the result of a direct interaction between the bentonite and the polymer, or possibly a byproduct of the associated change in pH. This flocculation process also apparently resulted in an extreme sensitivity of this fluid to mechanical degradation and handling. It was shown for example that agitation by hand of a container of flocculated fluid could result in a decrease in measured viscosity of over 30 percent. It is therefore important to note that great care should be taken in order to measure the viscosities of the "undegraded" fluid in a reproducible fashion. Naturally, the shear inherent in the measurement by capillary could also degrade the fluid during the test itself. This effect was usually not very significant, however. This was verified by running the same sample twice through the viscometer.

It should be emphasized, in any case, that this sensitivity of the viscosity to degradation is not as serious a problem as it may appear at first because the viscosity results obtained for an "undegraded" fluid are not used *as is* for the computations corresponding to the actual friction and heat transfer tests. Indeed, samples of fluid exiting the test pipe were taken during these tests and the viscosity of these samples measured as well. This measured viscosity corresponds then to fluid having been subjected to significant degradation in the main tube, especially for turbulent flow. This viscosity is naturally lower than that of the unused fluid and much less prone to further degradation. It is also much more appropriate for the computation of properties and dimensionless numbers pertaining to the flow in the main test tube. Friction and heat transfer results seem to confirm this belief.

It was considered at first that the degradation effect might correspond to the breakup of flocs, but the friction and heat transfer reduction results suggested instead that it is the polymer that becomes more susceptible to mechanical degradation. This conclusion is drawn from the typical decrease in viscoelastic drag and heat transfer reductions which are normally observed for pure polymer solutions. In future investigations of this phenomenon, direct measurement of the molecular weight of the polymer in the degraded combined fluid would be helpful in order to further evaluate the extent of this degradation. Studies of the chemistry of this type of mixture would also be useful in order to be able to understand better the reasons behind this apparent increased fragility of the fluid.

The suspensions show, as expected, a strong pseudoplastic behavior. For example, power-law exponents of about $n = 0.55$ were computed for the shear rates corresponding to the tests conducted at lowest speed with the 5 percent suspension. The temperature effect on the viscosity of these fluids could unfortunately not be correlated by a unique Arrhenius-type exponent over the whole range of shear rate, unlike in the case of pure polymer solutions. Consequently, high-order polynomials had to be curve-fitted to the viscosities measured at various temperatures. Similar relationships were computed for samples subjected to various degrees of degradation in the test tube during actual runs. All these polynomials were subsequently used in the computer programs for the processing of data. The trends exhibited by the viscosity of the samples collected during the experiments are similar to those shown in Fig. 2. Naturally, the magnitude of the viscosity of these samples was significantly smaller than that of the corresponding undegraded fluid.

Friction Results

The pressure drop along the main test tube was measured at various locations with pressure transducers. From this measurement, the wall shear stress can be easily computed by

$$\tau_w = D\,\Delta p/(4\Delta x).$$

This wall shear stress can then be used to estimate a corresponding newtonian laminar wall shear rate ($8V/D$) and power-law exponent by using the effective laminar viscosity results obtained in the capillary viscometers. These results can indeed be expressed as $[\tau_w/(8V/D)]$ as a function of $8V/D$, and n can then be obtained at that particular shear stress from

$$n = \partial(\log \tau_w)/\partial(\log (8\mathrm{V/D})).$$

Note that this procedure gives an equivalent power-law exponent that may vary as a function of shear rate. This equivalent power-law exponent can in turn be used to compute an associated non-newtonian laminar wall shear rate

$$\gamma_w = (3n+1)(8V/D)/(4n).$$

An "apparent viscosity" can then be determined as the ratio of the wall shear stress to this non-newtonian laminar wall shear rate

$$\eta_a = \tau_w/\gamma_w.$$

Downloaded 02 Jun 2010 to 171.66.16.66. Redistribution subject to ASME license or copyright; see http://www.asme.org/terms/Terms_Use.cfm

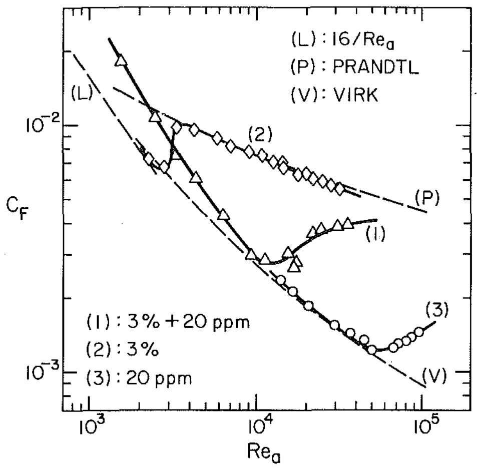

Fig. 3 Friction results at $x/D = 560$ for a solution of 20 ppm of polyacrylamide, a 3 percent bentonite suspension, and a fluid based on a combination of the two additives (C_F ± 5 percent; Re_a ± 10 percent).

This apparent viscosity is in turn used for the computation of an "apparent Reynolds number"

$$Re_a = \rho VD/\eta_a.$$

Note that this procedure is used for turbulent flow as well, and becomes then an approximation based on the quasi-laminarity observed very close to the wall. This approximation, in a sense related to the "law of the wall" concept appears to be physically reasonable, especially for drag-reducing fluids with extended viscous sublayers, and its validity seems to be confirmed by the results obtained with this method.

Indeed, the use of this apparent viscosity allows the development of adequate correlations for the friction and heat transfer results. These correlations proved indeed to fit fluids as different as simple shear-thinning polymer solutions and complex time-dependent discontinuously shear-thickening fluids [15, 16]. For this scheme to be valid, however, the power-law exponent and the apparent viscosity must be computed at the wall temperature. The degradation induced in the test tube itself must also be taken into account by using the viscosity of degraded samples in the computations.

When a generalized Reynolds number *Re'* [4] was used for the processing of the data, the laminar results for the suspensions of bentonite without polymer matched very well the laminar newtonian law, as expected. The turbulent friction results for these fluids exhibit then in this representation a typical pattern of curves parallel to the newtonian law. These results are in good agreement with the values obtained by Metzner [4] at comparable values of the power-law exponent [15].

On the other hand, and more importantly, the apparent viscosity described above can be used to compute the corresponding apparent Reynolds number. For the pure suspensions of bentonite, the laminar results expressed in terms of this apparent Reynolds number are then represented, as expected, by a curve parallel but slightly higher than that for newtonian laminar flow. Interestingly, the turbulent results for these purely viscous non-newtonian suspensions, however, show in turn an excellent match with the turbulent newtonian fluid correlation. This is evident in Fig. 3.

For example, the turbulent friction results obtained for the suspensions of 2, 3, and 5 percent bentonite between $Re_a = 2{,}500$ (the observed transition) and $Re_a = 50{,}000$ are best fitted by

$$C_F = 0.0781\ Re_a^{-0.252} \tag{1}$$

which gives values within approximately 2 percent of those predicted by Prandtl's expression for newtonian fluids. This apparent Reynolds number representation is thus capable of satisfactorily "absorbing" the reduction in friction caused by pseudoplasticity for purely viscous non-newtonian fluids. Consequently, this representation is the one we favor for the study of viscoelastic drag reduction which is then evidenced by a marked decrease of the friction coefficient below the newtonian values, even after this "subtraction" of the pseudoplastic reduction.

The excellent match with newtonian values reported above also supports the belief that the reduction in friction observed for the suspensions of clay particulates is due only to the pseudoplastic nature of the fluid and not to elastic interactions with the turbulence as in the case of viscoelastic fluids.

Friction results were also obtained for a mixture of 3 percent bentonite and 20 ppm polyacrylamide in water. These results are presented in Fig. 3 in the apparent Reynolds number representation, together with the results for the fluids based on bentonite alone and on polyacrylamide alone. All the data correspond to $x/D = 560$, a station close to the end of the tube, in order to minimize entrance effects. These results and the necessary properties were computed at the wall temperature. The viscosity used in these computations was obtained from samples collected at the end of the test tube during the actual runs, and takes therefore into account the degradation incurred in this tube itself.

As mentioned above, the results for the 3 percent bentonite suspension fit the newtonian correlations very well. The results for the pure 20 ppm polyacrylamide solution, on the other hand, are in good agreement with the drag-reduction asymptote up to the point ($Re_a = 60{,}000$) where mechanical degradation in the test tube starts to impair the viscoelastic drag-reducing ability of the solution.

The expression found [15] for the drag-reduction asymptote using the scheme described here is

$$C_F = 0.624\ Re_a^{-0.585} \tag{2}$$

for $6{,}000 < Re_a < 90{,}000$ which gives values somewhat smaller than Virk's correlation for $Re_a > 40{,}000$. This expression corresponds to fully-developed flow as it was shown that the turbulent hydrodynamic entrance length is only about 100 diameters for these dilute solutions.

The results obtained for the combination of bentonite and polymer show a trend significantly different from that exhibited by the curves corresponding to the pure bentonite suspension or to the pure polyacrylamide solution. For the lower flow rates, the friction coefficients appeared to be mostly intermediate between the newtonian and the asymptotic curves, although the data point for the lowest flow rate was higher than both laminar and turbulent newtonian values. The friction coefficient reached the asymptotic minimum value at higher flow rates, but mechanical degradation in the test tube thereafter caused the friction to increased very fast as in the case of the pure polymer solution.

This dramatic degradation effect appeared at $Re_a = 10{,}000$ however, rather than at $Re_a = 60{,}000$ as in the case of the pure polyacrylamide solution. This lower onset of the degradation effect on friction reduction shows the much greater susceptibility to shear exhibited by the fluid based on both bentonite and polymer additives. This effect is consistent with the observations made during the viscosity measurements.

The friction coefficient for the combined fluid exhibited large variations with distance along the length of the tube. This is in marked contrast with the behavior of both the pure bentonite suspension (which showed very short hydrodynamic entrance effects and no subsequent variations of the friction with distance) and with the pure polymer solution (which showed all the degradation effect concentrated at the beginning of the tube.) For $Re_a < 9{,}000$ the friction coefficient decreased uniformly over the whole length of the tube, and this very long "entrance effect" might explain why the results at low flow rate were found to be larger than for asymptotic conditions. As the Re_a reached 10,000 a sudden increase in

Downloaded 02 Jun 2010 to 171.66.16.66. Redistribution subject to ASME license or copyright; see http://www.asme.org/terms/Terms_Use.cfm

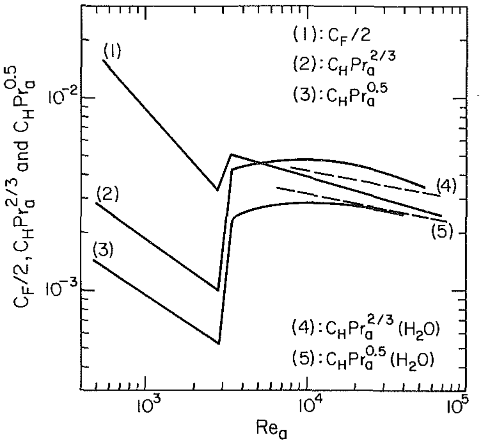

Fig. 4 Friction and heat transfer results measured at $x/D = 560$ for bentonite suspensions of concentration between 2 and 5 percent ($C_F \pm 5$ percent; $j_H \pm 10$ percent; $Re_a \pm 5$ percent).

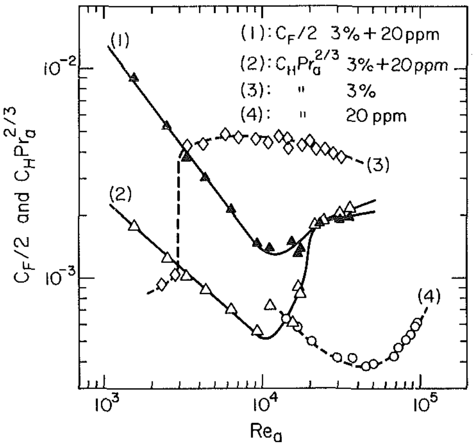

Fig. 5 Friction and heat transfer results at $x/D = 560$ for a combination of 3 percent bentonite and 20 ppm polyacrylamide in water. Heat transfer results for the corresponding pure bentonite suspension and pure polymer solution are also shown for comparison ($C_F \pm 5$ percent; $j_H \pm 10$ percent; $Re_a \pm 10$ percent).

friction was observed at the end of the pipe, the onset of which took place consistently earlier in the pipe for higher flow rates. This friction increase is naturally reflected in the data obtained at $x/D = 560$ by the increase in friction coefficient with Reynolds number. This decrease in the efficiency of the drag reduction process is very likely due to the degradation induced in the pipe, and it will be shown that, as expected, it is accompanied by an equivalent effect on the heat transfer.

Heat Transfer Results

The turbulent heat transfer results obtained at $x/D = 560$ for the various concentrations used in this study were shown to be well correlated by the same expression, provided these results are expressed in terms of Colburn factors and apparent Reynolds numbers. The best-fitting curves for the results are shown in Fig. 4, with the numerous individual data points omitted for clarity (the scatter being small as illustrated in Fig. 3 and 5 which include some of the same data points). As in the case of friction, the turbulent results are in good agreement with those for water. Additionally, it can be noticed on this graph that the Colburn analogy seems to apply for these suspensions as satisfactorily as it does for water. Indeed, as in the case of water, the values of $C_F/2$ found for the bentonite suspensions are intermediate between the Colburn factors obtained with apparent Prandtl number exponents of 2/3 and 1/2.

The small scatter observed for the Colburn factors (with exponent 2/3) corresponding to the different concentrations and shear rates indicates that the use of such a Colburn factor takes adequately into account even large variations in Prandtl number. (The apparent Prandtl number for these suspensions varied from 8 to 90 depending on the shear rate.) This property of the Colburn factor, taken for granted for newtonian fluids but *a priori* not so obvious for non-newtonian fluids, was also noticed for pure polymer solutions [15]. Also, as observed with other non-newtonian fluids, the Colburn factors with an exponent of 2/3 showed a smaller scatter than the Colburn factors computed with an exponent of 1/2, indicating that the former "absorbs" better the Prandtl number variations. Additionally, as anticipated, a Colburn factor with an exponent between 2/3 and 1/2 would appear to be in excellent agreement with the corresponding one for water, as well as with $C_F/2$.

The laminar results obtained at $x/D = 560$ indicated that the corresponding heat transfer coefficients were significantly larger than those that would be observed at that location in the case of newtonian fluids at the same Reynolds number. These high heat transfer rates are attributed to very long entrance regions which were probably due to the large Prandtl numbers typical of these fluids and flow conditions. Indeed, when the local heat transfer measurements were expressed in terms of Graetz numbers, the agreement with the following expression for non-newtonian laminar heat transfer in the entrance region [17]

$$\mathrm{Nu} = 1.41\ \mathrm{Gz}^{1/3}[(3n+1)/(4n)]^{1/3} \tag{3}$$

was excellent [15]. The turbulent results, on the other hand, indicated the existence of a much shorter thermal entrance length (less than 100 diameters) beyond which the Nu was constant. The transition to turbulent flow was observed to take place at about $Re_a = 3{,}000$ for the pure bentonite suspensions.

The heat transfer results obtained at $x/D = 560$ for a combination of polyacrylamide and bentonite in water are shown expressed in terms of Colburn factor and apparent Reynolds number in Fig. 5. For comparison, the results for the pure bentonite suspension and for the pure polyacrylamide solution are presented as well. Also shown is $C_F/2$ for the combined fluid. Because of the added polymer, the Colburn factors in the turbulent regime were naturally considerably lower for the combined fluid than for the pure bentonite suspension. Although the Reynolds number ranges do not overlap much, it appears that at low Re_a these results would also be lower than those for a pure polyacrylamide solution of the same 20 ppm concentration. Naturally, this only true up to the point where mechanical degradation in the test tube started to impair the viscoelastic heat transfer reduction. Indeed, for larger Re_a, the heat transfer increased significantly because of this degradation effect.

For the combined fluid, the Colburn factors before the onset of degradation were in good agreement with the expression found for asymptotic heat transfer reduction [15]:

$$C_H \mathrm{Pr}_a^{2/3} = 0.0596\ \mathrm{Re}_a^{-0.523} f(x/D) \tag{4}$$

where

$$f(x/D) = 6.32\ (x/D)^{-0.293} \tag{5}$$

for $0 < x/D < 600$. As in the case of pure polymer solutions, the Colburn factor for the combined fluid was much smaller than $C_F/2$ at low Reynolds numbers. These two parameters became then approximately equal in the range where the mechanical degradation plays an important role. Even in this region, however, they both remained smaller than the Colburn factor and $C_F/2$ for newtonian fluids and pure suspensions. As expected, the Reynolds number at which the friction showed a sharp increase due to degradation is the same as that at which the heat transfer began to be affected.

It was pointed out above that the local friction measurements for the combined fluid exhibited significant variations with distance. As expected, the local heat transfer

Downloaded 02 Jun 2010 to 171.66.16.66. Redistribution subject to ASME license or copyright; see http://www.asme.org/terms/Terms_Use.cfm

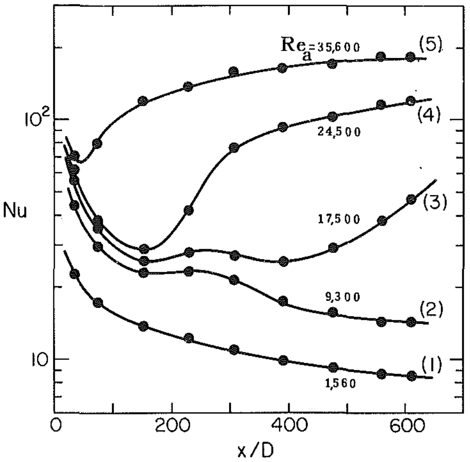

Fig. 6 Heat transfer results as a function of distance for a combination of 20 ppm of polyacrylamide and 3 percent of bentonite. Curve (1): Re_a = 1,560 (Pr_a = 30.2); (2): 9,300 (20.8); (3): 17,500 (17.1); (4): 24,500 (15.0); (5): 35,600 (13.1) (Nu ± 6 percent; x/D ± 0.5 percent).

measurements showed a pattern of variation very similar to that of the friction. For illustration, the Nusselt numbers for some typical runs are shown as a function of x/D in Fig. 6. It can be seen in this graph that at low Re_a the Nusselt number decreased uniformly over the whole length of the tube. This trend is typical of viscoelastic solutions which normally exhibit very long thermal entrance lengths in turbulent flow.

The trend is clearly different for $Re_a > 10{,}000$, which is the value at which the friction and heat transfer results became affected by degradation. For these larger Re_a, even though the Nusselt number decreased at the beginning of the tube, we can see that it did significantly increase further downstream. The onset of this increase was shifted towards the entrance of the tube as the flow rate was increased. This trend confirms again the belief that the combination of bentonite and polyacrylamide is much more sensitive to mechanical degradation than the pure solutions of polyacrylamide are.

Summary and Conclusions

An experimental study was conducted on the heat transfer, friction, and rheology characteristics of both suspensions of pure bentonite and suspensions of bentonite to which polyacrylamide was added.

The viscosity of the pure bentonite suspension was significantly increased by the addition of very small quantities of polyacrylamide. The resulting fluid flocculated with a separate upper region of clear water, and became extremely sensitive to mechanical degradation.

When an adequate apparent viscosity is used for the processing of data, the turbulent friction results for all the pure bentonite suspensions were well represented by newtonian relationships.

The turbulent friction results for the combined fluid showed signs of asymptotic drag reduction at low Reynolds number, but exhibited thereafter an abrupt increase typical of the high sensitivity of this fluid to the mechanical degradation induced in the test tube. The effect of degradation was also apparent in the variations of local friction measurements with distance along the pipe.

When Colburn factors and apparent Reynolds numbers were used, the turbulent heat transfer results for the various pure bentonite suspensions were well correlated by a unique expression regardless of the concentration of bentonite. In this representation, these results were also in good agreement with typical expressions for newtonian fluids.

The laminar results in the entrance region, on the other hand, were found to be well represented by a modified laminar expression for newtonian fluids.

The turbulent heat transfer results for the combination of bentonite and polyacrylamide exhibited a typical asymptotic reduction behavior at low Reynolds number. At higher flow rate, however, the strong sensitivity of this fluid to mechanical degradation impaired this viscoelastic reduction, causing the heat transfer to increase. The onset of this degradation-induced heat transfer increase occurred at the same Reynolds number as the corresponding friction increase.

Because of this sensitivity to mechanical degradation, the heat transfer results for the combined fluid exhibited large variations with distance along the test tube. These variations were identical in trend and relative magnitude to those observed in the case of the friction coefficient.

Acknowledgments

Partial support by the California Institute of Technology and the U.S. Department of Transportation is gratefully acknowledged. The authors would also like to thank Dr. V. Sarohia for his support and interest in this project, and Dr. T. Nguyen for providing some of the test materials.

References

1 Gregory, W. B., "Pumping Clay Slurry through a four-inch Pipe," *Mech. Eng.*, Vol. 49, No. 6, 1927, pp. 609–615.

2 Rogers, W. F., *Composition and Properties of Oil Well Drilling Fluids*, Gulf Pub. Co, Houston, 1948.

3 Metzner, A. B., and Reed, J. C., "Flow of Non-newtonian Fluids: Correlation of the Laminar, Transition, and Turbulent Regions," *AIChE J.*, Vol. 1, No. 4, 1955, pp. 434–440.

4 Metzner, A. B., "Heat Transfer in Non-newtonian Fluids," *Advances in Heat Transfer*, Vol. 2, 1965, pp. 357–397.

5 Eissenberg, D. M., and Bogue, D. C., "Velocity Profiles of Thoria Suspensions in Turbulent Pipe Flow," *AIChE J.*, Vol. 10, No. 5, 1964, pp. 723–727.

6 Poreh, M. et al., "Drag Reduction in Hydraulic Transport of Solids," *J. of the ASCE Hydraulics Division*, April 1970, pp. 903–909.

7 Ghassemzadeh, M. R., and Carmi S., "Drag Reduction in Flow of Coal-oil Suspensions," ASME JOURNAL OF FLUIDS ENGINEERING, Vol. 104, 1982, pp. 92–93.

8 Golda, J., "Drag Reduction in the Hydraulic Transport of Coal in Pipes," In *Proc. of 3d Int. Conf. on Drag Reduction*, Eds.: R. H. Sellin and R. T. Moses, University of Bristol, Bristol, England, 1984, paper D2.

9 Schowalter, W. R., "Stability and Coagulation of Colloids in Shear Fields," *Annual Review of Fluid Mechanics*, Vol. 16, 1984, pp. 245–261.

10 Russel, W. B., "Review of the Role of Colloidal Forces in the Rheology of Suspensions," *J. of Rheology*, Vol. 24, No. 3, 1980, pp. 287–317.

11 Gast, A. P., Hall, C. K., and Russel, W. B., "Phase Separations Induced in Aqueous Colloidal Suspensions by Dissolved Polmer," *Faraday Discuss. Chem. Soc.*, Vol. 76, 1983, pp. 189–201.

12 Orr, C., and Dalla-valle, J. M., "Heat Transfer Properties of Liquid-solid Suspensions," *Chem. Eng. Progr.*, Vol. 50, Symposium Ser. No. 9, 1954, pp. 29–45.

13 Thomas, D. G., "Heat and Momentum Transport Characteristics of Non-newtonian Aqueous Thorium Oxide Suspensions," *AIChE J.*, Vol. 6, No. 4, 1960, pp. 631–639.

14 Yoo, S. S., "Heat Transfer and Friction Factors for Non-newtonian Fluids in Turbulent Pipe Flow," Ph.D. dissertation, University of Illinois, Chicago, 1974.

15 Matthys, E F., "An Experimental Study of Convective Heat Transfer, Friction, and Rheology for Non-newtonian Fluids: Polymer Solutions, Suspensions of Fibers, and Suspensions of Particulates," Ph.D. dissertation, California Institute of Technology, Pasadena, 1985.

16 Matthys, E. F. and Sabersky, R. H. "Rheology, Friction, and Heat Transfer Study of a Discontinously Shear-thickening Antimisting Polymer Solution," To appear in *Journal of Non-newtonian Fluid Mechanics*.

17 Bird, R. B., Armstrong R. C., and Hassager O., *Dynamics of Polymeric Liquids*, Wiley, Vol. 1, New York, 1977.

Downloaded 02 Jun 2010 to 171.66.16.66. Redistribution subject to ASME license or copyright; see http://www.asme.org/terms/Terms_Use.cfm

K. K. Sheth
Sr. Associate Engineer,
Centrilift-Huges,
Claremore, Okla. 74017

G. L. Morrison
Associate Professor,
Department of Mechanical Engineering,
Texas A&M University,
College Station, Texas 77843

W. W. Peng
Professor,
Department of Mechanical and
Industrial Engineering,
California State University, Fresno,
Fresno, Calif. 93740

Slip Factors of Centrifugal Slurry Pumps

Experiments have been carried out in order to determine the effects on slip factor due to the various parameters affecting the performance characteristics of a centrifugal slurry pump. The experiments were conducted with water, sand slurry, and a glass bead slurry at three different pump speeds. Measurements of power, flow rate, head developed by the pump and the density of the slurry were made in order to obtain the characteristic curves of the pump. Using Euler's equation, equations were derived for calculating the slip and friction factors of the flow. The deduced slip factors for centrifugal slurry pump can be correlated well with suggested non dimensional groups. It shows a consistent trend of decreasing slip factor with increasing slurry mixture density and impeller rotation, or with a decreasing through flow rate. The sizes of the sand and glass bead particles are significantly different (0.71 mm versus 0.09 mm), however, the data correlations do not suggest its effect on the slip factors significantly as the other parameters. The slip factors deduced from head-flow rate curves are more reliable than those deduced from power-flow rate curves, since the shut-off power measurements are likely subjected to errors associated with the particles settling, or the transient effect if the measurements are taken momentarily.

Introduction

Studies on centrifugal slurry pump performance in the past have been mainly concerned with the additional friction losses in the through flow associated with the two-phase mixtures. In the early 1940s Fairbank [1] evaluated the effects of various parameters of solids (particle size, concentration ratio, and density) upon the performance characteristics of centrifugal pumps. He developed the first theoretical model and predicted that solids followed a path which was different from that of the liquid in a rotating impeller and resulted in a higher discharge relative velocity and a lower relative discharge angle than the liquid. He concluded that: (1) the drop in head velocity characteristic at constant speed varies not only with the concentration but also with the particle size of the material in suspension; (2) a slurry having colloidal properties has a different effect on pump characteristics than a slurry with a true suspension.

Twenty years later, Herbich [2, 3] carried out an in-depth study of the effects of solids in suspension on the performance characteristics of the centrifugal pump. He predicted the effects of pump design parameters on the slurry performance characteristics. Impellers having different vane shapes and different discharge angles were used. He also made high speed movies of rotating impellers through a transparent glass volute and traced the path of solid particles leaving the impeller.

Assuming a psuedo-homogeneous flow, Vocaldo and Charles [4] divided the head loss into three major terms:

$$\Delta H_m = I_i + I_l + I_s$$

where I_i is the pressure gradient which arises as a consequence of interaction between the particles and the liquids and among the particles themselves which also reflects the increase in density and the viscosity of the carrier liquid; I_l is the pressure gradient or head loss which could exist if the carrier liquid flowed alone at the same velocity as the slurry; I_s is the pressure gradient which contributes the energy required to maintain the solid particles in a state of suspension against the force of gravity. Vocaldo et al. [5] showed that these head losses increased with an increase in the velocity of the slurry.

Cave [6] gave an empirical formula for the effects of concentration ratio, specific gravity, and particle size. Duckham and Aboutaleb [6] have also obtained formulae for predicting the effect of the viscosity of liquid and slurry mixtures on the flow rate, head, and power by comparing the particle power number with particle Reynolds number. Their results were good for mixtures of different liquids, but the authors did not mention the effect of viscosity on the slurry mixtures.

Most of these studies are limited to either pure empirical correlations of the overall performances or some semi-empirical studies on the friction losses. Possible modifications on the slip factor or the energy-transfer effectiveness in the Euler's equation due to the presence of solid particles in the pumped fluid have never been seriously investigated.

Classical studies on slip factors of centrifugal pumps were mainly directed to the pumping of clear water. Several semi-empirical formulae relating slip factor with impeller geometries and operating conditions are well documented in the pump texts.

Contributed by the Fluids Engineering Division of THE AMERICAN SOCIETY OF MECHANICAL ENGINEERS and presented at the Winter Annual Meeting Symposium on Slurry Flows, Ahaheim, Calif., Dec. 7-12, 1986. Manuscript received of the Fluids Engineering Division October 9, 1986.

Copyright © 1987 by ASME

Downloaded 02 Jun 2010 to 171.66.16.66. Redistribution subject to ASME license or copyright; see http://www.asme.org/terms/Terms_Use.cfm

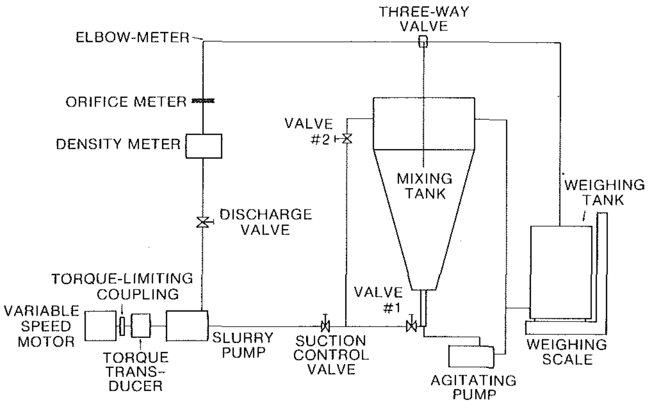

Fig. 1 Schematic diagram of test facility

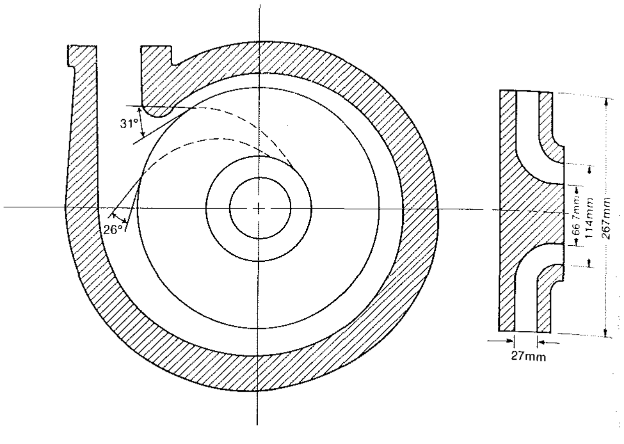

Fig. 2 Pump schematic

Experimental Facilities

The experiments were carried out with the test-rig shown in Fig. 1. The centrifugal slurry pump used for all the tests was designed and manufactured by Wilfley Pump Company. This pump was a horizontal, base mounted, single stage, rear intake centrifugal pump designed to handle abrasive slurries. The pump did not require usual stuffing box glands, or a mechanical seal for sealing around the shaft, but possessed a specially designed centrifugal seal consisting of a revolving expeller having vanes radiating from a recess in its center to its periphery and a die ring. The closed impeller has four pure radial-flow vanes, with 26.67 cm (10.5 in) outlet diameter, 2.697 cm (1.062 in) blade height and 31 deg blade angle at the discharge as shown in Fig. 2.

The closed flow loop shown in Fig. 1 was constructed for continuous operation. The 4.5 m^3 (900 gallon) conical tank was fabricated and connected to the pump by a 10.16 cm (4 in) diameter schedule 40 mild steel pipes with various gate valves. Three gate valves were installed in the suction line: The first to regulate solid flow; the second to regulate liquid flow; and the third to control the flow through the pump.

The slurry was prepared in the mixing tank and was fed to the suction line of the pump from the bottom of the tank. Another line which drew liquid from the top cylindrical portion of the mixing tank was also connected to the suction line of the pump for adjusting the concentration ratio. The pump returned the slurry to the tank through the discharge pipe.

A small centrifugal pump was used to prevent the settling of the solid particles within the tank. The suction line of the small pump ran from the top cylindrical portion of the mixing tank and the discharge line of the small pump was connected at the bottom of the mixing tank. The small pump produced an upward flow pattern in the mixing tank which kept the mixture in the tank agitated.

A nuclear density meter designed and built by Texas Nuclear was used to directly measure the slurry density with the help of a SGD E-Zcal multiprocessor. The density meter was chain mounted on the verticle discharge pipe. It used 100 mCi Cesium-137 as a radiation source. The system was self calibrating and would linearize to percent by weight of the solids. It had a precision of 1 percent of span at the 2.5 sigma confidence level, provided the process was free of entrained air. The system had the ability to measure not only concentration ratios of solids to mixture, but also could measure bulk density in any units. When a flow signal was provided, the system also calculated bulk, mass or volume flow rate. The density measurement obtained from the density meter was verified by diverting the discharge flow returning to the mixing tank to a weigh tank by a three way valve. The weigh tank was then used to verify the density of the mixture.

A 5.08 cm (2 in) diameter, standard 90 deg elbow having pressure taps at 45 deg was used as a flow meter. Two 0.3175

Nomenclature

a_2 = exit area of the pump impeller (m^2)
β = impeller discharge angle (degree)
C_v = concentration ratio of solids to mixture by volume
C_w = concentration ratio of solids to mixture by weight
D = impeller diameter (cm)
g = gravitational constant (m/s^2)
H = head (m)
ΔH_m = total head loss associated with slurry mixture (m)
I_i = head loss due to particles interacting with themselves and the liquid (m)
I_l = head loss with only liquid carrier present (m)
I_s = head loss required to keep particles in suspension (m)
K = fiction factor (s^2/m^5)
N = rotating speed of impeller (s^{-1})
P_d = disk friction power (watt)
P_i = power input to pumped fluid (watt)
P_l = power loss due to leakage (watt)
P_m = mechanical power loss (watt)
$P_{s/o}$ = input shaft power at shut off conditions (watt)
P_t = input shaft power (watt)
Pi_i = non dimensional parameter
Q = volumetric flow rate (m^3/s)
S_s = specific gravity of the solids
U_l = peripheral velocity of impeller at the inlet (m/s)
U_2 = peripherial velocity of impeller at the outlet (m/s)
W_2 = relative flow velocity at impeller outlet (m/s)
η_H = hydraulic efficiency
ν = kinematic viscosity of the carrier fluid (m^2/s)
μ = absolute viscosity ($N\ s/m^2$)
ρ_1 = density of the liquid (kg/m^3)
ρ_m = density of the mixture (kg/m^3)
σ_s = slip factor

Downloaded 02 Jun 2010 to 171.66.16.66. Redistribution subject to ASME license or copyright; see http://www.asme.org/terms/Terms_Use.cfm

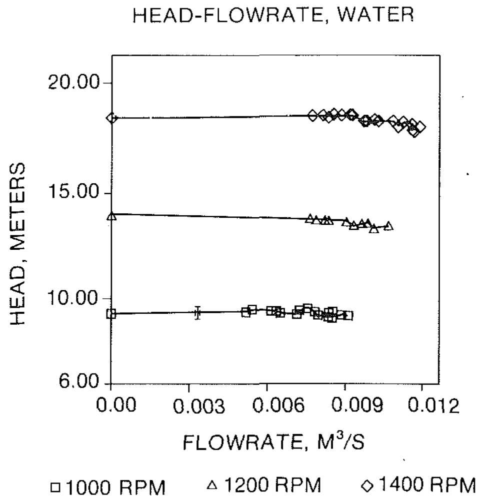

Fig. 3 **Head-flow rate performance for water**

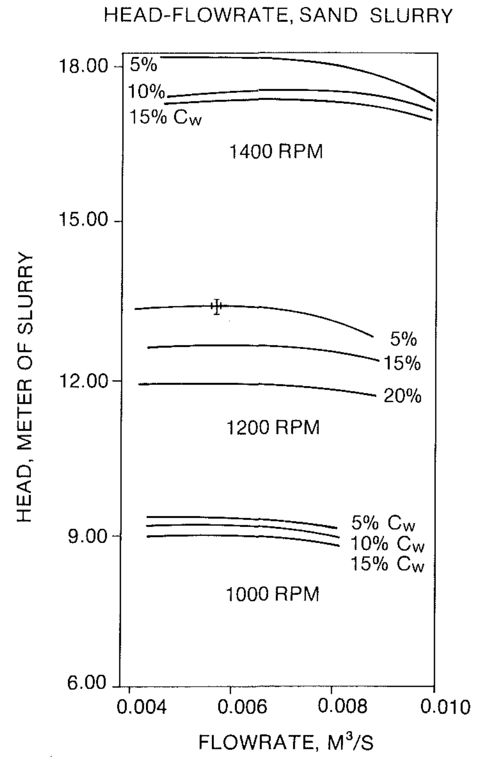

Fig. 4 **Head-flow rate performance for sand slurry**

cm (1/8 in) diameter pipe nipples were welded for pressure transducer connection. This flow meter was calibrated for water using both the weigh tank and an orifice flow meter. For measuring the slurry flow, the elbow flow meter was calibrated using the weigh tank for the different flow rates, concentration ratios, and slurry compositions.

A microprocessor based data acquistion system was used to collect and record the input shaft power, pump speed, discharge head, suction temperature, and volumetric flow rate for each operating condition. In addition, the density of the slurry and the concentration ratio of solids to liquid by either weight or volume were measured by the density meter and entered into the computer. The computer system then anaylzed the data and produced the various head, power, efficiency, etc. versus flow rate curves.

The slurry pump was operated at three different speeds: 1000, 1200, and 1400 rpm for each selected concentration ratio. The specific speed of the pump was 1150. The pump was first tested using pure water. Then a mixture of water and blasting sand was used. The specific gravity of the sand is 2.61. Particle size ranges from 0.297 to 2.00 mm with a mean particle size of 0.71 mm (0.029 in). After the sand slurry was removed from the testing facility, clear water was run again to determine the effect of any wear on the characteristics of the pump. No appreciable change in the performance characteristics was observed. Next, glass beads of specific gravity 2.42, having a mean particle size of 0.09 mm (0.0035 in) were mixed with the water and the pump tested. All particles are very fine and rounded. After removing the glass bead slurry, the pump was again tested with clear water and no change in the characteristics was observed. The size distribution for both the sand and glass beads were log normal.

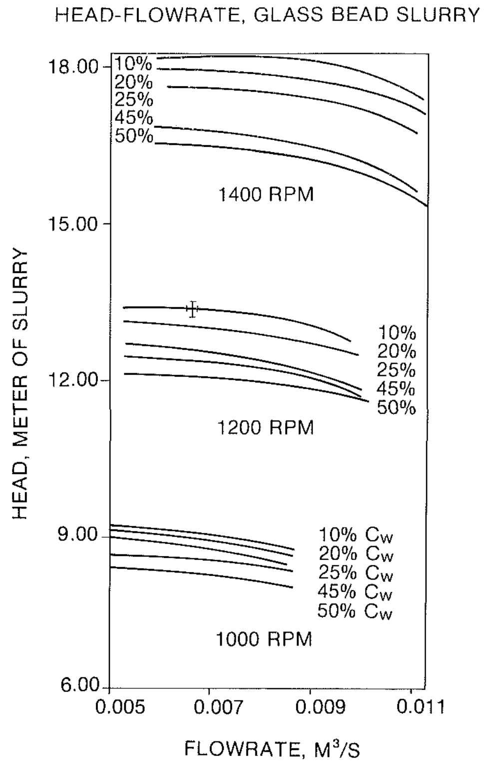

Fig. 5 **Head-flow rate performance for glass bead slurry**

The pump operating condition was varied from fully open to shut off, then to fully open position of the discharge valve while holding the pump speed and concentration ratio constant. The concentration ratio of solids to mixture was maintained by adjusting the solids and liquid mixing valves upstream of the pump.

Experimental Results

Figure 3 shows the head developed by the pump at three different speeds for water. It is interesting to note that the head was almost constant for the entire operating range of flow.

Figures 4 and 5 show the head-flow rate curves for the sand and glass slurries respectively. When the sand slurry was used in the system, the system jammed at concentration ratios higher than 25 percent by weight. The reason was that the particle size was relatively large which resulted in the settling of particles in the suction line at high concentration ratios. For the glass bead slurry (which consisted of substantially smaller particles), the data were taken up to 50 percent concentration ratio of solids to mixture by weight. As with the water, the head-flow rate curve was very flat. Again, an increase in pump speed resulted in an increase in the head. Conversly, an increase in the concentration ratio decreased the head produced.

Downloaded 02 Jun 2010 to 171.66.16.66. Redistribution subject to ASME license or copyright; see http://www.asme.org/terms/Terms_Use.cfm

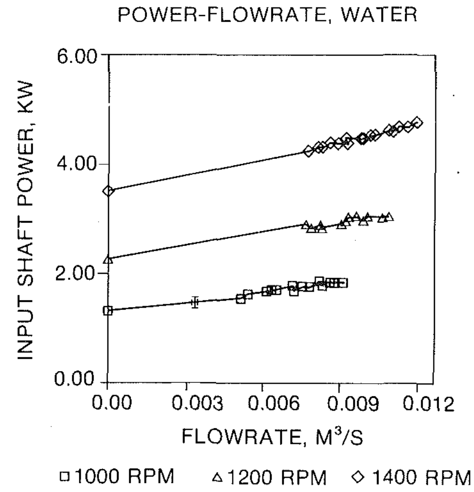

Fig. 6 Input shaft power-flow rate performance curve for water

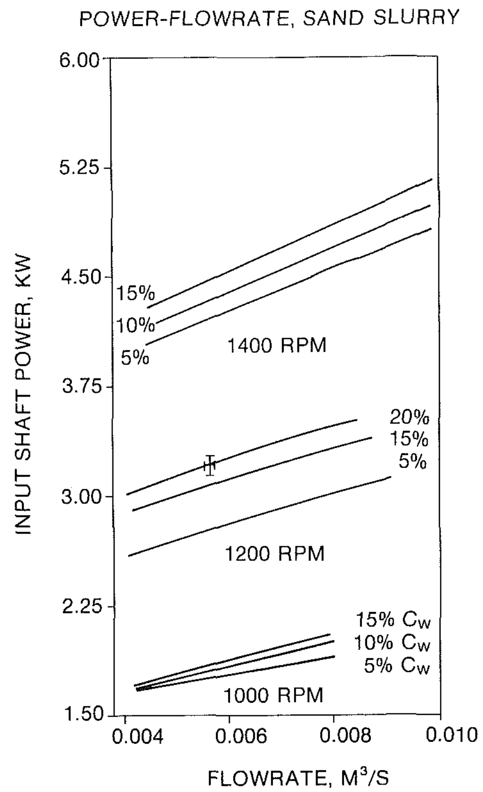

Fig. 7 Input shaft power-flow rate performance curve for sand slurry

The power input into the pump as calculated from the shaft torque and speed measurements for the various shaft speeds, slurry mixtures, and flow rates are presented in Figs. 6 to 8. The shaft power requirement increased with increasing concentration ratio, shaft speed, and flow rate as was expected.

Analysis

For a pump operating near the peak efficiency flow rate, the inlet flow velocity could be assumed swirl-free. So the actual head developed, can be calculated by the simplified Euler's equation as

$$H=\eta_H\frac{U_2}{g}\sigma_s\left(U_2-\frac{Q}{a_2\tan\beta}\right) \qquad (1)$$

where η_H is the hydraulic efficiency and σ_s is the slip factor.

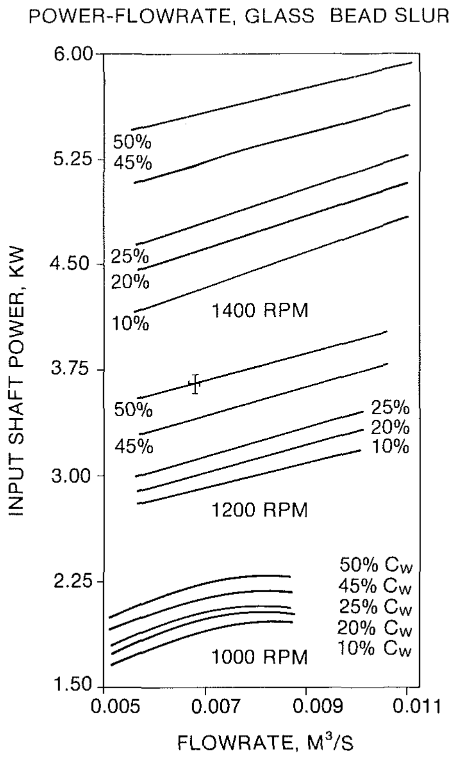

Fig. 8 Input shaft power-flow rate performance curve for glass bead slurry

Furthermore, near the peak efficiency point, the hydraulic losses can be assumed to be proportional to the square of the flow velocity or flow rate. Hence, equation (1) can be rewritten as

$$H=\sigma_s\frac{U_2}{g}\left(U_2-\frac{Q}{a_2\tan\beta}\right)-KQ^2 \qquad (2)$$

and the slope of the head-flow characteristics would be given as

$$-\frac{dH}{dQ}=\frac{\sigma_s U_2}{g a_2\tan\beta}+2KQ \qquad (3)$$

This assumption implies that the friction losses in the through-flow passage are similar to that within a stationary flow channel as long as there is no flow separation which would be the case if the pump was operating near the best efficiency point.

Equations (2) and (3) can be solved simultaneously using the data obtained in this study to determine the values of the unknowns: the friction factor (K) and the slip factor (σ_s), near the best efficiency range. The slip factor is dimensionless as it is the ratio of the actual tangential component of the flow velocity at discharge to the ideal one.

The slip factor can also be calculated from the input shaft power as follows:

Assuming that the total input shaft power, P_t can be divided into the power components as

$$P_t=P_i+(P_d+P_l+P_m) \qquad (4)$$

where P_i is the useful power delivered into the pump fluid, while P_d, P_l, and P_m are the power losses associated with disk friction, leakage, and mechanical losses in seals and bearings. Typically, these losses are assumed to be independent of the flow rate, especially for low and medium specific speed pumps, which is our case. Hence, measurements of the shaft power at shut off condition can be used to represent these losses, and $P_i=P_t-P_{s/0}$. Also

$$P_i=\rho QgH_i \qquad (5)$$

where

Downloaded 02 Jun 2010 to 171.66.16.66. Redistribution subject to ASME license or copyright; see http://www.asme.org/terms/Terms_Use.cfm

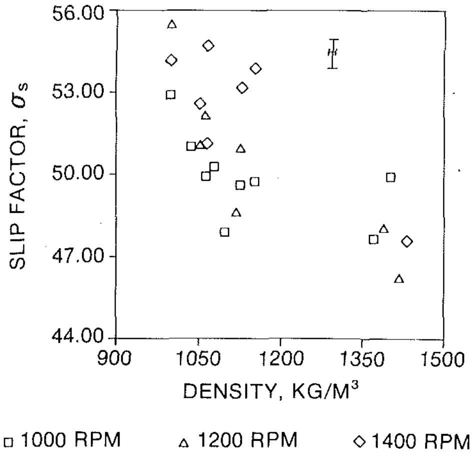

Fig. 9 Error bands of slip factors due to ± 10 percent variation of effective discharge area

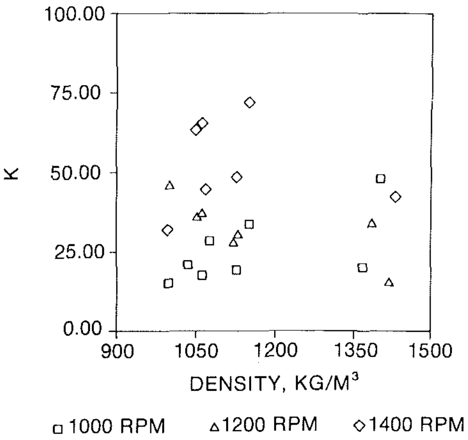

Fig. 10 Nondimensional K factor

$$H_i = \sigma_s \frac{U_2}{g}\left(U_2 - \frac{Q}{a_2 \tan\beta}\right) \tag{6}$$

is the ideal head rise of the pump without any friction loss associated with the through flow. The slip factor, therefore, could be determined from these equations. This methodology has been demonstrated by Peng and Jenkins [8] dealing with clear water. However the shut off power measurements in our case with slurry mixtures are less reliable due to the settling of solid particles at the low through flow. Hence the latter approach was not pursued further.

The density of the slurry depends on the densities of the solids and the carrier liquid and the concentration ratio of solids to mixture. Stepanoff [9] gave the relationship for determining the density of a slurry from the concentraton ratio by volume as,

$$\rho_m = \rho_l(1 - C_v + S_s C_v) \tag{7}$$

while Cave [6] gave the relationship for calculating the density of a slurry from the concentration ratio by weight as:

$$\rho_m = \frac{S_s \rho_l}{S_s - C_w(S_s - 1)} \tag{8}$$

The slip factors determined from these relationships, are subjected not only to the experimental errors, but also to the errors associated with the parameters in Euler's equation. The most likely error comes from the evaluation of the effective area (a_2) at the impeller discharge. The contraction factor due to the boundary layer blockage is difficult to estimate. However, the variation of the deduced slip factors associated with ±10 percent variation of the contraction factor is found to be insignificant compared with the overall variation range of the slip factors. The slip factors are plotted with respect to the slurry mixture density for sand slurry, glass bead slurry as well as the clear water flow at the three rotating speeds in Fig. 9. The error bands are due to the measurements and a ±10 percent change in the exit area (a_2) are also shown. All of the slip factors fall in the range of 46 to 56 percent. The associated non-dimensional K factors defined as:

$$K = \frac{g\Delta H_m}{0.5 W_2^2}$$

are shown in Fig. 10.

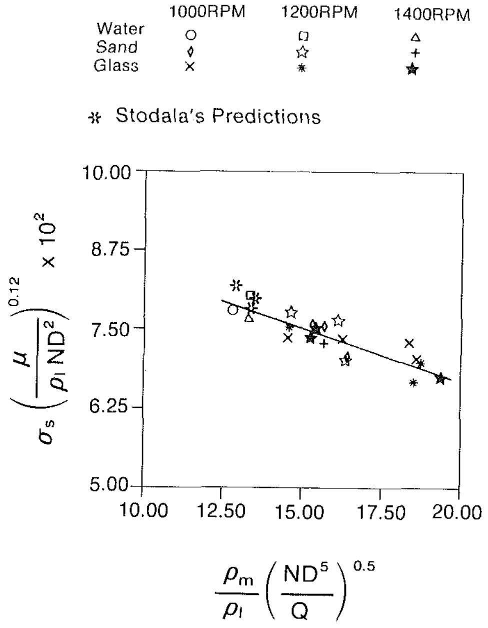

Fig. 11 Correlation of slip factors

Data Correlations

The slip factor is a parameter which accounts for the three dimensional flow phenomena in the one dimensional Euler's equation. Hence, it is difficult to analyze this parameter from a purely theoretical approach, even for the case of clear water flow.

With physical intuition, we expect that the slip factor, σ_s, to be a function of:

slurry mixture density	ρ_m
carrier fluid density	ρ_l
fluid viscosity	μ
impeller rotating speed	N
impeller diameter	D
and pump through flow rate	Q.

With Buckingham Pi theory of dimensional analysis, these relevant parameters can be grouped into three non-dimensional parameters, such as:

$$\mathrm{Pi}_1 = \frac{\rho_m}{\rho_l}, \qquad \mathrm{Pi}_2 = \frac{Q}{ND^3}, \qquad \mathrm{Pi}_3 = \frac{\rho_l ND^2}{\mu}$$

or Pi$_1$ and Pi$_2$ can be combined to become an alternative non-dimensional parameter

$$\mathrm{Pi}_4 = \frac{\rho_m Q}{\rho_l ND^3} = \frac{\rho_m NQ}{\rho_l N^2 D^3} = \frac{\rho_m NQ/D^2}{\rho_l N^2 D},$$

which in fact is the ratio of the characteristic Coriolis force over the centrifugal force.

In other words, the slip factors, σ_s, can be correlated with

Downloaded 02 Jun 2010 to 171.66.16.66. Redistribution subject to ASME license or copyright; see http://www.asme.org/terms/Terms_Use.cfm

Pi_1, Pi_2, and Pi_3 or $\sigma_s = f(Pi_1, Pi_2, Pi_3)$, since σ_s is also a nondimensional parameter. Effort has been made to correlate the deduced slip factors shown in Fig. 9 with all relevant nondimensional parameters. The best result is obtained with

$$\frac{\sigma_s}{(P_{i_3})^{0.12}} = \sigma_s\left(\frac{\mu}{\rho_1 ND^2}\right)^{0.12}$$

versus

$$\frac{Pi_1}{(P_{i_2})^{1.5}} = \frac{\rho_m}{\rho_1}\left(\frac{ND^5}{Q}\right)^{0.50}$$

as shown in Fig. 11. The exponents 0.5 and 0.12 were assigned to obtain the best-curve-fitting. A least squares polynomial curve fit of these data show that:

$$\sigma_s\left(\frac{\mu}{\rho_1 ND^2}\right)^{0.12} = 0.0989 - 0.00157\frac{\rho_m}{\rho_1}\left(\frac{ND^2}{Q}\right)^{0.50}$$

All classical formula for the slip factor account for the geometric effects, and are only applicable to clear water. Stodola's formula was used to calculate the slip factor for the clear water cases at the three rotating speeds. The results are also plotted on Fig. 11 for comparison.

Conclusions

The deduced slip factors for centrifugal slurry pumps can be correlated well with the suggested non dimensional parameters as shown in Fig. 11. The consistent trend of decreasing slip factor with increasing slurry mixture density and impeller rotation, or with a decreasing through flow rate is associated with the increasing phase-separation due to different Coriolis forces on the solids and the carrier fluid. These forces are acting in the direction transversed to the through flow.

The slip factors deduced from head-flow rate curves are more reliable than those deduced from power-flow rate curves, since the shut-off power measurements are likely subjected to errors associated with the particles settling, or the transient effect if the measurements at shut-off are taken momentarily. Hence, the data presented in Fig. 9 and 11 are based on the head-flow rate curves. Power-flow rate curves are only used for references.

In the present study, all tests were run with one pump. Further studies with tests of different pumps will be needed to extend the present correlations and the empirical formulae to account for both slurry mixture properties, and the pump geometric parameters before a unified slip factor formula can be achieved.

References

1 Fairbank, L. C., Jr., "Effects on the Characteristics of Centrifugal Pump," Solids in Suspension Symposium, *Proc. ASCE*, Vol. 129, 1941, p. 129.

2 Herbich, J. B., "Effect of Impeller Design Changes on Characteristics of a Model Dredge Pump," Paper No. 63-AHGT-33, ASME *Publications*, 1963.

3 Herbich, J. B., and Waddington, W. M., "Analysis of High Speed Movies of a Model Dredge Pump," Fritz Engineering Laboratory Report No. 277-M-11, Lehigh University, Bethlehem, Pa., June 1960.

4 Vocaldo, J. J., and Charles, M. E., "Prediction of Pressure Gradient for the Horizontal Turbulent Flow of Slurries," *Proc. Hydrotransport*, Vol. 2, BHRA Publications, 1972.

5 Vocaldo, J. J., Koo, J. K., Prang, A. J., "Performance of Centrifugal Pump in Slurry Service," *Proc. Hydrotransport*, Vol. 4, BHRA Publications, 1974.

6 Cave, I., "Effects of Suspended Solids on the Performance of Centrifugal Pumps," *Proc. Hydrotransport*, Vol. 4, BHRA Publications, 1976.

7 Duckham, C. D., Aboutaleb, Y. K. A., "Some Tests in a Single Stage Semi-Open Impeller Centrifugal Pump Handling Coal Dust Slurries," *Proc. Pumps and Turbines Conferences*, Vol. 1, 1976.

8 Peng, W. W., Jenkins, P. W., "Hydraulic Analysis on Component Losses of Centrifugal Pumps," *Symposium Performance Characteristics of Hydraulic Turbines and Pumps*, ASME, Nov. 1983.

9 Stepanoff, A. J., *Pumps and Blowers-Two Phase Flow*, Wiley, New York, N.Y., 1965.

Downloaded 02 Jun 2010 to 171.66.16.66. Redistribution subject to ASME license or copyright; see http://www.asme.org/terms/Terms_Use.cfm

Drag Coefficient and Settling Velocity of Particles in Non-Newtonian Suspensions

M. Y. Dedegil
Institut für Fördertechnik,
Abt. Strömungsfördertechnik,
University of Karlsruhe (TH),
Federal Republic of Germany

Drag forces on bodies in non-Newtonian fluids which are to be described by using the Reynolds number should only contain forces which are associated with the fluid velocity or particle velocity. Forces due to the yield stress τ_0 must be considered separately. According to its physical composition, the Reynolds number must be calculated by means of the fully representative shear stress including the yield stress τ_0. Then the drag coefficient c_D as a function of the Reynolds number can be traced back to that of Newtonian fluids.

I Introduction

Non-Newtonian suspensions are sometimes used as carrier media for coarse solids. An example of this application is the hydraulic transport of borings during the drilling of a tunnel or of a borehole. When drilling a tunnel in a sandy soil a water-bentonit suspension with a yield stress τ_0 is pumped to the working front which partly enters into the wall and stabilizes it. The excess of this suspension is used as carrier medium for the hydraulic transport of borings. The mixture of borings and bentonit-suspension is pumped into a settling tank where the borings settle and the clarified bentonit suspension is used again. The non-Newtonian characteristics of the bentonit suspension, especially its yield stress τ_0, have an influence on the settling velocity of the particles. This must be taken into account for the hydraulic transport as well as for the clarifying process in the settling tank. Similar conditions are given in the drilling of boreholes where scavenging suspensions are used to convey borings upward hydraulically.

The preparation and pumping of fresh concrete is another field where the settling velocity of particles in non-Newtonian cement-water-suspensions must be taken into account.

In the literature, a few experimental and theoretical studies are known. Slattery and Bird [1] determined the drag coefficient of spheres by measuring the settling velocity in CMC[1] solutions of different concentrations.

The theory they derived on the basis of the structural viscous fluid behavior was confirmed very well by their measurements. The fact that the most important data, such as sphere diameter, particle density and particle velocity, were not given makes it impossible to compare these results with those of other investigators.

Valentik and Whitmore measured the settling velocity of spheres in kaolin suspensions and listed all important data, thus facilitating the comparison of their results with those of other investigators.

Du Plessis and Ansley [3] all performed settling tests with glass spheres and natural sand particles in clay-water suspensions. The unfortunate choice of the parameters regarding grain size and test particle density on the one hand, and the density and viscosity of the suspension on the other hand often resulted in very low settling velocities and in inaccurate measurements. These facts were noticed by the authors themselves.

Pazwash and Robertson [4] measured the drag coefficient of spheres and differently shaped bodies, counterflowed by several clay-water suspensions in a circular channel. Direct measurements were not given, and the resulting diagrams do not allow coordinates to be determined for the suspensions used. Therefore, these measurements cannot be compared with those of other investigations, either. Moreover, the experimental design seems to have had a strong influence on the measured data.

Of the publications mentioned above only that of Valentik and Whitmore [2] contains data that are good enough to be used.

II Forces on Sinking Particles (Fig. 1)

The object of interest is a particle which is steadily settling at its final (settling) velocity in a homogeneous, incompressible slurry. The distance between the particle and the wall of the container is to be sufficient so that the wall has no effect on the settling motion.

The downward force on the particle results from its own weight G:

$$G = V \cdot \rho_s \cdot g \tag{1}$$

The normal and tangential forces act opposite to the weight. It is known that the integral taken over the surface of the normal force due to the hydrostatic pressure leads to the buoyant force A which is independent of the particle shape and does not require further explanation here:

---

[1] Carboxymethylcellulosis.

Contributed by the Fluids Engineering Division of THE AMERICAN SOCIETY OF MECHANICAL ENGINEERS and presented at the Winter Annual Meeting, Symposium on Slurry Flows, Anaheim, CA, December 7-12, 1986. Manuscript received by the Fluids Engineering Division June 3, 1986; revised manuscript received March 25, 1987.

Copyright © 1987 by ASME

Downloaded 02 Jun 2010 to 171.66.16.66. Redistribution subject to ASME license or copyright; see http://www.asme.org/terms/Terms_Use.cfm

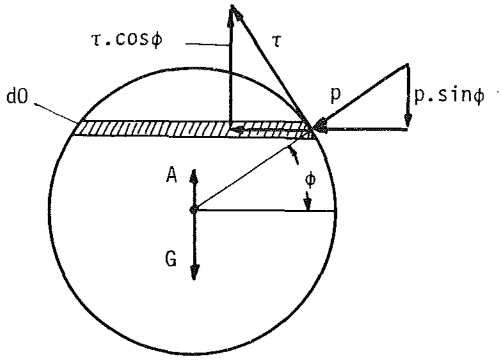

Fig. 1 Forces on a settling particle

$$A = V \cdot \rho_f \cdot g \tag{2}$$

The total drag force F caused by viscous effects results from the vertical components of the shear stress τ and the normal stress p. It can be calculated by the equation (3):

$$F = T + P = \iint \tau \cos\phi \, d0 + \iint p \sin\phi \, d0 \tag{3}$$

The shear stress τ in laminar flow of Newtonian fluids is expressed by equation (4)

$$\tau_N = \eta_N \cdot \frac{du}{dr} \tag{4}$$

For non-Newtonian fluids it must be expressed more generally, e.g., by equation (5)

$$\tau_{nN} = \tau_0 + f\left(\frac{du}{dr}\right) \tag{5}$$

If a yield stress $\tau_0 \neq 0$ exists, as in the case in Bingham and Herschel-Bulkley fluids, the frictional force T due to the shear stress can be separated into two components.

$$T = T_1 + T_2 = \iint \tau_0 \cos\phi \, d0 + \iint f(du/dr) \cos\phi \, d0 \tag{6}$$

The component T_1 of the yield stress

$$T_1 = \iint \tau_0 \cos\phi \, d0 \tag{7}$$

is independent of the velocity gradient. It is therefore also independent of the settling or slip velocity, and, of course, of the Reynolds number. T_1 can be calculated using τ_0 if the particle shape is given. For spherical particles T_{1K} is obtained from equation (7), as follows:

$$T_{1K} = \left(\frac{\pi}{2} d\right)^2 \tau_0 \tag{8}$$

Aside from that, the question of whether, and perhaps how much, the force T_1 depends on the surface condition cannot yet be answered. For small roughnesses and thick suspensions the suspension is assumed to fill the irregularities of the surface so a nearly smooth outer surface can be expected.

The real difficulty is to describe the sum of the normal force P and the second component of the tangential force T_2:

$$P + T_2 = \iint p \sin\phi \, d0 + \iint f(du/dr) \cos\phi \, d0 \tag{9}$$

In the case of Newtonian fluids, $(P + T_2)$ can be expressed as follows:

$$P + T_2 = c_D q \frac{\rho_f}{2} v_s^2 \tag{10}$$

Here, the drag coefficient c_D is expected to be a function of the Reynolds number.

If the drag coefficient is to be determined from the settling velocity, the calculation must be based upon the force equilibrium

$$G - A - T_1 - (P + T_2) = 0 \tag{11}$$

from which the drag coefficient c_D is obtained:

$$c_D = \frac{2}{v_s^2 \cdot \rho_f}\left[\frac{2}{3}(\rho_s - \rho_f) d \, g - \pi \, \tau_0\right] \tag{12}$$

Now the question is how to define the Reynolds number. The physical definition of the Reynolds number is the ratio of the inertial and frictional forces.[2] For the settling motion in Newtonian fluids the Reynolds number is indicated as

$$\mathrm{Re}_N = \frac{v_s d \, \rho_f}{\eta_N} \tag{13}$$

By rearranging equation (13) one obtains

$$\mathrm{Re}_N = \frac{v_s^2 \, \rho_f}{\eta_N \dfrac{v_s}{d}} \tag{13a}$$

so that in the numerator (besides the factors) the dynamic pressure is present as a measure of inertia, and in the

---

[2] An interpretation and a generalized definition of the Reynolds number for flow in pipes and channels is given by Brauer [5].

Nomenclature

A = Archimedian buoyancy
c_D = drag coefficient according to equation (12)
c_{D1} = drag coefficient according to equation (20)
d = particle diameter
$d0$ = differential element of the surface
du/dr = shear gradient
F = total drag force
G = weight of the particle
g = acceleration due to gravity
He = Hedström number according to equation (17)
P = normal force
p = pressure caused by counterflow
q = counterflow cross-sectional area of the particle
Re = Reynolds number according to equation (14) for the settling velocity v_s
Re_B = Reynolds number for Bingham fluids, equation (15)
Re_N = Reynolds number for Newtonian fluids, equation (13)
Re_1 = Reynolds number according to the former definition, equation (16)
T = frictional force due to the shear stress
T_1 = component of τ_0 in frictional force
T_{1K} = component of τ_0 in frictional force for spherical particles
T_2 = component of frictional force resulting from the viscosity
V = volume of the particle
v_s = settling velocity
ρ_f = density of the suspension
ρ_s = density of the particle
τ = shear stress
τ_N = shear stress for Newtonian fluids
τ_{nN} = shear stress for non-Newtonian fluids
τ_0 = yield stress for $du/dr = 0$
ϕ = angle which the surface normal makes with the horizontal
η_N = viscosity of Newtonian fluids
η_B = Bingham viscosity

Downloaded 02 Jun 2010 to 171.66.16.66. Redistribution subject to ASME license or copyright; see http://www.asme.org/terms/Terms_Use.cfm

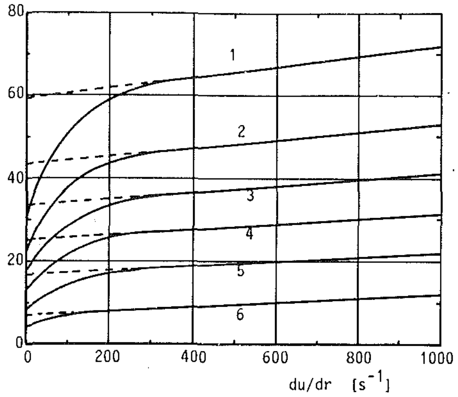

Fig. 2 **Shear diagrams of the suspensions according to Valentik and Whitmore [2]**

denominator the shear stress appears as a measure of friction. It must be emphasized that the shear stress was calculated by the representative shear gradient v_s/d.

An analogy of the function $c_D = f(\mathrm{Re})$ for Newtonian and non-Newtonian fluids can be expected only if the physical composition of the Reynolds number is the same in both cases. That means that the Reynolds number is defined more generally as:[3]

$$\mathrm{Re} = \frac{v_s^2 \rho_f}{\tau} \qquad (14)$$

The shear stress τ in the denominator will be defined by introducing the representative shear gradient v_s/d in equation (5).

For Bingham fluids the Reynolds number can be expressed, for instance, as:

$$\mathrm{Re}_B = \frac{v_s^2 \rho_f}{\tau_0 + \eta_B (v_s/d)} \qquad (15)$$

Often in the case of Bingham fluids the Reynolds number is arbitrarily defined as

$$\mathrm{Re}_1 = v_s d \frac{\rho_f}{\eta_B} \qquad (16)$$

which distorts the sense of the Reynolds number because the component τ_0 is missing in the shear stress. Therefore, it is often necessary to introduce the Hedström number

$$\mathrm{He} = \tau_0 d^2 \rho_f / \eta_B^2 \qquad (17)$$

as a parameter and thus to take τ_0 into account. Some authors [4] use the reciprocal value of Re_B and call it the "plasticity number."

III Non-Settling Particles

The existence of a yield stress $\tau_0 \neq 0$ leads to the fact that particles below a certain grain size in a suspension do not settle at all, but remain suspended. This is the case when the forces G, A, and T_1 are balanced.

For spherical particles the equations (1), (2), and (8) lead to

$$\frac{\pi d^3}{6}(\rho_s - \rho_f) g = \left(\frac{\pi}{2} d\right)^2 \tau_0 \qquad (18)$$

from which the sphere diameter for the critical case between settling and suspension amounts to:

$$d = \frac{3\pi}{2} \frac{\tau_0}{(\rho_s - \rho_f) g} \qquad (19)$$

Table 1 **Data for the suspensions used by Valentik and Whitmore [2]**

No.	ρ_f	η_B at high shear gradients	τ_0 (extrapolated) from high shear gradients	τ_0 (real)
-	kg/m³	Ns/m²	N/m²	N/m²
1	1280	0.0131	59.0	30.5
2	1254	0.0095	43.5	22.5
3	1226	0.0081	33.0	17.5
4	1207	0.0067	25.0	13.0
5	1184	0.0054	16.6	8.5
6	1149	0.0040	7.8	4.0

IV Evaluation of the Data of Valentik and Whitmore [2]

Six suspensions were used, and the resulting shear diagrams are displayed in Fig. 2. The rectilinear shape of the shear curves in the range of high shear gradients led the authors to assume Bingham suspensions. For this reason they calculated the yield stress τ_0 from the extrapolation of the shear curves at $du/dr = 0$. The data given by the authors and the real shear stresses are listed in Table 1.

The data for the spheres used, the settling velocities and the corresponding suspensions are compiled in Tables 2–7, columns 1–3. In column 5 the Reynolds number is defined as in equation (16), using the Bingham viscosities given in Table 1. In column 6 the drag coefficients c_{D1} are given; they are calculated according to equation (20) without taking the frictional force T_1 into account.

$$c_{D1} = \frac{4}{3} \frac{d\,g}{v_s^2} \frac{(\rho_s - \rho_f)}{\rho_f} \qquad (20)$$

The standard plotting of $c_{D1} = f(\mathrm{Re}_1)$ is displayed in Fig. 3. The drag coefficients for laminar flow result in a large deviation, so a system must be constructed using the Hedström number He.

If, however, the important shear gradients v_s/d (columns 4, Tables 2–7) are evaluated and compared with the shear curves of the supsensions in Fig. 2, it is obvious that the flow around the spheres has consistently taken place in the range of small shear gradients and that the Bingham behaviour of the suspension at high shear gradients had no influence.

However, if the Reynolds number is determined according to equation (14) with the shear stress τ being taken from Fig. 2 by $du/dr = v_s/d$, much smaller values are obtained (column 7, Tables 2–7).

The real drag coefficients calculated by using the real τ_0 from column 5 in Table 1 are indicated in column 8 of Tables 2–7 and are plotted versus the genuine Reynolds number (equation (14)) in Fig. 4.

Now one finds, without using the Hedström number, that in the laminar range a graph of the data forms the hyperbola 24/Re, known to be true for Newtonian fluids, and in the fully turbulent range approaches the constant value 0.4.

IV Conclusions

1) It appears that the Reynolds number should be calculated by means of the fully representative shear stress. This representative shear stress is obtained from the shear diagram of the fluid with the representative shear gradient, which is also contained in the Reynolds number for Newtonian fluids.

For the drag coefficient of particle, the representative shear gradient is given by: counterflow velocity/representative length of the particle.

---

[3] Metzner and Reed [6] used this generalized form of the Reynolds number to describe the laminar flow of Newtonian and non-Newtonian viscous fluids in pipes.

Downloaded 02 Jun 2010 to 171.66.16.66. Redistribution subject to ASME license or copyright; see http://www.asme.org/terms/Terms_Use.cfm

Table 2 Evaluation of the measurings from [2] with suspension 1

Particle		Measured velocity	v_s/d	Re_1	c_{D1}	Re	c_D
Diameter	Density						
mm	kg/m³	cm/s	1/s	-	-	-	-
15.9	6450	10.0	6.3	155	84.00	0.4	69.03
19.0	5832	21.0	11.1	390	20.04	1.7	16.65
19.0	6032	36.5	19.2	678	6.93	4.8	5.80
19.0	6513	65.0	34.2	1207	2.40	13.9	2.05
19.0	7290	98.0	51.6	1819	1.21	28.4	1.06
25.4	4804	41.0	16.1	1018	5.44	6.2	4.55
25.4	5237	78.0	30.7	1936	1.69	20.4	1.44
25.4	5544	98.0	38.6	2432	1.15	30.7	1.00
25.4	6142	130.0	51.2	3226	0.75	50.1	0.66
25.4	7034	163.0	64.2	4045	0.56	73.4	0.51
31.7	8195	228.0	71.9	7062	0.43	137.9	0.40
38.1	3431	48.0	12.6	1787	3.63	8.8	2.98
38.1	3603	57.0	15.0	2122	2.78	12.2	2.32
38.1	3742	72.0	18.9	2680	1.85	18.9	1.56
38.1	3990	88.0	23.1	3276	1.36	27.4	1.17
38.1	4025	95.0	24.9	3537	1.18	31.5	1.02
38.1	4479	116.0	30.4	4318	0.93	45.3	0.81
38.1	7160	225.0	59.1	8376	0.45	143.7	0.42
44.4	7712	252.0	56.8	10933	0.46	182.6	0.44
50.8	2673	30.5	6.0	1514	7.77	3.7	6.16
50.8	2909	58.0	11.4	2879	2.51	12.9	2.07
50.8	3416	121.0	23.8	6006	0.76	51.5	0.66
57.1	2728	51.0	8.9	2845	3.25	10.2	2.67
57.1	2981	81.0	14.2	4519	1.51	24.7	1.28
57.1	3124	94.0	16.5	5244	1.22	32.7	1.05
57.1	3621	125.0	21.9	6974	0.87	55.7	0.78
57.1	3958	147.0	25.7	8201	0.72	75.0	0.65

Table 3 Evaluation of the measurings from [2] with suspension 2

Particle		Measured velocity	v_s/d	Re_1	c_{D1}	Re	c_D
Diameter	Density						
mm	kg/m³	cm/s	1/s	-	-	-	-
12.7	6698	39.5	31.1	662	4.62	6.9	3.90
15.9	6450	73.0	45.9	1532	1.62	21.3	1.41
19.0	7290	154.0	81.1	3862	0.50	78.0	0.46
25.4	6123	150.0	59.1	5029	0.57	83.2	0.52
38.1	2937	48.0	12.6	2414	2.90	11.6	2.41
38.1	3214	83.0	21.8	4174	1.13	32.3	0.97
38.1	3815	140.0	36.7	7041	0.52	83.1	0.46
38.1	4179	166.0	43.6	8348	0.42	111.8	0.38
38.1	7160	250.0	65.6	12573	0.38	222.9	0.36
44.4	7712	256.0	57.7	15004	0.46	244.4	0.44
50.8	2437	41.0	8.1	2749	3.73	8.8	3.06
50.8	2673	85.0	16.7	5700	1.04	35.2	0.88
50.8	4082	183.0	36.0	12271	0.45	142.6	0.41
57.1	2352	54.0	9.5	4070	2.24	15.0	1.86
57.1	2765	114.0	20.0	8592	0.69	61.8	0.61
57.1	4003	204.0	35.7	15376	0.39	177.5	0.37

Table 4 Evaluation of the measurings from [2] with suspension 3

Particle		Measured velocity	v_s/d	Re_1	c_{D1}	Re	c_D
Diameter	Density						
mm	kg/m³	cm/s	1/s	-	-	-	-
9.5	6749	37.0	38.9	532	4.09	7.2	3.43
15.9	6732	110.0	69.2	2647	0.77	52.8	0.70
19.0	4199	54.0	28.4	1553	2.07	16.4	1.76
25.4	2795	22.0	8.7	846	8.78	3.2	6.93
25.4	3179	54.0	21.3	2076	1.81	17.2	1.51
25.4	3704	101.0	39.8	3883	0.66	53.0	0.57
25.4	6123	188.0	74.0	7228	0.38	150.3	0.35
31.7	3005	70.0	22.1	3359	1.23	28.8	1.04
31.7	8195	240.0	75.7	11515	0.41	242.8	0.39
38.1	2786	46.0	12.1	2653	3.00	13.4	2.57
44.4	2295	53.0	11.9	3562	1.80	17.8	1.48
44.4	2987	128.0	28.8	8602	0.51	91.7	0.45
50.8	2183	60.0	11.8	4613	1.44	22.9	1.19
50.8	2493	107.0	21.1	8227	0.60	67.7	0.52
50.8	3002	149.0	29.3	11457	0.43	123.8	0.39
50.8	4000	195.0	38.4	14994	0.40	199.5	0.37
57.1	2229	75.0	13.1	6482	1.09	35.3	0.93
57.1	2706	133.0	23.3	11495	0.51	103.0	0.46

Table 5 Evaluation of the measurings from [2] with suspension 4

Particle		Measured velocity	v_s/d	Re_1	c_{D1}	Re	c_D
Diameter	Density						
mm	kg/m³	cm/s	1/s	-	-	-	-
9.5	6751	68.0	71.6	1164	1.23	28.7	1.09
15.9	6432	129.0	81.1	3695	0.54	98.9	0.50
19.0	3560	65.0	34.2	2225	1.15	31.7	0.99
19.0	4035	97.0	51.1	3320	0.62	64.5	0.55
19.0	7290	175.0	92.1	5990	0.41	173.6	0.39
25.4	2711	15.0	5.9	686	18.40	2.0	15.39
25.4	2779	54.0	21.3	2471	1.48	23.6	1.25
25.4	3210	88.0	34.6	4027	0.71	58.0	0.62
25.4	3649	115.0	45.3	5262	0.51	93.5	0.46
31.7	2685	76.0	24.0	4340	0.88	46.0	0.76
38.1	2702	97.0	25.5	6658	0.66	74.3	0.58
44.4	2415	95.0	21.4	7599	0.64	73.0	0.57
50.8	2222	95.0	18.7	8694	0.62	74.2	0.54
57.1	1910	58.0	10.2	5966	1.29	29.2	1.09
57.1	2098	90.0	15.8	9258	0.68	67.8	0.60
57.1	2595	145.0	25.4	14915	0.41	166.0	0.38
57.1	3707	188.0	32.9	19339	0.44	267.2	0.42

Table 6 Evaluation of the measurings from [2] with suspension 5

Particle		Measured velocity	v_s/d	Re_1	c_{D1}	Re	c_D
Diameter	Density						
mm	kg/m³	cm/s	1/s	-	-	-	-
9.5	6751	94.0	98.9	1958	0.66	72.5	0.61
12.7	3332	28.0	22.0	780	3.84	9.4	3.27
15.9	3150	53.0	33.3	1848	1.23	31.7	1.07
15.9	6432	158.0	99.4	5508	0.37	204.4	0.35
19.0	2887	67.0	35.3	2791	0.80	50.1	0.70
19.0	3891	110.0	57.9	4583	0.47	119.6	0.43
19.0	7290	189.0	99.5	7874	0.36	292.3	0.35
25.4	2018	29.5	11.6	1643	2.69	11.2	2.17
25.4	2394	61.0	24.0	3397	0.91	44.3	0.79
25.4	2544	78.0	30.7	4344	0.63	69.6	0.55
25.4	3041	108.0	42.5	6015	0.45	125.0	0.41
25.4	4604	152.0	59.8	8465	0.42	226.3	0.40
25.4	6123	179.0	70.5	9969	0.43	298.0	0.42
31.7	2420	94.0	29.7	6533	0.49	101.8	0.44
38.1	2309	95.0	24.9	7936	0.52	106.9	0.47
38.1	7160	252.0	66.1	21052	0.40	603.0	0.39
57.1	1711	69.0	12.1	8639	0.70	61.1	0.60
57.1	2204	122.0	21.4	15274	0.43	180.2	0.40
57.1	2801	157.0	27.5	19656	0.41	287.5	0.40

Table 7 Evaluation of the measurings from [2] with suspension 6

Particle		Measured velocity	v_s/d	Re_1	c_{D1}	Re	c_D
Diameter	Density						
mm	kg/m³	cm/s	1/s	-	-	-	-
9.5	6751	126.0	132.6	3438	0.38	240.6	0.37
12.7	3319	76.0	59.8	2773	0.54	118.2	0.51
12.7	6693	140.0	110.2	5107	0.41	322.8	0.40
15.9	2984	86.0	54.1	3928	0.45	155.6	0.42
15.9	6432	154.0	96.9	7034	0.40	411.9	0.39
19.0	2516	82.0	43.2	4475	0.44	149.6	0.41
19.0	3838	126.0	66.3	6877	0.37	315.0	0.35
19.0	6032	164.0	86.3	8951	0.39	488.2	0.38
19.0	7290	190.0	100.0	10370	0.37	619.1	0.36
25.4	1708	42.0	16.5	3064	0.92	45.6	0.79
25.4	2009	71.0	28.0	5180	0.49	121.8	0.45
25.4	3006	118.0	46.5	8609	0.39	304.5	0.37
25.4	4102	149.0	58.7	10871	0.38	456.8	0.37
25.4	6023	192.0	75.6	14009	0.38	701.2	0.38
38.1	2000	77.0	20.2	8427	0.62	149.9	0.59
38.1	2310	102.0	26.8	11163	0.48	253.1	0.46
38.1	5932	231.0	60.6	25281	0.39	1087.7	0.38
44.4	2003	93.0	20.9	11861	0.50	217.7	0.47
57.1	1314	17.0	3.0	2788	3.71	8.1	2.95
57.1	1481	63.0	11.0	10333	0.54	106.1	0.49
57.1	2007	98.0	17.2	16074	0.58	247.2	0.56
57.1	2832	151.0	26.4	24767	0.48	555.8	0.47
57.1	3879	189.0	33.1	31000	0.50	838.7	0.49
57.1	6002	280.0	49.0	45926	0.40	1692.0	0.40

Downloaded 02 Jun 2010 to 171.66.16.66. Redistribution subject to ASME license or copyright; see http://www.asme.org/terms/Terms_Use.cfm

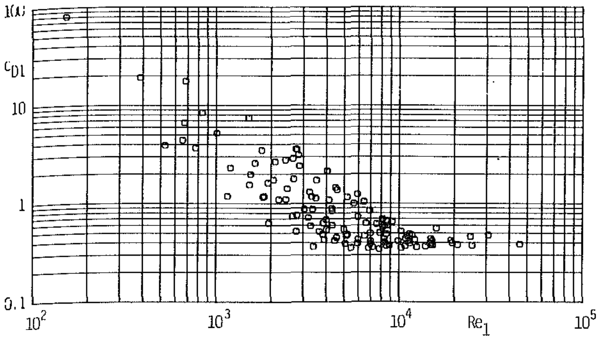

Fig. 3 Drag coefficient c_{D1} according to equation (20) as a function of the Reynolds number Re_1 according to equation (16) with the data of the suspensions 1-6 given by the authors [2]

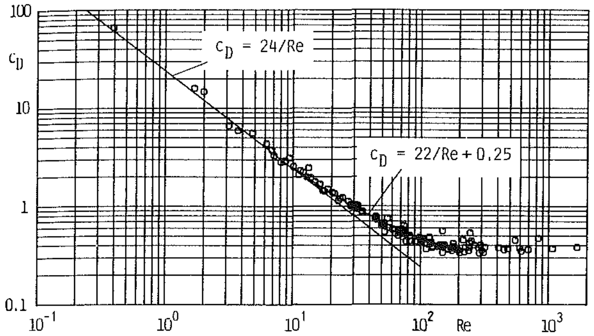

Fig. 4 Drag coefficient c_D according to equation (12) as a function of the Reynolds number Re according to equation (14) which was calculated by means of the actual values of τ_0 and τ from the shear diagrams (Fig. 2), from measurements of Valentik and Whitmore [2]

Thus many empirical regularities in non-Newtonian fluids can be traced back to those in Newtonian fluids. Often it is easier to describe them by analogy.

2) Flow forces which are to be described by using the Reynolds number should only contain components which are associated with the flow, i.e., the velocity of the fluid. Forces associated with the rheological properties of the fluid but independent of the velocity, as for instance T_1 resulting from the yield stress τ_0, must be considered separately because they are not functions of the Reynolds number.

3) For the drag coefficient of particles in structurally viscous fluids such as those of Bingham and Herschel-Bulkley, it is assumed that the function $c_D = f(\mathrm{Re})$ in laminar and fully turbulent counterflow, under consideration of the above mentioned items 1) and 2), can be traced back to the regularities determined for Newtonian fluids. The limits of the transition range and of the drag behavior in this range should be examined in detail.

According to the measurements of Valentik and Whitmore [2] for spheres, the following functions can be stated:

laminar $\mathrm{Re} < 8$ $\quad c_D = 24/\mathrm{Re}$ (21)

transition $8 < \mathrm{Re} < 150$ $\quad c_D = 22/\mathrm{Re} + 0.25$ (22)

turbulent $\mathrm{Re} > 150$ $\quad c_D = 0.4$ (23)

4) When yield stress τ_0 is included, the settling velocity of particles in suspensions is obtained from the force equilibrium (11) as:

$$v_s = \sqrt{\frac{2}{c_D \cdot \rho_f}\left[\frac{2}{3}(\rho_s - \rho_f) d\, g - \pi\, \tau_0\right]} \tag{24}$$

References

1 Slattery, I. C., and Bird, R. B., "Non-Newtonian Flow Past a Sphere," *Chem. Eng. Science*, Vol. 16 1961, pp. 231-241.

2 Valentik, L., and Whitmore, R. L., "The Terminal Velocity of Spheres in Bingham Plastics," *Brit. J. Appl. Phys.*, Vol. 16, 1965, pp. 1197-1203.

3 Du Plessis, P. M., and Ansley, R. W., "Settling Parameter in Solid Pipelining," *Journ. of the Pipeline Division*, Proc. Am. Soc. Civil Eng., Vol. 93, 1967, PL2, pp. 1-17.

4 Pazwash, H., and Robertson, J. M., "Forces on Bodies in Bingham Fluids," *Journ. of Hydr. Research*, Vol. 13, No. 1, 1975, pp. 35-55.

5 Brauer, H., "Grundlagen der Einphasen- und Mehrphasenströmungen," *Verlag Sauerländer Aarau und Frankfurt am Main*, 1971, pp. 143-144.

6 Metzner, A. B., and Reed, J. C., "Flow of Non-Newtonian Fluids—Correlation of the Laminar, Transition and Turbulent Flow Regions," *AICHE J.*, Vol. 1, No. 4, 1955, pp. 434-440.

Downloaded 02 Jun 2010 to 171.66.16.66. Redistribution subject to ASME license or copyright; see http://www.asme.org/terms/Terms_Use.cfm

Numerical Simulation of Fluid-Particle Flows: Geothermal Drilling Applications

R. C. Givler
Fluid Mechanics and
Heat Transfer Division 1511,
Sandia National Laboratories,
Albuquerque, NM

R. R. Mikatarian
The BDM Corporation,
Albuquerque, NM

In order to understand how a particulate plug may evolve within the flow of an essentially homogeneous suspension, we have developed a fluid-particle flow model. This theoretical model is based upon a monodisperse collection of rigid, spherical particles suspended in an incompressible, Newtonian liquid. Balance equations of mass and momentum are given for each phase within the context of a continuum mixture theory. The interactions between the phases are dominated by interfacial drag forces and unequilibrated pressure forces. The pressure associated with the solid particles is given by a phenomenological model based upon the flow dynamics. Of primary concern is the calculation of solid particle concentrations within a flow field to indicate the initiation of a particulate plug.

Introduction

During the drilling and completion of geothermal wells many problems are encountered that increase the cost of the well. One of the more difficult drilling problems to control is that of circulation loss of the drilling mud. Under normal operating conditions, the mud is pumped to the well bottom through the center of the drill pipe and returns to the surface in the annular region formed by the drill pipe and the open hole. The circulating fluid enhances the drilling operation in a number of ways which include lubrication and the removal of cuttings and heat from the drill bit. When the wellbore intersects geological strata that are severely fractured the circulating fluid can escape the confinement of the annular region and thereby flow into the formation. Even a partial loss of the circulating fluid can result in a stuck drill pipe which requires expensive remedies.

Subsurface fractures, characterized by their smallest dimension, vary in size from a few microns (porous media) to a meter or more (vugular or cavernous). Sedimentary geological formations, typical in oil and gas fields, exhibit a porous flow loss from the wellbore. Over the years the oil and gas drilling industries have developed special formulations for the drilling mud which mitigate circulation loss by the formation of an impermeable filter cake on the wellbore surface. In addition some success in plugging small fractures has been demonstrated with specially formulated shear-thickening fluids [1]. In contrast, in-situ, geothermally-active strata are typified by natural fractures and vugular regions of macroscopic dimensions. Moreover, due to the high temperatures (350–400°F) inherent in geothermal environments, many of the conventional, chemically-derived formulations for the mud do not work. For large scale cavernous voids the geological formation is often cemented and redrilled. Cementing procedures are expensive and time consuming and are preferred only after other conventional methods are exhausted. We will be concerned in this study with an intermediate fracture size whose nominal width is much less than the wellbore diameter yet greater than the diameter of a single suspended particle.

It has been proposed that intermediate-sized fractures in geothermal wells may be sealed by forming a particulate plug within the in-situ fracture. The candidate particles that are intentionally introduced into the drilling mud for this purpose must be of macroscopic size, temperature insensitive and economical; pulverized automobile battery casings are being considered as a candidate material [2]. Therefore, to determine the viability of particulate plugging mechanisms under the aforementioned conditions, we have initiated a theoretical study of fluid-particle flows. The theoretical problem becomes particularly difficult due to the wide range of solids concentrations that must be considered. One would ideally like to circulate a dilute concentration of solid particles in the wellbore, to reduce pumping pressures and minimize the chance of particle plug formation in unwanted regions such as inside the drill pipe. However, at the onset of plug formation, the local volume fraction of particles increases dramatically, thereby requiring a model which transcends the full range of concentrations from dilute to dense.

Our theoretical treatment of this problem begins with a review of the two-phase flow equations. We have considered a purely mechanical model of the flow process and therefore restrict our consideration to the balance of mass and momentum for each phase. The equation set is closed with constitutive assumptions for the interfacial drag and the solid phase pressure. In so doing we specialize the theory for rigid, spherical particles suspended in a Newtonian fluid. The transient equations are numerically solved using an explicit, flux-corrected transport (FCT) algorithm in one spatial dimension

---

Contributed by the Fluids Engineering Division of THE AMERICAN SOCIETY OF MECHANICAL ENGINEERS, and presented at the Winter Annual Meeting, Symposium on Slurry Flows, Anaheim, Calif., December 7–12, 1986. Manuscript received by the Fluids Engineering Division June 5, 1986; revised manuscript received March 25, 1987.

Copyright © 1987 by ASME

Downloaded 02 Jun 2010 to 171.66.16.66. Redistribution subject to ASME license or copyright; see http://www.asme.org/terms/Terms_Use.cfm

to reveal the features of the constitutive models. The numerical results are interpreted within the context of particulate plugging mechanisms.

Basic Equations

The type of multiphase flow that we consider in this study is comprised of solid, spherical particles suspended in a linearly viscous fluid. The particles are assumed to be rigid with constant density γ_s and of macroscopic size so that Brownian motion may be neglected. Moreover, the suspending fluid is assumed to be incompressible with density γ_f. We will consider exclusively isothermal motions of such fluid-particle systems and thereby we propose only a dynamic theory to describe the behavior of this two-phase flow.

The behavior of dispersed multiphase flow may be described by a continuum mixture theory. Such theories, which are based upon a general axiomatic framework [3], may be, in principle, expanded to include a wide range of two-phase flow problems. In particular, the mixture theory may be extended straightforwardly to include the behavior where the particle concentration exceeds the dilute limit. This is of special interest here as we endeavor to model the increase in solid particle concentration that precedes the formation of a particulate plug. Within the context of a continuum theory, the dispersed particles are modeled as an interacting continuum which we refer to as the *solid phase*. We denote a particular phase "a" to be either "s" for solid or "f" for fluid. We assume that each phase possesses a distinct density γ_a, velocity $\mathbf{v}_a$, and volume fraction ϕ_a. Moreover, at every location in space and for all time, we assume that the mixture remains saturated, viz.,

$$\phi_s + \phi_f = 1. \tag{1}$$

Each constituent of the mixture is governed by the balance laws of mass and momentum with the provision made for interactions between the phases. Thus, conservation of mass and momentum for the phases may be written, respectively, as

$$\grave{\phi}_a = -\phi_a \nabla \cdot \mathbf{v}_a, \tag{2}$$

$$\gamma_a \phi_a \grave{\mathbf{v}}_a = \nabla \cdot \mathbf{T}_a + \gamma_a \phi_a \mathbf{b}_a + \mathbf{m}_a, \tag{3}$$

where $\mathbf{T}_a$ is the constituent stress tensor defined to be the force acting on a particular phase per unit area of the phase, $\mathbf{b}_a$ is the external body force, and $\mathbf{m}_a$ is the momentum exchange vector resulting from the forces acting at the interface between phases. The backward prime (`) denotes the material derivative following the motion of a particular phase; for example

$$\grave{\phi}_a = \frac{\partial \phi_a}{\partial t} + \mathbf{v}_a \cdot \nabla \phi_a. \tag{4}$$

We assume that the phase stresses may be written as the sum of isotropic and deviatoric components given by

$$\mathbf{T}_a = -\phi_a p_a \mathbf{1} + \mathbf{T}_a^*, \tag{5}$$

where p_a is an isotropic pressure associated with a particular phase and $\mathbf{T}_a^*$ is an extra stress which results from the motion of a phase. The momentum exchange, $\mathbf{m}_s$, calculated from the forces acting over the surface of the solid particles is given by

$$\mathbf{m}_s = p_f \nabla \phi_s + \lambda(\mathbf{v}_f - \mathbf{v}_s), \tag{6}$$

where the first term in equation (6) is equivalent to the buoyant force acting on the particles [4] obtained from integrating the fluid pressure over the surface of the particles. The second term in equation (6) accounts for the drag exerted on the particles by the relative motion between the fluid and particles. We subscribe to the conventional treatment of the interaction forces [5] such that no net interaction force acts on the mixture; thus

$$\Sigma \mathbf{m}_a = 0. \tag{7}$$

Substituting equations (5)–(6) into equation (3), and noting the assumption that the only external body force is that due to gravity, renders the conservation of momentum for each of the phases as

$$\begin{aligned} \gamma_f(1-\phi_s)\grave{\mathbf{v}}_f = {} & -(1-\phi_s)\nabla p_f + \nabla \cdot \mathbf{T}_f^* \\ & + \gamma_f(1-\phi_s)\mathbf{g} - \lambda(\mathbf{v}_f - \mathbf{v}_s), \end{aligned} \tag{8}$$

$$\begin{aligned} \gamma_s \phi_s \grave{\mathbf{v}}_s = {} & -\phi_s \nabla p_s - (p_s - p_f)\nabla \phi_s \\ & + \nabla \cdot \mathbf{T}_s^* + \gamma_s \phi_s \mathbf{g} + \lambda(\mathbf{v}_f - \mathbf{v}_s). \end{aligned} \tag{9}$$

The constitutive behavior for the phase extra stresses is given by

$$\mathbf{T}_f^* = 2\mu_f(1-\phi_s)\mathbf{D}_f, \tag{10}$$

$$\mathbf{T}_s^* = 2\mu_s \phi_s \mathbf{D}_s, \tag{11}$$

where μ_f is the constant viscosity of the fluid and $\mathbf{D}_a$ is the rate of deformation tensor of a given phase defined by

$$\mathbf{D}_a = \frac{1}{2}(\nabla \mathbf{v}_a + \nabla \mathbf{v}_a^t) \tag{12}$$

where the superscript ^{t} denotes the transpose. We postpone the definition of the solid phase shear viscosity momentarily.

Empirical expressions for the friction coefficient λ, originally developed by Richardson and Zaki [6] to compute the pressure drop in particulate beds, have been extended by Wen and Yu [7] for low and moderate solids concentrations. The appropriate relationships for the friction coefficient are given by

$$\lambda = \frac{3}{4} C \phi_s |\mathbf{v}_f - \mathbf{v}_s| \gamma_f (1-\phi_s)^{-1.65}, \quad \phi_s \le 0.2 \tag{13}$$

where

Nomenclature

$\mathbf{b}$ = body force vector
$\mathbf{D}$ = rate of deformation tensor
d = particle diameter
f = function defined by equation (19)
g = gravitational acceleration
h = rectangular duct half-width
l = length of compliant segment of 1-D duct
$\mathbf{m}$ = momentum exchange vector
n = computational cell number
p = pressure
$q_0(t)$ = mixture volume flux
Re_p = particle based Reynolds number
$\mathbf{T}$ = phase stress tensor
$\mathbf{T}^*$ = phase extra stress tensor
t = time
u = velocity component in x direction
$\mathbf{v}$ = velocity vector
x' = axial coordinate along compliant duct segment
γ = material density
ζ = sphericity factor
λ = friction coefficient
μ = viscosity
ϕ = volume fraction

Subscripts

a = generic constituent
f = fluid constituent
m = mixture quantity
s = dispersed solid constituent

Downloaded 02 Jun 2010 to 171.66.16.66. Redistribution subject to ASME license or copyright; see http://www.asme.org/terms/Terms_Use.cfm

Table 1 The function $f(\phi_s)$ with increasing particle concentration derived from the theory of dense gases (after Kirkwood et al. [13])

ϕ_s	$f(\phi_s)$
0.0	1.00
0.0884	1.44
0.1563	1.91
0.2128	2.39
0.2618	2.89
0.3060	3.40
0.3443	3.91
0.3818	4.43
0.4160	4.93
0.4513	5.44
0.4835	5.95
0.5145	6.46
0.5400	6.99
0.5695	7.50
0.5968	7.93
0.7405	∞

$$C=\begin{cases}\dfrac{24}{\mathrm{Re}_p}(1+0.15\mathrm{Re}_p)^{0.687}, & \mathrm{Re}_p<1000\\[2ex] 0.44, & \mathrm{Re}_p\geq 1000\end{cases}\tag{14}$$

and Re_p is a particle Reynolds number weighted by the concentration of solids and given by

$$\mathrm{Re}_p=\frac{(1-\phi_s)\gamma_f\,|\mathbf{v}_f-\mathbf{v}_s|\,d}{\mu_f}.\tag{15}$$

The friction coefficient for large solids concentrations has also been given by Wen and Yu [7] for fluid flow through particulate beds

$$\lambda=150\frac{\phi_s^2\mu_f}{(1-\phi_s)(\zeta d)^2}+1.75\frac{\gamma_f\,|\mathbf{v}_f-\mathbf{v}_s|\,\phi_s}{\zeta d},\quad \phi_s>0.2\tag{16}$$

where d is the particle diameter and ζ is a particle shape factor taken to be unity for spherical particles. The empirical drag law detailed by equations (13-16) has been used with success by Ettehadieh et al. [8] to model numerically the hydrodynamics of fluidization in cylindrical beds.

We note from the discussion thus far, that equations (1), (2), (8), (9) provide 5 independent equations relating the 6 unknown quantities: ϕ_s, ϕ_f, $\mathbf{v}_s$, $\mathbf{v}_f$, p_s, and p_f. This symptomatic occurrence in multiphase flow modeling represents the classical closure problem. The dilemma may be resolved by introducing an independent relationship between the distinct phase pressures. Ramifications of this approach have been investigated by Stuhmiller [9], Prosperetti and Jones [10], and Nunziato [5] among others. The merit of introducing a consitutive model for the phase pressure difference resides in the additional physics of the flow process that can be modeled. Moreover, certain choices for the constitutive equation for the phase pressure difference can affect the stability of the mathematical solution for the two-phase flow equations [9].

We propose a phenomenological model for the pressure associated with the solid phase according to

$$p_s=p_f+p_s'\tag{17}$$

where p_s' is defined as a kinematic pressure of the solid phase given explicitly as

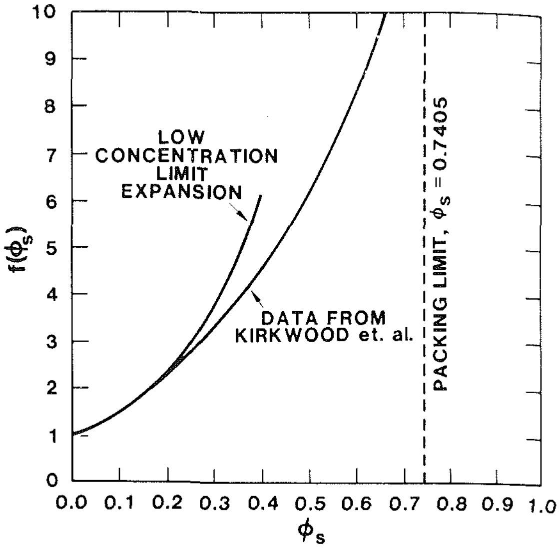

Fig. 1 The variation of f with solids volume fraction for rigid spheres (from the data of Kirkwood et al. given in Table 1); data from Kirkwood et al. is asymptotic to the maximum packing limit. The low concentration limit expansion is given by equation (19).

$$p_s'=\frac{1}{2}\gamma_f f(\phi_s)(\mathbf{v}_f-\mathbf{v}_s)\cdot(\mathbf{v}_f-\mathbf{v}_s).\tag{18}$$

In modeling fluid-particle flows one is often confronted with the idea of a pressure associated with the dispersed phase. If the concentration of the solid particles is small then it is common practice to consider only a fluid pressure. In this instance, the gradient of the solid pressure is deleted from the solid phase momentum equation. This is justified since the volume fraction of the fluid phase is assumed to remain near unity. However, in the current study, we anticipate that the concentration of solid particles in certain regions of the flow will far exceed the dilute limit as a plug evolves from a homogeneous concentration of particles. At this point particle interactions, either through direct contact or the interacting of local disturbance flow fields, become important and the postulation of a solid phase kinematic pressure becomes meaningful. The existence of interactions among suspended particles is usually dictated by the viscosity of the interstitial or carrier fluid [11]. For the problems we consider here, the viscosity of the fluid is less than 1 poise which, based upon general experience, implies that particle interactions are important.

An examination of eqs. (17)-(18) indicates that the solid phase pressure exceeds the fluid pressure by an inertial correction. The function $f(\phi_s)$ accounts for the increased interactions among the particles as the concentration increases giving rise to an increase in kinematic pressure. To determine the precise form for the factor $f(\phi_s)$ we associate the behavior of our macroscopic suspension with that of a dense gas composed of rigid, spherical particles of finite size. Enskog [12] has shown that the frequency of collisions among the molecules of a dense gas differs from that of a gas composed of point particles by the factor

$$f(\phi_s)=1+4\phi_s+10\phi_s^2+18.36\phi_s^3+29.44\phi_s^4 + \ldots \quad \phi_s<0.1\tag{19}$$

The expansion given by equation (19) is valid for low and moderate concentrations of gas molecules and is illustrated in Fig. 1. The increase in collisional frequency can be related to increases in the effective transport properties such as shear and bulk viscosities, thermal conductivity, and self-diffusion characteristics. For higher concentrations the form of the function $f(\phi_s)$ can be obtained from the data of Kirkwood et

Downloaded 02 Jun 2010 to 171.66.16.66. Redistribution subject to ASME license or copyright; see http://www.asme.org/terms/Terms_Use.cfm

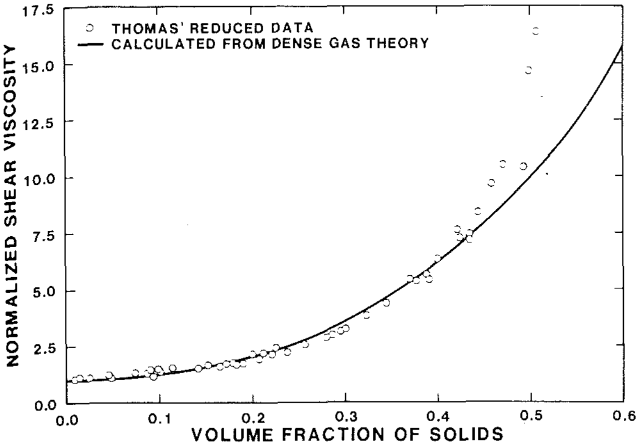

Fig. 2 A comparison between the reduced shear viscosity data of Thomas for macroscopic suspensions and the predictions from dense gas theory [14]

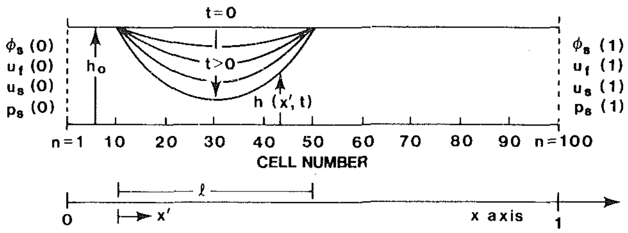

Fig. 3 One-dimensional, two-phase flow in a variable area duct. The compliant boundaries simulate a constriction in the flow as a function of time.

al. [13] shown in Table 1 and plotted as a function of concentration in Fig. 1. Their data have been calculated from the radial distribution function describing the frequency of collisions in dense gases. From equation (18) we note the following: (i) the kinematic pressure vanishes when there is no relative motion between the phases, (ii) the solid pressure rises dramatically with increasing concentration near the packing limit as is apparent from Fig. 1; this effect is inherently diffusive on particulate concentrations and will inhibit particulate plug formation, and (iii) the existence of a kinematic pressure is associated with a rise in the kinetic energy of the relative flow field. Thus, we take the function $f(\phi_s)$ to be given by equation (19) or interpolated from the data in Table 1 in the case where the solids concentration exceeds 0.1.

While the analogy between the molecular motion of dense gases and the flow of concentrated suspensions is not exact, the data seem to suggest that a useful correlation does indeed exist. In Fig. 2 we show the normalized shear viscosity calculated from the theory of dense gases and experimental data for a suspension of macroscopic, spherical particles. The theoretical calculation for the normalized shear viscosity, μ_m/μ_f, is based upon equation (9.3-41) from Hirschfelder et al. [14] for the transport properties of dense gases comprised of rigid sheres. This expression may be rewritten as

$$\mu_m/\mu_f = 4\phi_s\left(\frac{1}{f(\phi_s)-1} + 0.8 + 0.767(f(\phi_s)-1)\right)$$

where $f(\phi_s)$ is given by either equation (19) for low values of concentration or Table 1 otherwise. The solid curve illustrates the increase in shearing viscosity due to the presence of the particles and is calculated directly from the kinetic theory of dense gases which utilizes both equation (19) and the data of Kirkwood et al. [13]. This calculation is compared to the reduced data of Thomas [15] for measurements of the shear viscosity of macroscopic suspensions with increasing concentration in capillary and rotational viscometers. The agreement is very good for all concentrations with the notable exception at high concentrations ($\phi_s > 0.5$) where the comparison is suspect due to the quoted differences in maximum packing limits: $\phi_{s_{\text{Max}}} = 0.74$ in the case of dense gas theory versus $\phi_{s_{\text{Max}}} = 0.63$ in the case of Thomas' data. The latter corresponds to the packing limit for a collection of randomly packed, uniform spheres. In view of the comparisons in Fig. 2, there is strong evidence that the functional form for $f(\phi_s)$, although derived from the kinetic theory of dense gases, describes the transport properties of suspensions.

Finally, we calculate the solid phase viscosity, μ_s, by noting from the mixture theory [5] that

$$\mu_m = (1-\phi_s)\mu_f + \phi_s\mu_s, \tag{20}$$

where μ_m is the mixture viscosity. Rearrangement of equation (20) yields an expression for the solid phase viscosity given by

$$\mu_s = \frac{\mu_m}{\phi_s} - \frac{(1-\phi_s)}{\phi_s}\mu_f. \tag{21}$$

The shear viscosity of the mixture, normalized with respect to the shear viscosity of the fluid, is given by the results illustrated in Fig. 2. Definitions for other transport properties of the solid phase may be constructed in a similar manner.

One-Dimensional Simulation

The balance laws given by equations (2, 8–9) in conjunction with the constitutive assumptions, equations (10–11, 17), and empirical drag law, equations (13–16), form the model for our study of fluid-particle flows. Even for the case of a single spatial dimension, one must resort to a numerical technique to solve this set of equations because of the inherent nonlinearities in the constitutive and interfacial drag equations. In this section we address the problem of one-dimensional, two-phase flow in a variable area duct. The treatment of this problem serves to illustrate certain physical features of the model that become less transparent in multidimensional flows. Moreover, the simplicity of a one-dimensional problem enables one to understand better the relationship between the problem physics and the numerical method.

The problem of interest is depicted graphically in Fig. 3. Initially, a homogeneous concentration of spherical particles, suspended in a Newtonian fluid, is flowing in a duct with constant cross-sectional area. The flow is in the positive x direction. The phase velocities and the solids concentration are assumed to remain uniform across the entry and exit boundaries with the particles, in general, lagging the fluid. A portion of the duct wall ($10 \leq n \leq 50$) is assumed to be compliant so that the associated cross-sectional area varies directly with the change in the duct width, viz.,

$$h(x,t) = \begin{cases} h_0 & n < 10 \\ h_0 - h_0 t \sin\left(\dfrac{x'\pi}{l}\right) & 10 \leq n \leq 50 \\ h_0 & n > 50 \end{cases} \tag{22}$$

where n is the computational cell number, h_0 is the initial duct half-width, l is the length of the compliant segment and t is time. Thus, the constriction increases with time and has a sinusoidal profile over the length l. We wish to investigate the effect of the time-dependent constriction on the formation of a particle plug and isolate the mechanisms responsible for the increase/decrease in solid particle concentration.

In one spatial dimension, the balance of mass equations for the solid and fluid phases reduce respectively to

$$\frac{\partial}{\partial t}\phi_s + \frac{\partial}{\partial x}(\phi_s u_s) = 0, \tag{23}$$

Downloaded 02 Jun 2010 to 171.66.16.66. Redistribution subject to ASME license or copyright; see http://www.asme.org/terms/Terms_Use.cfm

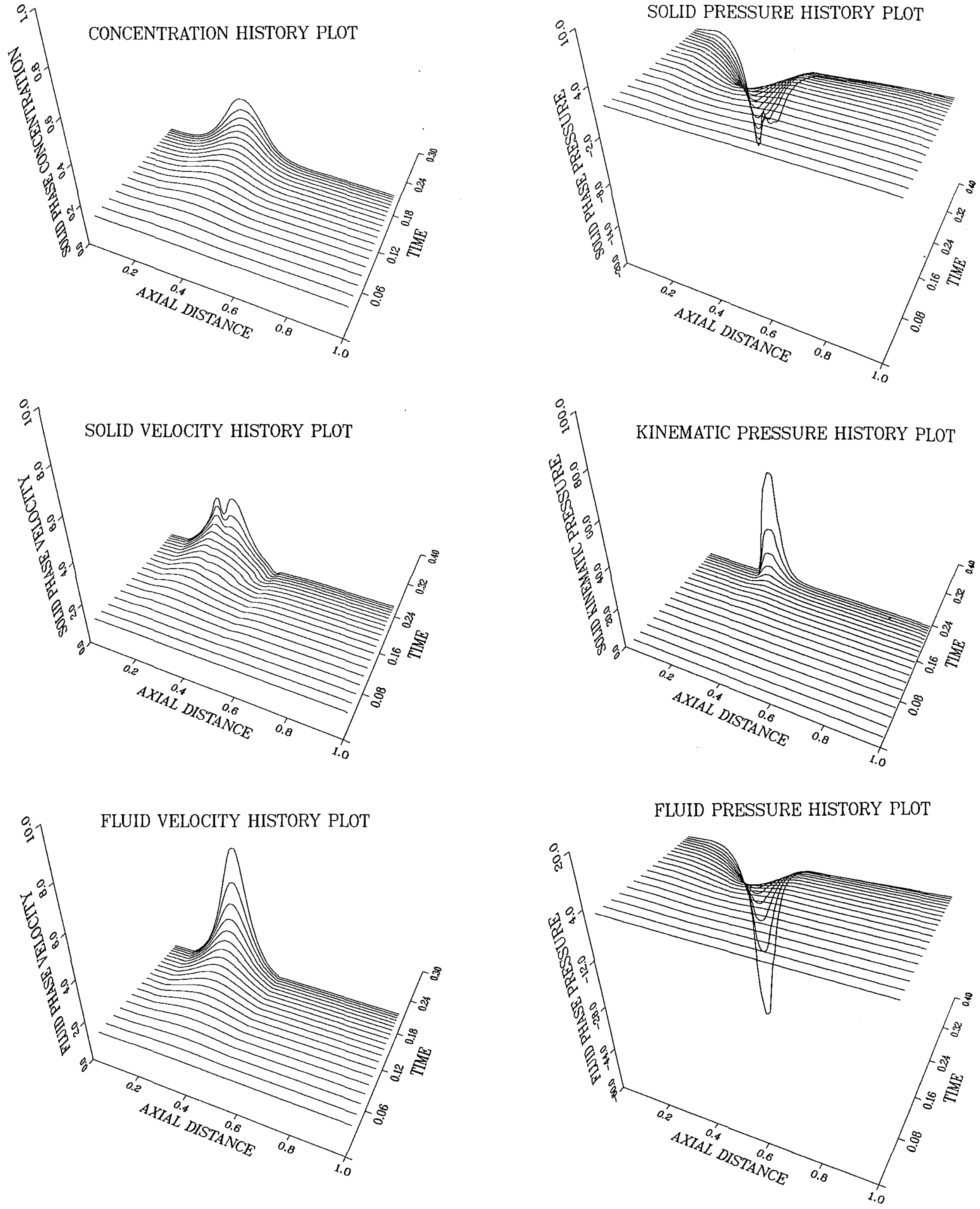
CONCENTRATION HISTORY PLOT

SOLID PRESSURE HISTORY PLOT

SOLID VELOCITY HISTORY PLOT

KINEMATIC PRESSURE HISTORY PLOT

FLUID VELOCITY HISTORY PLOT

FLUID PRESSURE HISTORY PLOT

Fig. 4 Numerical results for a one-dimensional particle plugging simulation; the behavior of the fluid-particle system is dominated by interfacial pressure forces; from top to bottom and left to right: (*a*) solid particle concentration, (*b*) solid particle velocity, (*c*) fluid velocity, (*d*) solid phase pressure, (*e*) solid phase kinematic pressure, (*f*) fluid pressure

$$\frac{\partial}{\partial t}(1-\phi_s)+\frac{\partial}{\partial x}((1-\phi_s)u_f)=0. \tag{24}$$

In the absence of viscous stresses for either phase the solid and fluid momentum equations are given by

$$\frac{\partial}{\partial t}(\phi_s u_s)+\frac{\partial}{\partial x}(\phi_s u_s u_s)=$$

$$-\frac{\phi_s}{\gamma_s}\frac{\partial p_s}{\partial x}-\frac{p_s'}{\gamma_s}\frac{\partial \phi_s}{\partial x}-\phi_s g+\frac{\lambda}{\gamma_s}(u_f-u_s), \tag{25}$$

Downloaded 02 Jun 2010 to 171.66.16.66. Redistribution subject to ASME license or copyright; see http://www.asme.org/terms/Terms_Use.cfm

$$\frac{\partial}{\partial t}((1-\phi_s)u_f)+\frac{\partial}{\partial x}((1-\phi_s)u_fu_f)=$$

$$-\frac{(1-\phi_s)}{\gamma_f}\frac{\partial p_f}{\partial x}-(1-\phi_s)g-\frac{\lambda}{\gamma_f}(u_f-u_s). \qquad (26)$$

For this one-dimensional flow we assume that the body force due to gravity opposes the flow, $\mathbf{b}_a=(-g,0)$. Because of the relative simplicity of this one-dimensional equation set we may reduce the number of equations which must be integrated numerically in space and time. Combining equation (23) and equation (24) yields an expression for the fluid velocity

$$u_f=\frac{q_0(t)-\phi_s u_s}{(1-\phi_s)}, \qquad (27)$$

where $q_0(t)$ is the mixture volume flux which enters the duct. The fluid pressure may be eliminated by adding equation (25) and equation (26) which gives

$$\frac{\partial}{\partial t}(\phi_s u_s+(1-\phi_s)u_f)+\frac{\partial}{\partial x}(\phi_s u_s u_s+(1-\phi_s)u_fu_f)$$

$$=-\frac{\phi_s}{\gamma_s}\frac{\partial p_s}{\partial x}-\frac{p_s'}{\gamma_s}\frac{\partial \phi_s}{\partial x}-\frac{(1-\phi_s)}{\gamma_f}\frac{\partial p_f}{\partial x}$$

$$-g+\left(\frac{\lambda}{\gamma_s}-\frac{\lambda}{\gamma_f}\right)(u_f-u_s). \qquad (28)$$

The divergence of equation (28) in conjunction with the fact that $\partial/\partial x(\phi_s u_s+(1-\phi_s)u_f)=0$ renders equation (28) of the form

$$\frac{\partial^2 p_s}{\partial x^2}+\left(\frac{(\gamma_s-\gamma_f)}{\phi_s(\gamma_s-\gamma_f)-\gamma_s}\frac{\partial \phi_s}{\partial x}\right)\frac{\partial p_s}{\partial x}=$$

$$\frac{\gamma_s\gamma_f}{\phi_s(\gamma_s-\gamma_f)-\gamma_s}\frac{\partial}{\partial x}\left(-\frac{(1-\phi_s)}{\gamma_f}\frac{\partial p_s'}{\partial x}+\frac{p_s'}{\gamma_s}\frac{\partial \phi_s}{\partial x}\right.$$

$$\left.-\lambda\frac{\gamma_f-\gamma_s}{\gamma_s\gamma_f}(u_f-u_s)+\frac{\partial}{\partial x}(\phi_s u_s u_s+(1-\phi_s)u_fu_f)\right). \qquad (29)$$

Equations (23), (25), and (29) comprise the model system in the three unknowns ϕ_s, u_s, and p_s. Conservation of mass and momentum of the solid phase, equations (23) and (25), are discretized with finite differences and advanced explicitly in time with a sixth order, flux corrected transport algorithm developed by Boris and Book [16] and recently refined by Gross and Baer [17]. This algorithm is extremely efficient and adept at handling the convective transport[1] terms on the left side of equations (23) and (25). The terms on the right side of equation (25) are treated as source terms. The time scales associated with the source terms may be calculated to ensure that the convective transport is numerically stable; the equations have been advanced with a Courant number of 0.1 based upon a characteristic velocity and the cell size. An analysis of the characteristics of the model equations is presented in the Appendix. The solid phase pressure is calculated from the elliptic equation, equation (29), at each time step with a second-order finite difference approximation. The resulting tridiagonal system of algebraic equations is solved with the Thomas [19] algorithm. The fluid velocity and fluid pressure are computed using equations (27) and (18), respectively.

In order to gain insight into the formation of a particulate plug, we compare the quantitative features of the model when pressure forces or interfacial drag forces dominate the two-phase flow process, respectively. Typical numerical results for the one-dimensional particle plugging simulation are illustrated in Fig. 4. The initial conditions as well as the boundary conditions imposed at the entry and exit sections were $u_f=1$, $u_s=0.9$, $\phi_s=0.1$ and $p_s=1$. The fluid viscosity, which affects the friction coefficient was maintained at 0.00001 and the diameter of the suspended particles was $d=0.05$.[2] The

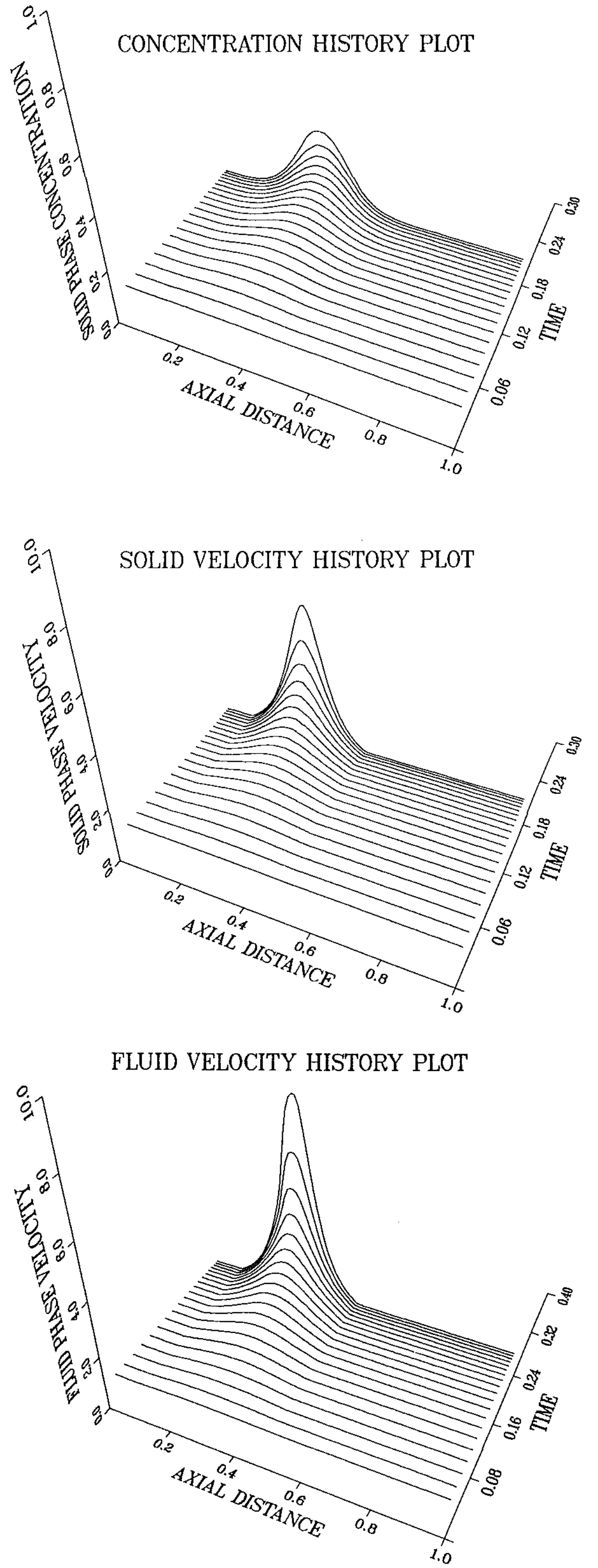

CONCENTRATION HISTORY PLOT

SOLID VELOCITY HISTORY PLOT

FLUID VELOCITY HISTORY PLOT

Fig. 5 Numerical results for a one-dimensional particle plugging simulation; the behavior of the fluid-particle system is dominated by interfacial drag forces; from top to bottom: (*a*) solid particle concentration, (*b*) solid particle velocity, (*c*) fluid velocity

---

[1] Stewart and Wendroff [18] point out that successful numerical schemes for two-phase flow modeling are based upon on effective treatment of the convective transport terms.

[2] Units are defined consistently with the (cgs) system

Downloaded 02 Jun 2010 to 171.66.16.66. Redistribution subject to ASME license or copyright; see http://www.asme.org/terms/Terms_Use.cfm

constriction was reduced to a value of 15 percent of the initial duct width during 300 time steps corresponding to a total of 0.236 s. This initial data represents a flow situation where pressure forces on the solid particles are dominant.

The increase in particle concentration shown in Fig. 4(*a*) is caused by the reduction in fluid pressure through the constriction. The fluid pressure acts on the solid particles through the definition of the solid pressure, equation (17). The first term on the right side of equation (25) imparts an increase in momentum to the particles as they enter the constriction and correspondingly decreases the momentum upon exiting. The net result is an increase in the particle concentration in the constriction.

At elevated concentration levels the second term on the right side of equation (25) becomes large which tends to diffuse the concentration peak. This effect is visible by a reduction in the peak solid velocity near the end of the simulation. The maximum solids concentration in the constriction for the initial conditions of Fig. 4 was 0.49.

Figure 5 is indicative of the numerical results when the two-phase flow is dominated by interfacial drag. All initial/boundary conditions remain the same as previously defined with the following exceptions: $d=0.01$ and $\mu_f=0.001$. Despite the initial disparity in phase velocities, the relatively high drag between phases rapidly equilibrates the phase velocities. Also, it is seen from Fig. 5(*a*) that the shape of the concentration pulse is less diffuse. At equal times during the simulation the drag-dominated, concentration profiles are higher than before. Cases with intermediate proportions of drag and pressure forces can be inferred from the two cases discussed here.

Conclusions

A theory based upon the hydrodynamics of fluid-particle flows and formulated from continuum mixture ideas provides a basis for the development of a model for particulate plug formation. While the proposed model is incapable of predicting the fluid-particle behavior at extreme particle concentrations, $\phi_s > 0.5$ (plug compaction problem), several one-dimensional simulations do offer insight into the mechanisms responsible for plug formation.

Acknowledgments

The authors wish to acknowledge the assistance of R. J. Gross and M. R. Baer during the implementation of the numerical techniques. Also, initial discussions with A. Auslender contributed to the development of the two-phase plugging model. This work was supported by the U.S. Department of Energy under contract DE-AC04-76DP00789.

References

1 Hamburger, C. L., Yuh-Hwang, T., Drake, E. N., and Morrison, M. E., "Development and Application of a New Fluid for Stopping Unwanted Flows In and Around Wellbores," *SPE 12122, Proc. 58th Annual Technical Conference*, San Francisco, CA, 1983.

2 Caskey, B. C., and Loeppke, G. E., "Lost Circulation in Geothermal Wells: Research and Development Status," *Geothermal Resources Council Transactions*, Vol. 7, 1983, pp. 403-407.

3 Truesdell, C., *Rational Thermodynamics*, Second Edition, Springer-Verlag, New York, 1984.

4 Raats, P. A. C., "Forces Acting Upon the Solid Phase of a Porous Medium," *ZAMP*, Vol. 19, 1968, pp. 606-613.

5 Nunziato, J. W., "A Multiphase Mixture Theory for Fluid-Particle Flows," *Theory of Dispersed Multiphase Flow*, R. E. Meyer, Ed., Academic Press, New York, 1983, pp. 191-226.

6 Richardson, J. F., and Zaki, W. N., "Sedimentation and Fluidization: Part 1," *Trans. Inst. Chem. Engrs.*, Vol. 39, 1961, p. 175.

7 Wen, C. Y. and Yu, Y. H., "Mechanics of Fluidization," *Chem. Eng. Prog. Symp. Ser.*, Vol. 62, 1966, p. 100.

8 Ettehadieh, B., Gidaspow, D., and Lyczkowski, R. W., "Hydrodynamics of Fluidization in a Semicircular Bed with a Jet," *AIChE Journal*, Vol. 30, 1984, pp. 529-536.

9 Stuhmiller, J. H., "The Influence of Interfacial Forces on the Character of Two-Phase Flow Model Equations," *Int. J. Multiphase Flow*, Vol. 3, 1977, pp. 551-560.

10 Prosperetti, A. and Jones, A. V., "Pressure Forces in Disperse Two-Phase Flow," *Int. J. Multiphase Flow*, Vol. 10, 1984, pp. 425-440.

11 Metzner, A. B., "Rheology of Suspensions in Polymeric Liquids," *J. Rheology*, Vol. 29, 1985, pp. 737-775.

12 Chapman, S. and Cowling, T. G., *The Mathematical Theory of Non-Uniform Gases*, Cambridge University Press, 1939, Chapter 16.

13 Kirkwood, J. G., Maun, E. K., and Adler, B. J., "Radial Distribution Functions and the Equation of State of a Fluid Composed of Rigid Spherical Molecules," *J. Chem. Physics*, Vol. 18, 1950, pp. 1040-1047.

14 Hirschfelder, J. O., Curtiss, C. F., and Bird, R. B., *Molecular Theory of Gases and Liquids*, Wiley, New York, 1954, p. 647.

15 Thomas, D. G., "Non-Newtonian Suspensions, Part 1: Physical Properties and Laminar Transport Characteristics," *Ind. Eng. Chem.*, Vol. 55, 1963, pp. 18-29.

16 Boris, J. P., and Book, D. L., "Flux-Corrected Transport: Part I. SHASTA: A Fluid Transport Algorithm That Works," *J. Comp. Phys.*, Vol. 11, 1973, pp. 38-69.

17 Gross, R. J., and Baer, M. R., "ETBFCT: A Solver for One-Dimensional Transport Equations," SAND85-1273, Sandia National Laboratories Technical Report, Oct. 1985.

18 Stewart, H. B., and Wendroff, B., "Two-Phase Flow: Models and Methods," *J. Comp. Phys.*, Vol. 56, 1984, pp. 363-409.

19 Blottner, F. G., "Introduction to Computational Techniques for Boundary Layers," SAND79-0893, Sandia National Laboratories Technical Report, Apr. 1981.

20 Gidaspow, D., "Modeling of Two-Phase Flow," Proc. Round Table Discussion RT-1-2, Fifth Int. Heat Transfer Conference, Tokyo, Japan, Sept. 3-7, 1974; *Heat Transfer 1974*, Vol. VII, 1974, p. 163.

21 Ramshaw, J. D. and Trapp, J. A., "Characteristics, Stability, and Short-Wavelength Phenomena in Two-Phase Flow Equation Systems," ANCR-1272, Aerojet Nuclear Company Technical Report, 1976.

APPENDIX

It has been known since early studies on multiphase flows that model systems which possess complex characteristics are ill-posed and generate unstable solutions [20, 21, 9]. Many approaches to correct this dilemma have been the subject of numerous studies within the two-phase flow community. We illustrate here that the inclusion of a phenomenologically motivated pressure for the solid phase renders real characteristics of the model equation set. Moreover, the calculation of the characteristics precisely determines the time step needed for numerical evaluation of the equations.

The characteristics of the model set (equations (23) and (25)) may be computed most directly by recasting the equations in terms of conserved variables defined by the vector $\mathbf{w}=(\phi_s, \phi_s u_s)$ so that equations (23) and (25) may be written compactly as

$$\mathbf{A}\frac{\partial \mathbf{w}}{\partial t}+\mathbf{B}\frac{\partial \mathbf{w}}{\partial x}+\mathbf{c}(\mathbf{w})=0. \qquad (A1)$$

For the particular equation set under consideration the matrices which enter into the characteristic analysis may be identified as

$$\mathbf{A}=\mathbf{1}, \quad \mathbf{B}=\begin{bmatrix} 0 & 1 \\ b_{21} & b_{22} \end{bmatrix},$$

where

$$b_{21}=-u_s^2(1-\beta)+\frac{p_s'(1-\beta)}{\gamma_s}-\beta\left(u_f^2-\frac{(1-\phi_s)}{\gamma_f}\,\frac{\partial p_s'}{\partial \phi_s}\right),$$

$$b_{22}=2u_s(1-\beta)+\beta\left(2u_f-\frac{f(\phi_s)}{\phi_s}(u_f-u_s)\right),$$

for which $\beta=\phi_s\gamma_f/(\phi_s\gamma_f+(1-\phi_s)\gamma_s)$ and $f(\phi_s)$ is given by equation (19). It is useful to note that $0\le\beta\le 1$.

The characteristic roots of equation (A1) are the solutions of the quadratic equation $\det(\mathbf{B}-\alpha\mathbf{A})=0$, which may be expanded to yield

$$\alpha^2-b_{22}\alpha-b_{21}=0. \qquad (A2)$$

Note that the vector **c** does not enter into the characteristic

Downloaded 02 Jun 2010 to 171.66.16.66. Redistribution subject to ASME license or copyright; see http://www.asme.org/terms/Terms_Use.cfm

analysis. It follows that the characteristic roots of equation ($A2$) are given by

$$\alpha = u_s + \beta(u_f - u_s)\left(1 - \frac{f(\phi_s)}{2\phi_s}\right) \pm (u_f - u_s)\sqrt{\Omega}, \qquad (A3)$$

where Ω is the discriminant of equation ($A2$) given by $(b_{22}^2/4 + b_{21})$ which is given by

$$\Omega = \beta^2 + \beta^2 \frac{f(\phi_s)}{\phi_s}\left(\frac{f(\phi_s)}{4\phi_s} - 1\right) + \beta(f(\phi_s) - 1) + \frac{\gamma_f}{2\gamma_s} f(\phi_s)(1-\beta) + \frac{\beta}{2}(1-\phi_s)\frac{\partial f(\phi_s)}{\partial \phi_s}. \qquad (A4)$$

The characteristics of equation ($A1$) will be real provided $\Omega \geq 0$; this is true for all parameter values provided two conditions on the function $f(\phi_s)$ are satisfied, viz.,

$$f(\phi_s) \geq 1 + 4\phi_s,$$

$$\frac{\partial f(\phi_s)}{\partial \phi_s} \geq 0. \qquad (A5)$$

Inspection of equation (19) verifies that the criteria specified in equation ($A5$) are satisfied; hence the characteristics for the model equation set are real. It has been illustrated by Stuhmiller [9] that two-phase flow equations based upon equal pressures lead to ill-posed problems. This, in fact, can be reaffirmed from our development here where from equation ($A4$) we observe that if $f(\phi_s)$ is taken to be zero (which implies equal phase pressures), then

$$\Omega = \beta(\beta - 1).$$

In this instance Ω is never positive thereby yielding complex characteristics. Thus, a two-phase flow model based solely upon equal pressures leads to initial value problems with complex characteristics.

Finally, we acknowledge the admonition by Ramshaw and Trapp [21] that real characteristics do not guarantee stability. Rather a system of equations with real characteristics imparts stability to short-wavelength disturbances in space and time which is a necessary condition for properly posed problems. Instabilities which do occur for problems with real characteristics are of physical nature and are *not* due to ill-posedness or numerical artifacts. A better understanding of the overall stability of the model system proposed in this paper can be obtained from a thorough stability analysis, which is yet to be completed.

Downloaded 02 Jun 2010 to 171.66.16.66. Redistribution subject to ASME license or copyright; see http://www.asme.org/terms/Terms_Use.cfm

Numerical Calculations of the Breakup of Highly Loaded Slurry Jets

M. Situ
Research Engineer,
Beijing Research Institute,
Beijing, China

J. A. Schetz
Professor and Department Head,
Department of Aerospace and Ocean
Engineering,
Virginia Polytechnic Institute and State
University,
Blacksburg, Va.

A complete numerical calculation procedure for predicting the effects of mass loading and particle diameter on laminar slurry jet breakup in a low velocity, coaxial gas stream has been developed. The method is based on the Volume of Fluid technique for the Navier-Stokes equations. The severe restrictions involved in earlier treatments have been relaxed. The influence of particle loading on liquid phase density and the influence of particle spacing on drag are included. The particular case considered is a slurry with a methanol liquid phase with aluminum oxide beads in order to compare with some related experimental results. The methanol liquid in the slurry is vaporized due to mass transfer in the gas stream. The variation of the instantaneous jet shape of the methanol slurry jet at low loadings is generally similar to that of an all-liquid methanol jet, but the final shapes at breakup are different. In the region of low mass loading (up to 20 percent), the effects of mass loading are to stabilize the interface and increase the breakup time of the slurry jet with increasing mass loading. Above that region of mass loading (more than 20 percent), the effects of mass loading are to destabilize the interface and decrease the breakup time of the slurry jet with increased mass loading. At the same mass loading condition, a slurry jet with large diameter particles has a more stabilizing effect than one with small diameter particles. Therefore, a slurry jet with higher mass loading and smaller diameter particles breaks up faster.

Introduction

By adding metal powders to liquid fuels, the energy per unit volume of the fuel can be greatly increased. That fact has long been recognized. Jet engines that burn slurry fuels could be compact and yet possess high specific thrust, high speed, and high continuous thrust. This increase in heat per unit volume could affect a significant increase in range or decrease in the size of a missile propulsion system. Another application for slurry fuels is pulverized coal as the solid constituent in oil or water to fuel gas turbine and internal combustion engines.

The fundamental nature of liquid fuel injection has received much attention and is now understood well enough to produce efficient liquid fuel jet engines. But, the problems of slurry injection and combustion have yet to be adequately resolved, especially for highly loaded slurry jets. The present computational study was undertaken to study the fundamental similarities and differences between the breakup of liquid and slurry jets with different loadings. This work was directed toward analyzing the behavior of the idealized case of laminar, lightly loaded and highly loaded slurry jets injected into a gas stream including mass and heat transfer.

Slurry jet breakup and droplet formation with the effects of heat and mass transfer are complicated phenomena, especially in the complex real flowfields in engines. The problem is complex even under idealized conditions. The laminar liquid jet has been extensively investigated analytically using approximate solutions. A great many experimental investigations have also been performed. The earliest analysis of liquid jets was published by Rayleigh [1]. Weber [2] attempted to extend Rayleigh's analysis to include viscosity. Other researchers have conducted further analyses and experiments [3-8], and recently, numerical solutions for simplified flow conditions have been found. A clear precis of low loading slurry jet breakup is presented by Ogg and Schetz [9]. Liquid jet breakup in a gas stream with mass and heat transfer has been studied by Situ, Hewitt, and Schetz [10-12].

The present work is an attempt to develop a numerical calculation of the breakup and subsequent droplet formation for low and highly loaded laminar slurry jets issuing into a gas stream with mass and heat transfer. All thermodynamic and transport properties in the flowfield are treated as variables expressed as functions of the temperature and the component mass fraction. It is assumed that the solid particles are not vaporized because the temperature in the flowfield is too low. A numerical code for solving the unsteady Navier-Stokes equations for flows with a free surface, developed by Los Almos Scientific Laboratories [13], was modified extensively by the addition of energy and diffusion equations for the gas stream, particle phase equations in the liquid-solid flow and suitable boundary conditions on the interface in the gas

---

Contributed by the Fluids Engineering Division of THE AMERICAN SOCIETY OF MECHANICAL ENGINEERS and presented at the Winter Annual Meeting, Symposium on Slurry Flows, Anaheim, Calif., December 7-17, 1986. Manuscript received by the Fluids Engineering Division June 12, 1986; revised manuscript received March 25, 1987.

Copyright © 1987 by ASME

Downloaded 02 Jun 2010 to 171.66.16.66. Redistribution subject to ASME license or copyright; see http://www.asme.org/terms/Terms_Use.cfm

flowfield for flows with mass transfer. Also, the most restrictive assumptions corresponding to low loadings used in earlier work have been relaxed here.

In order to compare the detailed results for different mass loaded slurry jets with previous results for all-liquid methanol jet breakup, the slurry is taken here as a methanol liquid phase with aluminum oxide beads. The methanol in the slurry can be vaporized due to heat and mass transfer with the gas stream. For perspective, it is important to note that the calculations described above take long computer times, thus we could not investigate all the effects of wave number (*WN*) and other factors on the breakup of the slurry jets within the limits of our computer budget. The somewhat limited results obtained in present work are useful since they show some important phenomena and point to directions for further work.

Mathematical and Numerical Analysis

The full, viscous equations of motion were required for the slurry jet to model the nonlinear effects of the free surface for large amplitudes as well as to model interactive forces between the liquid and solid phases. For the heat and mass transfer problem, the liquid at the interface vaporizes, and the vapor is entrained into the gas stream through convection and diffusion. The liquid and gas motion are assumed laminar. The temperature of the slurry jet has to be determined by a heat balance. Axisymmetric, nearly incompressible motion and "compressible" solid particle motion with heat and mass transfer are governed by the following equations.

Liquid,

$$\frac{1}{\rho_F C_F^2}\frac{\partial p_F}{\partial t}+\nabla\cdot\bar{v}_F=0 \tag{1}$$

$$\frac{\partial \bar{v}_F}{\partial t}+(\bar{v}_F\cdot\nabla)\bar{v}_F=\bar{g}-\frac{1}{\bar{\rho}_F}\nabla P_F+\frac{\mu_F}{\rho_F}\nabla^2\bar{v}_F-K_m\left(\frac{\rho_p}{\rho_F}\right)F(\bar{v}_F-\bar{v}_p) \tag{2}$$

$$\frac{\partial T_F}{\partial t}+\bar{v}_F\cdot(\nabla T_F)=\left(\frac{k_F}{\rho_F C_{PF}}\right)\nabla^2 T_F \tag{3}$$

Gas,

$$\frac{1}{\rho_g C_g^2}\frac{\partial p_g}{\partial t}+\nabla\cdot\bar{v}_g=0 \tag{4}$$

$$\frac{\partial \bar{v}_g}{\partial t}+(\bar{v}_g\cdot\nabla)\bar{v}_g=\bar{g}-\frac{1}{\rho_g}\nabla p_g+\frac{\mu_g}{\rho_g}\nabla^2\bar{v}_g \tag{5}$$

$$\frac{Dm_j}{Dt}=D_{av}\nabla^2 m_j \tag{6}$$

$$\frac{DT_g}{Dt}=\left(\frac{k_g}{\rho_g C_{Pg}}\right)\nabla^2 T_g+\frac{1}{\rho_g C_{Pg}}\nabla\cdot\left(\rho_g\sum_j D_{av}h_j\nabla m_j\right) \tag{7}$$

Solid particle,

$$\frac{\partial \rho_p}{\partial t}+\nabla\cdot(\rho_p\bar{v}_p)=0 \tag{8}$$

$$\frac{\partial \bar{v}_p}{\partial t}+(\bar{v}_p\cdot\nabla)\bar{v}_p=F(\bar{v}_F-\bar{v}_p)-\frac{1}{\bar{\rho}_p}\nabla p_F \tag{9}$$

$$\frac{\partial T_p}{\partial t}+\bar{v}_p\cdot(\nabla T_p)=\left(\frac{k_p}{\rho_p C_{P_p}}\right)\nabla^2 T_p \tag{10}$$

The treatment of the fluid and gas dynamical aspects of the present problem parallels the treatment in references [10] and [14] for all-liquid jets. The treatment of solid particle dynamics extends the treatment in references [9] following suggestions in reference [15]. Here, assuming that the particles are all the same size and sparsely distributed, there is negligible interaction between particles. Thus, the particle momentum equation is free of any viscous terms, and the particles in the slurry are treated as a continuous, compressible, fluid-like phase cohabiting the volume with the liquid constituent of the slurry. The volume displaced by the particle phase is not considered negligibly small for highly-loaded slurries. Because of this, the density of the liquid phase ρ_F is not equal to the liquid phase material density $\bar{\rho}_F$, but it can be considered that the density of the liquid phase is uniform throughout the flowfield. The volume ν_F occupied by the liquid phase is given by the relation

$$\nu=\nu_F+\nu_p=\nu_F+\nu\frac{\rho_p}{\bar{\rho}_p}$$

where ν_p is the volume occupied by the solid particles. Then, we get the apparent local density of the liquid phase,

$$\rho_F=\bar{\rho}_F\left(1-\frac{\nu_p}{\nu}\right)=\bar{\rho}_F\left(1-\frac{\rho_p}{\bar{\rho}_p}\right) \tag{11}$$

Assuming a relative loading $E=1-\rho_p/\bar{\rho}_p$, equation (11) is $\rho_F=E\bar{\rho}_F$. For example, if $E=0.8$, then $\nu_p=0.2\,\nu$, this means that loading is 20 percent. Only for a system of extremely low fraction solid does $\rho_F\approx\bar{\rho}_F$. Therefore, the density of the liquid for a highly loaded slurry jet will be changed, and the particle phase behaves similar to a compressible fluid without a pressure term [15]. In the above equations, F is the time constant of fluid-particle interaction;

Nomenclature

a = jet radius
A = perturbation amplitude
A_0 = initial perturbation amplitude
C = adiabatic speed of sound
C_D = drag coefficient
C_P = specific heat at constant pressure
D = jet diameter
D_{av} = diffusion coefficient
E = relative loading, $\left(1-\frac{\rho_p}{\bar{\rho}_p}\right)$
F = time constant of momentum transfer
$\bar{g}$ = vector of body acceleration
k = thermal conductivity
K_m = momentum transfer effectiveness
p = pressure
R = radius of solid particle
Re = Reynolds number
t = time
T = temperature and nondimensional time
u, v = radial and axial fluid velocity component, respectively
$\bar{v}$ = velocity vector
WN = wave number, λ/D
ρ = local density
$\bar{\rho}$ = material density
μ = viscosity
λ = wavelength
σ = coefficient of surface tension
ν = volume

Subscripts

a = air
B = breakup
F = fluid
g = gas
j = component
p = solid phase
v = vapor phase

Downloaded 02 Jun 2010 to 171.66.16.66. Redistribution subject to ASME license or copyright; see http://www.asme.org/terms/Terms_Use.cfm

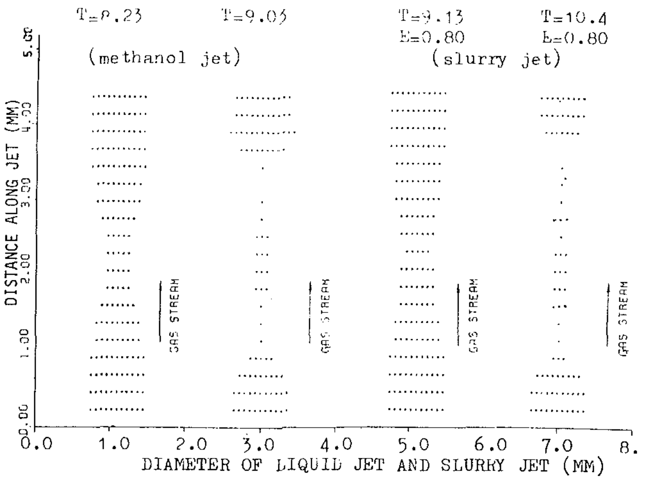

Fig. 1 Fluid configuration calculated for methanol jet and slurry jet (v_a = 2.0m/s, WN = 5.43, T_F = 302 K, T_a = 299 K, R = 0.01 mm).

$$F=\frac{3}{8}\,C_D\,(\bar{\rho}_F/\bar{\rho}_p)\left(\frac{\bar{v}_F-\bar{v}_p}{R}\right),$$

where C_D is the drag coefficient at relative speed $(\bar{v}_F-\bar{v}_p)$, and R is the particle radius. Using the Stokes drag law and considering the effect of particle loading on the drag coefficient, we get

$$C_D=\frac{24}{\mathrm{Re}}\times 10^{2.65\,(1-E)} \tag{12}$$

Here, we have used a curve fit to the drag data of reference [15]. Thus, F becomes a function of E and R based on the properties of the fluid phase and the particles

$$F=\frac{9}{2}\,\frac{\mu_F}{\bar{\rho}_p R^2}\times 10^{2.65\,(1-E)} \tag{13}$$

The effectiveness of momentum transfer K_m from solid particles to the liquid is assumed to be unity [15].

The treatment of the mesh boundaries, interface boundaries, thermodynamic, transport properties and free surface aspects of the present problem closely parallel the treatment in references [10] and [14]. The reader should consult those references for details. The emphasis here is on the treatment of the interaction between the liquid and solid particles and the effects of a highly loaded particle cloud on slurry jet breakup. In order to compare the highly loaded slurry jet breakup with the liquid jet breakup results from reference [10], the wave number, $WN(=\lambda/D)$, was fixed at WN = 5.43. The computational grid used was 20 × 20 cells; the solid-liquid slurry occupied about 40 percent of the total cells, and the gas occupied the other part of the total. The computational region is one wavelength long.

Numerical Results

For the selection of a representative case for the calculations, one would like to have a set of conditions that had been studied experimentally. That would enable a direct comparison of predictions and observations. Unfortunately, we known of no experiment that fits the idealized flow problem under study here – a laminar, highly loaded-slurry jet in a low-speed gas stream with heat and mass transfer. In an earlier work (references [9] and [16]), one of us (JAS) conducted experiments and calculations on slurry jets in quiescent air or issuing across a supersonic stream, but those results are not very useful for comparison with the present numerical results. In another earlier work (reference [10]), we conducted experiments for a vaporizing laminar, liquid (methanol) jet in a gas stream. Our numerical calculations for that case were in good agreement with the experimental observations. We have, therefore, chosen to make calculations for a similar methanol jet vaporizing in a gas stream without and with solid particles. Direct comparison of those results enables one to document the effects of high particle loading on the jet breakup process.

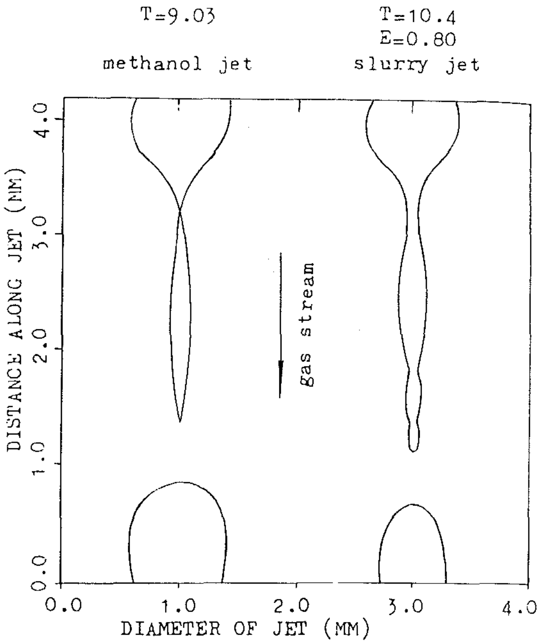

Fig. 2 Numerical prediction of a slurry jet surface shape compared with a surface shape of methanol jet at v_a = 2.0m/s, WN = 5.43, T_F = 302 K, T_a = 299 K, R = 0.01 mm. At breakup.

Nondimensional time T is determined by

$$T=t\left(\frac{\sigma}{\bar{\rho}_F D^3}\right)^{1/2}.$$

The initial surface perturbation amplitude/jet diameter was set at 0.0005. The predicted instantaneous shapes of the slurry jet surface for cases with an air velocity of 2.0 m/s and an imposed disturbance with a wavelength of 5.43 jet diameters, both for a methanol jet and a slurry jet of 20 percent particles loading are shown in Figs. 1 and 2. Figure 1 shows the instantaneous shapes of the methanol and slurry jets from the numerical solution plotted by computer before and at breakup. Figure 2 shows the detailed shapes at jet breakup, when the nondimensional time is 9.03 for the methanol jet and 10.4 for the slurry jet with loading 20 percent. The jet shapes are slightly different. The swells of the waves are on the extreme top and bottom of the graph, and in the middle are the necks of the jet waves. At advanced times, as a satellite drop grows at the second neck, this region becomes the swell of the satellite droplet. It can be seen that for this low-loaded slurry jet (20 percent), the effect of the particle cloud on the jet interface has a stabilizing effect, and the shape of the slurry jet is slightly thinner than that of the methanol jet. The slurry jet also has several necks in the middle region.

For highly loaded slurry jets, the instantaneous jet shapes are very different. Figure 3 shows the jet shapes from the numerical solution plotted by computer for loadings of 20, 40, and 45 percent. The swells on the highly-loaded slurry jet are much larger. The detailed shapes of the all-methanol and two slurry jets for loading 20 and 40 percent are compared in Fig. 4. It can be seen that the shapes are very different at roughly the same nondimensional time. The highly-loaded slurry jet has a large center swell and shows a destabilizing effect. The highly loaded slurry jet also does not have more than one neck appearing in the middle region. The highly loaded slurry jet required larger amplitudes than the liquid jets to achieve regular breakup. This means that the highly loaded slurry jet breakup produces a larger droplet, and it is difficult to have satellite

Downloaded 02 Jun 2010 to 171.66.16.66. Redistribution subject to ASME license or copyright; see http://www.asme.org/terms/Terms_Use.cfm

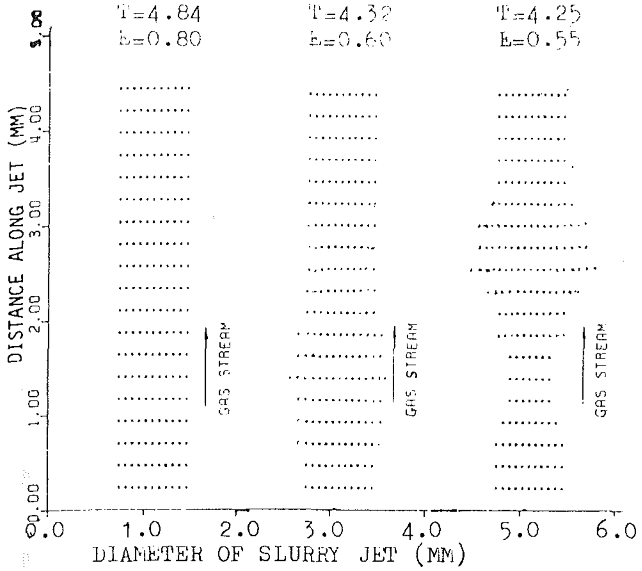

Fig. 3 Fluid configuration calculated for slurry jets of different mass loadings ($v_a = 2.0$m/s, $WN = 5.43$, $T_F = 302$ K, $T_a = 299$ K, $R = 0.01$ mm).

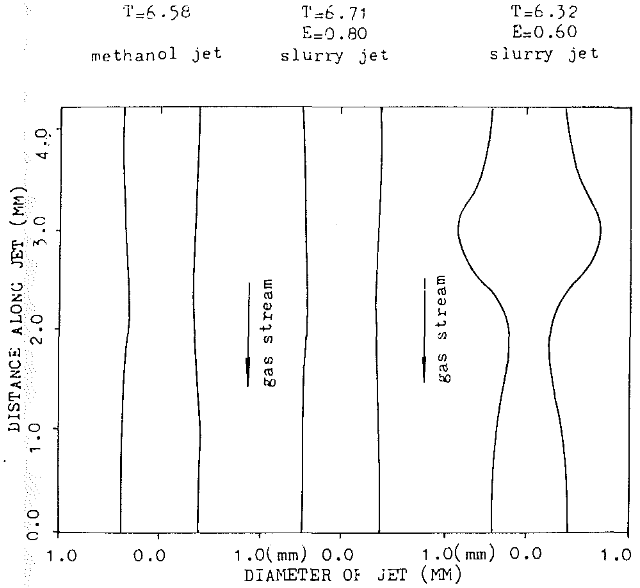

Fig. 4 Numerical prediction of slurry jet surface shape compared with a surface shape of methanol jet at $v_a = 2.0$m/s, $WN = 5.43$, $T_F = 302$ K, $T_a = 299$ K, $R = 0.01$ mm

drops. As suggested in reference [15], we found that the radial velocity of the particles is less than that of the liquid, so the solid particles concentrate in the inner region away from the jet surface.

The relation of the nondimensional perturbation amplitude against nondimensional time is shown in Figs. 5 and 6. The curves on Fig. 5 represent the effects of particle loading on the nondimensional disturbance amplitude growth. It is obvious that for the slurry jet with low particle loading (20 percent), the growth rate of the swells of the slurry jet is less than that of the methanol jet. The contraction rate of the neck of the slurry jet is also less than that of the methanol jet. These curves are both similar, but the curves for the slurry jet show a more nonlinear influence, and the nondimensional perturbation amplitude of the swell of the slurry jet is less than that of the methanol jet. Both decrease and are actually less than the initial value, 0.0005, due to gas flow, vaporization and the effect of the particle cloud. Inversely, a very different phenomena is found for the highly loaded slurry jet (45 percent). As indicated above, the highly loaded slurry jet has a larger swell, and the growth rate of the swell is fast. The contraction rate of the neck of the highly loaded slurry jet is also more rapid. The nondimensional breakup time of the highly loaded slurry jet is less than that of the all-methanol jet. It is clear that the effects of the nonlinear characteristic of the highly loaded slurry jet are very strong.

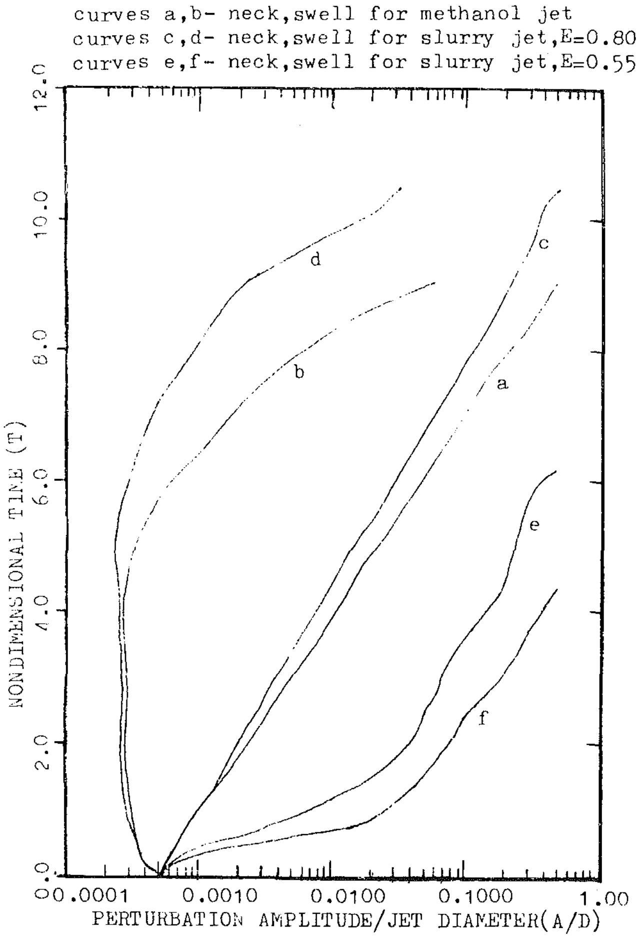

Fig. 5 Perturbation amplitude of the slurry jets with different mass loadings plotted against nondimensional time ($v_a = 2.0$m/s, $WN = 5.43$, $T_F = 302$ K, $T_a = 299$ K, $R = 0.01$ mm).

At the same loading, if the diameter of the solid particles is smaller, the particle cloud has a large number of solid particles. In Fig. 6, we show the effects of particle diameter on a low-loaded slurry jet (10 percent). It can be seen that the actions of the larger particles on the low-loaded slurry jet has a stabilizing effect. It requires a slightly longer breakup time, because the particle diameter influences the nonlinear terms in the momentum equations.

Seven cases for slurry jets with different loadings were calculated. The numerical results for breakup time for different loading slurry jets are shown in Fig. 7. It is clear that the breakup times of slurry jets slowly increase with increasing particle loadings in the region of 0–20 percent loadings. Beyond a 20 percent loading, one finds an inverse influence, because the nonlinear terms in the momentum equations, which are caused by the interaction between the particles and liquid, and the local liquid density influence the perturbation amplitude and breakup time for highly loaded slurry jets strongly.

Discussion

The main purpose of this study was to investigate the effects of different particle loadings on the instability and breakup of

Downloaded 02 Jun 2010 to 171.66.16.66. Redistribution subject to ASME license or copyright; see http://www.asme.org/terms/Terms_Use.cfm

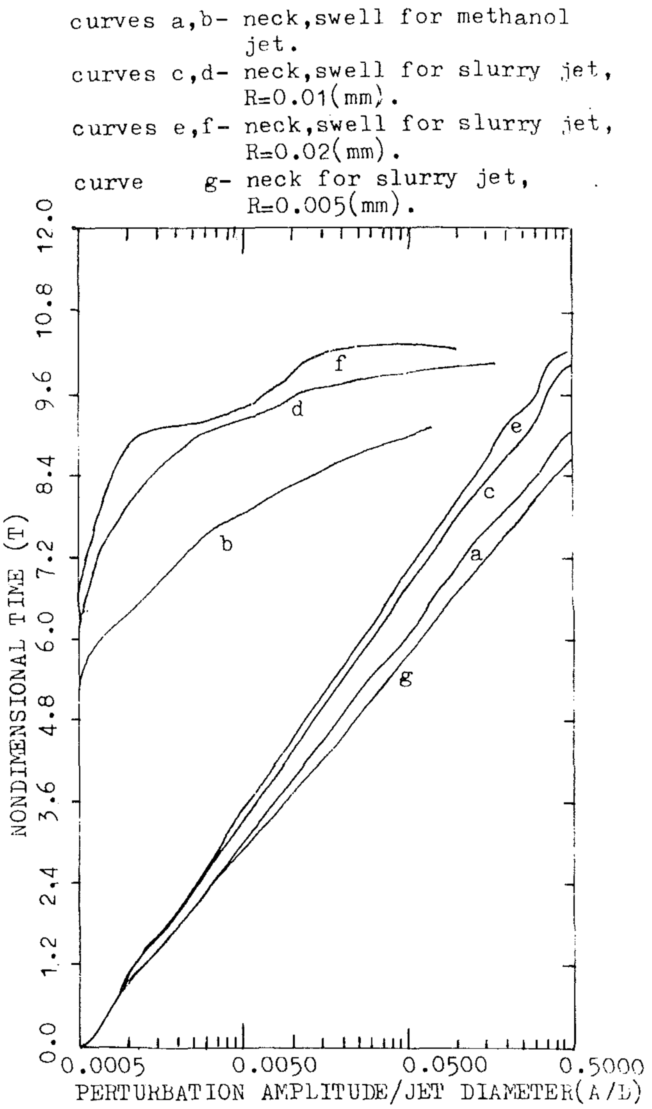

Fig. 6 Perturbation amplitude of the slurry jets with different particle diameter plotted against nondimensional time ($v_a = 2.0$m/s, $WN = 5.43$, $T_F = 302$ K, $T_a = 299$ K, $E = 0.90$).

a slurry jet, especially for highly loaded slurry jets.

In all the regimes of different loaded slurry jets, a small axisymmetric perturbation that is spatially sinusoidal along the length of the slurry jet column grows and thus causes breakup, but the phenomena of breakup and droplet formation vary for the different loading regimes in slurry jets. It was found in the region of low particle loadings that the basic effect of the addition of solid particles is to decrease the growth rate of the disturbance. Perhaps most importantly, the addition of a solid phase greatly enhances the damping action on the disturbance of the liquid phase. For the highly loaded slurry jet, the solid particle motion has the most important effects on the liquid motion. It causes an increase of the velocity of the liquid phase and thus increases the growth rate of the swells and the contraction rate of the necks and decreases the breakup time to form a larger droplet.

At a fixed particle loading, the variation of the diameter of solid particles influences the time constant of fluid-particle interactions. Slurry jets with large particle diameters show a stabilizing effect and increase the breakup time.

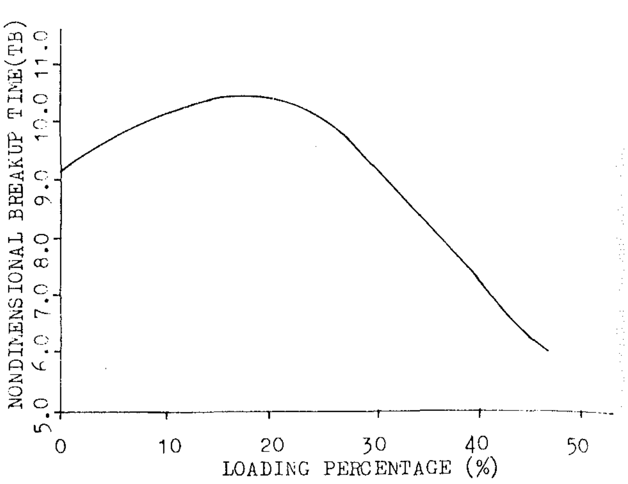

Fig. 7 Nondimensional breakup time of slurry jet plotted against mass loadings of particles

It can be seen that this numerical solution procedure can predict the highly-loaded slurry jet breakup and droplet formation including the complex effects of surface mass transfer in a gas stream.

References

1 Rayleigh, L., "On the Instability of Jets," *Proceedings of the London Mathematical Society*, Vol. 10, 1878.

2 Weber, C., "Zum Zerfall eines Flussigkeitsstrahles," *Zeitschrift fuer Angewandte Mathematik und Mechanik*, Vol. 11, No. 3, 1931.

3 Joshi, P. B., and Schetz, J. A., "Hydrodynamic Stability of Liquid Films Adjacent to Incompressible Gas Stream Including Effects of Interface Mass Transfer," VPI-Aero-058, AFOSR-74-2584, 1976.

4 Chandrasekhar, S., *Hydrodynamic and Hydromagnetic Stability*, 1961, Clarendon Press, Oxford, England, 1961; Republished by Dover Publications, New York, 1981.

5 Crane, L., Birch, S., and McCormack, P. D., "The Effect of Mechanical Vibration on the Break-up of a Cylindrical Water Jet in Air," *British Journal of Applied Physics*, Vol. 15, 1964, p. 743.

6 Shokoohi, F., "Numerical Investigation of the Disintegration of Liquid Jets," PhD. dissertation, Columbia University, New York, 1976.

7 Bogy, D. B., "Drop Formation in a Circular Liquid Jet," *Annual Review of Fluid Mechanics*, Vol. 11, 1979, pp. 207–228.

8 Goedde, E. F., and Yuen, M. C., "Experiments on Liquid Jet Instability," *Journal of Fluid Mechanics*, Vol. 40, 1970, pp. 495–511.

9 Ogg, J. C., and Schetz, J. A., "Breakup and Droplet Formation of Slurry Jets," *AIAA Journal*, Vol. 23, No. 3, 1985, p. 432.

10 Situ, M., and Schetz, J. A., "Computational and Experimental Study of the Effect of Mass Transfer on Liquid Jet Breakup," *AIAA Journal*, Vol. 23, No. 2, 1985, p. 254.

11 Situ, M., and Schetz, J. A., "Computational Study of Ignition and Combustion Effects of Liquid Fuel Jet Breakup," AIAA-84-1180, 20th Joint Propulsion Conference.

12 Schetz, J. A., Hewitt, P. W., and Situ M., "Transverse Jet Breakup and Atomization with Rapid Vaporization Along the Trajectory," *AIAA Journal*, Vol. 23, No. 4, 1985, p. 596.

13 Nichols, B. D., Hirt, C. W., and Hotchkiss, R. S., "SOLA-VOF: A Solution Algorithm for Transient Fluid Flow with Multiple Free Boundaries," University of California, Los Angeles, Rept. LA-8355, 1980.

14 Situ, M., and Schetz, J. A., "A Computer Program for Liquid Jet Breakup with the Mass and Heat Transfer in Coaxial, Gas Streams," VPI-Aero-135, Oct. 1983.

15 Soo, S. L., *Fluid Dynamics of Multiphase Systems*, Blaisdell, Waltham, Maine, 1967.

16 Less, D. M., and Schetz, J. A., "Penetration and Breakup of Slurry Jets in a Supersonic Stream," *AIAA Journal*, Vol. 21, No. 7, July 1983, p. 1045.

Downloaded 02 Jun 2010 to 171.66.16.66. Redistribution subject to ASME license or copyright; see http://www.asme.org/terms/Terms_Use.cfm